Astrophysical and Geophysical Flows as Dynamical Systems
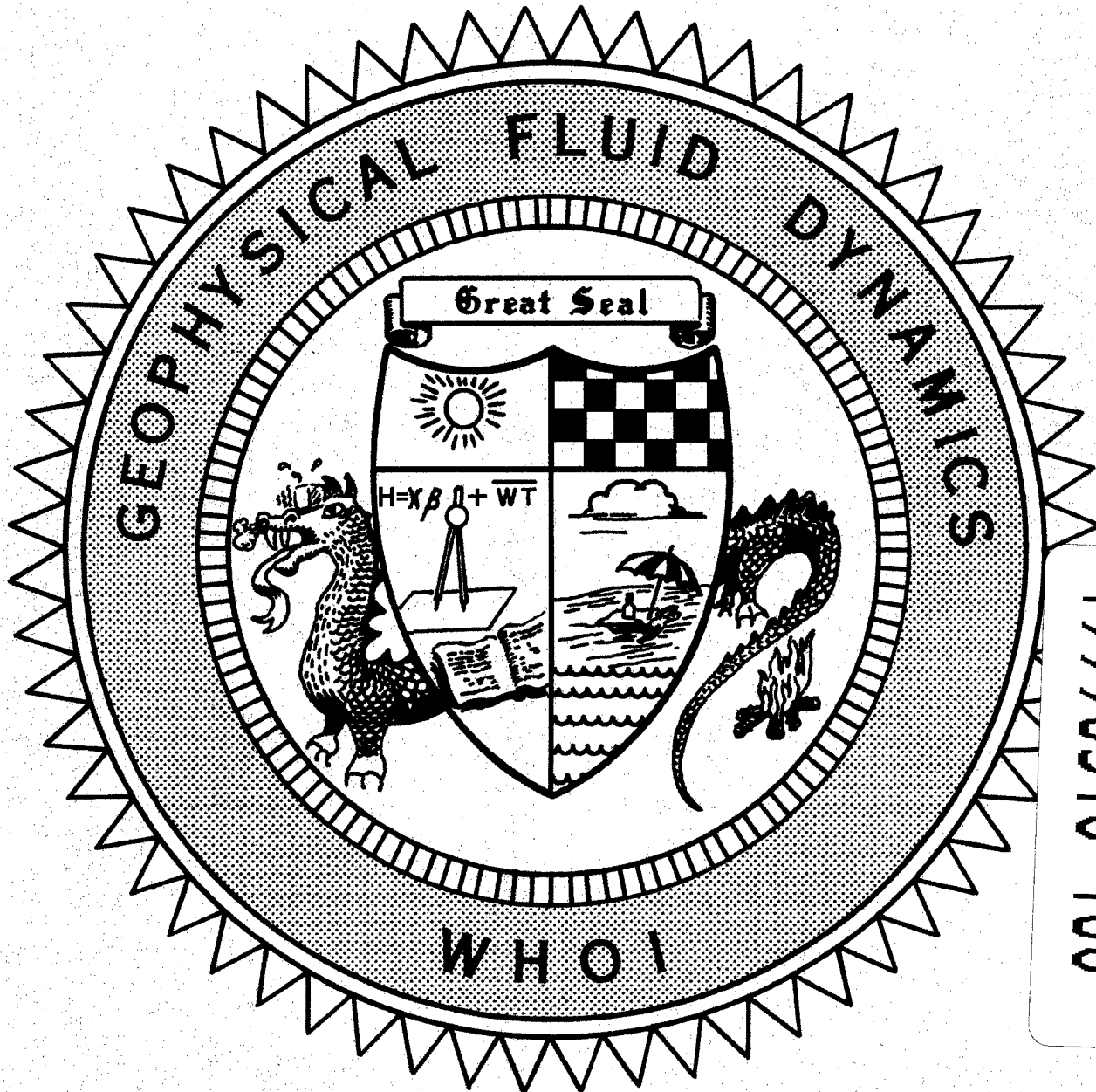
1998 Summer Study Program in Geophysical Fluid Dynamics

Great Seal

$H = \chi\beta\Omega + \overline{WT}$

GEOPHYSICAL FLUID DYNAMICS

WHOI

**Course Lectures
Fellows Project Reports**

Astrophysical and Geophysical Flows as Dynamical Systems; 1998 Summer Study Program in Geophysical Fluid Dynamics

by

Neil J. Balmforth, Director

Woods Hole Oceanographic Institution
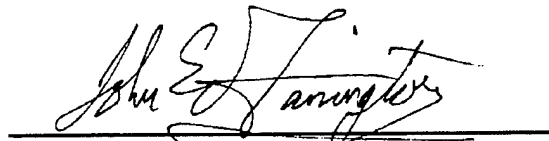Woods Hole, Massachusetts 02543

January 1999

Technical Report

Approved for Distribution:

_____

John W. Farrington
Education

PREFACE

Astrophysical and Geophysical Flows as Dynamical Systems was the theme of the 1998 GFD Summer Program. With Antonello Provenzale at the helm we sailed headlong into the nonlinear world of astrophysical and geophysical fluid mechanics. Simultaneously, Charles Tresser gave several energetic presentations surrounding the dynamics of circle maps.

Unfortunately our third planned speaker, John David Crawford, fell ill just prior to the program and could not participate. Sadly, John David passed away later in the summer. We will remember him at GFD from the excellent lectures he gave at the cottage during the summer of 1993.

In a departure from usual practice, and in an effort to lend more coherence to the, at times, very wide ranging topics discussed at Walsh, GFD '98 included three "theme weeks." The first, championed by Steve Meacham, organized a week long series of lectures on climate dynamics. Alastair Rucklidge subsequently gathered together several experts on bifurcation and pattern theory. Lastly, Diego del Castillo-Negrete organized the "Mixing Week." These themes, and especially the third, proved so popular that we doubled the total number of visitors to the program.

In tandem to the extensive seminar schedule, the Fellows progressed significantly in their projects; their reports reflect the impressive progress made. Overall, I believe that 1998 was a particularly productive summer.

Of the participants, Steve Meacham and Eric Chassignet deserve special mention for the maintainance of the computer network. Mike Shelley was voted by the Fellows to be the most helpful "tool" amongst the staff. Jean-Luc Thiffeault and Joe Biello were especially appreciated by the Fellows and greatly assisted with the preparation of the GFD proceedings. Lastly, I am indebted to Lee Anne Campbell, the real organizer of the summer. It is also my pleasure to acknowledge the support of the Woods Hole Oceanographic Institution, especially John Farrington and the Education Office, and the National Science Foundation and the Office of Naval Research for the financial backing of the program.

Finally, this summer saw the election of Philip J. Morrison to the GFD Steering Committee. I emphasize that this decision was not solely due to his expertise at softball.

N. J. Balmforth
Director

i

CONTENTS

V   FELLOW'S LECTURES, continued

1998 GFD Fellows, Staff and Visitors

The Fellows

Aaron C. Birch	Stanford University
Sarah L. Dance	Brown University
Blanca Gallego	University of California at Los Angeles
Andrew R. Jacobson	Pennsylvania State University
Panayotis Kevrekidis	Rutgers University
Andrew E. Kiss	Australian National University, AUSTRALIA
Carolyn R. Mockett	Scripps Inst. of Oceanography, Univ. of Calif. at San Diego
Claudia Pasquero	Istituto di Cosmogeofisica, Torino, ITALY
Mark S. Roulston	California Institute of Technology
Amy Qing Shen	University of Illinois at Urbana-Champaign

Staff and Visitors

Alistair Adcroft	Massachusetts Institute of Technology
James L. Anderson	Stevens Institute of Technology
Steven D. Antinucci	Columbia University
Steven Balbus	University of Virginia
Neil J. Balmforth	Scripps Inst. of Oceanography, Univ. of Calif. at San Diego
Andrew J. Bernoff	Harvey Mudd College
Joseph A. Biello	University of Chicago
Kenneth P. Bowman	Texas A&M University
Annalisa Bracco	Istituto di Cosmogeofisica, Torino, ITALY
J. Robert Buchler	University of Florida
Alexander Casti	Columbia University
Paola Cessi	Scripps Inst. of Oceanography, Univ. of Calif. at San Diego
Eric P. Chassignet	University of Miami
Jon Xinzhong Chen	Columbia University
Stephen W. Childress	New York University
Chad Coulliette	California Institute of Technology
Richard Craster	Imperial College, UK
Diego del Castillo-Negrete	Scripps Inst. of Oceanography, Univ. of Calif. at San Diego
Charles Doering	University of Michigan
Robert J. Douglas	University of Reading, UK
Jinqiao Duan	Clemson University
John M. Finn	Los Alamos National Labs
Glenn Flierl	Massachusetts Institute of Technology
Rupert Ford	Imperial College, UK
Claude J. Frankignoul	Massachusetts Institute of Technology
Anand Gnanadesikan	Princeton University

Peter Goldreich	California Institute of Technology
Jerry Gollub	Haverford College
Jason Goodman	Woods Hole Oceanographic Institution
Jost Graf von Hardenberg	Istituto di Cosmogeofisica, Torino, ITALY
Rainer Hollerbach	University of Glasgow, UK
Louis N. Howard	Florida State University
James W. Hurrell	National Center For Atmospheric Research
Andrew P. Ingersoll	California Institute of Technology
Edward R. Johnson	University College of London, UK
Christopher Jones	Brown University
Keith Julien	University of Colorado at Boulder
Joseph B. Keller	Stanford University
Sun-Chul Kim	Chung-Ang University, KOREA
Sergey Kravtsov	Florida State University
Juergen Kurths	Universitat Potsdam, GERMANY
Yochanan Kushnir	Lamont-Doherty Earth Observatory, Columbia University
Norman R. Lebovitz	University of Chicago
Anthony Leonard	California Institute of Technology
Stefan G. Llewellyn Smith	University of Cambridge, UK
Willem V.R. Malkus	Massachusetts Institute of Technology
Aldo Manfroi	Scripps Inst. of Oceanography, Univ. of Calif. at San Diego
Jochem Marotzke	Massachusetts Institute of Technology
Stephen Meacham	Massachusetts Institute of Technology
Ian Melbourne	University of Houston
Patrick D. Miller	Stevens Institute of Technology
Philip J. Morrison	University of Texas at Austin
Keith Ngan	University of Chicago
Anatoly B. Odulo	Applied Science Associates, Inc.
Edward Ott	University of Maryland
Nathan Paldor	Hebrew University of Jerusalem, ISRAEL
Matheos P. Papadakis	University of Miami
Francesco Paparella	Woods Hole Oceanographic Institution
Andrew Poje	Brown University
Vakhtang Poutkaradze	University of Chicago
Joana Prat	University Politecnica de Catalunya, SPAIN
Kevin Prendergast	Columbia University
Michael Proctor	University of Cambridge, UK
Antonello Provenzale	Istituto di Cosmogeofisica, Torino, ITALY
Vered Rom-Kedar	Weizmann Institute of Science, ISRAEL
Claes G. Rooth	University of Miami
Alastair Rucklidge	University of Cambridge, UK

George Schmidt	Stevens Institute of Technology
Michael J. Shelley	New York University
Leonard Smith	University of Oxford, UK
Tom Solomon	Bucknell University
Andrew M. Soward	University of Exeter, UK
Lynn C. Sparling	Goddard Space Flight Center
Michel Speetjens	Eindhoven University of Technology, the NETHERLANDS
Edward A. Spiegel	Columbia University
Melvin Stern	Florida State University
Harry Swinney	University of Texas at Austin
Ronald Taam	Northwestern University
Patrick Tabeling	Ecole Normale Superieure, FRANCE
Louis Tao	Columbia University
Roger M. Temam	Indiana University
Jean-Luc Thiffeault	University of Texas at Austin
Charles Tresser	IBM - T.J. Watson Research Labs
Eli Tziperman	Weizmann Institute of Science, ISRAEL
Orkan Matt Umurhan	Columbia University
Jeff S. Urbach	Georgetown University
George Veronis	Yale University
Martin Visbeck	Lamont-Doherty Earth Observatory, Columbia University
Shouhong Wang	Indiana University
Jeffrey Weiss	University of Colorado
Jack Whitehead	Woods Hole Oceanographic Institution
Steve Wiggins	California Institute of Technology
Sean M. Winkler	Brown University
Rodney A. Worthing	University of Michigan
Philip A. Yecko	University of Florida
William R. Young	Scripps Inst. of Oceanography, Univ. of Calif. at San Diego
Yuan-Nan Young	University of Chicago
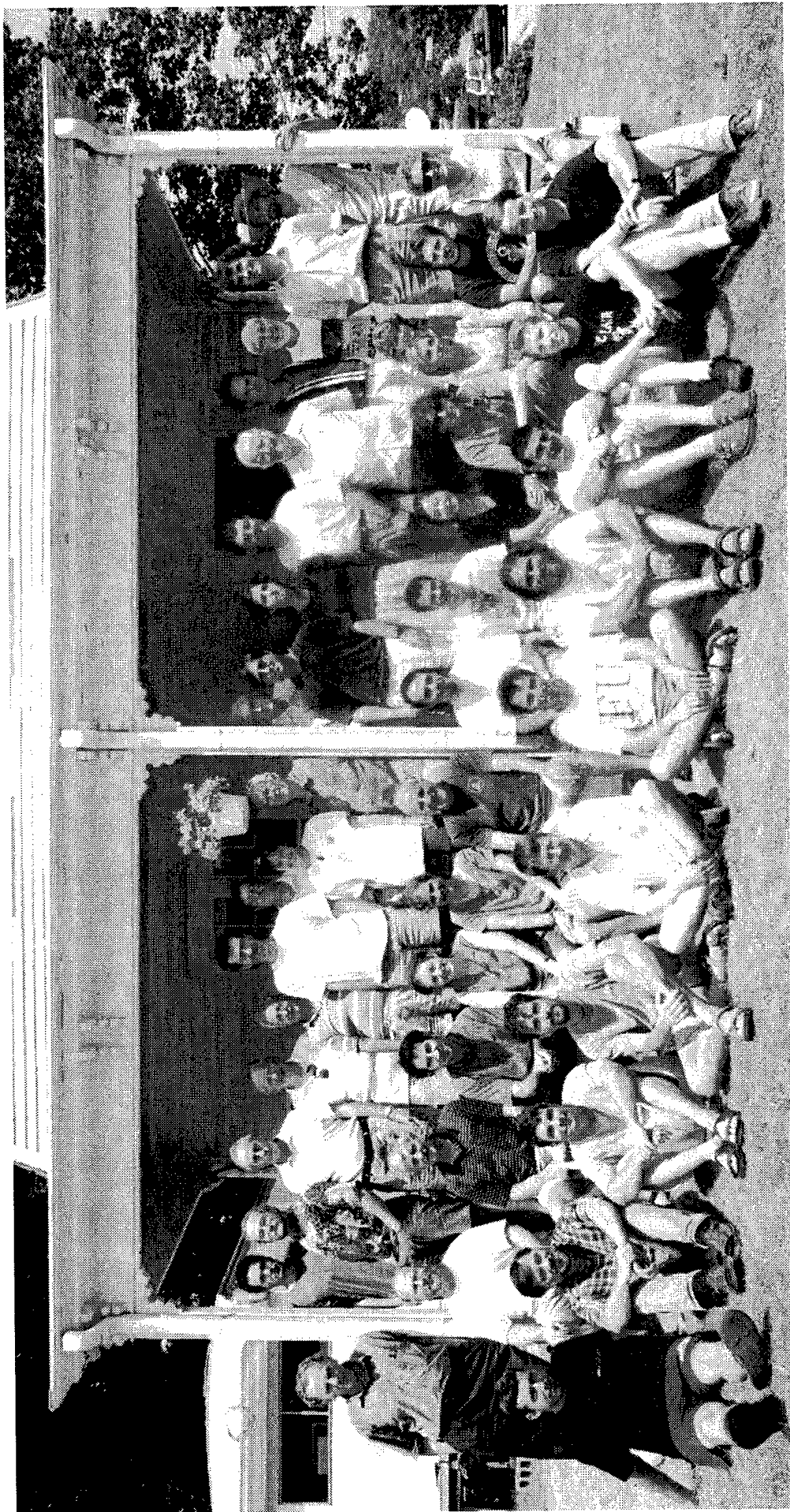
1998

Standing (left to right): E. Spiegel, P. Yecko, A. Jacobson, N. Lebovitz, J. Anderson, G. Schmidt, A. Provenzale, S. Balbus, A. Bracco, W. Malkus, L. Howard, J. Weiss, B. Gallego, R. Ford, C. Rooth, I. Melbourne, J. Keller, A. Rucklidge, R. Worthing

Seated on porch (left to right): C. Doering, S. Childress, P. Kevrekidis, S. Dance, C. Mockett, G. Veronis, A. Kiss, M. Roulston, A. Shen, E. Chassignet, C. Pasquero, J. Prat, F. Paparella, L. Campbell (WHOI)

Seated on ground (left to right): A. Birch, J. Kurths, M. Umurhan, J. Biello, R. Hollerbach, N. Balmforth, P. Morrison, M. Papadakis, A. Casti, J. Graf von Hardenberg

Not pictured: A. Adcroft, S. Antinucci, A. Bernoff, K. Bowman, J.R. Buchler, P. Cessi, J. Xinzhong Chen, C. Coulliette, R. Craster, D. del Castillo-Negrete, R. Douglas, J. Duan, J. Finn, G. Flierl, C. Frankignoul, A. Gnanadesikan, P. Goldreich, J. Golub, J. Goodman, J. Hurrell, A. Ingersoll, E. Johnson, C. Jones, K. Julien, S.C. Kim, S. Kravtsov, Y. Kushnir, A. Leonard, S. Llewellyn Smith, A. Manfroi, J. Marotzke, S. Meacham, P. Miller, K. Ngan, A. Odulo, E. Ott, N. Paldor, A. Poje, V. Poutkaradze, K. Prendergast, M. Proctor, V. Rom-Kedar, M. Shelley, L. Smith, T. Solomon, A. Soward, L. Sparling, M. Speetjens, M. Stern, H. Swinney, R. Taam, P. Tabeling, L. Tao, R. Temam, J.L. Thiffeault, C. Tresser, E. Tziperman, J. Urbach, M. Visbeck, S. Wang, J. Whitehead, S. Wiggins, S. Winkler, W. Young, Y.N. Young

vii
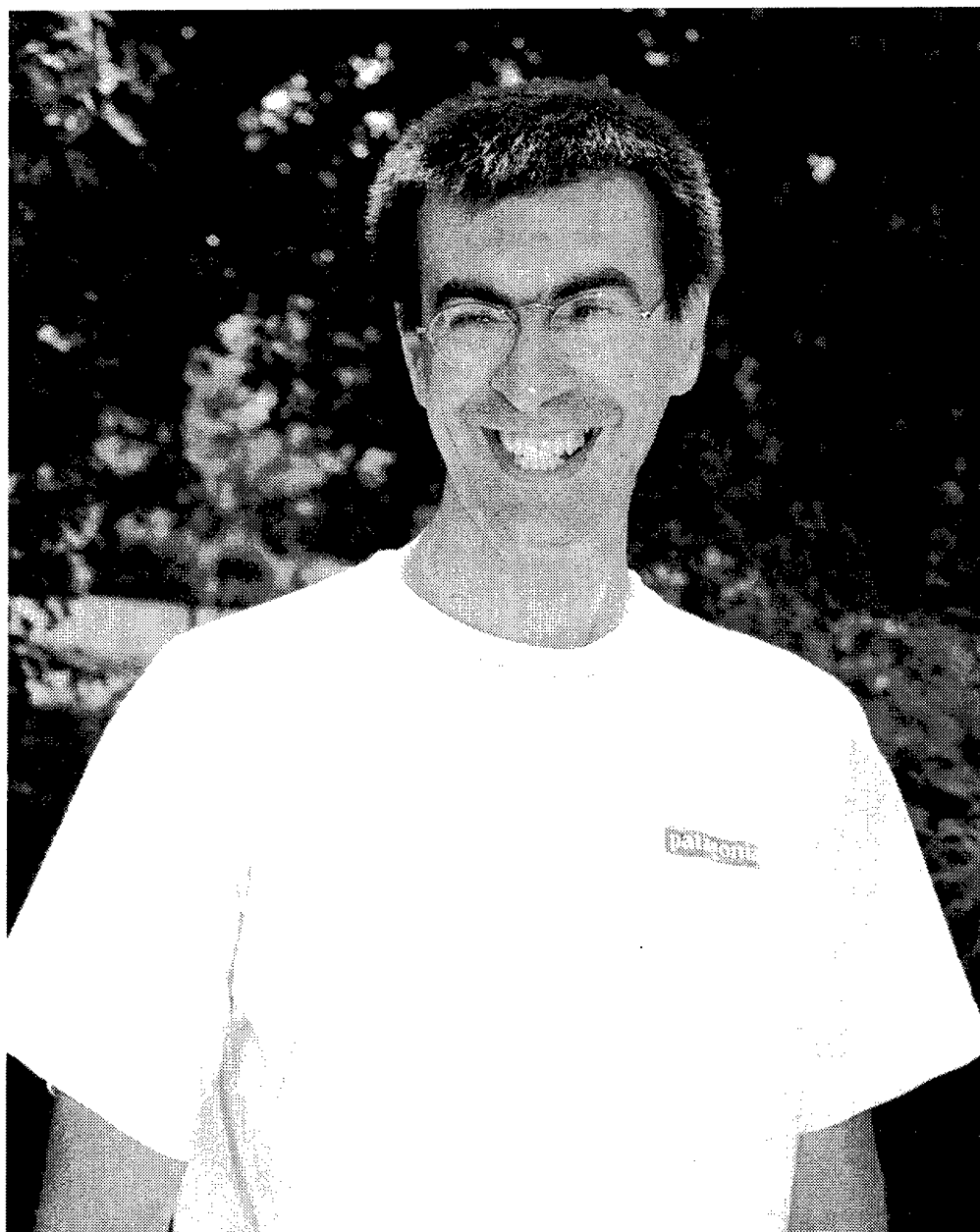
1998 GFD Principal Lecturers

Antonello Provenzalle (above) and Charles Tresser (not pictured)

GFD 1998 Lecture Schedule

Monday, June 22, 1998

    10:00 am   Neil Balmforth, GFD Coordinator, Scripps Institution of Oceanography, University of California, San Diego – *Welcome to GFD*

                    Ed Spiegel, Columbia University - *Introduction*

    2:30 pm   Antonello Provenzale, Instituto di Cosmogeofisica, Torino, Italy – *Introduction to Dynamical Systems With the Example of a Dust Grain in a Stratified Atmosphere (tutorial)*

Tuesday, June 23

    10:00 am   Antonello Provenzale -
- *Energy Balance Models*
- *The Lorenz 63 Model (derivation)*
- *The Lorenz 84 Model for the Atmosphere*

Wednesday, June 24

    10:00 am   Antonello Provenzale - *Time Series Analysis and Phase-Space Reconstruction: The Example of the Light Curve of 3C 345*

Thursday, June 25

    10:00 am   Antonello Provenzale - *Driving Chaotic Systems:*
- *Seasonal Forcing in Lorenz 84*
- *Stochastic Driving of a Thermohaline Box Model*
- *Stochastic Resonance*

    2:00 pm   Antonello Provenzale and Ed Spiegel - *Coupling Chaotic Systems I: On-Off Intermittency (including the PST model for the solar dynamo)*

Friday, June 26

    10:00 am   Antonello Provenzale- *Coupling Chaotic Systems II:*
- *Analysis of Coupled Lorenz 84 Models*
- *Chaotic Resonance*
- *Synchronization and On-Off Desynchronization*

    2:00 pm   Antonello Provenzale & Lenny Smith (University of Oxford, UK) –
- *Predictability and Prediction in Dynamical Systems*
- *Predictability of Coupled Systems*
- *Prediction Methods*

Monday, June 29, 1998

10:00 am   Antonello Provenzale –
- *Extended Systems*
- *Coherent Vortices*
- *The Vortices of 2D Turbulence*
- *Coherent Flux Tubes in 2D-MHD*

1:30 pm   Charles Tresser, IBM – *Transition to Chaos, Part I*

Tuesday, June 30

10:00 am   Antonello Provenzale -
- *Point Vortices*
- *Chaotic Advection in 2D Flows*

1:30 pm   Charles Tresser – *Transition to Chaos, Part II*

Wednesday, July 1

10:00 am   Antonello Provenzale -
- *Dynamics of Dust Grains in 2D Flows*
- *A Scenario for the Formation of Planetesimals*
- *Vortices on Keplerian Disks*

2:30 pm   Charles Tresser – *Transition to Chaos, Part III*

Thursday, July 2

10:00 am   Antonello Provenzale - *Density Singularities in Self-Gravitating Systems*

2:30 pm   Charles Tresser – *Transition to Chaos, Part IV*

Friday, July 3   Happy Fourth of July!

10:00 am   *Discussion of Projects*

Monday, July 6, 1998

10:00 am   Yochanan Kushnir, Lamont-Doherty Earth Observatory, Columbia University - *Patterns of Atmosphere-Ocean Interaction*

1:30 pm   James Hurrell, National Center for Atmospheric Research (NCAR) – *Relationships Between Recent Changes in Atmospheric Circulation, Global Warming and Satellite Temperatures*

Tuesday, July 7

10:00 am   Eli Tziperman, Weizmann Institute of Science, ISRAEL – *On ENSO's Chaos and Phase Locking to the Seasonal Cycle*

1:30 pm   Eli Tziperman – *On the Proximity of the THC to an Instability Threshold*

Wednesday, July 8

    10:00 am   Jochem Marotzke, Massachusetts Institute of Technology – *Abrupt Climate Change and the Thermohaline Circulation*

    1:30 pm   Paola Cessi, Scripps Institution of Oceanography, UCSD – *Coupled Dynamics of Storm Tracks and Ocean Gyres*

Thursday, July 9

    10:00 am   Martin Visbeck, Lamont-Doherty Earth Observatory, Columbia University - *Climate Variability in the Extratropical Atlantic*

    1:15 pm   Jason Goodman, Woods Hole Oceanographic Institution - *A Model of Decadal Middle-Latitude Atmosphere-Ocean Coupled Modes*

    2:30 pm   *Discussion*

Friday, July 10

    10:00 am   Claude Frankignoul, Massachusetts Institute of Technology – *Stochastic Approach to Climate Modelling*

Week of July 13-17, 1998

Monday, July 13, 1998

    10:30 am   Stephen Childress, New York University - *Convection in Glycerol*

Tuesday, July 14

    10:30 am   Kevin Prendergast, Columbia University - *Dwarf Ellipticals*

    2:00 pm   Philip J. Morrison, University of Texas, Austin - *Physicist Gone Bad: Lp Solutions of the Linear Vlasov-Poisson Equation*

Wednesday, July 15

    2:30 pm   Lou "Diamond" Howard, Florida State University - *Special Seminar: The Missing Diamonds are in the Plastic Bag*

Thursday, July 16

    10:30 am   Philip Yecko, University of Florida - *Strange Cepheid Variables*

    2:30 pm   J. Robert Buchler, University of Florida - *Chaos in the Music of the Spheres*

Friday, July 17   No Lectures

Week of July 20-24, 1998

Monday, July 20, 1998

    10:30 am   Norman R. Lebovitz, University of Chicago - *Elliptic Instability: Nonlinear Development*

Tuesday, July 21

    10:30 am   Juergen Kurths, University of Potsdam - *Phase Synchronization in Chaotic Systems*

    1:30 pm   Alastair Rucklidge, University of Cambridge, UK - *Steady State Bifurcations of Symmetric Periodic Orbits*

Wednesday, July 22

    10:30 am   Steven Balbus, University of Virginia - *MHD Turbulence in Disks and Other Systems*

    2:30 pm   Rainer Hollerbach, University of Glasgow - *Time-Dependent Taylor Vortices in Wide-Gap Spherical Couette Flow*

Thursday, July 23

    10:30 am   Joana Prat, University Politecnica de Catalunya, SPAIN - *Resonant Mode Interactions in Rayleigh-Benard Convection*

    2:30 pm   Ian Melbourne, University of Houston - *Magnetic Dynamos in MHD Using Dynamical Systems Theory*

Friday, July 24

    10:30 am   Charles Doering, University of Michigan - *Bounds for Heat Transport in a Porous Layer*

    2:30 pm   Michael Proctor, University of Cambridge, UK - *Noise Sensitivity in Travelling-Wave Instabilities*

Week of July 27-31, 1998, Redfield Auditorium
"Transport and Mixing in Fluids: The Dynamical Systems Approach"

Monday, July 27, 1998

    10:00 am   Christopher Jones, Brown University - *Dynamical Systems Challenges in Assessing Ocean Transport*

    2:00 pm   Jeffrey B. Weiss, University of Colorado - *Lagrangian Dynamics in High-Dimensional Point-Vortex Systems*

    3:00 pm   Jerry Gollub, Haverford College - *Transient Mixing*

    3:45 pm   Tom Solomon, Bucknell University - *Experimental Studies of Chaotic Transport*

Tuesday, July 28

    9:30 am   Edward Ott, University of Maryland - *Multifractal Properties of Passive Scalar and Vector Fields Convected by Lagrangian Chaotic Flows*

    1:30 pm   John Finn, Los Alamos National Labs - *Lagrangian Chaos and the Magnetic Dynamo Problem*

Wednesday, July 29

    10:00 am   Harry L. Swinney, University of Texas at Austin - *Anomalous Diffusion and Levy Flights in a Quasi-Geostrophic Flow*

    2:00 pm   William Young, Scripps Institution of Oceanography, University of California at San Diego - *Horizontal Mixing in the Mixed Layer*

    3:00 pm   Patrick Tabeling, Ecole Normale Superieure, FRANCE - *Dispersion and Turbulence in 2D Systems*

Thursday, July 30

    10:00 am   Stephen Wiggins, California Institute of Technology - *A Dynamical Systems Approach to Lagrangian Transport in a Double-Gyre*

    2:00 pm   Vered Rom-Kedar, Weizmann Institute of Science, ISRAEL - *Chaotic Cooling of a Hot Core*

    3:00 pm   Nathan Paldor, Hebrew University, ISRAEL - *Dynamical Systems Approach to Balance Flows*

    3:45 pm   Michel Speetjens, Eindhoven University of Technology, the NETHERLANDS - *Mixing in a 3D Cylindrical Container*

Friday, July 31

    9:30 am   Open discussion on *Diffusion and Lagrangian Transport (in Models, Experiments, and the "real world")*

Week of August 3-7, 1998

Monday, August 3, 1998

    10:30 am   Andy Ingersoll, California Institute of Technology - *Dynamics of Giant Planet Atmospheres*

Tuesday, August 4

    10:30 am   Ron Taam, Northwestern University - *Variability in Black Hole X-Ray Binary Systems*

Wednesday, August 5

    10:30 am   Peter Goldreich, California Institute of Technology - *MHD Turbulence*

Week of August 10-14, 1998

Monday, August 10, 1998
      10:30 am   Melvin Stern, Florida State University - *Beyond Chaos*

Tuesday, August 11
      10:30 am   Mike Shelley, New York University - *Modelling the Visual Cortex*

Thursday, August 13
      10:30 am   Joe Keller, Stanford University - *Random Problems*
      2:30 pm   Alistair Adcroft, Massachusetts Institute of Technology - *How Do Ocean Models Really Work?*

Friday, August 14
      2:00 pm   Vachtang Poutkaradze, University of Chicago - *Selective Withdrawal in Oil/Water Systems*

Week of August 17-21, 1998

      No Lectures

Week of August 24-28, 1998 - Fellows' Lectures

Monday, August 24, 1998
      10:30 am   Panayotis Kevrekidis, Rutgers University - *What If the World Were Discrete?*
      2:15 pm   Mark Roulston, California Institute of Technology - *Data Assimilation in Chaotic Systems*
      3:30 pm   Aaron Birch, Stanford University - *Spicules?*

Tuesday, August 25
      10:00 am   Carolyn Mockett, Scripps Institution of Oceanography, University of California at San Diego - *Dispersion & Reconstruction*
      11:15 am   Andy Jacobson, Pennsylvania State University - *"Pandora's Lattice"*
      2:15 pm   Claudia Pasquero, Istituto di Cosmogeofisica, Torino, ITALY - *Hill's Horseshoes: Chaos in a Forced System*
      3:30 pm   Sarah Dance, Brown University - *Optimal Forecasting, A Toy Model*

Wednesday, August 26
      10:30 am   Amy Shen, University of Illinois at Urbana-Champaign - *Models of Lava Domes*
      2:15 pm   Andrew Kiss, Australian National University, AUSTRALIA - *Chaos in the "Sliced Cone" Model of Ocean Circulation*
      3:30 pm   Blanca Gallego, University of California at Los Angeles - *Oscillations in the Mid-Latitude Ocean/Atmosphere System*

Lecture 1

Fundamentals

1.1 Introduction

Even though our limited perceptions provide us with only a brief glimpse of the Universe, the main lesson that we learn from our observation is that the world is complicated. Very complicated. Every part of the universe interacts with the other parts; the responses of each component are never proportional to the applied forces, and the feedbacks of one subsystem on another cannot be discarded. As a result, processes are unpredictable, and chaotic behavior is a common occurrence. Disorder and turbulence become rife. Yet from the chaotic background, coherent structures sometimes emerge, patterns form, and local order is generated.

In the face of the wealth of phenomena, the myriad of details and the richness of quality and quantity, the quest for scientific understanding might seem to be a hopeless endeavour. Perhaps it is a fundamental human flaw that leads us to challenge this point of view. But challenge it we do. And at end of our struggles, perhaps we will find some comfort in judging how far we have come, and how infinitely further we could continue. At the very least, it may cure the crisis of mid-life. Thus, even if it may be pointless to try to describe what can happen in the universe, in these lecture notes, for reasons obscured to all but the fellows, we begin to do so.

There are indeed several ways of approaching the overwelming complexity of nature. One is simply to observe the natural world, and make quantitative measurements. This is what is often done in astrophysics and geophysics, where little or no control can be obtained on the system under study. But this approach is always limited if we have no scientific framework with which we can rationalize the observations.

The other approaches seek to establish some foundation on which to build our understanding. But to build such a foundation, we must meet head-on the complexity of the problems we seek to explain, and this constitutes an impossible undertaking: we cannot study the full complexity of things by a unique approach, and sometimes we do not even know whether there is a meaningful "universal law" behind the observations (as in biological evolution or human psychology).

Instead, we progress like ancient Romans; we divide, then conquer. Put more scientifically,

we begin by isolating some natural phenomenon, separating parts of a whole that should probably stay together. Moreover, we simply ignore most of the physical ingredients and deal only with those parts that can be couched as mathematical problems. Then we formulate idealized problems that model what we deem to be the most essential pieces of the selected phenomena. Finally, we attempt to solve those simple models. In other words, we conjure incomplete images of the real world, then disect them.

More troubles, however, arise. For many systems, we do not have a clean mathematical formulation of the problem (such as in problems of landscape evolution, or earthquake dynamics, or sociology). In other instances, even though we deal with problems that can be couched in terms of mathematical equations, we are not always able to solve them in their full generality. This is especially true in geophysics (and sometimes in astrophysics), where we believe that fluid mechanics offers a formalism to understand the atmosphere and oceans: the Navier-Stokes equations have been known for two centuries, but we have yet to solve them. Thus, even our attempts to divide and conquer run into trouble.

These fundamental difficulties lead to a division in scientific ideology regarding how one should approach the idealized problems. As Ed Spiegel pleasantly puts it, one ideology suggests a method that is championed by the "slobs", the other to methods advocated by the "bores".

The first methodology involves efforts to incorporate *as much as possible*. The tools are numerical simulation and big computers; the results are GCMs, numerical climate models, galaxies of point particles, and stars made of treacle. In these hi-tech approaches, researchers invent a new, virtual world, wherein they perform sophisticated numerical simulations that incorporate as many aspect of reality as possible - and parametrize those which are left out. But with the mass of the included details comes an unweildiness, an inability to truly assess the robustness of solutions, and even at times to correctly solve the equations.

The second ideology could be described as escapism. We abstract even more from the physics, idealize yet further, until we arrive at a problem that, though totally divorced from reality, can be solved precisely and elegantly. The solutions may not be relevant to the problem that motivated the mathematical analysis, but it is pretty, inexpensive and very alluring.

Of course, this description makes mockery of the two approaches. But there are dangers in the two ideologies, and perhaps this mockery will make the reader aware of their respective pitfalls. From a different perspective, both methodologies amount to true attempts to learn about the real world. And any serious explanation should no doubt consist of both. There are settings in which one may be more useful than the other, and instances in which real progress can only be made when the two methods are used in concert.

As in true Walsh Cottage Tradition, the lecture notes that follow are devoted to an approach that more closely follows the second ideology. In particular, we shall explore a few simplified - in fact, always oversimplified - models of various geophysical and astrophysical processes, mainly using concepts from dynamical system theory. In such an effort, we do not expect to find quantitative correspondence between the models and reality, but we aim at understanding some aspects of some of the main processes at work, possibly estimating their respective roles and importance. And, perhaps surprisingly, from time to time we hope that we succeed in understanding something of the complicated Universe that surrounds us.

1.2 Some elementary dynamical systems theory

There are many books devoted to the properties of dynamical systems (*e.g.* Drazin 1992; Ott 1993; Ott *et al.* 1994). Here, we simply mention some of the relevant concepts which will be used in the rest of the lectures.

A dynamical system is a mathematical model or law,

$$\mathbf{X}_t \mapsto \mathbf{X}_{t+\delta t} = \Phi_{\delta t}(\mathbf{X}_t), \tag{1.1}$$

where $\mathbf{X}_t$ is a vector of variables that completely describes the state of the system at time t,

$$\mathbf{X}_t \equiv (X_t^{(1)}, X_t^{(2)}, X_t^{(3)}, \cdots, X_t^{(N)}), \quad X_t \in \mathbb{R}^N, \tag{1.2}$$

and $\mathbf{X}_{t+\delta t}$ is the state of the system at time $t + \delta t$. The particular choice of state variables is dictated by the nature of the system. For example, in thermodynamics of ideal gases we might choose temperature, pressure and volume as dynamical variables.
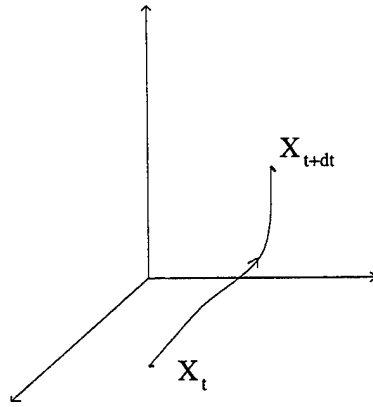
Figure 1.1: A trajectory in phase space

The state of the system at any time may be represented by a point in *phase space*; that is, an $N-$dimensional space spanned by the N dynamical variables. The number of degrees of freedom (DOF) of a system is defined by the dimensionality of its phase space (N).

Example: The logistic map One of the most commonly used examples of a chaotic dynamical system is the logistic map (see Fig. 1.2):

$$\begin{aligned} X_{n+1} &= 4aX_n(1 - X_n), \\ & 0 \le X_n \le 1 \ , \ 0 \le a \le 1. \end{aligned} \tag{1.3}$$

This system has been used in applications as diverse as describing insect population outbreaks and the generation of pseudo-random numbers. The behavior of the system depends on the value of the parameter a, which determines the height of the parabola (*c.f.* a_1, a_2, a_3 in Fig.

3

1.2). An important characteristic of this system is that, for sufficiently large a, the time series of X_n is chaotic and two points with similar initial conditions may not remain close under iteration of the map. That is, there is sensitive dependence on initial condition.

Figure 1.2: *La mappa logistica*. The logistic map. The dotted lines show sample evolution sequences. For smaller values of a, such as a_1, the system iterates to $X = 0$. For larger a (like a_2) the system converges to the nontrivial fixed point. At the largest values of a (a_3), the system is chaotic, with initial close trajectories from nearby initial conditions diverging exponentially quickly.
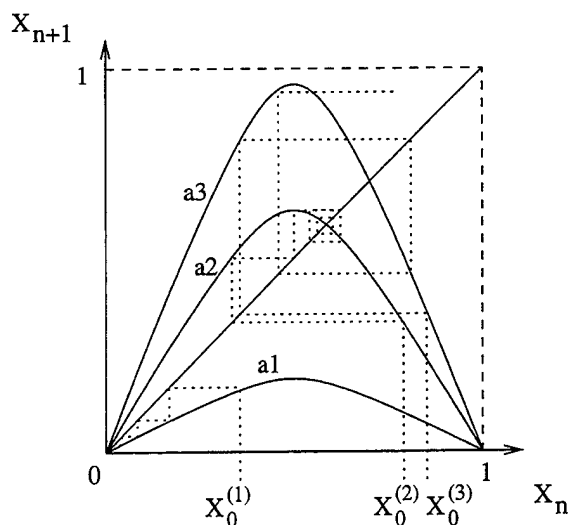
1.2.1 Linear versus nonlinear dynamics

A crucially important feature of the logistic map that is essential in creating complicated dynamics is nonlinearity. This highlights the fact that nonlinear systems are fundamentally different from linear ones.

A linear system may be considered to have outputs which are proportional to its inputs. This leads to a relatively simple range of dynamical behaviour. By contrast, a nonlinear system does not in general obey this law of proportionality. In other words, the evolution law of a nonlinear system cannot be expressed in terms of a linear transformation of a previous state: $\mathbf{X}_{t+\delta t} = \mathbf{f}(\mathbf{X}_t) \neq \mathbf{M} \cdot \mathbf{X}_t$, for some matrix or linear operator (M).

For nonlinear systems, the principle of superposition does not, in general, hold. That is, if we are given two solutions X_t and Y_t of a nonlinear system, $\alpha X_t + \beta Y_t$ is not necessarily a solution.

Nonlinear systems may exhibit many types of temporal evolution, depending on the structure of the system. The behaviour can be a simple as the relaxation to an equilibrium or a *fixed point*, for which $\mathbf{X}(t + \delta t) = \mathbf{X}(t)$. Linear systems can also display this behaviour, but

4

a key difference in a nonlinear system is that there can be *multiple equilibria*.

Another simple solution to a nonlinear system is a periodic orbit. These reflect oscillations of the system and are again familiar from linear dynamics. But the evolution of a nonlinear system can be substantially more complicated. Notably, it can be *chaotic*.

1.2.2 Determinism and randomness

An important distinction between dynamical systems surrounds whether the dynamics is completely deterministic, or whether the evolution proceeds at least partly as a result of stochastic effects.

For deterministic dynamical systems, if we are given an initial state X_t, then the state at some later time, $X_{t+\delta t}$, is uniquely determined via the evolution law. This property of uniqueness implies that for deterministic systems, trajectories in phase space may never cross at finite time.

For stochastic dynamical systems, only the probability $P(X_{t+\delta t})$ may be determined from the knowledge of X_t, and trajectories in phase space may cross. It is sometimes useful to consider deterministic dynamical systems as stochastic ones simply because we do not possess a full description of all the variables, or if the system has many degrees of freedom and it proves more expedient to eliminate some variables and treat the system as if it were stochastic.

1.2.3 Types of Dynamical Systems

Dynamical systems come in many different shapes and forms, and it is often convenient to introduce some sort of classification scheme. So we do here.

The simplest types of dynamical systems are those for which the evolution law takes the form of a simple algebraic operation. Such an operation arises when we consider systems in which time is *discrete*. Then,

$$\mathbf{X}_{t+1} = f(\mathbf{X}_t) \tag{1.4}$$

where $\mathbf{X} \in \mathbb{R}^N$, and $f(\mathbf{X}_t)$ is a known algebraic function. Such dynamical systems are often called "maps of the interval" if there is a single dependent variable, or "maps of the plane" (for two such variables), or simply "maps". The logistic map that we have already encountered is one of the canonical examples of a one-dimensioanl map. Discrete-time systems are not always maps of $\mathbb{R}^N$ into itself. Cellular automata and games of life are also discrete-time dynamical systems.

When the time variable is continuous, the evolution law of the dynamical system takes the form of a set of differential equations. Then we deal with continuous-time dynamical systems, the simplest examples of which are governed by ordinary differential equations:

$$\frac{d\mathbf{X}}{dt} = \dot{\mathbf{X}} = \mathbf{F}(\mathbf{X}), \tag{1.5}$$

with $\mathbf{X} \in \mathbb{R}^N$ and $\mathbf{F}(\mathbf{X})$ again a prescribed function. Typically we solve the system as an initial-value problem with the image in mind of the system evolving from some known initial state. Much of lecture 2 will be concerned with these kinds of systems.

5

ODEs of the form (1.5) are finite dimensional; the solutions can be envisioned as orbits within a space of N−dimensions. More complicated continuous-time dynamical systems have infinite dimension. Two commonly encountered examples of such systems are delay-differential equations and partial-differential systems.

The evolution law for delay-differential equations contains the entire history of the trajectory:

$$\frac{d\mathbf{X}}{dt} = \int_0^t \mathbf{K}[\mathbf{X}(t'), t']dt', \tag{1.6}$$

where $\mathbf{K}[\mathbf{X}(t), t]$ is a known kernel. Such models usually arise in systems with long-term memory.

Partial differential equations (PDEs) may be expressed as

$$\frac{\partial \omega}{\partial t} = K[\omega, \nabla \omega, \cdots], \tag{1.7}$$

where ∇ is the gradient operator in the spatial variables. Along with the spatial dimensions come a variety of boundary conditions. An example relevant to these lectures is two-dimensional Navier-Stokes flow:

$$\frac{\partial \omega}{\partial t} + [\psi, \omega] = \nu \nabla^2 \omega, \tag{1.8}$$

where $\omega = \nabla^2 \psi$ is vorticity and ψ is the stream function.

Solutions to continuous-time dynamical systems can be described as trajectories in the phase space that begin from a single point characterizing the initial condition. The set of all possible trajectories can be thought of as defining a velocity field, $\mathbf{u} = d\mathbf{X}/dt$ in the phase space. For this reason, continuous-time dynamical systems are sometimes referred to as "flows".

Finally, stochastic systems are described by equations where a random term enters the dynamics. A classic example is the linear Langevin equation (or Ornstein-Uhlenbeck process)

$$du = -\frac{u}{T}dt + \frac{\sigma}{T^{1/2}}dW, \tag{1.9}$$

where T is a decorrelation time for the random variable u, σ^2 is the variance of u and dW is a random white noise term characterized by $\langle dW \rangle = 0$ and $\langle dW(t)dW(t') \rangle = 2dt\delta(t - t')$. Here, $\langle ... \rangle$ indicates ensemble average. System (1.9) generates a time series $u(t)$ with a gaussian amplitude distribution $p(u)$ and exponentially decaying autocorrelation, $\langle u(t)u(t + \tau) \rangle \propto \exp(-\tau/T)$. Given the present state of such a stochastic system, say $u(0)$, we cannot determine its future state precisely. We can just determine the probability of a future state given the present one, i.e., $P[u|u(0)]$. Nonlinear stochastic processes are also possible. First-order (in time) nonlinear processes take the general form

$$dv = f(v)dt + g(v)dW, \tag{1.10}$$

where dW is still a white-noise process (Wiener process). For such a model, the probability distribution $p(v)$ is not necessarily gaussian. We shall encounter one of these nonlinear stochastic systems in Lecture 3.

6

1.2.4 Conservative dynamical systems

A dynamical system is called conservative if there is a quantity $E(\mathbf{X}_t)$ which is constant during the evolution:

$$\dot{E} = 0. \tag{1.11}$$

This implies that the system dynamics takes place on a manifold with dimension $N-1$, defined by $E = \text{constant}$.

Conservative systems are referred to as Hamiltonian systems if they can be written in the form,

$$\left.\begin{array}{rcl} H & = & E \\ \dot{q}_j & = & \frac{\partial H}{\partial p_j} \\ \dot{p}_j & = & -\frac{\partial H}{\partial q_j} \end{array}\right\}, j = 1, ..., \frac{N}{2}, \tag{1.12}$$

where q and p are canonically conjugate variables. For such a system, the number of degrees of freedom is traditionally defined as $N/2$, *i.e.*, as the number of pairs of canonically conjugate variables.

Dynamical systems of the form $\dot{\mathbf{X}} = \mathbf{F}(\mathbf{X})$ preserve phase-space volume if

$$\nabla \cdot \mathbf{F} = 0. \tag{1.13}$$

To see this, let us take the Taylor expansion of a solution $\mathbf{X}(t+h)$ for small h:

$$\mathbf{X}(t+h) = \mathbf{X}(t) + h\dot{\mathbf{X}}(t) + o(h). \tag{1.14}$$

Note that $o(h)$ refers to terms with powers of h greater than one, including fractional powers. The time evolution of a volume element is described by the determinant of the Jacobian matrix $\frac{\partial X_i(t+h)}{\partial X_j(t)}$. This is given by

$$\begin{array}{rcl} \det J & = & \det \left\{ \frac{\partial X_i(t+h)}{\partial X_j(t)} \right\} \\ & = & \det \left\{ \delta_{ij} + h \left(\frac{\partial F_i}{\partial X_j} \right)_t + o(h) \right\} \\ & = & 1 + h \, \nabla \cdot \mathbf{F} + o(h). \end{array} \tag{1.15}$$

For example, in two-dimensional flow, after discarding terms $o(h)$,

$$\begin{array}{rcl} \det J & = & \begin{vmatrix} 1 + \frac{\partial F_1}{\partial X_1} h & \frac{\partial F_1}{\partial X_2} h \\ \frac{\partial F_2}{\partial X_1} h & 1 + \frac{\partial F_2}{\partial X_2} h \end{vmatrix} \tag{1.16} \\ & = & \left(1 + h\frac{\partial F_1}{\partial X_1}\right)\left(1 + h\frac{\partial F_2}{\partial X_2}\right) - h^2 \frac{\partial F_1}{\partial X_2} \frac{\partial F_2}{\partial X_1} \\ & \approx & 1 + h\left(\frac{\partial F_1}{\partial X_1} + \frac{\partial F_2}{\partial X_2}\right). \tag{1.17} \end{array}$$

7

Thus if $\nabla \cdot F = 0$ then $\det J = 1$ and the phase space volume does not change.

The existence of a conserved quantity, E, and volume preservation in phase space are independent properties of dynamical systems. However, many conservative systems of physical interest are also characterized by preservation of volumes in phase space. If the system does preserve volume, then the associated velocity field of the flow, $\mathbf{u} = d\mathbf{x}/dt$, is *incompressible*.

1.2.5 Dissipative dynamical systems

Dissipative systems are those for which the volume of phase space occupied by a set of initial conditions is not conserved, and, in fact, decreases over the course of time: $\nabla \cdot \mathbf{F} < 0$. In other words, the flow of the dynamical system is *contracting*. Provided the system is bound, then this contraction implies that, as $t \to \infty$, the motion becomes confined to a set A with zero volume in phase space and dimension $D < N$. This set is an "attractor" of the system.

Two useful concepts are the following:

Invariant Set: An invariant set A is one which maps to itself under the flow: $A \overset{t}{\to} A$.

Attracting Set: An invariant set A is an attracting set (an attractor) if there exists a set B with non-zero measure, $A \subset B$, such that $B \overset{t}{\to} A$. B is called the *basin of attraction* of A.

In dissipative systems there can be many qualitatively different types of attractors. The most commonly encountered attractors are:

- Fixed points
- Limit cycles
- Quasi-periodic motion
- Chaotic (strange) attractors

1.3 Dust Grains in a Stratified Atmosphere

We now use the simple example of a dust grain in a stratified atmosphere to illustrate some of the concepts introduced above. Imagine an infinitesimally small particle in a stably stratified atmosphere (Fig. 1.3). The density of the ambient fluid is $\rho(z)$, and the particle is at equilibrium at $z = C$, where $\rho(C) = \rho_p$. The motion of the particle satisfies

$$\ddot{z} = g\frac{\rho(z) - \rho_p}{\rho_p}, \qquad (1.18)$$

which can be written in the form,

$$\begin{aligned} \dot{z} &= v \\ \dot{v} &= \frac{g}{\rho_p}(\rho(z) - \rho_p). \end{aligned} \qquad (1.19)$$

This is a continuous-time dynamical system with a two-dimensional phase space.
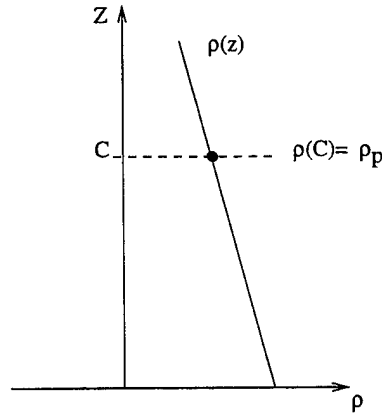
Figure 1.3: An illustration of a dust grain moving in a stratified atmosphere.

1.3.1 Linear stratification

Suppose that $\rho(z) = \alpha(z - C) + \rho(C)$, where α is a constant, and that $\rho(C) = \rho_p$. Then we may choose $C = 0$ with no loss of generality. Then Eq. (1.19) becomes

$$\begin{aligned} \dot{z} &= v \\ \dot{v} &= \frac{g\alpha}{\rho_p}z. \end{aligned} \qquad (1.20)$$

This is a linear system and is equivalent to the simple harmonic oscillator.

If the atmosphere is stably stratified, α is negative and we have stable oscillations. The flow in phase space is shown in figure 1.4; this type of picture, which shows the character of typical orbits, is called a phase portrait. The stable oscillations appear as closed circles in the phase portrait. There is a single equilibrium point at $z = v = 0$. Because of the shape of the orbits surrounding this equilibrium, it is called an elliptic fixed point.

When α is positive, the atmosphere is unstably stratified and the particle trajectory exhibits exponential divergence from the fixed point; the phase portrait is shown in Fig. 1.5. The point $z = 0, v = 0$ is now a saddle point; because of the hyperbolic shape of nearby orbits, it is referred to as a hyperbolic fixed point.

The fixed points of the system are the positions of static equilibrium for the dust particle. These points are the solutions $\mathbf{X}_f$ to $\mathbf{F}(\mathbf{X}_f) = 0$. For our illustrative example, $\mathbf{X} = (z, v)$, and the fixed point is given by $(\dot{z}, \dot{v}) = (0, 0)$:

$$\begin{aligned} v &= 0 \\ \rho(z) - \rho_p &= 0. \end{aligned} \qquad (1.21)$$

Hence, for a linear stratification, $\rho(z) = \rho_p + \alpha z$, and the fixed point is $z_f = 0$ (linear systems can only ever have a single fixed point).

The linear stability of a fixed point can be examined via linear perturbation analysis, in which one studies the evolution from an infinitesimal displacement from the fixed point. In
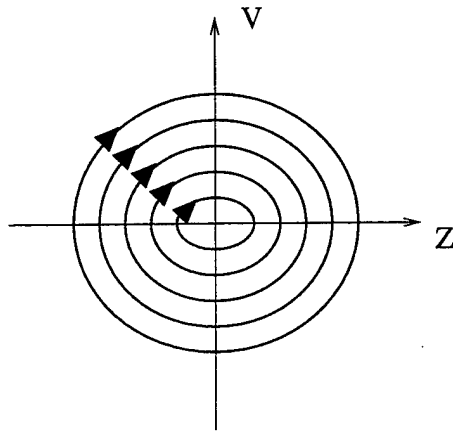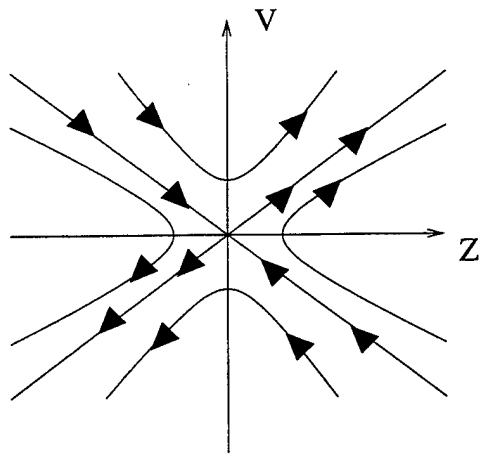
9

Figure 1.4: Elliptic fixed point

Figure 1.5: Hyperbolic fixed point

10

general, suppose that $\dot{\mathbf{X}} = \mathbf{F}(\mathbf{X})$ has a fixed point at $\mathbf{X}_f$. Consider a point close to $\mathbf{X}_f$ given by $\mathbf{X} = \mathbf{X}_f + \xi$. Then, $\dot{\xi} = \mathbf{F}(\mathbf{X}_f + \xi)$ which may be expanded in a Taylor series as

$$
\begin{aligned}
\dot{\xi} &= \mathbf{F}(\mathbf{X}_f) + \left(\frac{\partial \mathbf{F}}{\partial \mathbf{X}}\right)_{\mathbf{X}_f} \xi + \cdots \\
&\approx \left(\frac{\partial \mathbf{F}}{\partial \mathbf{X}}\right)_{\mathbf{X}_f} \xi,
\end{aligned}
\tag{1.22}
$$

where $(\partial \mathbf{F}/\partial \mathbf{X})$ is the Jacobian of $\mathbf{F}$. This is a linear system; the eigenvalues of the Jacobian matrix determine whether the infinitesimal perturbation grows or decays. In other words, stability is only ensured if all the eigenvalues of the Jacobian have negative real part.

For the example above,

$$
\begin{aligned}
z &= z_f + \zeta \\
v &= v_f + \theta,
\end{aligned}
\tag{1.23}
$$

and

$$
\begin{aligned}
\dot{\zeta} &= \theta \\
\dot{\theta} &= \frac{g\alpha}{\rho_p} \zeta.
\end{aligned}
\tag{1.24}
$$

Thus the fixed point is stable if $\alpha < 0$, or unstable if $\alpha > 0$, exactly as indicated above. Indeed, since the system is linear in this case, linear stability theory provides information also about the global stability of the fixed point. This example is also rather trivial for precisely this reason. Nonlinear stratifications, however, lead to less trivial dynamics.

1.3.2 Nonlinear stratification

Let us now parameterize the density as $\rho(z) = \rho_0 + \alpha z + \gamma z^3$. Then

$$
\begin{aligned}
\dot{z} &= v \\
\dot{v} &= \frac{\alpha g}{\rho_p} z + \frac{\gamma g}{\rho_p} z^3,
\end{aligned}
\tag{1.25}
$$

which is a nonlinear system. The fixed points satisfy

$$
\begin{aligned}
v &= 0 \\
z(\alpha + \gamma z^2) &= 0,
\end{aligned}
\tag{1.26}
$$

the solutions of which are $v = 0$, and $z = z_0 = 0$ or $z = z_{1,2} = \pm\sqrt{-\alpha/\gamma}$. It is clear that $z_{1,2}$ exist only if α and γ have opposite signs.

Phase portraits of the system are shown in Figs. 1.6 and 1.7. In the first case, $\alpha > 0$ and $\gamma < 0$, and there are two elliptic fixed points and one saddle. Orbits either circulate around one of the two elliptic fixed points, or with larger amplitude around all three. There are two
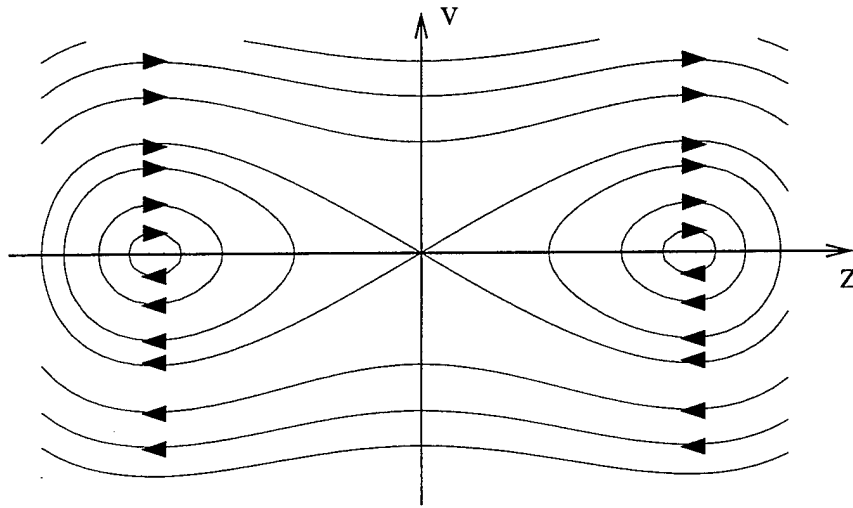
11

Figure 1.6: Phase space portrait for the nonlinear atmospheric stratification with $\alpha > 0$ and $\gamma < 0$.

special orbits that connect the origin to itself; these are called "separatrices" or "homoclinic orbits", and correspond to trajectories that begin at the origin for $t \to -\infty$, then circulate around one of the elliptic fixed points before returning to the origin for $t \to \infty$.

In the second example, $\alpha < 0$ and $\gamma > 0$, and there are two hyperbolic fixed points beside the elliptic fixed point at the origin. The special orbits that connect the two saddle points are again separatrices; they are also referred to as "heteroclinic orbits". There are only unbounded orbits in this case when the initial condition lies inside the separatrices.

In contrast to the single fixed point of the linear case, the nonlinear system therefore has multiple equilibria. The stability of the fixed points can again be examined using linear stability theory. For the fixed point z_0,

$$\ddot{\xi} = \frac{g}{\rho_p} \alpha \xi, \tag{1.27}$$

the same result as was obtained for the case of linear stratification. For the fixed points $z_{1,2}$, we expand $\ddot{\xi}$ as:

$$
\begin{aligned}
\ddot{\xi} &= \frac{g}{\rho_p} \left[\alpha \left(\pm\sqrt{-\frac{\alpha}{\gamma}} + \xi \right) + \gamma \left(\pm\sqrt{-\frac{\alpha}{\gamma}} + \xi \right)^3 \right] \\
&= \frac{g}{\rho_p} \left(\pm\alpha\sqrt{-\frac{\alpha}{\gamma}} + \alpha\xi \mp \alpha\sqrt{-\frac{\alpha}{\gamma}} - 3\alpha\xi + \cdots \right) \\
&\approx -\frac{2g}{\rho_p} \alpha \xi. \tag{1.28}
\end{aligned}
$$

The linear stability of the fixed points $z_{1,2}$ is thus determined by the value of α. If $\alpha < 0$, z_0 is stable and $z_{1,2}$ are unstable. If $\alpha > 0$, z_0 is unstable and $z_{1,2}$ are stable. This parallels
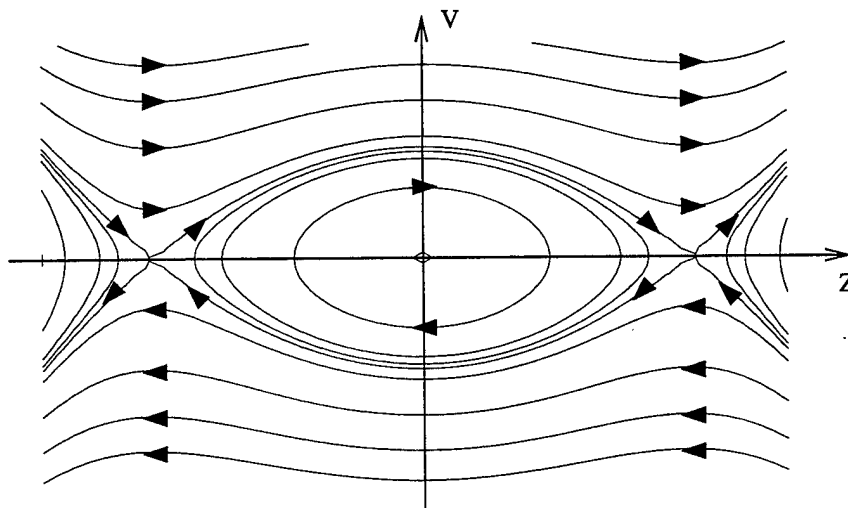
Figure 1.7: As in Figure 1.6, except for $\alpha < 0$ and $\gamma > 0$.

the conclusions one draws from the phase portraits in Figs. 1.6 and 1.7. Note that at leading order, γ does not play a role in the stability result.

1.3.3 Parameter variation

Suppose that in the above example we fix $\gamma < 0$ and vary the parameter α. For $\alpha < 0$, there is only a single fixed point, namely that at the origin. According to equation (1.27), this fixed point is stable. But when $\alpha > 0$, we have three equilibria and a situation like that shown in the phase portrait 1.6. Here the origin is unstable, and the two nontrivial fixed points are stable. In other words, when α passes zero, there is a change in the equilibrium points of the system. This is an example of a bifurcation; that is, a change in the system properties. The particular bifurcation displayed in this example is called a "pitchfork" bifurcation (Fig. 1.8), in which a fixed point loses stability and sheds two new, stable fixed points.

1.3.4 Conservative and Dissipative Systems

The equations (1.19) also form a conservative system. In particular, the energy,

$$H = E = \frac{1}{2}v^2 - \frac{g}{\rho_p} \int [\rho(z) - \rho_p]\, dz, \tag{1.29}$$

is conserved: $\dot{H} = 0$. This system is also Hamiltonian, since the equations may be obtained from

$$\dot{z} = \frac{\partial H}{\partial v}$$
$$\dot{v} = -\frac{\partial H}{\partial z}, \tag{1.30}$$

13
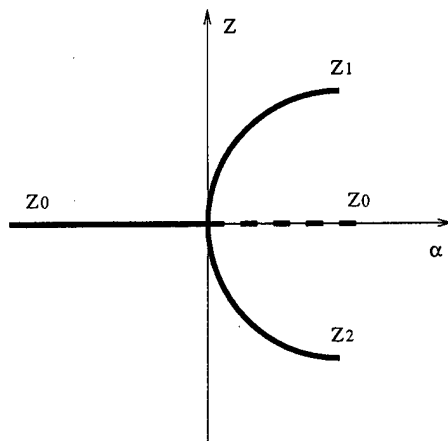
Figure 1.8: "Pitchfork" or "trident" bifurcation of the dust grain example with $\gamma < 0$. For $\alpha < 0$ there exists only one stable fixed point. As α increases beyond 0, three solutions exist: two stable fixed points, z_1 and z_2, and one unstable solution, z_0.
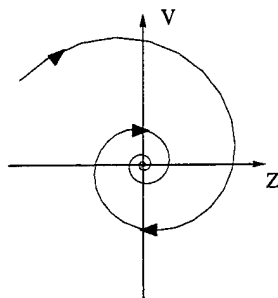
Figure 1.9: Attracting spiral point (focus) for a dissipative nonlinear system

where the Hamiltonian H is just the energy. Note that z and v are canonically conjugate variables.

In the presence of friction, the system becomes dissipative:

$$\ddot{z} = \frac{g}{\rho_p}(\rho(z) - \rho_p) - \mu\dot{z}, \tag{1.31}$$

where $\mu\dot{z}$ is a Stokes drag. In this case, $\dot{E} < 0$, energy is not conserved, and the phase space volume shrinks. An example of such a case is shown in Fig. 1.9. This displays a phase portrait in which there is an attracting spiral point at the origin. In other words, all of the oscillations of the conservative system disappear under the dissipative perturbation leaving only a stable spiral point where the elliptic fixed was once located. If such a damped system is forced, however, the asymptotic state may be a state of motion, such as a limit cycle.

14

1.4 Bifurcations

One of the key concepts of dynamical systems theory is a *bifurcation*. Basically. this term means simply that as we vary one of the intrinsic properties of the system, a transition takes place in the dynamical behaviour. The threshold at which the transition occurs is *the point of bifurcation*. Before the bifurcation there is one type of dynamical behaviour, and beyond it there is another.

In the flow of fluids down a pipe, for example, we might vary the viscosity or the forcing pressure gradient. Either way, we have a control parameter, the Reynolds number, that we vary in order to observe changes in the fluid dynamics. For low Reynolds number, the flow is laminar. But beyond a certain threshold, the fluid motion becomes turbulent, and this is one example of a bifurcation.

Another example is in fluid convection. Here we confine a fluid between two plates and impose a vertical temperature gradient (see lecture 2). As we ramp up this gradient by heating the two plates to a stronger and stronger temperature difference, we observe a bifurcation - the onset of fluid convection.

In dynamical systems theory, bifurcations are classified. One of the most important features of nonlinear systems is that many bifurcations are universal. That is, many transitions have a common form, independently of the physical system in which they take place. Thus, from an understanding of the most common types of bifurcations, we can understand many behavioural transitions.

It is presumably from such simple dynamics that we ultimately build up to the extensive, violently unstable systems in which we observe turbulent cascades over many scales of motion, and the emergence of coherent structures. More specifically, turbulence is usually thought to originate as a result of a bifurcation sequence that leads from a simple, regular or laminar flow to the turbulent state. Part of this sequence is the famed "transition to chaos". But the sequence itself, is merely a succession of known types of bifurcations.

The main types of bifurcations encountered in low-order dynamical systems that we shall mention in these lectures are the following:

Pitchfork bifurcation: We have already encountered this type of bifurcation. It corresponds to a situation in which an equilibrium point changes its stability by shedding two new ones. In the example considered earlier, the original equilibrium lost stability, and the two new fixed points were stable. This situation is called a *supercritical* pitchfork bifurcation. When the new equilibria are unstable, they co-exist with the stable equilibrium, and the pitchfork is *subcritical*.

Hopf bifurcation: In the simplest form of a Hopf bifurcation, a fixed point loses stability by shedding a limit cycle. That is, the equilibrium loses stability to perturbations that take the form of growing oscillations. In a *supercritical Hopf bifurcation*, the growing oscillations saturate on a nearby limit cycle. But for *subcritical Hopf bifurcations*, an unstable limit cycle collides with the stable fixed point, leaving it unstable beyond the bifurcation.

Period doubling bifurcation: A limit cycle may undergo a bifurcation where its basic period doubles, and the system "makes two turns" on nearby loops before returning to the initial position. A period-doubling bifurcation is revealed by the appearance of sub-harmonics

15

in the power spectrum of the system. A celebrated scenario of transition to chaos is based on a sequence of period doubling bifurcations, during which the basic period T is modified as $T \to 2T \to 4T \to ... \to 2^n T$ until chaotic behavior (associated with $n \to \infty$) is met.

1.5 Poincaré and stroboscopic maps

When the dimension of the dynamical system becomes larger than two, it is no longer possible to visualize the behaviour of typical orbits in terms of simple phase portraits like those shown in figures 1.6 and 1.7; projections of the solution onto a plane often obscures the structure of the attractor. Instead, we must develop other tools; one such tool is the Poincaré section.

Consider a simple flow of the form:

$$\frac{d\mathbf{X}}{dt} = \mathbf{F}(\mathbf{X}), \quad \mathbf{X} = (x, y, z). \tag{1.32}$$

The Poincaré section (Fig.1.10) of such a flow is formed by finding the intersections of a trajectory with a given surface or "manifold" in the phase space. This manifold is the "surface of section". It is sometimes useful to further take only those intersections with the same directionality with respect to the manifold. (Clearly, one requires the selected manifold to be nowhere tangent to the trajectory.) The set of intersection points is the Poincaré section. Given these points, we may then associate a dynamical law that maps one intersection point into the following one. This is the "Poincaré map" on the particular surface of section.

The Poincaré map (1.33) reduces a system from continuous to discrete time, and from dimension N to dimension $N - 1$. Thus, one goes from $\dot{\mathbf{X}} = \mathbf{F}(\mathbf{X})$, $\mathbf{X} \in \mathbb{R}^N$, to $\xi_{n+1} = f(\xi_n)$, $\xi_n \in \mathbb{R}^{N-1}$, where ξ_n is the n-th intersection of $\mathbf{X}(t)$ with the selected manifold:

$$X(t) \to \xi_n, \ n = 1, 2, \cdots, \ X \in \mathbb{R}^N, \ \xi_n \in \mathbb{R}^{N-1} \tag{1.33}$$

Another type of map is the stroboscopic map, obtained by reducing the trajectory to a series of snapshots taken at equal intervals of time. In this case, one goes from $\dot{\mathbf{X}} = \mathbf{F}(\mathbf{X})$ to $\eta_{n+1} = g(\eta_n)$ where $\eta_n = \mathbf{X}(t_0 + n\Delta t)$. For stroboscopic maps, the dimensionality of the system is not reduced.

16

(a)
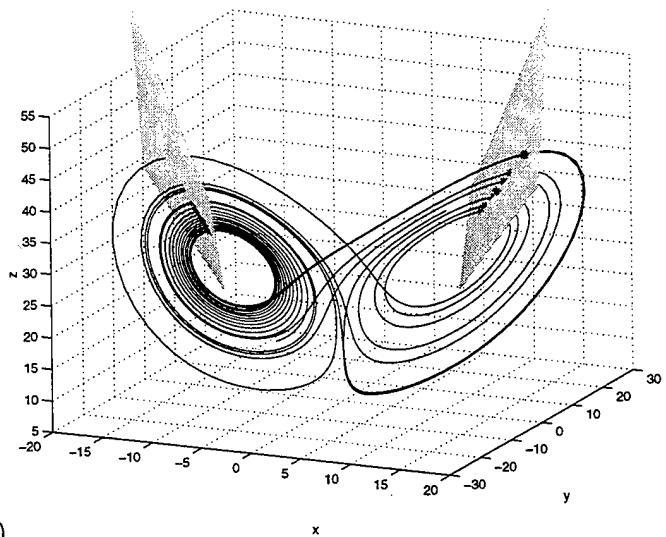
(b) Map of z–maxima
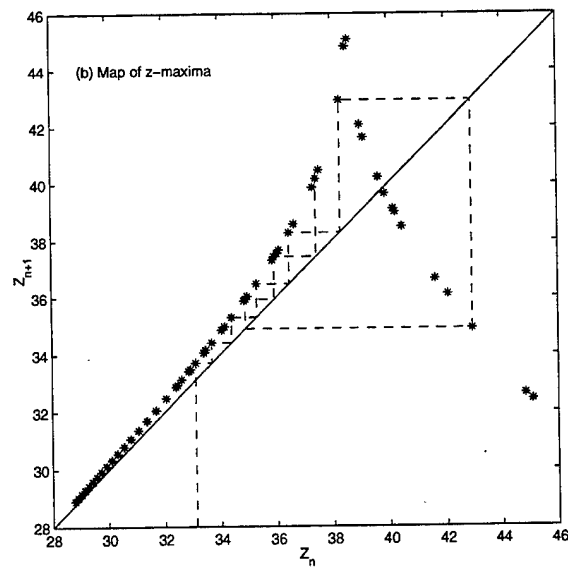
(b)

Figure 1.10: Poincaré section and map. Panel (a) shows the trajectory of a solution to the Lorenz equations (see lecture 2), with a Poincaré section determined by the maxima of z: $xy - 8z/3 = 0$. The values of z determined from each intersection with this manifold, Z_n, are plotted as a map, $Z_{n+1} = Z_{n+1}(Z_n)$ in panel (b). The stars in panel (a) show the intersection points.

Lecture 2

Multiple equilibria, limit cycles and strange attractors

In this lecture we introduce some of the classic low-order geophysical models exhibiting multiple equilibria, limit cycles and chaos.

2.1 Energy-balance models of the global climate

The global climate shows variability on many different time scales. Indirect observations (using the ratio of oxygen isotopes ^{16}O and ^{18}O in deep-sea sediment cores) provide an indication of past temperatures. In the quaternary period the average temperature has fluctuated by several degrees on timescales of hundreds of thousands of years, coinciding with periods of widespread glaciation and deglaciation. These and other evidences indicate that the global climate is capable of producing internal fluctuations and amplifying external forcings.

Simple models have been proposed in order to develop some understanding of the global climate (see, for example, Ghil & Childress 1987 for a review). We now derive the simplest of these models, which includes only the energy balance between incoming solar radiation and its re-radiation back into space from the Earth's surface.

From the first law of thermodynamics we have

$$\Delta E = Q_{in} - Q_{out} = c\Delta T, \tag{2.1}$$

where ΔE is the change in the internal energy of the system, induced by difference between the incoming energy Q_{in} and the outgoing energy Q_{out}. The change in internal energy has been parameterized as $\Delta E = c\Delta T$ where ΔT is the change in the temperature of the system and c is the specific heat. In the time Δt we have

$$c\frac{\Delta T}{\Delta t} = \mathcal{F}_{in} - \mathcal{F}_{out}, \tag{2.2}$$

where $\mathcal{F}_{in,out} = \frac{Q_{in,out}}{\Delta t}$ are the incoming and outgoing heat fluxes. By taking the limit $\Delta t \to 0$

we obtain

$$c\frac{dT}{dt} = \mathcal{F}_{in} - \mathcal{F}_{out}. \tag{2.3}$$

The incoming flux $\mathcal{F}_{in}$ is at short wavelengths, whilst the outgoing flux is at longer wavelengths, primarily in the infrared.

The total incident power per unit area of solar radiation is referred to as the "solar constant", S. At the top of the atmosphere, $S = 1.368kW/m^2$ (with a variation of 3.5% due to the ellipticity of the Earth's orbit). This incoming radiation is partly absorbed, and partly reflected back into space. The proportion reflected is given by the albedo parameter α. This parameter varies with both position and time because land, sea, ice and clouds all reflect light differently. However, for simplicity, we take a global, average value: $\alpha = 0.3$.

The total solar energy reaching the Earth per unit time is $\pi R^2 S$ (where R is the radius of the Earth), giving on average a flux of $\pi R^2 S/4\pi R^2 = \frac{1}{4}S$ at the top of the Earth's atmosphere. The total absorbed flux is therefore $\mathcal{F}_{in} = \frac{1}{4}S(1-\alpha)f(\phi) \approx 240f(\phi)W/m^2$, where $f(\phi)$ is a latitude correction accounting for geometrical projection.

The outgoing flux can be found by using a modification of Stefan-Boltzmann law, giving $\mathcal{F}_{out} = g(T)\sigma T^4$, where $g(T)$ is a 'greyness' correction to account for the fact that the Earth is not a perfect black body.

If we assume a local equilibrium ($\mathcal{F}_{in} = \mathcal{F}_{out}$) we obtain

$$\frac{1}{4}S(1-\alpha)f(\phi) = g(T)\sigma T^4. \tag{2.4}$$

This expression predicts equilibrium temperatures of $270K$ at the equator, $170K$ at the north pole and $150K$ at the south pole. The average temperature predicted by (2.4) is significantly underestimated due to the omission of the atmospheric greenhouse effect, which raises global temperatures by inhibiting the transmission of thermal radiation from the surface into space. This simple calculation also predicts a much larger difference between polar and equatorial temperatures than that seen on the Earth - this is due to neglecting the mean transport of heat from the tropics to the polar regions by atmospheric and oceanic circulation. The difference between the observed values of $\mathcal{F}_{in}$ and $\mathcal{F}_{out}$ as a function of latitude (see Figure 2.1) provides means of estimating the meridional heat transport of the ocean and atmosphere, as shown in Figure 2.2. More sophisticated analyses have estimated the proportions of this transport due to the oceanic circulation and the mean and fluctuating atmospheric circulation.

2.1.1 The effect of temperature-dependent albedo

We now consider the globally averaged energy balance, at first ignoring, for simplicity, the greyness factor. The energy balance in stationary conditions then becomes

$$\frac{1}{4}S(1-\alpha) = \sigma T^4,$$

which has the unique, physically meaningful solution,

$$T_0 = \left[\frac{S(1-\alpha)}{4\sigma}\right]^{\frac{1}{4}}.$$
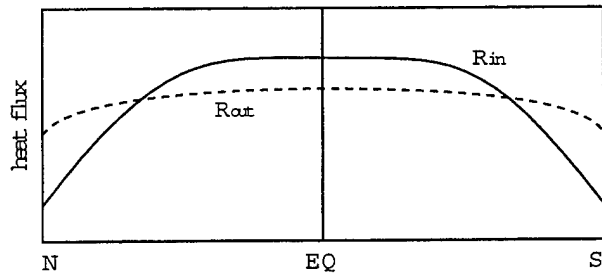
19

Figure 2.1: Sketch of observed dependence of radiation balance on latitude (redrawn from Ghil & Childress 1987)
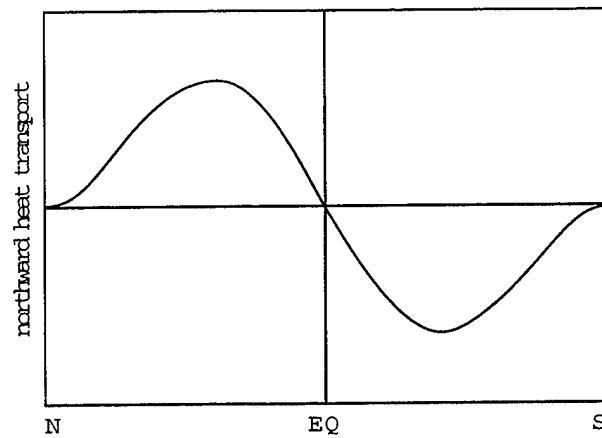

Figure 2.2: Sketch of atmospheric and oceanic heat transport versus latitude, deduced from local radiation imbalances (redrawn from Ghil & Childress 1987)
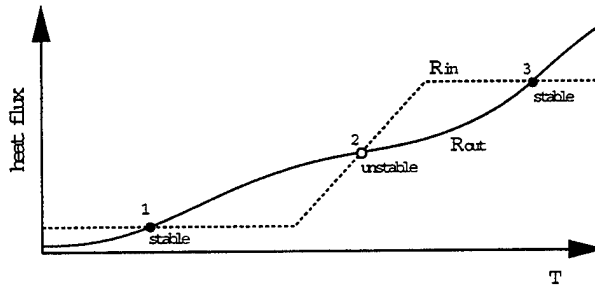
Figure 2.3: Fixed points of a simple energy-balance climate model (redrawn from Ghil & Childress 1987)

The average albedo α depends, however, on temperature. When the temperature is low and ice covers a large fraction of the Earth, the albedo is larger than for an ice-free Earth. Denoting by α_f and α_i the albedos corresponding to a minimal and maximal ice cover respectively, we can approximate the ice-albedo feedback as

$$\alpha(T) = \alpha_i, \quad T \leq T_i,$$

$$\alpha(T) = \alpha_f, \quad T \geq T_f$$

and

$$\alpha(T) = \alpha_i + (\alpha_f - \alpha_i)\frac{T - T_i}{T_f - T_i}, \quad T_i < T < T_f,$$

where T_i is the temperature below which ice has its maximum extend, and T_f is the temperature above which ice has its minimal extent.

The dependence of albedo on temperature can result in multiple equilibria, in contrast to the case of a constant albedo in which only one equilibrium is possible. The energy balance can be solved graphically by plotting $\mathcal{F}_{out}$ and $\mathcal{F}_{in}$ as functions of T and looking for intersections of the two curves (see figure 2.3, where a greyness correction to $\mathcal{F}_{out}$ has also been included). The number of fixed points depends on the values of the parameters chosen. When we have three fixed points as in figure 2.3, a linear stability analysis shows that point 2 is unstable and points 1 and 3 are stable. The instability of point 2 is due to the positive feedback between ice and albedo: a small temperature increase will reduce the extent of ice cover, reducing the albedo and increasing the temperature still further.

This example demonstrates the existence of multiple equilibria even for very simple nonlinear models. Note that the phase space of the above model is one-dimensional, as the dynamics is fully described by the global temperature T. For one-dimensional dissipative systems with continuous time and without an explicit time-dependent external forcing (i.e., an autonomous ordinary differential equation), stationary equibria (fixed points) are the only possible attractors.
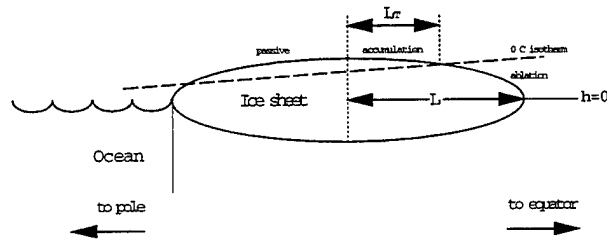
21

Figure 2.4: Idealized model of an ice sheet (redrawn from Ghil & Childress 1987).

2.1.2 Ice-sheet dynamics

The simple model described above displays multiple equilibria but it does not have any time-dependent behavior in its asymptotic states. In order to obtain self-sustained oscillations (i.e., limit cycles) in an autonomous system, at least a phase space of at least two dimensions is required.

In order to produce self-sustained climatic oscillations, we thus need a second dynamical variable to be coupled with global temperature. One way to achieve this is to include the dynamics of the ice sheets. Consider an idealized ice sheet as shown in figure 2.4.

The air temperature is assumed to decrease with altitude and with latitude, leading to accumulation of ice above the $0°C$ isotherm and ablation below it. The ice sheet is bounded on the northern side by the ocean, which is assumed to prevent the growth of the ice sheet on that side. Thus we shall consider only the variation in the extent L of the ice sheet to the right of the midpoint. If the height h of the ice sheet above ground varies with north-south position y according to

$$h(y) = \lambda^{\frac{1}{2}}(L - |y|)^{\frac{1}{2}},$$

then the volume of ice is

$$V = 2c_L\lambda^{\frac{1}{2}}L^{\frac{1}{2}}\int_0^L \left(1 - \frac{|y|}{L}\right)^{\frac{1}{2}} dy = \frac{4}{3}\lambda^{\frac{1}{2}}L^{\frac{3}{2}}c_L,$$

where c_L measures the longitudinal extent of the ice sheet.

The rate of change of ice volume can be written as $\dot{V} = aA - a'A'$, where $A = c_L L_T$ is the area with accumulation at the rate a, and $A' = c_L(L - L_T)$ is the area with ablation at the rate a'. This gives

$$\dot{V} = c_L a'[\epsilon L_T - (L - L_T)],$$

where $\epsilon = \frac{a}{a'}$. This expression can be used to find the rate of change of the extent of the ice sheet:

$$\dot{L} = \frac{a'}{2\lambda^{\frac{1}{2}}L^{\frac{1}{2}}}[(1 + \epsilon)L_T - L]$$

where L_T is a given function of L and of the (fixed) slope of the $0°C$ isotherm.

The variation in ice cover influences the energy balance through changes in albedo. The global average albedo can be written as

$$\alpha = \gamma(\alpha_0 + \alpha_1\mu) + (1 - \gamma)\alpha_{oc}(T),$$

where γ is the fraction of the earth's surface covered by land, and α_0 and α_{oc} are the albedo of the land and ocean, respectively. The quantity μ represents the fraction of land covered by ice, and α_1 is the correction to the albedo of the land due to the presence of ice.

The precipitation is supposed to increase with temperature, resulting in an increase in ϵ, the ratio of accumulation and ablation rates. The positive feedback of T on ϵ is a crucial but delicate point of this model. The hypothesis behind this choice is that increased temperatures produce both a more active hydrological cycle (more precipitation) and more melting of the ice sheet, but the ratio of the two effects is such that more ice is formed than melted when increasing T. The real dependence of ϵ on T is, of course, very complicated, and at high temperatures ϵ is clearly decreasing for increasing T. The choice $\epsilon \sim T$ should thereby be taken as a local approximation to $\epsilon(t)$ in the small range of temperature where the model is applied. The system of equations which results from coupling the energy balance model of the previous section with the ice model is

$$\begin{cases} c\dot{T} = Q[1 - \gamma(\alpha_0 + \alpha_1\mu) - (1 - \gamma)\alpha_{oc}(T)] - \sigma g T^4 \\[2mm] c'\dot{L} = \frac{1}{L^{\frac{1}{2}}}\{[1 + \epsilon(T)]L_T(L, T) - L\}. \end{cases} \tag{2.5}$$

It is clear from the first equation that $\dot{T} \sim -\alpha$, so $\dot{T} \sim -L$ since $\alpha \sim L$. The second equation shows that $\dot{L} \sim \epsilon$. Since ϵ grows with T (an increase in temperature leads to increased precipitation and more accumulation) we have $\dot{L} \sim T$. These equations can be combined to yield $\ddot{T} \sim -T$, the equation for an oscillator. Using parameters appropriate to the earth, this system shows oscillations with a period of a few thousand years and an amplitude of a few degrees Celsius. Note that these temperature fluctuations have a period much shorter than the glacial-interglacial time scale, and thus describe other forms of climate variability. The amplification of external disturbances by climate variability on the glaciation time scales will be reconsidered in lecture 4.

On more general grounds, we recall that autonomous, two-dimensional dissipative dynamical systems with continuous time may display only stationary equilibria or limit cycles at asymptotically large times (the dynamics is deterministic implying that orbits cannot cross at any time, but the phase space is a plane, so points or closed curves are the only non-intersecting geometrical objects with dimension less than 2). More complicated attractors, such as quasi-periodic motions and chaotic behavior, require at least three dimensions in phase space if the system dynamics is described by ordinary differential equations (ODEs). In the following section, we introduce a classic three-dimensional dynamical system displaying chaotic behavior.

2.2 Rayleigh-Benard convection

We now discuss a classic example of a chaotic low-dimensional dynamical system, namely, the Lorenz (1963) model for Rayleigh-Benard convection.
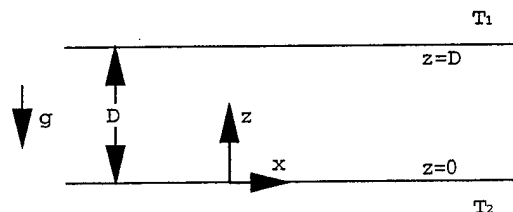
Figure 2.5: Fluid layer contained between two rigid horizontal plates kept at different temperatures.

Consider the behaviour of a layer of viscous fluid under gravity, contained between rigid horizontal plates (see figure 2.2). The plates are separated by a distance D and maintained at temperatures T_1 and T_2 at the top and bottom, respectively.

For a fluid with coefficient of thermal expansion $\alpha > 0$ we have denser fluid overlying less dense fluid when $T_2 - T_1 > 0$. The flow which results from this heating depends on the Rayleigh number $Ra = \frac{g\alpha D^3 (T_2 - T_1)}{\nu\kappa}$, where g is the acceleration due to gravity, ν is the kinematic viscosity of the fluid and κ is its thermal conductivity. The behaviour of this system as a function of Ra is illustrated in figure (2.2). For small Ra, heat is transferred between the plates purely by conduction and there is no motion in the fluid (case (a)). If the Rayleigh number exceeds a critical value the conductive solution becomes unstable and steady convection cells are formed, as shown in case (b). With a further increase of Ra the cells start to oscillate (case (c)) and further increases lead to quasiperiodic and/or chaotic motion. When Ra is sufficiently large the convection becomes turbulent, as illustrated in case (d).

2.2.1   Derivation of the Lorenz model

The Navier-Stokes equations for an incompressible fluid of density ρ in a gravitational field $\mathbf{g}$ are

$$\rho\frac{\partial \mathbf{u}}{\partial t} + \rho\left(\mathbf{u} \cdot \nabla\right)\mathbf{u} = -\nabla p + \mu\nabla^2\mathbf{u} + \mathbf{g}\Delta\rho \tag{2.6}$$

and

$$\nabla \cdot \mathbf{u} = 0, \tag{2.7}$$

where $\mathbf{u}$ is velocity, p is pressure, μ is viscosity and $\Delta\rho = \rho - \rho_0$ is the local difference in density from the reference value ρ_0. The quantity $\Delta\rho$ can be expressed in terms of the difference ΔT from the temperature at which $\Delta\rho = 0$:

$$\Delta\rho = -\rho_0\alpha\Delta T. \tag{2.8}$$

This system of equations is closed by the heat equation

$$\frac{\partial T}{\partial t} + \left(\mathbf{u} \cdot \nabla\right)T = \kappa\nabla^2 T, \tag{2.9}$$
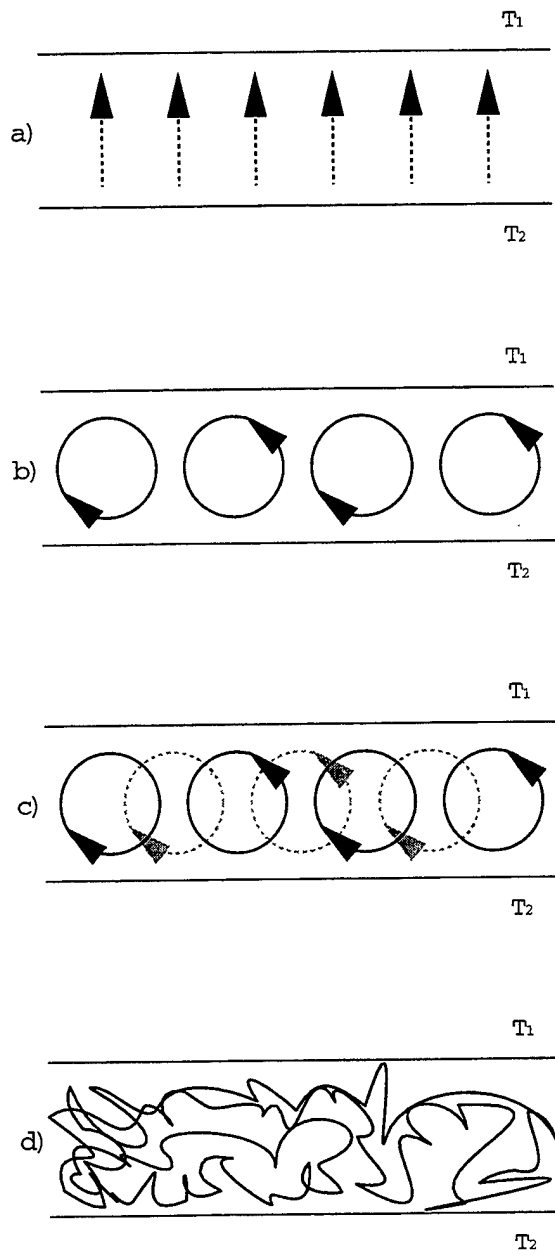
24

Figure 2.6: Transition to turbulent motion in a fluid layer between two rigid boundaries as the Rayleigh number Ra is increased. (a): conduction only; (b): steady convection; (c): time-dependent convection; (d): turbulent convection.

25

where κ is the thermal diffusivity.

Next we use the Boussinesq approximation to simplify equation (2.6). This assumes that $\Delta\rho \ll \rho$, so we can replace ρ by ρ_0 on the left-hand side of (2.6), retaining the density variations only in the third (buoyancy) term on the right-hand side. The resulting equation is

$$\frac{\partial \mathbf{u}}{\partial t} + (\mathbf{u} \cdot \nabla) \mathbf{u} = -\frac{1}{\rho_0} \nabla p + \nu \nabla^2 \mathbf{u} - \mathbf{g}\alpha\Delta T, \qquad (2.10)$$

where $\nu = \mu/\rho_0$ is the kinematic viscosity and the equation of state (2.8) has been incorporated into the final term. Taking the curl of (2.10) yields an equation for the vorticity $\boldsymbol{\omega} \equiv \nabla \times \mathbf{u}$:

$$\frac{\partial \boldsymbol{\omega}}{\partial t} + (\mathbf{u} \cdot \nabla) \boldsymbol{\omega} = (\boldsymbol{\omega} \cdot \nabla) \mathbf{u} + \nu \nabla^2 \boldsymbol{\omega} - \alpha \nabla \times (\mathbf{g}\Delta T). \qquad (2.11)$$

If we choose Cartesian coordinates so that $\mathbf{g} = (0, 0, -g)$ and assume that all the fields are independent of y, then the vorticity has a non-zero component only in the y direction, $\boldsymbol{\omega} = (0, \omega, 0)$, and (2.11) becomes the scalar equation

$$\frac{\partial \omega}{\partial t} + (\mathbf{u} \cdot \nabla) \omega = \nu \nabla^2 \omega - g\alpha \frac{\partial \Delta T}{\partial x}. \qquad (2.12)$$

where now the velocity is zero in the y direction, i.e. $\mathbf{u} = (u, 0, w)$. Note that the assumption of two-dimensionality eliminates the first term (vortex stretching) on the right hand side of (2.11). Since the velocity is now two-dimensional and incompressible, it can be written in terms of a streamfunction ψ as $u = \partial\psi/\partial z$ and $w = -\partial\psi/\partial x$. The scalar vorticity is related to ψ by the Poisson equation $\omega = \nabla^2 \psi$, allowing the vorticity equation (2.12) to be written in terms of ψ as

$$\frac{\partial \nabla^2 \psi}{\partial t} - [\psi, \nabla^2 \psi] = \nu \nabla^4 \psi - g\alpha \frac{\partial \Delta T}{\partial x}, \qquad (2.13)$$

where $[a, b] \equiv \frac{\partial a}{\partial x}\frac{\partial b}{\partial z} - \frac{\partial a}{\partial z}\frac{\partial b}{\partial x}$ is the two-dimensional Jacobian operator.

We now write the temperature field T in terms of a background profile $\overline{T}$ which depends only on z and a perturbation θ:

$$T(x, z, t) = \overline{T}(z) + \theta(x, z, t).$$

The heat equation (2.9) then takes the form

$$\frac{\partial \theta}{\partial t} - [\psi, \theta] - \frac{\partial \psi}{\partial x}\frac{\partial \overline{T}}{\partial z} = \kappa \nabla^2 \theta + \kappa \frac{\partial^2 \overline{T}}{\partial z^2}.$$

In the absence of convection ($\psi = 0$), a linear temperature profile is a stationary solution of the equations of motion. Thus, if we assume a linear background temperature profile of the form,

$$\overline{T} = T_2 + \frac{T_1 - T_2}{D}z,$$

26

the equation for θ becomes

$$\frac{\partial \theta}{\partial t} - [\psi, \theta] - \frac{\partial \psi}{\partial x} \frac{T_1 - T_2}{D} = \kappa \nabla^2 \theta. \tag{2.14}$$

The governing equations for this system are (2.13) and (2.14).

Conditions of no slip and no normal flow at the upper and lower boundaries imply that $\psi = \nabla^2 \psi = 0$ on $z = 0, D$. The temperature at the top and bottom boundaries is fixed, so $\theta = 0$ on $z = 0, D$.

2.2.2 Expansion in Fourier Modes

Given a nonlinear system of partial differential equations:

$$\partial_t \omega = L\omega + N(\omega),$$

where L and N are linear and nonlinear operators respectively, the variable ω can be written as a combination of the eigenmodes $\Phi_j(x)$ of the linear operator (constant in time):

$$\omega = \sum_j a_j(t)\Phi_j(x)$$

and the dynamics is described by the time dependence of the expansion coefficients $a_j(t)$:

$$\frac{da_j}{dt} = \mathcal{F}(\{a_j\}),$$

which is a set of an infinite number of coupled ordinary differential equations.

As an example, the method is applied to a modified Burgers equation:

$$\frac{\partial u}{\partial t} + c\frac{\partial u}{\partial x} + \alpha u \frac{\partial u}{\partial x} = \nu \frac{\partial^2 u}{\partial x^2},$$

with periodic boundary conditions $u(0, t) = u(2\pi, t)$. The eigenmodes of the linear operator are the Fourier modes e^{inx} and the equation becomes:

$$\sum_{n=-\infty}^{\infty} (\dot{a}_n + inca_n)e^{inx} + \sum_{l=-\infty}^{\infty} \sum_{m=-\infty}^{\infty} \alpha a_l ima_m e^{i(l+m)x} = \sum_{n=-\infty}^{\infty} (-\nu n^2)a_n e^{inx}.$$

Considering $l + m = n$, the exponential term e^{inx} can be eliminated and the sum can be split into an infinite number of equations:

$$\dot{a}_n + inca_n + \sum_{l=-\infty}^{\infty} i\alpha(n - l)a_l a_{n-l} = -\nu n^2 a_n.$$

From a numerical perspective, only a finite number of these equations can be solved and so a truncation of the higher order modes is usually performed.

27

2.2.3 The Lorenz '63 model

It is possible to obtain a simple dynamical model for Rayleigh-Benard convection by expanding equations (2.13) and (2.14) in terms of three Fourier modes. As mentioned above, we assume no slip and no normal flow boundary conditions, i.e., $\psi = \nabla^2\psi = 0$ on $z = 0, D$. The thermal boundary condition is $\theta = 0$ on $z = 0, D$. If we assume ψ and θ to be periodic in x, then they can be represented in terms of infinite Fourier sums. By retaining only the first Fourier mode for the stream function ψ and the first two modes for the temperature θ, we may write the variables as

$$\psi = \frac{(1+a^2)k\sqrt{2}}{a} X \sin(\pi a\xi)\sin(\pi\zeta),$$

$$\theta = \frac{Ra_{cr}(T_1 - T_2)}{\pi Ra}[\sqrt{2}Y\cos(\pi a\xi)\sin(\pi\zeta) - Z\sin(2\pi\zeta)],$$

where $\xi = X/D$, $\zeta = Z/D$, a is the aspect ratio of the unstable perturbation, and $Ra_{cr} = \pi^4(1+a^2)^3/a^2$ is the critical Rayleigh number at which the conductive solution becomes unstable to convection.

By substituting the truncated Fourier expansions of ψ and θ into equations (2.13) and (2.14) we obtain three coupled ordinary differential equations for the coefficients X, Y and Z of the expansion:

$$\begin{cases} \dot{X} = -\sigma X + \sigma Y \\[2mm] \dot{Y} = -XZ + RX - Y \\[2mm] \dot{Z} = XY - bZ, \end{cases} \tag{2.15}$$

where the differentiation refers to the nondimensional time $\tau = \pi^2(1+a^2)kt/H^2$, $R = Ra/Ra_{cr}$ is a normalised Rayleigh number, $b = 4/(1+a^2)$ is related to the aspect ratio of convective cells, and $\sigma = \nu/k$ is the Prandtl number. X is proportional the intensity of the convective motion, Y is proportional to the difference in temperature between the upgoing and downgoing currents, and Z describes the horizontally averaged deviation from the linear temperature profile. This is a dissipative system, since its divergence is negative:

$$\partial_x\dot{X} + \partial_y\dot{Y} + \partial_z\dot{Z} = -\sigma - 1 - b < 0,$$

implying that the volume of the attractor in the three-dimensional phase space is zero.

Fixed points are given by the system:

$$\begin{cases} X - Y = 0 \\[2mm] -XZ + (R-1)X = 0 \\[2mm] XY - bZ = 0. \end{cases} \tag{2.16}$$
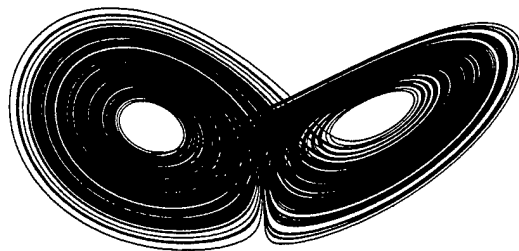
Figure 2.7: Lorenz attractor with $R = 28$, $\sigma = 10$, $b = 8/3$. Shown is the path of the orbit in the phase space (X, Y, Z).

For $R < 1$ there is only one fixed point $\mathbf{X}_0$, $X_0 = Y_0 = Z_0 = 0$, corresponding to a linear (conductive) temperature profile, with no convection.

For $R > 1$ there are two additional fixed points $\mathbf{X}_1$ and $\mathbf{X}_2$, $X_1 = Y_1 = \sqrt{b(R-1)}$, $Z_1 = R - 1$, and $X_2 = Y_2 = -\sqrt{b(R-1)}$, $Z_2 = R - 1$, corresponding to steady convection in parallel rolls.

By a linear stability analysis it can be shown that $\mathbf{X}_0$ is the only stable fixed point for $R < 1$; at $R = 1$ there is a pitchfork bifurcation in which $\mathbf{X}_0$ becomes unstable and $\mathbf{X}_1$ and $\mathbf{X}_2$ appear as new, stable equilibria. If $\sigma > b + 1$, $\mathbf{X}_1$ and $\mathbf{X}_2$ become unstable through a subcritical Hopf bifurcation at $R = R_c = \frac{\sigma(\sigma+b+3)}{\sigma-b-1}$. The consequence of the disappearance of the stable fixed point is chaotic motion (see Sparrow, 1982). In the phase space the attractor of the system (figure 2.7) is a "strange" object, with a non-integer fractal dimension (see below). Roughly speaking, the trajectory of the solution follows a path in phase space that spirals away from one unstable fixed point (say, $\mathbf{X}_1$), then loops in close to the other unstable fixed point ($\mathbf{X}_2$). It then spirals away from this second unstable focus until it loops back to the neighbourhood of the first unstable fixed point. The switching between orbiting around one unstable fixed point and the other follows an irregular, aperiodic sequence.

29
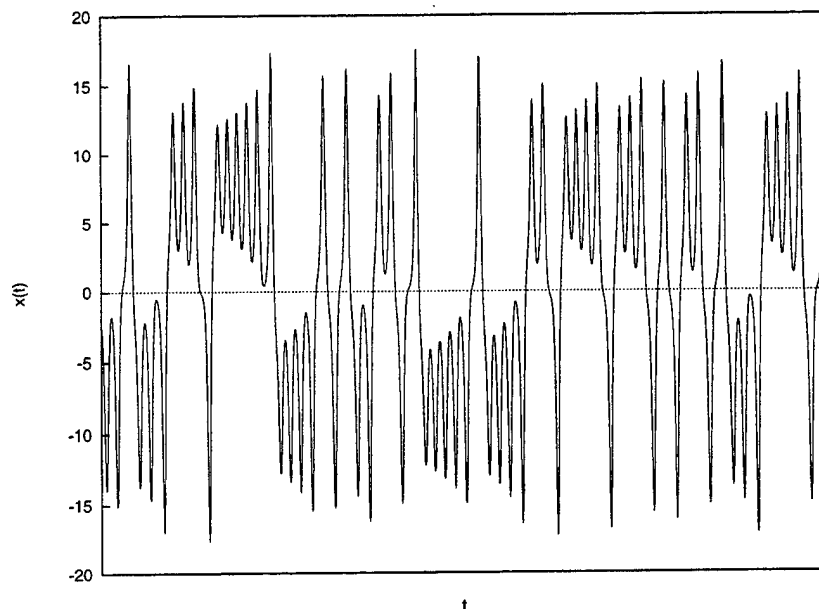
Figure 2.8: Time series of X from the Lorenz system with $R = 28$, $\sigma = 10$, $b = 8/3$.

The time dependence of the X variable is shown in figure 2.8. Note the irregular transitions from positive to negative values of X, corresponding to the system orbiting around one or the other unstable fixed point.

Trajectories started from nearby points on the strange attractor diverge rapidly from one another, though they remain on the attractor. This sensitivity to initial conditions makes prediction of the trajectory impossible in practice even though the system is deterministic. This is the origin of the popular vision of the "butterfly effect" in weather prediction.

2.3   Properties of strange attractors

Strange attractors are intimately associated with chaotic dynamics and unpredictability in dissipative systems. Roughly speaking, a strange attractor is a collection of an infinite number of unstable periodic orbits that is, in some sense, globally attractive. Geometrically, these objects are very complicated. Chaotic motion can crudely be thought of as the motion of the

Figure 2.9: Fractal Structure of a Strange Attractor

trajectory of the system as it meanders through this collection of unstable orbits, wandering close to one orbit at one time, then switching to the neighbourhood of another in an apparently random fashion.
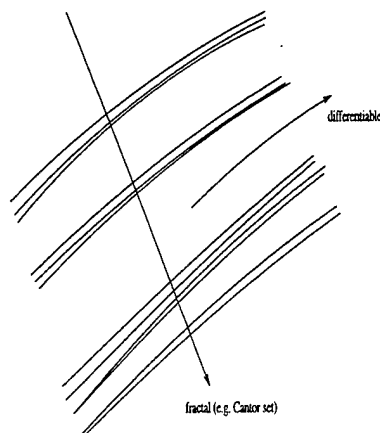
There are two basic properties of strange attractors that lead to measures that can be used to characterize these objects. The properties are:

- Sensitive dependence on initial conditions. This sensitivity can be quantified by a "Lyapunov exponent", the exponential rate of divergence of neighbouring trajectories in phase space (evidently, for chaos, this exponent must be positive).

- Fractal structure. Fractals can be characterized by a "Hausdorff dimension" which is not integer and is (usually) larger than the "topological dimension". This feature is associated with the self-similarity (self-affinity) of such geometrical structures.

We discuss these properties more completely below.

In the lectures, we use the term strange attractor to indicate a chaotic attractor with sensitive dependence on initial conditions. Although there are non-fractal chaotic attractors, as well as fractal non-chaotic attractors, in most systems chaotic attractors have a fractal nature. A pictorial image of this structure is shown in figure 2.9.

2.3.1 Lyapunov exponents

Here, we encounter for the first time the issue of predictability in dynamical systems. Given a deterministic dynamical system, we can calculate a future state, say $\mathbf{X}(t)$, from the knowledge of its state at a given time, say $\mathbf{X}_0 = \mathbf{X}(0)$, by (analytically or numerically) solving the equations of motion. However, often the initial conditions are known only with finite precision. Thus, we are interested in knowing how an initial error, or perturbation, on the initial conditions. say δ_0, will evolve in time.

Systems dominated by stationary equilibria or limit cycles are characterized by the fact that the initial error increases at most linearly with time, and thus predictability is assured

31

for long times. In the case of a globally attracting fixed point, the system will always tend to the fixed point itself, and the initial error will decrease with time. On a limit cycle, on the other hand, there is a phase error that may grow at most linearly with time, leading to a slow loss of knowledge about the exact phase of the oscillation.

Now suppose that we consider a system with two stable equilibria and an unstable saddle point between them, such as the double-well oscillator pictured in figure 1.7 of lecture 1. In the vicinity of the unstable fixed point, a small perturbation on the initial conditions may force the system to tend toward one or the other fixed point, thus leading to unpredictability of the final state even for small initial perturbations. This happens, however, only for a very small, special region of phase space, the vicinity of the unstable point, and elsewhere the dependence on initial condition is much less extreme.

The key feature of the saddle point that leads to the system behaving in this way is the "division" of the phase space by the orbits that emerge or converge to the saddle point. These special trajectories are the "unstable" and "stable manifolds" of the saddle point (the set of all points that either diverge from, or converge to, that equilibrium). These particular orbits demark the directions of flow in phase space near the saddle. Importantly, at the locations where these manifold intersect, it takes only a slight change in initial condition to produce a very different evolution (namely, a perturbation for which the initial condition hops across one of the manifolds).

Systems undergoing deterministic chaotic dynamics, such as the Lorenz '63 model discussed above, are also characterized by "sensitive dependence on initial conditions." In these systems, the attractor itself contains infinitely many unstable elements (limit cycles). Like the saddle point considered above, each of the unstable cycles possesses intersecting stable and unstable manifolds that again partition the direction of flow in phase space. Thus, in the vicinity of each cycle, there must be a sensitive dependence on the initial condition. But the main difference between the two-well oscillator and the chaotic system is that the unstable cycles form the dense skeleton of the strange attractor. Hence there are intersecting manifolds densely populating the attractor and there is sensitivity to the initial state throughout the object.

For strange attractors, then, small initial perturbations can amplify exponentially fast and destroy the predictability of the system after a finite time. This behavior can be taken as a definition of deterministic chaos.

A quantitative way of defining sensitive dependence on initial conditions is based on the concept of Lyapunov exponents. If we consider a solution X of an n-dimensional dynamical system (such as $\dot{X} = F(X)$), the evolution of an infinitesimally small perturbation $\delta(t)$ can be considered linear to first order, and the governing equation becomes

$$\dot{\delta} = \frac{\partial F}{\partial X}\delta. \qquad (2.17)$$

Each one of the n eigenvalues of the matrix $\frac{\partial F}{\partial X}$ gives an estimate of the growth rate of an infinitesimal initial perturbation aligned with the corresponding eigenvector of the matrix. The maximum Lyapunov exponent is then defined as

$$\lambda_{max} = \lim_{t \to \infty} \lim_{\delta_0 \to \infty} \frac{1}{t} \ln \frac{\delta(t)}{\delta_0}$$
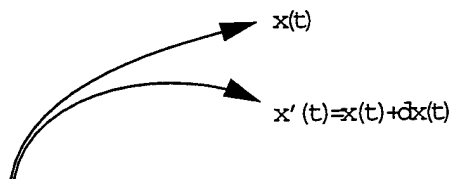
32

Figure 2.10: Divergence of nearby trajectories in phase space for a chaotic system.

and it measures the fastest long-time growth rate of an infinitesimal error on the initial conditions.

Since a generic initial perturbation will have components along all the eigenvectors of the matrix $\partial \mathbf{F}/\partial \mathbf{X}$, the fastest growth will in general dominate and the infinitesimal error will approximately grow as $\delta(t) = \delta_0 e^{\lambda_{max} t}$ where $\delta_0 = \delta(t = 0)$, leading to rapid divergence of nearby trajectories (figure 2.10).

A dynamical system is generally considered to be chaotic if $\lambda_{max} > 0$. Note that the presence of the two limits in the previous definition is very important and cannot be neglected nor inverted: the perturbation must be infinitesimal in order to be considered linear, and the average on an infinite time is necessary as the Lyapunov exponent is a measure of the average error growth over the entire trajectory. Locally, the growth rate can be very different and may depend on the part of the attractor spanned during the evolution. For this reason, even if the maximum Lyapunov exponent is useful for the definition of a chaotic system, in practice it does not always give a good indication of how rapidly infinitesimal errors will grow at short times, as this may depend on the initial location on the attractor and on the initial direction of the error. Nor does it describe how finite errors grow.

2.3.2 Fractal Dimension

Due to the instabilities associated with sensitive dependence on initial conditions, most physically interesting strange attractors have a fractal nature. What is a fractal? A fractal is an object whose "fractal dimension", or better, "Hausdorff dimension" D_H is strictly larger than its topological dimension D_T. A fractal set is characterized by some form of scaling; that is, fragments of the sets, when suitably rescaled, display the same properties of the whole set, on every scale.

One way to introduce the fractal dimension of a set is the notion of box-counting. By splitting the phase space domain where the set is contained into square boxes of length ϵ one can count the number of boxes containing at least one point of the set, $N(\epsilon)$ (see figure 2.11). The box-counting dimension is then defined as:

$$D_0 = \lim_{\epsilon \to 0} \frac{\log N(\epsilon)}{\log(1/\epsilon)}. \tag{2.18}$$

This dimension coincides with the topological dimension for simple geometrical objects such as points, lines or planes but may be different for more complex objects.
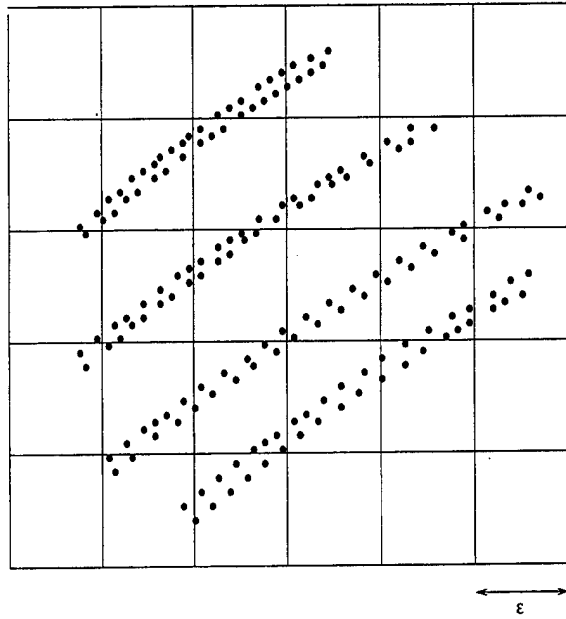
33

Figure 2.11: The notion of box-counting dimension. The object is divided into square boxes and the number of points is counted in each box. The lengths of the boxes are then successively reduce to generate data to compute D_0 via equation (2.18). Such a set of points could be generated by taking a Poincaré section of a strange attractor like that in figure 2.9.

An example of the latter is the Cantor set, which is obtained by taking a segment with unit length, cutting it in thirds, removing the middle third, and repeating the operation on the remaining two disconnected thirds, and so on forever (see figure 2.12). At the beginning, we have one segment with length $\epsilon_0 = 1$, $N(\epsilon_0) = 1$. At the first step, we have two segments with length $\epsilon_1 = 1/3$, $N(\epsilon_1) = 2$. At the second step, we have four segments with length $\epsilon_2 = 1/9$, $N(\epsilon_2) = 4$. At the n-th step, we have 2^n segments with length $\epsilon_n = 1/3^n$. It is easy to see that the fractal dimension of the Cantor set is

$$D_0 = \lim_{n \to \infty} \frac{\log 2^n}{\log 3^n} = \frac{\log 2}{\log 3}.$$ (2.19)

Since the topological dimension of the cantor set is $D_T = 0$, it is clear that this set is a fractal.

An extension of the box-counting dimension leads to the multifractal (or Renyi) dimensions D_q. One can define a partition function

$$B(\epsilon, q) = \sum_{i=1}^{N_{box}} [p_j(\epsilon)]^q,$$ (2.20)

where $p_j(\epsilon) = \frac{n_j(\epsilon)}{N}$ is the fraction of points found in the j-th box. For $q = 0$, B counts the number of non-empty boxes; thus one retrieves the definition of the box-counting dimension. For arbitrary q, the asymptotic scaling of B is $B(\epsilon, q) \sim \epsilon^{(q-1)D_q}$ at small ϵ. One should note

34

————   ———— $N(\epsilon)=2$ $\epsilon=1/3$

—— ——   —— —— $N(\epsilon)=4$ $\epsilon=1/9$

—— ——   —— —— —— —— $N(\epsilon)=8$ $\epsilon=1/27$

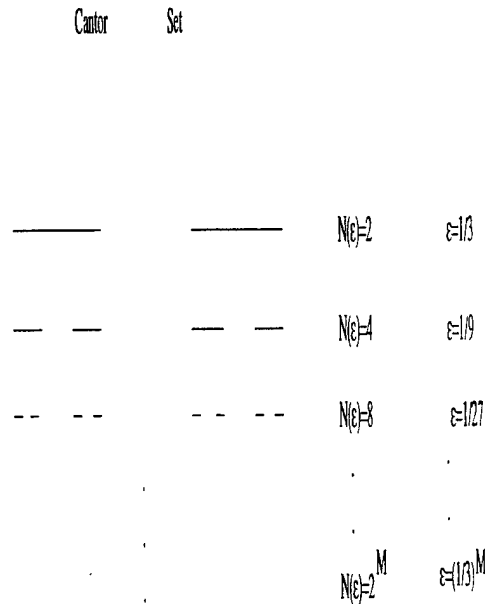$N(\epsilon)=2^M$ $\epsilon=(1/3)^M$

Figure 2.12: The Cantor Set

that D_q is a monotonically non-increasing function of q. The most frequently encountered multifractal dimension is D_2, since it is the simplest one which is sensitive to statistics and that can also be explicitly calculated in experiments.

2.3.3   Conceptual implications of deterministic chaos

The discovery that even very simple mathematical models can lead to unpredictable behavior has, of course, several conceptual implications. Probably, the two most important ones are:

- The presence of unpredictability in deterministic systems does not require random external influences or quantum fluctuations, and it is an intrinsic property of many dynamical systems;

- An observed irregular and unpredictable behavior does not necessarily imply the presence neither of a large number of degrees of freedom in the system dynamics, nor of randomness, as three nonlinearly coupled variables can generate it.

This "hope for simplicity in unpredictability" has triggered many attemps to discover whether an observed "random" dynamics was really due to turbulent-like behavior or to the presence of a low-dimensional (in phase space) strange attractor. Some of these attempts are described in the next Lecture.

35

Lecture 3

Time Series Analysis and Phase Space Reconstruction

Ever since the discovery of deterministic chaos and strange attractors, researchers have developed methods of nonlinear time series analysis based on dynamical system theory, with the aim of detecting the possible presence of low-dimensional chaos in measured time series. This lecture is devoted to introducing some of the techniques used to characterize chaos from measured data. Thorough introductions to these subjects are given by Ott *et al* (1994) and Kantz and Schreiber (1997).

3.1 Phase Space Reconstruction

To properly describe the dynamics of a system, one needs to have access to its phase space. However, experimental measurements rarely provide direct information on the whole ensemble of phase-space variables of the system. The typical outcome of an experiment, or of observation, is a time series of a scalar variable, $h(t)$, $t \equiv t_n = n\Delta t$, $1 \le n \le N$, whose relationship to the phase-space variables is not known a priori. In such a situation, the first thing to do is to try to reconstruct an approximation to the phase space of the system. One interesting approach to this problem has been proposed, in the early 80's, by Takens (1981) and Packard *et al.* (1981). This is now known as the procedure of time embedding, and it is briefly recalled below.

3.1.1 Time embedding

First, we suppose that our measured time series is a smooth function of *all* the phase space variables, $h(t) = f(\mathbf{X}(t))$. We also note that, in principle, the same information is provided by the set of M phase-space variables, $\mathbf{X} = (X_1, X_2, ..., X_M)$ and by the derivatives up to order $M - 1$ of any of them; that is, by $(X_j, dX_j/dt, d^2X_j/dt^2, ..., d^{M-1}X_j/dt^{M-1})$, given the generic situation that X_j interacts with all the other variables in phase space. The extension to the experimental case is then obtained by realizing that a similar information is provided

36

by the signal $h(t)$ and its time derivatives; that is, by $(h, dh/dt, d^2h/dt^2, ...)$. Since, however, we deal with a signal measured at discrete time intervals, the first derivative is really $(h(t) - h(t - \tau))/\tau$. Takens and Packard *et al.* then suggested to use the time-delayed variables $(h(t), h(t-\tau), h(t-2\tau), ...)$ as an approximate representation of the phase space of the system. This approach is called time embedding, and the space spanned by h and its time-delayed values is called the embedding space. The dimensionality of this space is called the embedding dimension. Schematically, this procedure can be depicted as follows:

$$(\mathbf{X} \equiv (X_1, X_2, ..., X_M)) \tag{3.1}$$

$$\Downarrow$$

$$(X_j, \dot{X}_j, \ddot{X}_j, ...) \tag{3.2}$$

$$\Downarrow$$

$$(h(t), \dot{h}(t), \ddot{h}(t), ...) \tag{3.3}$$

$$\Downarrow \qquad \dot{h} = \frac{h(t) - h(t-\tau)}{\tau}$$

$$\mathbf{Z}_M = (h(t), h(t - \tau), h(t - 2\tau), ..., h(t - (M-1)\tau)). \tag{3.4}$$

For time series of infinite length and finite variance, Takens (1981) has demonstrated that there is a diffeomorphic equivalence between $\mathbf{X}$ and $\mathbf{Z}_M$ (that is, they have a smooth functional relationship). In this case, the specific value of the time delay is not important. For time series with finite length, the above approach is necessarily heuristic, and the choice of the value of the time delay τ becomes important.

In general, the procedure followed in the analysis of a time series is based on the definition of a hierarchy of embedding spaces of increasing dimension. In each of these spaces, some relevant dynamical measures are computed (such as the dimension of the supposedly existing attractor, the maximum Lyapunov exponent, and so on), until a saturation in the value is reached. That is, saturation is achieved when the value of the chosen dynamical quantity does not change for a further increase of the embedding dimension, M, beyond a saturation value, M_s. In this case, the value of M_s is thought to provide information on the dimensionality of the "true" phase space of the system, and the value of the dynamical quantity that we computed (provided we have selected a quantity which is invariant under phase-space coordinate changes) approximates its true value. While this expectation is justified for long time series generated by low-dimensional dynamical systems, the embedding approach has often been applied to short time series of unknown origin. In this case, troubles can easily be encountered, and false results are often obtained, as discussed in the next section.

3.1.2 Choice of the time delay

An important step in the procedure of time embedding is the choice of the time delay τ. For a time series of finite length, measured with a finite sampling time, too small a value of the time

delay results in a crowding of points along the diagonal of the reconstructed space, and the dynamics cannot be properly unfolded. On the other hand, too large a value of τ leads to a lack of correlation between the different variables in the reconstructed space, with a resulting loss of information. Thus, one needs to choose τ in a range such that the dynamics is unfolded but the values $h(t), h(t - \tau), \ldots$ are not fully decorrelated. Traditional choices of τ are:

- $T_0/4$ if there exits a dominant period T_0 in the signal.

- The first zero of the autocorrelation function,

$$R(s) = \lim_{T \to \infty} \frac{1}{T} \int_0^T h(t)h(t + s)dt, \tag{3.5}$$

where $h(t)$ denotes the signal under study.

- The first minimum of the mutual information function,

$$I(\tau) = \sum_{h_1, h_2} p_{jo}(h_1, h_2; \tau) \log_2 \left[\frac{p_{jo}(h_1, h_2; \tau)}{p(h_1)p(h_2)} \right] \tag{3.6}$$

(Fraser & Swinney 1986), where $p(h)$ is the (empirical) probability of observing the value h and $p_{jo}(h_1, h_2; \tau)$ is the joint probability of observing the value h_1 at some time and the value h_2 a time delay τ afterwards.

In general, it is important to verify that the results of the analysis do not depend too sensitively on the exact choice of τ; that is, they should hold over a sufficiently large range of values of the time delay, centred on the "optimal" value defined by one of the methods mentioned above.

3.1.3 Correlation Dimension

Once one has reconstructed a (pseudo) phase space with dimensionality M, one way to quantify the dynamics underlying a given time series is to measure the dimension of the data set in the reconstructed space. Grassberger & Procaccia (1983) developed a simple algorithm to get an estimate of the attractor dimension. First, we compute the correlation integral,

$$C_M(r) = \frac{2}{N'(N' - 1)} \sum_{i=1}^{N'} \sum_{j=i+1}^{N'} \Theta(r - |\mathbf{Z}_i - \mathbf{Z}_j|), \tag{3.7}$$

where Θ is the Heaviside step function and N' is the number of points in the reconstructed (vector) time series $\mathbf{Z}$, $N' = N - (M - 1)m$ where $m = \tau/\Delta t$ and Δt is the sampling interval.

We are then interested in the behavior of $C_M(r)$ as r tends to zero. If the system dynamics is governed by a low-dimensional attractor, then the correlation integral has a small-scale power-law behavior, $C_M(r) \propto r^{\nu(M)}$. Below saturation, the value found for the correlation exponent $\nu(M)$ generally depends on M, the embedding dimension. As M is increased, however, for
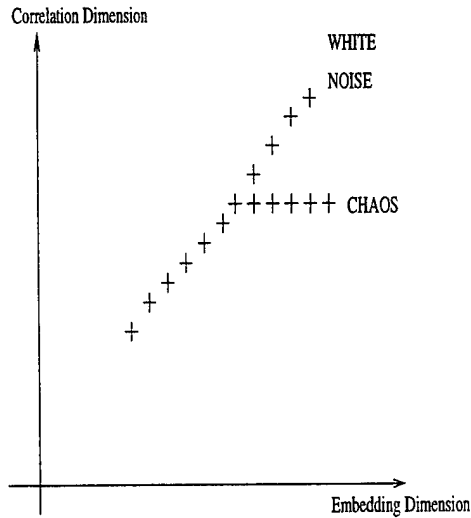
Figure 3.1: Different behavior of the correlation dimension for chaos and white noise

systems dominated by an attractor with finite (and possibly small) dimensionality, the value of $\nu(M)$ approaches a finite limit D_2, called the correlation dimension, which provides an estimate of the fractal dimension of the attractor. Fixed points and limit cycles are characterized by dimension of respectively zero and one, while quasi-periodic motion has a dimension equal to the number of independent (incommensurate) frequencies. Strange attractors, associated with chaotic motion, are usually characterized by a non-integer dimension.

The value of D_2 gives important information on the number of excited degrees of freedom in the system. In particular, phase-space dynamics characterized by a small value of the correlation dimension may be described by a system of a few (usually, at most $2D_2 + 1$) coupled ordinary differential equations. Note, however, that a (reliable) detection of a finite and small value of D_2 only indicates that a description in terms of a low-dimensional deterministic model should be possible. No information is provided on how the appropriate collective degrees of freedom can be identified.

Conversely, white noise is associated with a non-convergent value of the correlation dimension (see figure 3.1). Thus, if in the analysis of a measured time series no convergence in $\nu(M)$ is observed for increasing M, it is generally assumed that the number of excited degrees of freedom in the system is large: in this case, a stochastic model might be more appropriate.

Two remarks are in order here. Curves plotted on log-log coordinates have often the tendency to look like power laws, even though the power-law behavior is that of the tangent to the curve rather than of the curve itself. For this reason, it is usually better to plot the local logarithmic derivative of the correlation integral, $\nu_M(r) = d \log C_M(r)/d \log r$, versus $\log r$, to verify whether there is a sufficently extended scaling interval where $\nu_M(r)$ is constant, $\nu_M(r) = \nu(M)$. A practical way of obtaining $\nu_M(r)$ is, for example, by taking the local least-square fit of $\log C_M(r)$ versus $\log r$ over three consecutive points.

The second remark concerns the statistical requirements for a reliable estimate of the

correlation dimension. This issue has been discussed by several papers (Smith 1988, Eckmann & Ruelle 1992), with conflicting estimates on the minimal number of points that is required to reliably detect a dimension D_2. Here, we simply say that, on average, $N_{min} \approx 10^{D_2}$ points are required in order to safely detect a correlation dimension D_2. When a convergent correlation dimension D_2 is detected with less than N_{min} points, there is the danger that the convergence of D_2 has been forced by lack of statistics rather than by low-dimensional dynamics.

3.2 Finite dimension from stochastic processes

If a measured time series is produced by low-dimensional (chaotic) dynamics, saturation of the correlation dimension for increasing embedding dimension is observed. On the other hand, in the analysis of measured data one does not know whether the system is low-dimensional. Indeed, this is exactly one of the questions the analysis should answer, and it is not possible to assume the presence of low-dimensional chaos a priori. However, in the early days of phase-space reconstruction and analysis (i.e., in the early 80's), the detection of a finite and small value of the correlation dimension was considered a safe indication of the existence of low-dimensional chaos. In this way, several works claimed the presence of strange attractors in the most diverse systems.

Later on, some studies (Osborne & Provenzale 1989; Provenzale *et al* 1992) revealed that the sole detection of a finite value of the correlation dimension from a measured time series is not enough to infer the presence of low-dimensional chaos, since there are stochastic processes that provide a spurious convergence of the correlation exponent under time-embedding.

These stochastic processes are, in general, characterized by power-law power spectra and self-similar behavior over an extended range of scales. One example is provided by the Gaussian stochastic process defined by

$$s(t_i) = \sum_{j=1}^{N/2} A_j cos(\omega_j t_i + \phi_j),$$
(3.8)

where $A_j^2 \propto \omega_j^{-\alpha}$ and ϕ_j are random uniformly distributed phases. In this case, the correlation dimension is given by $\nu = \nu(\alpha) = \frac{2}{\alpha-1}$ for $1 < \alpha \leq 3$ (see figure 3.2).

A second popular example is the linear Ornstein-Uhlenbeck (OU) process:

$$ds = -\gamma \, s(t)dt + \sigma\gamma^{1/2}dW,$$
(3.9)

where $\gamma = 1/T_d$ is the inverse of the signal decorrelation time T_d, σ^2 is the variance of the signal and dW is a gaussian-distributed random increment with $\langle dW \rangle = 0$ and $\langle dW^2 \rangle = 2\,dt$ (a Wiener process). Equation (3.9) generates a scalar time series, $s(t)$, that is gaussian distributed and becomes stationary at large times. The power spectrum of $s(t)$ is $P(\omega) \propto [1 + (\omega/\gamma)^2]^{-1}$, which is of power-law form, $P(\omega) \approx \omega^{-2}$ at high and intermediate frequencies, and it becomes constant at low frequency.

Another example is provided by a nonlinear stochastic process, that may be written as

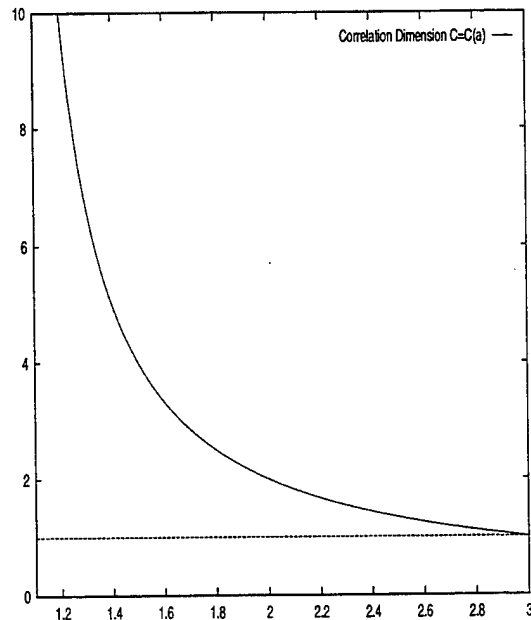$$dS = (1/2 - S(t))dt + (2S(t))^{1/2}dW.$$
(3.10)

40

Figure 3.2: Correlation dimension, $\nu(\alpha)$, of the Gaussian stochastic process (3.8).

The time series generated by this process has a power spectrum that is very similar to that generated by the OU process (see figure 3.3), but it is characterized by well-defined intermittency properties and correlated Fourier phases (ref).

The apparent value of the correlation dimension, as computed from time-embedding of $s(t)$ or $S(t)$, depends in this third example on the length T of the time series. For very long series, $T \to \infty$, the correlation exponent $\nu(M)$ grows without bound with M, due to the stationarity of the signals. For time series with intermediate length, however, full stationarity has not yet been reached, and the value of the correlation exponent converges to a finite value ν_c for growing M. This value is related to the approximate self-similarity of the signals, and has nothing to do with the true phase-space dimensionality of the system (which is unbounded since the process is stochastic). This behavior is due to a failure of the time-embedding procedure, which cannot reconstruct the true phase space of the system due to the non-stationarity of the time series. Such a behavior has been observed in several instances, since for many measured time series the record is not long enough to ensure full stationarity. Note also that the time series $S(t)$ generated by the nonlinear process provides a positive answer to nonlinearity tests, showing that nonlinearity and a finite estimate of the correlation dimension from a measured signal (with finite length) is not enough to infer the presence of low-dimensional chaos.

In past years, other stochastic processes have also been shown to induce a spurious convergence of the correlation exponent. This demonstrates the impossibility to distinguish practically between a low order, deterministically chaotic system and a stochastic one, using just the above developed tools. For this reason, various other methods have been developed that allow us to recognize some of these "false positive" results. Some of these methods are described below.
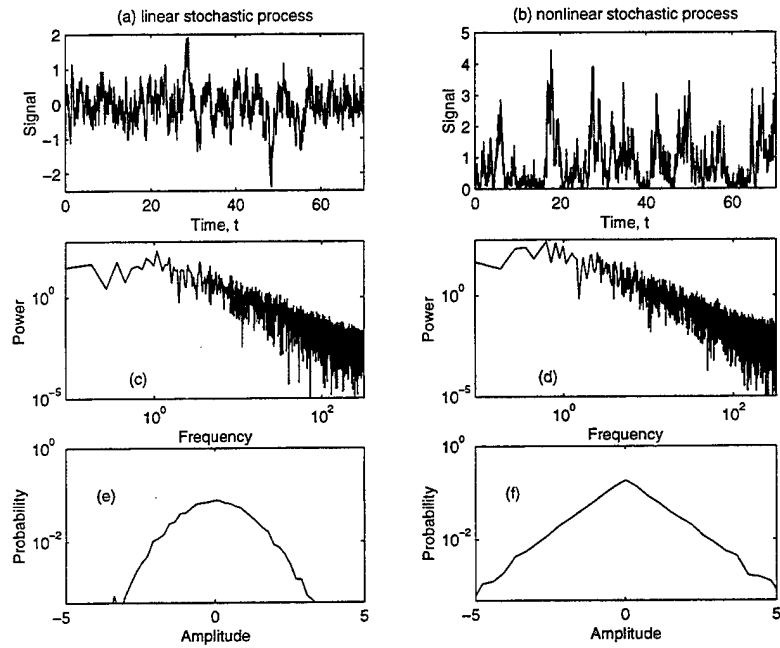
41

Figure 3.3: Time series for the stochastic processes (3.9) and (3.10), shown in panels (a) and (b) respectively. Panels (c) and (d) show the corresponding Fourier power spectra, and (e) and (f) show histograms displaying the approximate probability distributions of the temporal derivative of the signal.

3.3   Distinguishing chaos from noise

The reason why one cannot detect differences between chaos and noise in the previous cases is because of the intrinsically fractal nature of the noise. The fractal curves encountered above have a fractal dimension completely defined by the spectral slope and thus exhibit saturation. On the other hand, the reconstructed space is not the real phase space of the system, due, for example, to non-stationarity of the signal, or to an insufficient length of the time series. Therefore, by computing the value of the correlation dimension one cannot distinguish between differentiable strange attractors and non-differentiable fractal stochastic curves if they have the same dimension.

In order to solve this problem several methods have been proposed. Most of these methods are based on the concept of "surrogate data." That is, we generate a synthetic time series that has all but one of the properties of the measured signal, in order to verify whether the value of the correlation dimension, or the Lyapunov exponents, depends on the modified property.

3.3.1   Phase randomization

One of the most common tests is that based on the randomization of Fourier phases. This test is the simplest and less refined one of the many available surrogate data techniques; however, it has proven to be quite useful on many occasions. The phase-randomization test allows us to verify whether an observed convergence of the correlation exponent is due to the presence of a self-similar stochastic process. In the case of self-similar stochastic processes, the convergence of the correlation exponent is related to the power-law form of the power spectrum; that is, to the properties of the second-order moment. By contrast, the finite value of the correlation dimension for a low-order deterministic system is due to close returns in phase space; these are in turn related to the distribution of the Fourier phases of the signal.

Based on this observation, it has been suggested (Theiler *et al.* 1992; Osborne *et al.* 1986) to test the origin of an observed convergence in the correlation exponent by generating a synthetic time series having the same power spectrum as the measured data, but random Fourier phases. This surrogate signal has a gaussian distribution with the same second-order moment as the time series under study. If the correlation exponent converges also for this surrogate signal, then the origin of the convergence in the original time series cannot be related to its phase-space structure, and the hypotesis of low-dimensional chaos has to be rejected. The test does not, however, unambiguously identify low-dimensional chaos: if the surrogate signal does not generate a convergent value of the correlation exponent, one cannot conclude that the system is governed by low-dimensional chaos; in this case, other surrogate data tests have to be applied before any safe conclusion might be reached.

3.3.2   Method of close returns

This method uses one of the main properties of strange attractors. It is well known that the phase-space trajectories of a low-dimensional dynamical system return close to their initial positions from time to time, whereas this is not the case for stochastic systems. Consequently, one can plot the separation in space against the separation in time for these two different types
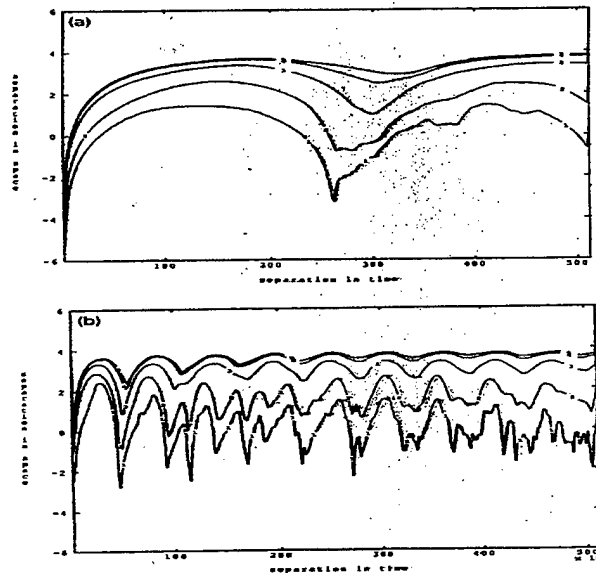
Figure 3.4: Separation in Space .vs. Separation in Time for the Lorenz attractor. Adapted from Provenzale *et al.* 1992.

of systems. Then, the existence of these close returns will yield a non-monotonic graph and a further piece of evidence of the presence of a strange attractor.

Plots of separation in space against separation in time are displayed in figures 3.4 and 3.5. The close returns in the Lorenz model clearly distinguish it from the nonlinear stochastic process.

In general, surrogate data tests have been applied to many apparent detections of low-dimensional chaos from measured data, and most of the time series measured outside controlled laboratory conditions have not survived a careful scrutiny of the results. For example, the light curve of the optical, violently variable quasar 3C 345 is seemingly characterized by a low value of the correlation dimension when analyzed improperly (*e.g.* Provenzale *et al.* 1994). This indicates that the simple view of a low-dimensional attractor in most physical systems is unsatisfactory. Instead, we must search for richer dynamical possibilities, although we do not necessarily need to abandon approaches based on "simple" models. Some of these approaches - chaos outside the ivory tower - are discussed the next lectures.
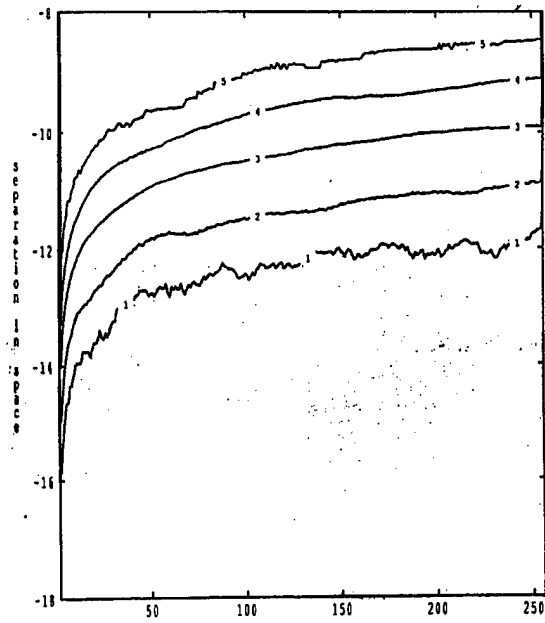
44

Figure 3.5: Separation in Space .vs. Separation in Time for the nonlinear stochastic process (3.10). Adapted from Provenzale *et al.* 1992.

45

Lecture 4

Externally Driven Chaos

4.1 Out of the ivory tower

In the first two lectures, we have seen how three-dimensional dynamical systems (such as the Lorenz 63 model) are capable of generating multiple equilibria, periodic and quasiperiodic oscillations and chaotic trajectories without any external forcing mechanism.

Do these models have anything to do with reality? This is indeed an eternal question in dynamical systems theory, and for the simplified approaches described in these notes. At first, simplified models were introduced mainly as metaphors, without claiming a direct link with specific phenomena. Later on, researchers became excited by their simplicity, and tried to literally interpret natural events in terms of low-order, autonomous dynamical systems: Like Frankenstein's monster, modelling by low-order dynamical systems took on a life of its own. More recently, many methods of time series analysis have become available, some of which are reviewed in Lecture 3. The main outcome of the application of such analyses, however, has been a realization that natural phenomena (outside controlled laboratory conditions) are seldomly described by low-order, autonomous dynamical systems. So seldomly in fact, that should one find a genuine low-order, dissipative chaotic system in nature, the discovery should be suitably celebrated (for example, by a bottle of properly aged Barolo).

Given this inability of low-order models to explain natural phenomena, what should we do instead? We have first to remember that our little dynamical system is really just a metaphor. When motivated by a specific problem, we can write a simplified model that provides a mathematical framework to formulate relevant questions. Typically, the model is only appropriate to address the issues for which it has been fabricated. It is a serious mistake to push it beyond its limits, or to use it for completely different questions.

But, once we appreciate the limits, we may press further afield and we need not be so conservative; we must only be ready to modify the metaphors when appropriate. For example, most natural systems are driven by external forcings, are coupled with each other, and have different coexisting time scales. In dealing with these new physical ingredients, it is neither expedient nor feasible to resort to sophisticated models. Instead, it is more sensible to explore these processes by exploiting appropriate simple models. Thus, in the coming three lectures,

we lose our virginal low dimensionality, leave the ivory tower (which lies in ruin around us anyway), and build metaphors for forced and coupled systems. Perhaps, in doing so, we move no closer to reality, but we can nevertheless discover and explore new possibilities and intriguing mechanisms.

4.2 A metaphor for large-scale atmospheric motions

In the following, we introduce another three-dimensional dynamical system, namely the model that Lorenz (1984) proposed as a simplified description of midlatitude atmospheric dynamics. After a brief discussion of the model behavior, we explore what happens when the model is subject to external periodic forcing.

4.2.1 Chaos in the midlatitudes

In 1735 Hadley proposed that the large scale circulation of the atmosphere consisted of air rising at the equator, travelling aloft away from the equator before sinking at the poles (Hadley, 1735). However, this picture neglects the effects of the Coriolis force which leads to geostrophic balance at mid-latitudes. In fact, due to rotation, such a cell (now called the Hadley circulation) would produce easterly winds at midlatitudes, the opposite of what is observed. Thomson (1857) and Ferrel (1859) modified this picture and introduced a second circulation cell which is now called the Ferrel cell (see Figure 4.1). With this modification, westerlies at midlatitudes and easterlies (trade winds) at low latitudes are recovered.

The circulation described by this simple picture is zonally symmetric. However, it is not actually observed. Rather, strong transient perturbations dominate the atmospheric circulation, especially at midlatitudes. These perturbations take the form of strong cyclones (storms) that induce irregularities which completely dominate any ordered zonal pattern such as the Ferrel cell.

In the past, two possible reasons for the lack of zonal symmetry have been proposed. One possibility is that a zonally symmetric circulation is not a solution of the equations of motion, and the basic state is fundamentally asymmetrical. Alternatively, a second possibility is that the Ferrel cell is a solution to the equations, but it is unstable to asymmetrical perturbations; these growing perturbations spawn the mid-latitudes cyclones.

To address this specific issue, Lorenz proposed a simple model for large scale circulation in one hemisphere (Lorenz, 1984). The model equations are

$$\frac{dX}{dt} = -Y^2 - Z^2 - aX + aF \tag{4.1}$$

$$\frac{dY}{dt} = XY - bXZ - Y + G \tag{4.2}$$

$$\frac{dZ}{dt} = bXY + XZ - Z. \tag{4.3}$$

In these equations X represents the intensity of the symmetric westerly wind, which (in the usual thermal wind balance) is proportional to the average meridional temperature gradient
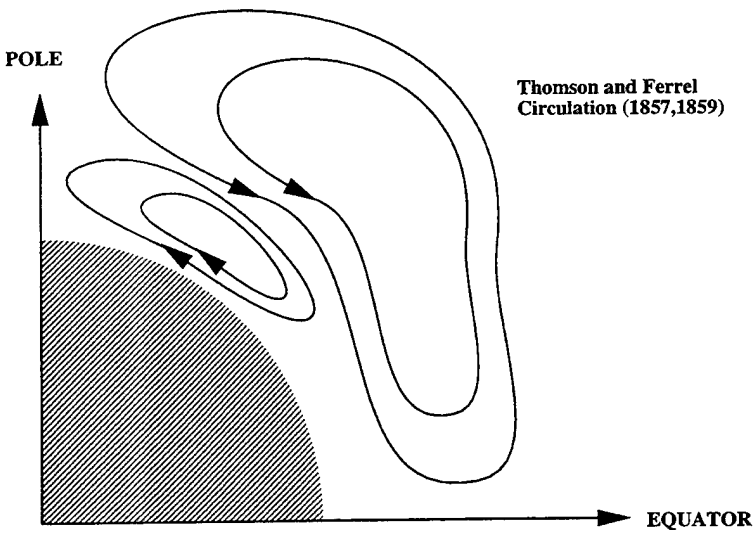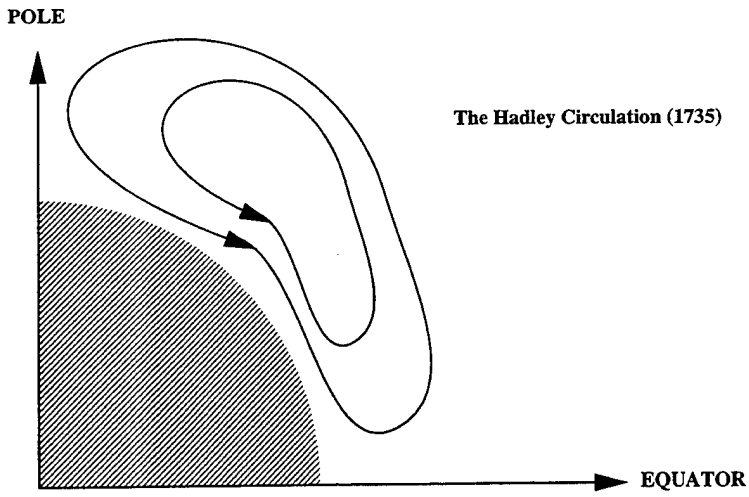
47

Figure 4.1: A schematic representation of the atmospheric circulations proposed by Hadley and by Thomson and Ferrel.

48

between Equator and Pole. The variables Y and Z are Fourier amplitudes characterixing a chain of large-scale eddies. The eddies transport heat poleward at a rate proportional to Y^2 and Z^2, which reduces the pole-equator temperature diference and, thence, the wind. The term aF represents the symmetric forcing, due to the Equator-Pole difference in solar heating, and G is a longitunally dependent (nonsymmetric) forcing term that models the temperature differences between continents and oceans. If we ignore the nonlinear coupling terms, then the equations predict that X relaxes to F and Y relaxes to G.

The solutions to the system of equations are bounded:

$$X^2 + Y^2 + Z^2 < E_{max} \quad t \to \infty, \tag{4.4}$$

for some constant E_{max}. Furthermore, the phase space divergence can be calculated:

$$\frac{\partial \dot{X}}{\partial X} + \frac{\partial \dot{Y}}{\partial Y} + \frac{\partial \dot{Z}}{\partial Z} = -a - 2 + 2X. \tag{4.5}$$

Thus it can be seen that the phase space volume contracts only if $X < 1 + a/2$. Since the phase space volume does not contract everywhere in phase space, attractors may have finite volume.

The fixed points of the system are given by

$$Y = \frac{(1 - X)G}{1 - 2X + (1 + b^2)X^2}, \tag{4.6}$$

$$Z = \frac{bXG}{1 - 2X + (1 + b^2)X^2} \tag{4.7}$$

and

$$a(F - X)(1 - 2X + (1 + b^2)X^2) - G^2 = 0. \tag{4.8}$$

From equations (4.6)-(4.8) it can be seen that if $G = 0$ then the fixed points are $X = F$, $Y = Z = 0$. This solution corresponds to the symmetric Hadley circulation. In this case, if $F < 1$ the solution is stable, whereas if $F > 1$ the solution is unstable and eddies are produced by the instability of the symmetric state. For cases when $G \neq 0$ there can be multiple equilibria as shown in Figure 4.2. For small values of G, there is only one solution which is similar to the Hadley circulation (point A). For intermediate values of G there are three equilibria. One of these is similar to the Hadley circulation (point B), the second is unstable (point C) and the third corresponds to an asymmetric, non-Hadley circulation (point D). This final state could be described as "blocked"; that is, a strongly nonzonal circulation whose structure is locked into place as a result of the nonsymmetrical thermal forcing between land and sea (entering through G). This asymmetric circulation is reminiscent of blocking by topographic forcing (Charney & DeVore 1979). For large values of G, only this latter equilibrium exists (point E).

Thus, even such a simple model shows that midlatitude disturbances can be produced by either instability of a symmetric, Hadley-like circulation ($G = 0, F > 1$) or as fundamental, non-Hadley states (*e.g.*, case E).
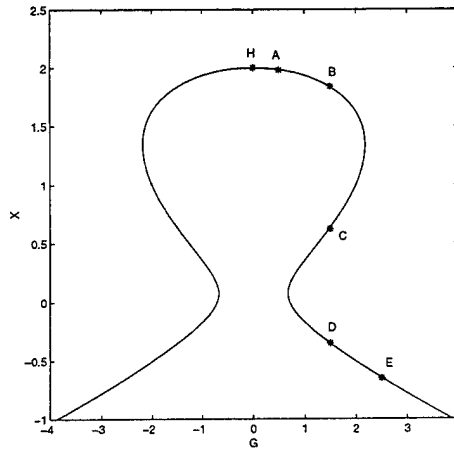
Figure 4.2: The equilibria curve for the Lorenz 84 model plotted in the $G - X$ plane, where X is the strength of the zonal flow and G is the strength of the zonally asymmetric forcing.

An interesting feature of this model is that it produces multiple steady states (as many other models before it). This multiplicity of attractors, sometimes called *intransitivity*, extends also to more complicated solutions such as limit cycles and chaotic attractors: For the case $G = 0$ and $F > 1$, equations 4.1-4.3 have a stable, attracting periodic solution:

$$X = 1, \tag{4.9}$$

$$Y(t) = \sqrt{a(F - 1)} \cos(bt - \phi_0), \tag{4.10}$$

$$Z(t) = \sqrt{a(F - 1)} \sin(bt - \phi_0). \tag{4.11}$$

This solution undergoes period doubling as G is increased. For $G = 0.8$, there are two coexisting attractors; both are limit cycles (see Figure 4.3). Therefore, for these parameters values, the model has two stable "climate" states. At larger values of G, the two attractors merge and the model behaves chaotically, as shown in Figure 4.4.

4.2.2 Periodic driving of an intransitive system

The model discussed above does not contain any external forcing, and still it is capable of producing an internal (periodic or chaotic) variability. On the other hand, the real atmosphere has significant external forcings at diurnal and annual periodicities, and it is therefore of interest to explore how an external, periodic forcing modifies the internal variability of the model.

For linear systems, periodic forcing introduces a periodic response except at resonance when the frequency of the driver coincides with an internal frequency of the driven system.
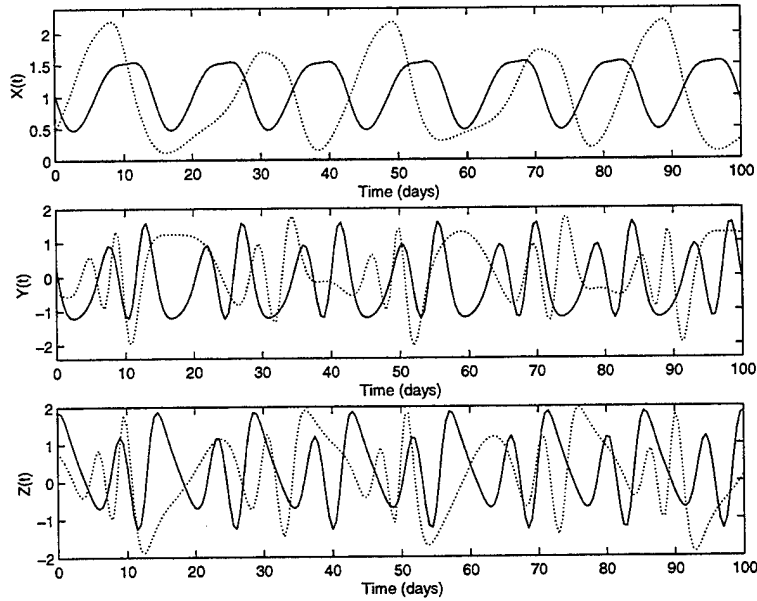
50

Figure 4.3: Time series of X, Y and Z for the two stable periodic solutions that exist when $G = 0.8$. The solution shown by solid lines is the "weak" attractor, and that by dotted lines is the "strong" one. Note that one time unit of the model corresponds to 5 days, and that $a = 0.25$, $b = 4$ and $F = 8$.
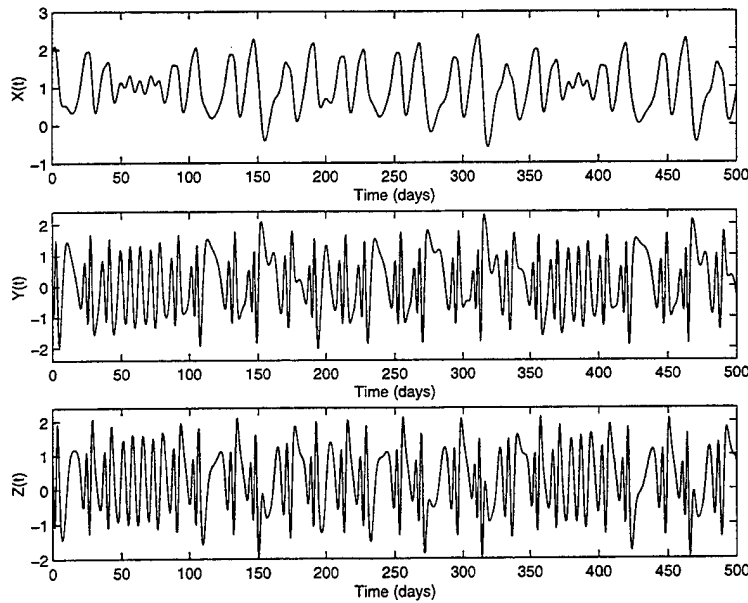
Figure 4.4: Time series of the aperiodic behavior of X, Y and Z when $G = 1$, $a = 0.25$, $b = 4$ and $F = 8$.

For nonlinear systems, even a simple periodic driving may generate a vart range of new and interesting effects.

A particularly interesting case is when one of the control parameters of the system (e.g., F or G in the Lorenz 84 model) is paramterically driven. Notably, if the parameters are driven through a point of bifurcation of the the unforced system, then "switching" can occur as the system turns "on" and "off" (this idea recurs in the next lecture). For example, take the Lorenz 84 model in the vicinity of a transition from periodicity to chaos, and vary F periodically such that its extreme values correspond to periodic or chaotic behavior in the undriven system. In this case, the system undergoes transitions between these two regimes, switching between regular cycling and chaos. Sometimes, the timescale for switching can be lengthy, and this introduces a simple form of low-frequency (interannual) variability into the model. However, this behavior strictly depends on the fact that the system is close to a bifurcation.

Another interesting case, with richer dynamics, is obtained when the system is intransitive, and has at least two attractors. In the simple case of multiple steady states, periodic driving can precipitate regular transitions of the system from one equilibrium to the other. Clearly, the driver must have a sufficient amplitude as to force the system to cross the potential barrier between the two equilibria (equivalently, for a simple oscillator, to modify the form of a double potential well and allow the system to roll from one equilibrium to the other).

Even more interesting is when the undriven system has time-dependent multiple states, such as periodic oscillations or chaotic attractors. This case was considered by Lorenz (1990), who studied a situation where the system is forced to move through a bifurcation between
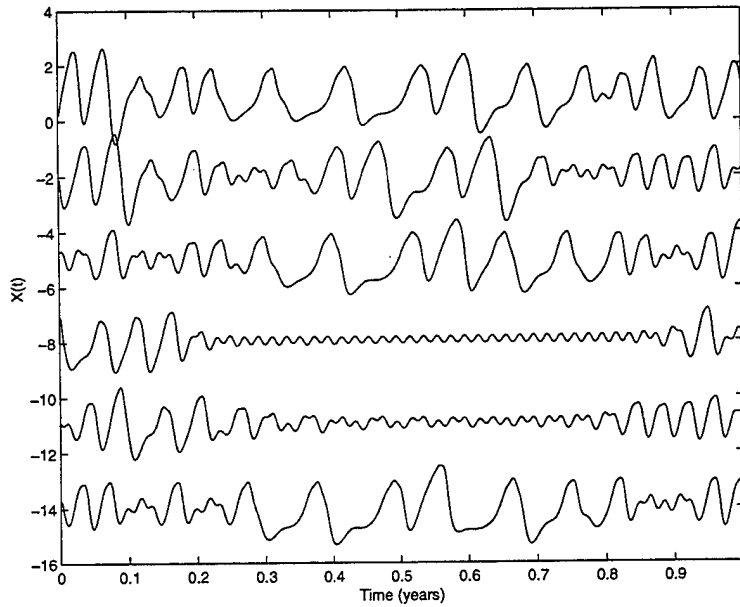
Figure 4.5: The variations in X for the case when $G = 1$, $A = 0.25$, $b = 4$, and $F = 7 + 2\cos(2\pi t/\tau)$, with τ corresponding to 12 months. The time series are divided into successive yearly segments and offset downwards.

periodicity and chaos, with the addition feature that the periodic dynamics is intransitive (as in figure 4.3).

Lorenz's motivaton was climatological, and the periodic perturbaton modelled the seasonal cycle. More specifically, Lorenz used the model described above, but with F parameterically forced to represent the variation in the Equator-Pole temperature difference from summer to winter. Lorenz identified the chaotic, transitive regime found at larger values of F (figure 4.4) with winter and the periodic, intransitive regimes at lower F with summer (figure 4.3). The summer regime has a so-called "weak" attractor which has a small basin of attraction and a small oscillation amplitude (the solid lines in figure 4.3), and a "strong" attractor with a larger basin and larger oscillations (the dotted lines in figure 4.3). An example with $A = 0.25$, $b = 4.0$, $G = 1.0$ and $F = 7.0 + 2.0\cos(2\pi t/T)$, where T corresponds to 12 months is shown in Figure 4.6.

As suggested above, this system changes from a chaotic behavior in winter to a periodic dynamics during summer. However, during summer the system can approach either the weak or the strong periodic attractor, depending on the conditions encountered at the end of the winter. During winter the system loses almost all memory of its state in the previous summer, and at the end of the winter it lies at a point on the chaotic attractor which is practically independent of the conditions at the beginning of the winter. Thus, the probability of approaching the weak or the strong attractor in the following summer depends chiefly on how the winter attractor is distributed within the basins of the two summer limit cycles. This produces irregular

53

sequences of weak and strong summers, which generate significant low-frequency variability.

The interesting dynamics generated by this model is due to both the passage of the system through a bifurcation, and, even more importantly, to the intransitivity of the summer dynamics. We are thus faced with a dynamically "bimodal" system where the choice between the two possible states is dictated by a chaotic process. Presumably, we could have obtained similar effects by considering a purely intransitive dynamics where, at periodic intervals, an external random noise resets the system and forces it to choose again one of the two possible states. The interest of the Lorenz 84 model, however, is that this process is obtained in a very simple and self-consistent, deterministic way.

4.3 A stochastically forced model of the thermohaline circulation

We next consider another type of external forcing, namely, random white noise acting on a low-order dynamical system. This case is quite important as most systems are subject to the influence of unresolved "turbulent" dynamics that can alter the simple behavior of the unforced model. In particular, we consider the effects of random noise acting as a driver in the equations of motion. We have encountered a simple example of this in Lecture 3, when dealing with the (linear and nonlinear) Langevin equation. In that case, the deterministic dynamics was extremely simple. By contrast, here we consider situations where the deterministic part has an interesting behavior even without external noise. Note, also, that the case of dynamical noise is more relevant and much more complicated than pure additive noise superposed onto a signal produced by a low-order system, as happens, for example, if there is a random error in taking measurements.

As a specific example, we consider the noise-driven dynamics of a simple box model of the thermohaline circulation of the ocean, following Cessi (1994). Again, most of the interesting effects are due to the intransitive nature of the unforced model.

The oceanic thermohaline circulation (THC; see Whitehead 1995, for a review) is due to the joint effect of temperature and salinity on water density. Consider, in particular, a simple model of an ocean that extends from the Tropics to high latitudes. If, over some extensive region of ocean, the water is denser at the surface than at the bottom, then fluid sinks and drives a convection current through the entire ocean. This circulation can maintain itself if there is a suitable influx or outflux of the two components contributing to the local density (heat and salt). Such fluxes are provided by differential solar heating, evapouration and precipitation.

The density ρ of sea water may be approximately expressed as

$$\rho - \rho_0 = \alpha_s(S - S_0) - \alpha_T(T - T_0), \tag{4.12}$$

where T is temperature, S is salinity, and ρ_0 is a reference density with salinity S_0 and temperature T_0. Thus, density increases on lowering the temperature, or in raising the salinity.

At high latitudes, surface cooling may be very effective. In the Atlantic, this happens in the Labrador Sea, for example. In the Mediteranean, cooling takes place in the Gulf of

Lyon south of Marseille and in the northern Adriatic Sea. Thus, cold water sinks at these high latitudes, and a "direct" circulation is established with warm surface water flowing from the tropics to high latitudes, and cold bottom water flowing toward the Equator. This is the circulation pattern observed today in the Atlantic and the Pacific, with the Gulf Stream being part of the northward "conveyor belt" transporting heat at high latitudes.

On the other hand, intense evaporation at low latitudes generates salty water at the surface in the tropics, and precipitation and the melting of ice produces fresh surface water at higher latitude. If the evaporation or flux of fresh water is large enough, then the contribution of salinity to density may become more important than that of temperature. In this case, the surface water becomes denser at low latitudes, and sinking occurs in the tropics. Then, the surface flow becomes Equatorward, and it is composed of fresh, cold, high-latitude water. The bottom flow is a warm and very salty current flowing towards high latitudes. This type of circulation, "inverted" with respect to that observed today, may have dominated the oceanic circulation in some periods of the past, such as intervals of deglaciation characterized by a large amount of fresh water produced in high-latitude seas from melting glaciers.

In the early sixties, Stommel (1961) proposed a simple low-order model for the thermohaline circulation. This model reduces the oceanic pool to two homogeneous boxes, representing respectively the high-latitude and the tropical halves of the original pool. In such a *box model*, box 1 represents the tropical ocean and box 2 is the high-latitude ocean. The variables of the model are T_1, T_2, S_1, S_2, where T_j is the temperature and S_j the salinity of box j, for $j = 1$ and 2.

The evolution of the system is then modelled by the following equations:

$$\frac{dT_1}{dt} = -\frac{1}{\tau_r}\left(T_1 - \frac{\theta}{2}\right) - \frac{1}{2}Q(\Delta\rho)\Delta T \qquad (4.13)$$

$$\frac{dT_2}{dt} = -\frac{1}{\tau_r}\left(T_2 + \frac{\theta}{2}\right) + \frac{1}{2}Q(\Delta\rho)\Delta T \qquad (4.14)$$

$$\frac{dS_1}{dt} = \frac{F(t)}{2H}S_0 - \frac{1}{2}Q(\Delta\rho)\Delta S \qquad (4.15)$$

$$\frac{dS_2}{dt} = -\frac{F(t)}{2H}S_0 + \frac{1}{2}Q(\Delta\rho)\Delta S, \qquad (4.16)$$

where Δ denotes the difference between the two boxes:

$$\Delta T = T_1 - T_2, \qquad \Delta S = S_1 - S_2, \qquad \Delta\rho = \alpha_s \Delta S - \alpha_T \Delta T. \qquad (4.17)$$

In equations 4.11 and 4.14, τ_r is the time scale on which the temperature in boxes 1 and 2 relaxes towards $T_0 + \theta/2$ and $T_0 - \theta/2$ respectively. $F(t)$ models the concentrating effect of evaporation in the tropics, or the dilution by precipitation and melting in high-latitude regions; H is the depth of the ocean. This model differs from the original Stommel model in that different "boundary" conditions for salinity are used. In the Stommel model, both temperature and salinity have restoring boundary conditions. Here, restoring boundary conditions are retained for temperature, while for salinity a fixed salinity flux ($F(t)$) is imposed.

55

The quantity $Q(\Delta\rho)$ is the water flux due to the density difference $\Delta\rho$ between the two boxes. In the past, various forms of $Q(\Delta\rho)$ have been proposed. These include:

$$(i) \qquad Q_1 = \tau_d^{-1}, \tag{4.18}$$

where τ_d is another relaxation time. This is a constant water flux, independent of $\Delta\rho$, and generates linear equations with at most one stable equilibrium.

$$(ii) \qquad Q_2 = \tau_d^{-1} + \frac{9}{v}|\Delta\rho|, \tag{4.19}$$

where v is another parameter. This form of the flux is appropriate for connecting capillary pipes, and was the form originally proposed by Stommel. Recent analyses of ocean circulation models have made the suggestion that this may provide an appropriate parameterization of the water flux (Rahmstorf 1996).

$$(iii) \qquad Q_3 = \tau_d^{-1} + \frac{9}{v}(\Delta\rho)^2, \tag{4.20}$$

a form of the flux based on simple theories of turbulence.

In this model, it is convenient to introduce new variables given by the temperature and salinity differences, ΔT and ΔS. One then obtains, for the evolution of ΔT and ΔS:

$$\frac{d\Delta T}{dt} = -\frac{1}{\tau_r}(\Delta T - \theta) - Q(\Delta\rho)\Delta T \tag{4.21}$$

and

$$\frac{d\Delta S}{dt} = \frac{F(t)}{H}S_0 - Q(\Delta\rho)\Delta S. \tag{4.22}$$

These are the basic equations of the THC two-box model. We next introduce the following nondimensional variables:

$$x = \frac{\Delta T}{\theta} \qquad y = \frac{\alpha_s \Delta S}{\alpha_T \theta} \qquad t' = \tau_d^{-1}t. \tag{4.23}$$

On substituting these variables, with the choice $Q = Q_3$, into equations (4.21) and (4.22), we find the following equations:

$$\frac{dx}{dt} = -\alpha(x - 1) - x(1 + \mu^2(x - y)^2) \tag{4.24}$$

and

$$\frac{dy}{dt} = p(t) - y(1 + \mu^2(x - y)^2), \tag{4.25}$$

where

$$\alpha = \frac{\tau_d}{\tau_r}, \qquad \mu^2 = 9\frac{\tau_d(\alpha_T\theta)^2}{v} \qquad \text{and} \qquad p = \frac{\alpha_s S_0 \tau_d F(t)}{\alpha_r \theta H}. \tag{4.26}$$

56

Equations (4.25)-(4.26) are the nondimensional equations of the THC box model.

In general, the diffusive time scale τ_d is much larger than the relaxation time τ_r, and so the value of α is usually very large. This allows us to simplify the equations still further: On assuming $\alpha \gg 1$, the above equations become

$$x = 1 + O(\alpha^{-1}) \tag{4.27}$$

and

$$\frac{dy}{dt} = -[1 + \mu^2(y^2 - 1)]y + p(t) + O(\alpha^{-1}). \tag{4.28}$$

For the case of constant salinity flux p, Eq. (4.28) can be written in the form of an overdamped oscillator with potential $V(y; p)$:

$$\frac{dy}{dt} = -\frac{\partial V}{\partial y}, \tag{4.29}$$

where

$$V(y; p) = \mu^2 \left(\frac{y^4}{4} - \frac{2y^3}{3} + \frac{y^2}{2} \right) + \frac{y^2}{2} - py \tag{4.30}$$

describes a double-well potential. Thus, the system has two stable equilibria: one corresponds to a direct, temperature-driven circulation, and the other to an inverted, salinity-driven circulation. The two equilibria are separated by a potential barrier and, in the absence of external forcing, the system settles to one of the two steady circulations.

The presence of external noise may, however, induce transitions from one equilibrium state to the other. Cessi explicitly considered the case of a random perturbation superposed on the mean salinity flux. In this case we write $p(t) = \bar{p} + p'(t)$, where $\bar{p}$ is the mean and $p'(t)$ is the perturbation in the salinity flux. Here, p' is modelled described by white noise. The system discussed above now behaves like a particle in the time-independent potential, $V(y; \bar{p})$, subject to a Brownian force, $p'(t)$.

If p' is large enough, the presence of the potential $V(y; \bar{p})$ plays a minor role, and the particle undergoes almost unconstrained Brownian motion. On the other hand, if p' is so small that the perturbed particle cannot cross the potential barrier between the two wells of $V(y; \bar{p})$, then the resulting motion takes the form of a noisy fluctuation around one of the two stable equilibrium points. For intermediate stengths of p', the particle still feels the potential, but it is now able to randomly jump from one well to the other. The resulting motion is a random fluctuation between the two equilibria, with a significant fraction of time spent around each fixed point and intermittent jumps from one state to the other. This case was studied in detail by Cessi, and illustrates how random dynamical noise may induce irregular fluctuations from one attractor to another. Of course, the noise should be of large enough amplitude to force the system to cross the potential barrier between different attractors.

57

4.4 Stochastic Resonance

In the models described above, if the amplitude of the periodic forcing or noise is too small, then the system does not cross the barriers between the unperturbed attractors. However, if both kinds of perturbations are present, then interesting new effects can arise even when both are sub-threshold. More specifically, for an oscillator with a double potential well, a resonance can occur between the periodicity of the forcing and the (probabilistic) escape rate from each potential well induced by the noise (Benzi *et al.* 1981; McNamara & Weisenfeld 1989; Bulsara & Gammaitoni 1996). This phenomenon has been named *stochastic resonance*.

To illustrate this phenomenon, consider the equation,

$$\frac{dX}{dt} = -\frac{\partial U}{\partial X} + F(t) + A\sin(\omega_0 t), \tag{4.31}$$

where F is a white noise term with the properties $\langle F \rangle = 0$ and $\langle F(t)F(t') \rangle = 2D\delta(t-t')$. Here $\langle .. \rangle$ means ensemble average and $\delta(t-t')$ is a Dirac delta function.

For a potential with a given shape, U, the noise induces occasional escapes from the well. This is characterized by the Kramers escape rate and depends on the noise amplitude, D. Stochastic resonance occurs when the periodicity $2\pi/\omega_0$ of the forcing matches the escape time.

The resonance can be visualized by imagining a quartic potential U with two wells, whose shape is periodically modified by the forcing. At certain phases of the modulation, one of the wells is lower than the other. At that specific time, it is "easier" for the system to pass from the higher equilibrium to the lower. Half a period afterwards, the opposite situation is encountered, and the system is more likely to switch back. If the amplitude of the noise is such that the escape time is similar to the period of the oscillation of the potential well, one observes the birth of a noisy periodicity at the frequency of the forcing. As a result, the system becomes an amplifier, capable of enhancing a small (sub-threshold) external periodic forcing through its noise-driven internal dynamics.

The idea of stochastic forcing was originally introduced by Benzi *et al.* (1982) and Nicolis (1982) as a mechanism for cycles of glaciation, and has been explored further in hundreds of papers since then. The main motivation for this explanation arises from various records of past climatic variability (e.g., the ratio $\delta^{18}O/\delta^{16}O$ in sea sediment cores; see Ghil & Childress 1987) which indicate that glaciations during the last million years possess broad periodicities at about 100,000, 40,000 and 20,000 years. Interestingly, similar periodicities are present in the variations of the Earth's orbital parameters, suggesting a direct orbital forcing on the terrestrial climate. However, by itself, the variation due to orbital changes is definitely too small to account for the large temperature difference between glacial and interglacial periods. Thus, if we want to insist on this explanation, an amplification mechanism is needed.

Stochastic resonance has been proposed explicitly as such a mechanism. In this context, the potential wells are associated with the multiple equilibria of the global climate due to the ice-albedo feedback (see Lecture 2), the periodic forcing is the variation of the Earth's orbit, and the white noise is provided by high-frequency temperature fluctuations in the atmosphere and oceans. To see how the model works, consider the energy balance equation introduced in

Lecture 2:

$$c\frac{dT}{dt} = Q(t)[1 - \alpha(T)] - \sigma g(T)T^4, \tag{4.32}$$

where the solar forcing Q is now taken to be time-dependent:

$$Q(t) = Q_0(1 + A\cos\omega_0 t) \ . \tag{4.33}$$

Variations in eccentricity of the Earth's orbit have a period of $2\pi/\omega_0 \approx 100,000$ years and an amplitude of $A \approx 10^{-3}$ in units of the mean solar constant, Q_0. For constant solar forcing ($A = 0$), equation (4.32) has three equilibrium solutions, T_1, T_2 and T_3. If the system is located at one of the stable fixed points, is far from any bifurcations and adjusts rapidly to changes in Q, then the temperature variations through the eccentricity cycle can be computed from the equilibrium curve, $T = T(Q)$, found from equating the right-hand side of (4.32) to zero. For $A = 10^{-3}$ and $T = T_1$ or T_3, this predicts a variation of about 0.1°C, which is much smaller than the inferred difference in the mean global temperatures between glacial and interglacial periods.

The addition of white noise, however, may cure the problem, as it can lead to stochastic resonance. It is not difficult to see that the addition of a white-noise term with appropriate amplitude to the right-hand side of equation (4.32) is the standard setup of stochastic resonance. Provided the resonance is of sufficient quality, this can force the system to jump from one stable equilibrium to the other, with an amplified, noisy periodicity of 100 kyr.

To conclude, may we say that stochastic resonance is the right explanation for glaciation cycles? Clearly, it is not easy to answer this question. Stochastic resonance is a very important concept, which can be extended to more general situations including non-periodic external forcing, coloured noise, and high-frequency chaotic dynamics replacing stochastic noise. The main problem with this type of resonance, however, is that the noise amplitude must be rather finely tuned to the shape of the potential and to the amplitude and period of the driver in order to obtain significant amplification. For example, stochastic resonance has been invoked in several biophysical and physiological amplification mechanisms; here, however, one can imagine that the system has evolved to a state in which amplification is optimized (e.g., natural selection could have tuned the shape of the potential). In the climatic case, however, there is no reason why the resonance should be there a priori, and it would be a fortunate coincidence if the amplitude of the noise induced by weather variability were resonating with the shape of the climatic potential and the periodicity of the orbital variations. Of course, more work is needed in order to understand whether some form of resonance can be observed in more complicated dynamical systems with less stringent requirements.

Lecture 5

Chaos driving Chaos

In Lecture 4 we have explored some examples of what can happen when a nonlinear dynamical system is driven by external periodic forcing, noise, or a combination of both. Here, we briefly consider the case of a nonlinear system, call it system B, which is driven by another nonlinear system (the driver), which we call system A. A particularly interesting situation is when there is no feedback of the driven system on the driver. Such systems are often more easily understood than systems that drive each other. Mathematically, the global system formed by A plus B is said to have a *skew-product structure*. An example of this is provided by the solar forcing on terrestrial climate, where the Sun is the driver, the climate is driven, and most people think that there is no feedback of the Earth's climate on the solar output.

5.1 On-off intermittency

In driven-driver systems with skew-product structure, many interesting things can happen. Among these, we concentrate on the phenomenon called *on-off intermittency*, which produces bursting behavior in the output of the driven system (see e.g. Platt, Spiegel & Tresser 1993a). A second possible phenomenon is synchronization, which we consider in the next lecture.

Consider the general system

$$\dot{\mathbf{X}} = \mathbf{F}(\mathbf{X}, \mathbf{Y})$$

and

$$\dot{\mathbf{Y}} = \mathbf{G}(\mathbf{Y}),$$

with $\mathbf{X} \in \mathcal{R}^k$, $\mathbf{Y} \in \mathcal{R}^{n-k}$. The dimensionality of the whole system is n. We suppose that the global system has an invariant manifold in the subspace $\mathbf{X} = \mathbf{0}$. That is, if $\mathbf{X} = \mathbf{0}$ initially, then it will remain so, whatever the vaue of $\mathbf{Y}$. We also suppose, however, that the stability of the manifold $\mathbf{X} = \mathbf{0}$ depends on the value of $\mathbf{Y}$. More specifically, we briefly ignore the evolution equation for $\mathbf{Y}$ and consider $\mathbf{Y}$ to be a constant parameter in the equation determining $\mathbf{X}$. Then, the invariant object, $\mathbf{X} = \mathbf{0}$, has stability characteristics depeding on the value of $\mathbf{Y}$.
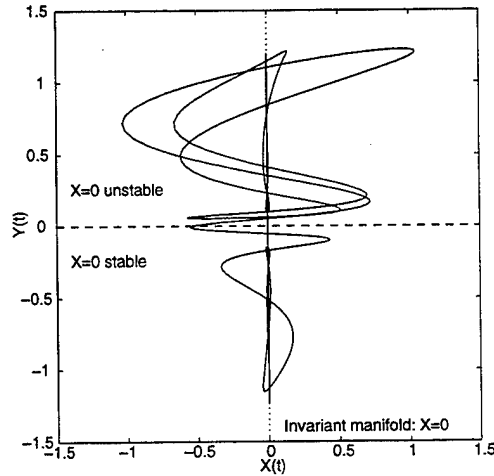
Figure 5.1: Effect of the variations of the driver Y on the dynamics of X. The variable Y controls the stability of the invariant manifold $X = 0$ of the driven system; where Y is positive, $X = 0$ is unstable, and where it is negative, the invariant manifold is stable.

The important feature of the system is that there is a region of the phase space for **Y** for which **X** = **0** is stable, the region $\mathcal{S}$ say. But if **Y** lies outside this region, then **X** = **0** is unstable:

$$Y \in \mathcal{S} \Rightarrow \mathrm{X} = 0 \; is \; stable$$

$$Y \notin \mathcal{S} \Rightarrow \mathrm{X} = 0 \; is \; unstable.$$

Now let **Y** evolve according to its own equation. The driver is set up such that the trajectory of the solution, $\mathbf{Y}(t)$ wanders through the phase space, with some periods of time spent largely in $\mathcal{S}$, then other intervals mainly outside this region. This means that the driver alternates between periods in which it typically stabilizies the invariant manifold, and intervals over which it destabilizes **X** = **0**. As a result, the variable **X** may spend long periods of time in the proximity of **X** = **0**, and undergo sudden bursts of activity far from **X** = **0** when the driver makes that manifold unstable.

In the simplest case, **X** = **0** is a fixed point, but in general the invariant manifold can contain an attractor of whatever dimensionality less than k. On-off intermittency thus provides a simple mechanism for bursting away from an attractor in low-dimensional systems. Figure 5.1 illustrates the behaviour.

A simple example of on-off intermittency is provided by the map,

$$X(n + 1) = R(n) X(n) [1 - X(n)] \tag{5.1}$$

in which we vary the control parameter, $R(n)$, according to another logistic map:
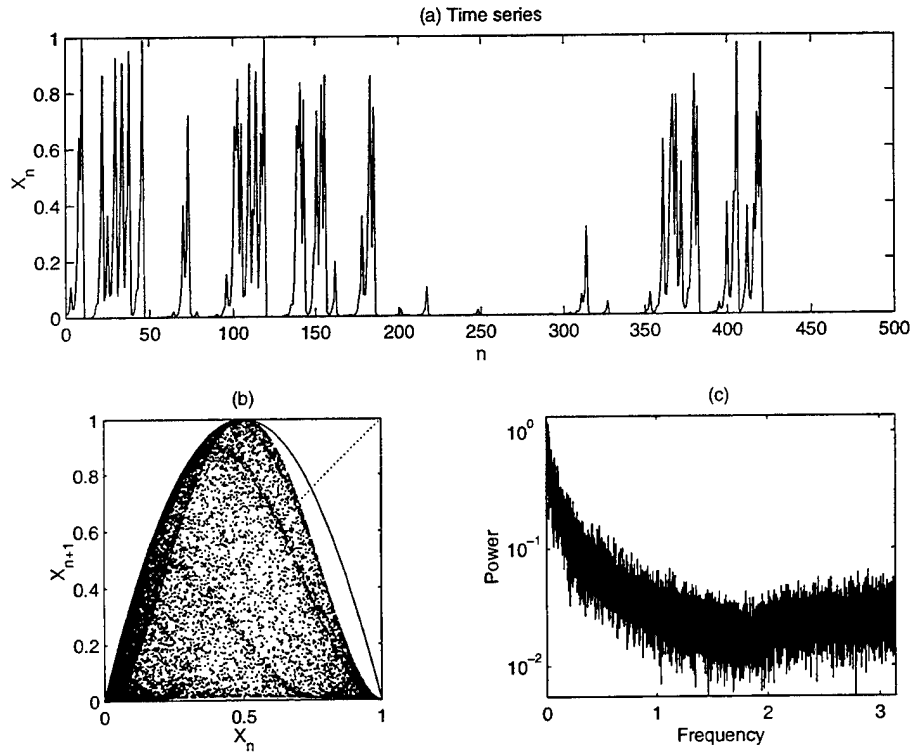
$$R(n) = aY(n) + b \tag{5.2}$$

61

Figure 5.2: On-off intermittency in the coupled maps (5.2)-(5.3). Panel (a) shows a short time series of X_n; the dotted lines indicate the corresponding signal of Y_n. In (b) we display X_n against X_{n+1}, and in (c) a power spectrum obtained from averaging spectra from ten different realizations of the system.

and

$$Y(n+1) = 4Y(n)[1 - Y(n)] \tag{5.3}$$

with $a = 3.95$ and $b = 0.05$. Figure 5.2 shows a time series of $X(n)$, which shows the bursty behavior typical of this form of intermittency. Time series of this kind are characterized by a *red* power spectrum (i.e., a spectrum with ever-increasing variance at low frequencies Balmforth *et al.* 1999; see figure 5.2c).

5.2 A model of the intermittent solar cycle

On-off intermittency has been proposed as a possible mechanism for the alternation between active and inactive periods in the solar dynamo (Platt, Spiegel & Tresser 1993b).

Sunspots are formed where strong magnetic fields inhibit fluid convection and the flow of heat in the turbulent solar envelope; where the fields pierce the solar photosphere, the mag-

netized fluid appears dark. The spots persist for timescale of order weeks, and understanding their origin is one of the most challenging problems in solar physics.

One of the most surprising aspects of sunspot phenomemology is the *solar cycle*: the number of sunspots observed on the solar surface varies roughly periodically with a timescale of eleven years or so. Though this eleven-year cycle appears to have existed for centuries, it does not appear to have maintained a constant amplitude. Notably, during the "Maunder Minimum" in the seventeenth century, there was a significant shortage of sunspots.

To rationalize the appearance of the Maunder Minimum (and other apparent declines in the solar activity) we turn to another metaphor. This time we interpret the Minimum in terms of the "off" period of an intermittent, low-order dynamical system. The particular system we choose is that described by Platt, Spiegel & Tresser. There are crude physical arguments supporting this model; at the risk of sounding ridiculous, we repeat some of these.

The solar cycle is basically a magnetohydrodynamical phenomenon. Our image behind the cycle is one in which magnetic flux is amplified by dynamo action in the convective solar envelope, then is swept into localized tubes by the action of turbulemt eddies. These tubes contain sufficient flux to impede the fluid flow and maintain their structure in the face of the turbulence. Upto this point, the image is plausible and largely agreed upon by solar physicists; beyond it, however, the image becomes sketchy and more controversial. The tubes are transported around by large-scale convective cells and ultimately expelled beneath the convection zone. Here, they build up in a thin zone between the radiative interior and the convective envelope where there is a high degree of shear due to the differential solar rotation. This is the solar tachocline. Here too, there is dynamo action due to the differential rotation. But it is the evolution of this magnetic layer on a longer timescale that may be responsible for producing the solar cycle.

To model the magnetic tachocline we take a nonlinear oscillator such as might be expected from a simple dynamo process:

$$\dot{x} = \beta x - \omega y - (x^2 + y^2)x \tag{5.4}$$

and

$$\dot{y} = \omega x + \beta y - (x^2 + y^2)y, \tag{5.5}$$

where ω is the frequency of the oscillator, and β is its growth rate. x and y could be, for example, the time-dependent amplitudes of a spatial mode as in the Galerkin projection described in lecture 2.

If β were constant, the oscillator models the magnetic content of the tachocline and its amplification through the action of differential rotation. But there is also the magnetic flux tubes that are expelled from the convection zone above, and "rain down" onto the tachocline. We account for this effect by adopting a time-dependent form for β that includes a term modelling the fluctuating process which adds to the field. In particular, we describe the turbulent convective dynamo by the Moore-Spiegel model (Moore & Spiegel 1966):

$$\ddot{X} = AX - X^3 - B\dot{X} + Z \tag{5.6}$$

63

$$\dot{Z} = -\delta[Z - CX(X^2 - 1)], \tag{5.7}$$

where A, B, δ and C are parameters. Again, $X(t)$ and $Z(t)$ could be the amplitudes of Galerkin modes. Then, we define

$$\beta = \beta_0(X - X_0), \tag{5.8}$$

where β_0 and X_0 are constants. This form for β is then fed into the oscillator equations (5.4)-(5.5).

A solution to our model system (5.4)-(5.8) is shown in figure 5.3. This shows how the activity in $x^2(t)$ bursts intermittently in the fashion of the on-off mechanism. Note that the dimensionless time unit corresponds to several years; the duration of the quiescent phases is of order 50 years.

Notably, outbursts are closely correlated with the periods over which $X(t)$ takes positive values. Evidently, in this model, the Maunder minimum and it predecessors should have a rough periodicity given by the timescale on which the Moore-Spiegel oscillator crosses from one side of the "bowtie" to the other (about 50 of the dimensionless time units). This feature of the model is not actually consistent with observations, calling, perhaps, for some further parameter tuning.

A simple modification of this model, that provides a more realistic alternance between active periods and "Grand Minima" (quiescent phases such as the Maunder Minimum), is obtained by breaking the skew-product structure of the system and introducing a small feedback of (x, y) on (X, Z) (Claudia Pasquero, *Thesis of Laurea*, 1996). This specific example indicates that, often, a richer behavior is found in systems which do not have a pure skew-product structure, but rather allow for a small feedback of the driven system on the driver. In these systems, the basic mechanism of on-off intermittency is still present, even though it is slightly modified by the presence of the (small) feedback. In the words of Ed Spiegel, these are systems with "broken asymmetry."

5.3 In search for the motor

We now return to pure skew-product nonlinear systems, and consider their properties from the point of view of time series analysis. In particular, we can imagine a situation where we measure only the output of the driven system B (thus considering what one might call a non-generic variable), and try to reconstruct some of the properties of the whole system, or of its individual constituents, A (the driver) and B.

Among the possible questions, we concentrate on the following one: Given that we have measured the output of the driven system, what can we say about the properties of the driver? In this context, we consider the driven system as a nonlinear dynamical filter acting on the driver, and we want to extract the characteristics of the driver embedded in the driven behavior. An example of this situation is when we attempt to extract from analysis of climatic data the hidden solar forcing.

In general, this question does not have a simple or unique answer, as the possibility of detecting a sign of the driver in the dynamics of the driven system depends on the nature of

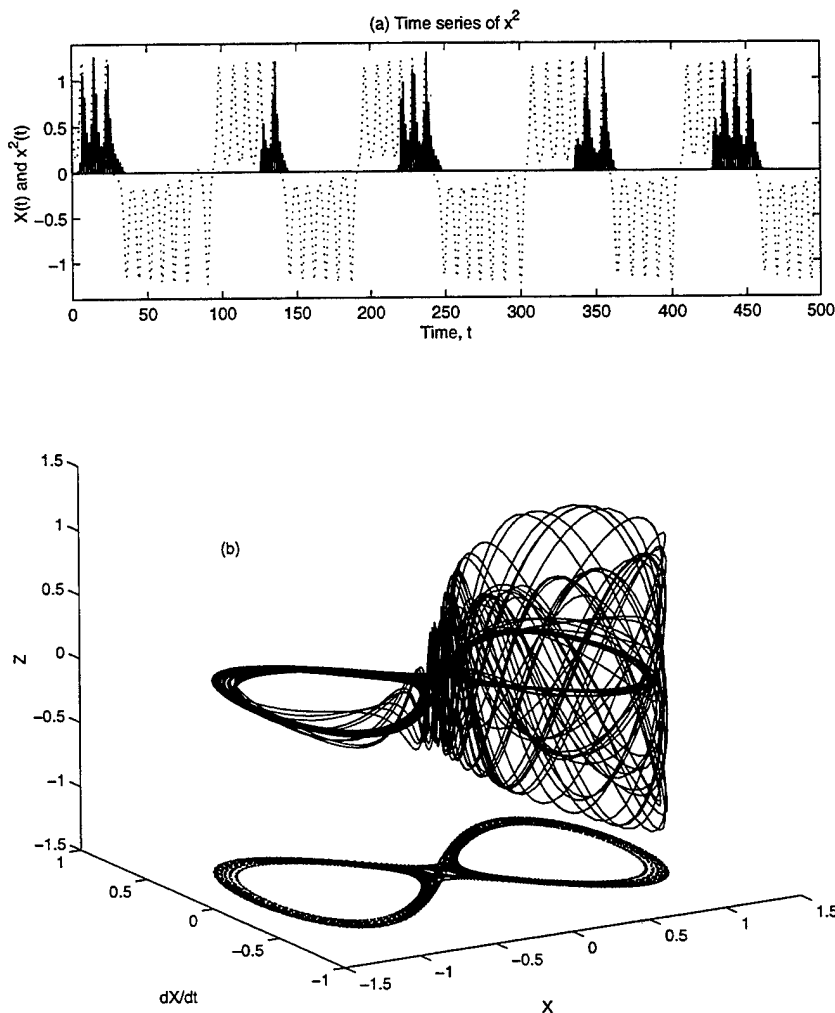64

(a) Time series of x^2

Figure 5.3: Intermittent solution of the system (5.4)-(5.8), with $A = 0.7$, $B = 0$, $C = -0.5$, $\delta = 0.03$, $\omega = 2$, $\beta_0 = 1$ and $X_0 = -0.15$. Panel (a) shows a time series of $x^2(t)$ (solid lines) and $X(t)$ (dotted lines), and panel (b) shows a phase portrait in $(X, \dot{X}, x)$–space; the projection of the Moore-Spiegel attractor is also displayed.

65

both systems, and on the strength of the driving. Thus, we qualify the above question, and explore whether we can at least distinguish between stochastic and deterministic driving in a system undergoing on-off intermittency (Platt, Spiegel & Tresser 1993a; von Hardenberg *et al.* 1997).

To this end, consider a simple tent-like map

$$x_{n+1} = \begin{cases} \mu x_n & x_n \leq \frac{1}{4} \\ \frac{\mu}{3}(1 - x_n) & x_n > \frac{1}{4}, \end{cases} \tag{5.9}$$

where μ is the control parameter. This map has a fixed point at $x_n = 0$; it is stable for $\mu < 1$ and unstable otherwise. For $\mu > 1$ there is another fixed point at $x_1 = \mu/(\mu + 3)$, which is stable for $\mu \leq 3$ and unstable otherwise.

Now, let us suppose that the control parameter is not constant, but varies according to another dynamics, which pushes it across the bifurcation sequence of the driven system. The dynamics of the control parameter is described by

$$\mu = a y_n \tag{5.10}$$

where a is a coupling constant. For the driver y_n, we take either a stochastic model,

$$y_n = \text{white noise}, \tag{5.11}$$

or a low-dimensional dynamical system,

$$y_{n+1} = 2y_n (\text{mod } 1). \tag{5.12}$$

In both cases, the driven map displays on-off intermittency, with long periods of quiet behavior intermixed with spikes of strong activity. Figure 5.4 shows two time series of the x_n variable, for the deterministic driver (panel a) and the white noise driver (panel b). In general, the amount of bursting is controlled by the value of a, and it is possible to find (different) values of a such that signals produced by the deterministically and the stochastically driven maps are apparently indistinguishable.

The indistinguishability extends also to simple calculations of the correlation dimension D_2, the Lyapunov exponents, or other dynamical measures obtained from a time embedding of the output of the driven system. For example, using $a = 2.88$ for the white noise and $a = 3.5$ for the deterministic driver gives the same correlation dimension in the embedded output signal. In other words, standard techniques do not appear to be able to distinguish stochastic and determinisitic, on-off signals. Worse still, the application of surrogate data tests (phase randomization, etc) is also of limited help, as the two signals remain apparently indistinguishable.

However, a clear (albeit qualitative) difference between the stochastic and deterministic drivers can be seen by plotting x_{n+1} vs x_n (panels (c) and (d) of figure 5.4; see also figure 5.2). The stochastic driver has a power-law divergence in the density of points near the origin and a uniform distribution of points far from the origin, while the deterministic driver has complicated large-scale structures in addition to the density divergence around $x = 0$.
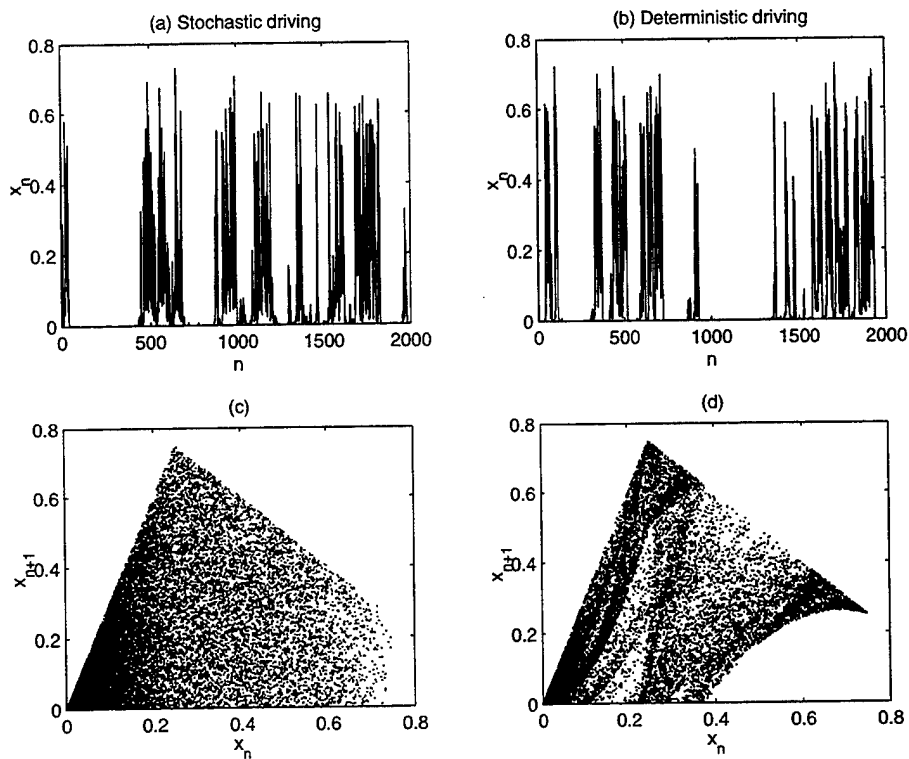
Figure 5.4: On-off intermittency in the coupled maps (5.9)-(5.12). The first two panels show short time series of x_n for (a) stochastic and (b) deterministic driving. Panels (c) and (d) show the same results plotted on the (x_n, x_{n+1}) plane. $a = 3$.

67

The strong clustering of points near the origin is a result of the off periods, present for both stochastic and deterministic driving, and it strongly influences the dimension determination. In fact, the approximate power-law distribution of points near the origin in phase-space induces a spuriously small value of the correlation dimension, that wipes out the dynamically significant differences between the stochastic and the deterministic driving which are present in the other portions of phase space.

To distinguish properly between the two drivers, one needs to reduce the effect of the points near the origin. To this goal, Hardenberg *et al.* have proposed to modify the definition of distance in phase space, in order to "spread" the points clustered near $x = 0$ and consequently allow for the dynamical differences to appear. With this modification, it was then shown that the correlation dimension takes the correct value, allowing for a distinction between the two types of driver. This result was achieved, however, only after a close scrutiny of the data, as the "automatic" procedures employed did not provide the correct results. This story indicates that one has to be careful when analysing the dynamics generated by on-off intermittent signal, as standard methods can give misleading results. Nevertheless, in this specific case, the other side of the coin is that a careful analysis of the reconstructed dynamics gives information on the nature of the driver, even if though it is processed by a bursting, nonlinear dynamical filter.

5.4   More intermittency

In this lecture we have explored some of the properties of systems undergoing on-off intermittency. However, "intermittency" is an abused term in nonlinear dynamics. For this reason, we now briefly mention some of the main usages of this term.

The most elementary, and general, definition of intermittency is in terms of the probability distribution of extreme fluctuations. For an intermittent system, large fluctuations (extreme events) are much more probable than for a gaussian process. In this sense, a system with slowly-decaying tails in the probability distribution of the dynamical quantities that characterize it can be called intermittent. Thus, an intermittent signal has non-gaussian probability distributions (for example, with exponential or power-law tails), and it cannot be generated by a linear process. The linear Orstein-Uhlenbeck process discussed in Lecture 3 is non-intermittent, while its nonlinear extension, also discussed there, is "intermittent." (This is evident from the probability distributions displayed in that lecture; figure 3.3.) Note, however, that a simple nonlinear change of variables may make a linear signal to appear intermittent. Thus, this definition of intermittency does not distinguish between signals produced by a truly nonlinear dynamical system and linear signals that have been nonlinearly transformed.

A more quantitative measure of intermittency is provided by the study of the (possibly) multifractal properties of the signal. Multifractality can be uncovered by evaluating the structure functions of order m:

$$S_m(\tau) = \; < |x(t+\tau) - x(t)|^m >_t$$

where $x(t)$ is the time series under study and $< .. >_t$ indicates a time average along the signal. The parameter m defines the order of the moment. For a signal characterized by scaling

68

properties (a fractal signal), one has that

$$S_m(\tau) \propto \tau^{\zeta(m)}$$

at small τ. Moreover, for a multifractal, intermittent signal, $\zeta(m)$ increases more slowly than m, and so $\zeta(m)/m$ is a decreasing function. Thus, detecting decreasing values of $\zeta(m)/m$ for increasing m is a sign of intermittency. One must keep in mind, however, that statistical errors and limitations become stronger and stronger as the order of the moment increases, and spurious positive results can be easily found (see e.g. Provenzale *et al.* 1993).

Another way of quantifying intermittency is by the evaluation of the generalized dimensions, D_q. For a multifractal signal, the generalized dimensions, D_q, decrease with increasing q. Various definitions of the generalized dimensions are possible; here, we use the simplest and most intuitive one. To this end, first define a probability measure, $p(t)$, from the measured signal $x(t)$. For example, one may use $p(t) = x(t)$ for a signal produced by one of the intermittent maps discussed above, or $p(t) = (dx/dt)^2$ for a signal provided by a velocity measurement in a turbulent flow. The choice of the measure is crucial, and it should be dictated by the physics of the system under study. Unfortunately, many details of the results depend on the choice of the measure. Definitions which do not employ a measure are possible, and used in several contexts. Here, however, for simplicity we stick to the definitions based on a measure $p(t)$.

Once we choose a measure, we then define

$$P_i(\Delta) = \int_{t_i - \frac{\Delta}{2}}^{t_i + \frac{\Delta}{2}} p(t)\, dt$$

and

$$B(\Delta, q) = \sum_{i=1}^{L} [P_i(\Delta)]^q$$

where time is been divided into L segments of duration Δ. Note also that the above definition is not correct for $q = 1$, in this case one should use

$$B(\Delta, 1) = \sum_{i=1}^{L} [P_i(\Delta)] \log P_i(\Delta)$$

If the chosen measure is self-affine, then in the limit $\Delta \to 0$ one finds that

$$B(\Delta, q) \sim \Delta^{(q-1)D_q}$$

where the D_q's are the generalized fractal dimensions, and q is the order of the moment.

If the measure is almost always non-zero on the time axis (so the measure "fills" the line), then $D_0 = 1$. This implies that the chosen measure has no fractally-distributed "holes" on the time axis. For monofractal, non-intermittent measures, $D_q = D_0$ for all q. In contrast, for an intermittent measure the generalized dimensions D_q decrease with increasing q.

69

For example, the linear Ornstein-Uhlenbeck process of Lecture 3 generates signals with $D_q \approx 1$ for all q, when the measure $p(t) = (dx/dt)^2$ is used. By contrast, the nonlinear version of the process generates multifractal signals which are intermittent: $D_0 = 1$ and $D_q < D_{q'}$ for $q > q'$. For this process, therefore, the simple definition of intermittency based on the distribution of the dynamical variable coincides with the more sophisticated definition based on the multifractal nature of the signal.

In the dynamical systems folklore, at least another definition of intermittency has been introduced (Pomeau & Manneville 1980). This type of intermittency is observed when the system is close to a bifurcation. A particularly visible example arises for a one-dimensional map near a saddle-node bifurcation. Figure 5.5 shows one such example; this is the logistic map, with parameter r set to be just below the point at which the period–3 orbit appears in a saddle-node bifurcation. As shown in the first panel, the third iterate of the map then contains three points that are very close to the diagonal; these points touch the diagonal and develop into equilibria as we pass through the saddle node on raising r. Whenever the system passes close to one of these points, it spends a significant amount of time in that "bottleneck". As a result, one observes long periods of quiescent behavior with occasional bursting away from the region where the curve representing the map and the 45° line almost intersect. This behavior, however, is strictly associated with an incipient saddle-node (or other) bifurcation and requires a very fine tuning of parameters. It is therefore less generic than the on-off intermittent bursting discussed above.
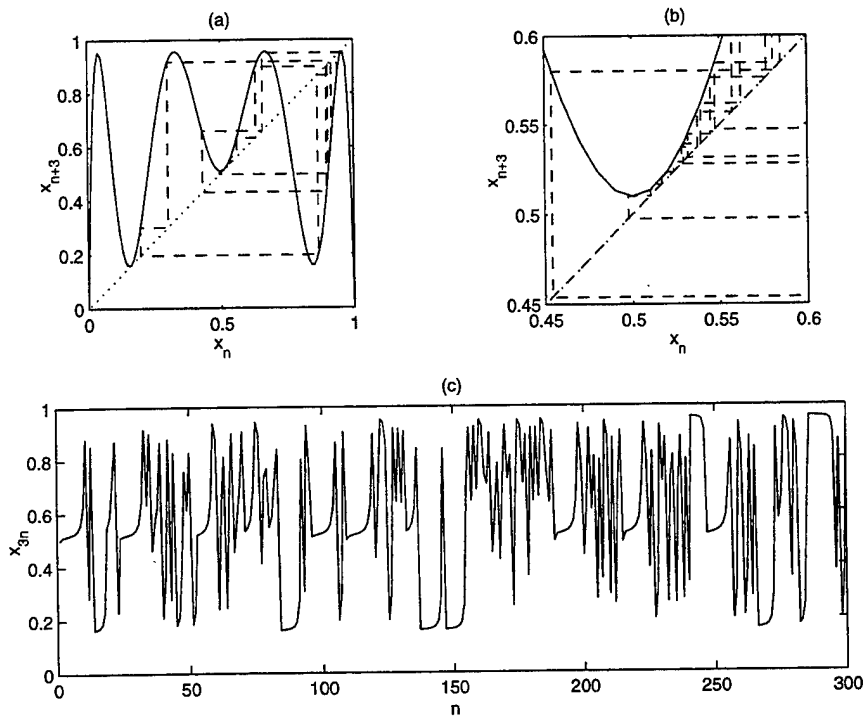
Figure 5.5: Pomeau-Manneville type I intermittency in the logistic map, $x_{n+1} = rx_n(1 - x_n)$ with $r = 3.827$. Every third iteration is shown which illustrates the close passage of the trajectory (the dashed lines) to the points that, for larger r, develop into the period-3 orbit. The first panel shows the map, and the second a magnification around the middle "bottleneck". The third panel shows part of the time series.

71

Lecture 6

Coupled Chaos

In lecture 5 we have studied the situation where one system (the driver) forces another (the driven). We now turn to the general issue of the dynamics of coupled systems.

There are many instances in which such dynamics are relevant to geophysics and astro-physics. For example, oceanographers often account for the atmosphere in terms of only a simply wind forcing in their circulation models, and meteorologists occasionally ignore the ocean altogether. But, as every climate dynamicist appreciates, the two are intimately cou-pled, and many phenomena in the global climate arise as a result of the coupling.

In this lecture we focus on some consequences of coupling that can be explored using simple dynamical systems. The possible synchronization of dynamically similar systems is the first such consequence that we discuss. The second issue we raise is, given that the system we consider is composed of coupled elements with complicated internal dynamics, how much can we say about the full system if we have information from only one of its subsystems. It turns out that a full reconstruction is impossible. Then we follow on to explore systems with widely different timescales, and describe tools that attempt to distinguish between fast and slow dynamics. These tools have some degree of success and lead us to hope that it might prove possible to "filter out" the faster dynamics in favour of understanding the slower processes that are at work in real applications.

These latter issues have obvious application to weather prediction, where we attempt to forecast the future of a complicated, coupled system with many timescales given information from only certain observing "sites" on certain subsystems.

6.1 Synchronization of Coupled Systems

In 1673, Huygens observed the phase-locking of two clocks. He attributed this *synchronization* to a weak coupling of the clocks. However, the phenomenon occurs in much more general situations, and with whole arrays of coupled systems. For example, one of the most spectacular (and also frequently cited) properties of populations of coupled nonlinear oscillators is the convergence to mutual synchrony which is observed in many contexts, ranging from firefly communities and networks of neurons to charge density waves.

These examples invariably involve simple oscillators for which coupling opens up the possibility of synchronization in phase; the oscillators, in fact, need not even be identical. But the systems that we hope to explore in geophysics and astrophysics are composed of much more complicated subsystems. In fact, the subsystems we would typically like to couple together are chaotic. But, can chaotic systems synchronize?

One of the hallmarks of chaos is the sensitivity to the initial condition of the system. This means that two identical systems with slightly different initial states will diverge from one another in phase space exponentially quickly. This idea conveys the impression that chaotic systems are difficult to control and, in particular, if we couple two together, the systems are unlikely to follow identical orbits. In fact, this is not the case; chaotic systems can synchronize.

To illustrate the point consider two identical dynamical systems that, in isolation, are described by the equation $\dot{\mathbf{x}} = \mathbf{f}(\mathbf{x})$. We may coupled the systems together in various ways, some of which will be mentioned shortly. However, for the moment, we introduce one of the simplest form of coupling:

$$\dot{\mathbf{x}}_1 = \mathbf{f}(\mathbf{x}_1) + \epsilon(\mathbf{x}_2 - \mathbf{x}_1) \quad \text{and} \quad \dot{\mathbf{x}}_2 = \mathbf{f}(\mathbf{x}_2) + \epsilon(\mathbf{x}_1 - \mathbf{x}_2). \tag{6.1}$$

Here, ϵ measures the strength of the coupling.

Clearly, if $\epsilon = 0$, the two systems are uncoupled and freely evolve. Provided the two systems are chaotic, there is no reason to believe that they will synchronize. However, $\mathbf{x}_1 = \mathbf{x}_2$ is nevertheless a solution. In fact, this is a solution for all ϵ; that is, it is an invariant manifold. We call this object the *synchronization manifold* of the coupled system, and it is described by an orbit of the uncoupled equations. Note that the synchronization manifold must be an invariant manifold of the full system, or synchronization is not possible. This means that non-identical systems do not normally synchronize.

For ϵ sufficiently small, the coupling is too weak to affect appreciably each subsystem and so they must again evolve almost independently. The sensitivity to initial condition implies that the two susbsystems diverge from one another if they are initially close. Hence the synchronization manifold is in this sense *unstable*.

At large coupling strength, on the other hand, the largest terms in the equations are the coupling terms, and so (as Ed Spiegel puts it) "they must be zero". In other words, there are no terms in the equations that can balance the strong coupling other than the time derivative:

$$\dot{\mathbf{x}}_1 \sim \epsilon(\mathbf{x}_2 - \mathbf{x}_1) \quad \text{and} \quad \dot{\mathbf{x}}_2 \sim \epsilon(\mathbf{x}_1 - \mathbf{x}_2). \tag{6.2}$$

This simplified system predicts a relaxation to the synchronization manifold. Equivalently, when ϵ is large, we *slave* the subsystems to one another and adiabatically eliminate one variable in favour of the other (to use the terminology of amplitude expansions).

Thus even chaotic systems can synchronize. This remains the case even for very different forms of coupling as some of the examples to follow indicate. Before describing these examples, we first formalize the definition of stability of the synchronization manifold.

Consider the coupled systems,

$$\dot{\mathbf{x}}_1 = \mathbf{F}(\mathbf{x}_1, \mathbf{x}_2; \epsilon) \quad \text{and} \quad \dot{\mathbf{x}}_2 = \mathbf{F}(\mathbf{x}_2, \mathbf{x}_1; \epsilon). \tag{6.3}$$

This generally expresses the form of two symmetrically coupled systems with coupling strength ϵ. We consider an orbit in the synchronization manifold, $x_1 = x_2 = x$, and then perturb the system around this trajectory:

$$x_1 = x + u_1 \quad \text{and} \quad x_2 = x + u_2, \tag{6.4}$$

with $|u_1| \ll 1$ and $|u_2| \ll 1$. By substituting these forms into the system (6.3) and linearizing, we arrive at

$$\dot{u}_1 = F_1 u_1 + F_2 u_2 \quad \text{and} \quad \dot{u}_2 = F_2 u_1 + F_1 u_2, \tag{6.5}$$

where

$$F_1 = \left[\frac{\partial F(x_2, x_1; \epsilon)}{\partial x_1} \right]_{x_1 = x_2 = x} \quad \text{and} \quad F_2 = \left[\frac{\partial F(x_2, x_1; \epsilon)}{\partial x_2} \right]_{x_1 = x_2 = x}. \tag{6.6}$$

Thus,

$$\dot{u}_1 + \dot{u}_2 = (F_1 + F_2)(u_1 + u_2) \tag{6.7}$$

and

$$\dot{u}_1 - \dot{u}_2 = (F_1 - F_2)(u_1 - u_2). \tag{6.8}$$

The formulation of the stability problem in terms of the sums and differences effectively organizes the perturbation in terms of a component that preserves the synchronization and one that destroys it. The second component therefore describes perturbations away from, or *transverse* to, the synchronization manifold.

Both linear systems (6.7) and (6.8) are not straightforward to solve: the coefficients embodied in $F_1 \pm F_2$ involve the variables describing the synchronized, chaotic trajectory. Thus we can only make sense of stability in terms of a temporal average. In fact, the system (6.7) corresponds to the stability of the orbit inside the synchronization manifold, and therefore is identical to the system that one must solve to compute the Lyapunov exponents, λ, of the uncoupled system.

Likewise, the solution of the transverse stability equation (6.8) is understood in terms of exponents much like Lyapunov exponents:

$$u_\perp \equiv u_1 - u_2 \sim \exp \Lambda t \quad \text{as } t \to \infty. \tag{6.9}$$

The synchronization exponent, Λ, is sometimes called the *transverse stability* or *Lyapunov exponent*, or the *conditional Lyapunov exponent*. Provided the leading exponent, Λ_1 say, is negative, the synchronization manifold is stable in the sense of a linearized perturbation and an infinite-time average.

The organization into synchronized and transverse perturbations follows also for systems that are not coupled symmetrically. Hence, we may define transverse stability exponents whatever the form of coupling. These dictate the stability of the synchronization manifold.

74

However, since we can only understand the stability exponents in terms of the limits of infinite time and infinitesimal perturbation, there are some limitations on how useful these exponents really are in predicting synchronization: sometimes systems can desynchronize due to finite time and amplitude effects even in situations in which the stability exponents predict that the synchronization manifold is stable (Pecora *et al.* 1997).

We next describe some specific examples of synchronizing chaotic systems. These illustrations all involve cases in which the subsystems can synchronize *exactly*. That is, situations for which $x_1 - x_2 \to 0$ as $t \to \infty$. However, more general forms of synchronization are also possible. For example, systems can synchronize upto an amplitude scaling, a phase lag, or some particular functional relationship. There are also weaker forms of synchrony in which the phase of the oscillators shows some degree of synchrony, but the amplitudes remain unsynchronized; this is called "phase synchronization" (Rosenblum *et al.*, 1996). With these generalized definitions, it becomes possible to synchronize non-identical chaotic elements.

Complete replacement

The most commonly cited example of chaotic synchronization involves a special form of coupling that involves the complete replacement of a variable in one subsystem with the corresponding variable from another (Pecora & Carroll 1990). This coupling is quite different from that used above because one system evolves independently of the other, and we must throw away the equation for the replaced variable, which is now redundant. This one-way coupling scheme is also called "master-slave" synchronization, and is an example of a system with skew-product structure.

By way of example, we couple two Lorenz '63 systems $\{x_1, y_1, z_1\}$ and $\{x_2, y_2, z_2\}$ via the complete replacement $x_2 \to x_1$. This produces the system,

$$
\begin{aligned}
\dot{x}_1 &= -\sigma(y_1 - x_1) \\
\dot{y}_1 &= -x_1 z_1 + r x_1 - y_1 \\
\dot{z}_1 &= x_1 y_1 - b z_1 \\
\dot{y}_2 &= -x_1 z_2 + r x_1 - y_2 \\
\dot{z}_2 &= x_1 y_2 - b z_2.
\end{aligned}
\tag{6.10}
$$

Alternatively, we may write the system in terms of the Lorenz equations and two equations for the differences, $\Delta_y = y_2 - y_1$ and $\Delta_z = z_2 - z_1$:

$$
\begin{aligned}
\dot{\Delta}_y &= -x_1 \Delta_z - \Delta_y \\
\dot{\Delta}_z &= x_1 \Delta_y - b \Delta_z.
\end{aligned}
\tag{6.11}
$$

A pictorial representation of the synchronization manifold, given by $\Delta_y = \Delta_z = 0$, is displayed in figure 6.1. Parameter values are the usual $r = 28$, $\sigma = 10$ and $b = 8/3$. The solid lines show a solution that converges to the synchronizes manifold, suggesting that this object is stable.

In fact, the coupled system *always* synchronizes: equations (6.11) can be combined into the relation,

$$
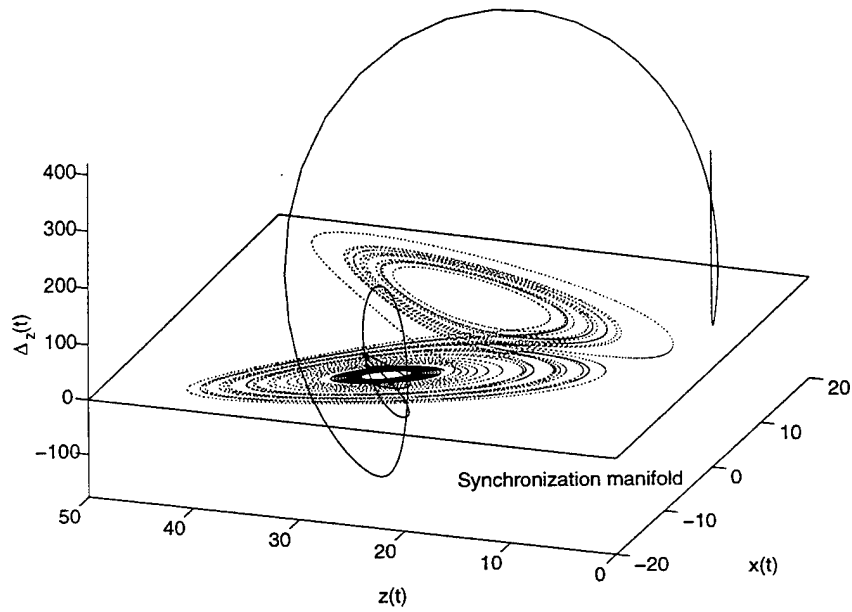\frac{1}{2}\frac{d}{dt}(\Delta_y^2 + \Delta_z^2) = -\Delta_y^2 - b\Delta_z^2.
\tag{6.12}
$$

75

Figure 6.1: A projection of the synchronization manifold for two Lorenz '63 systems coupled through the complete replacement of the x−variable of one subsystem. The solid line shows a sample orbit converging to synchrony.

The right-hand side of this expression is always negative, provided one of Δ_y and Δ_z is finite (and b is positive). This indicates the differentiated quantity on the left must decrease in time to its minumum value, which is $\Delta_x = \Delta_y = 0$. Thus, synchronization is the fate of the system. (This argument amounts to the identification of a Lyapunov functional.)

Coupled Rossler systems

Both the coupled Lorenz systems and the example used to introduce the concept of chaotic synchronization exhibit synchronization, but this behaviour is by no means automatic. Moreover, for different forms of coupling, it is not necessarily the case that the systems synchronize for sufficiently large coupling strength.

For example, two Rössler systems can be coupled as follows:

$$
\begin{aligned}
\dot{x}_1 &= -(y_1 + z_1) \\
\dot{y}_1 &= x_1 + ay_1 \\
\dot{z}_1 &= b + z_1(x_1 - c) \\
\dot{x}_2 &= -(y_2 + z_2) + \alpha(x_1 - x_2) \\
\dot{y}_2 &= x_2 + ay_2 \\
\dot{z}_2 &= b + z_2(x_2 - c)
\end{aligned}
\tag{6.13}
$$

(*cf.* Pecora *et al.* 1997). This is a form of diffusive coupling (as used in the introduction to this lecture), but it appears only in one of the equations.

The stability of this diffusively-coupled system is determined by the equation,

$$
\frac{d}{dt}\begin{pmatrix} x_\perp \\ y_\perp \\ z_\perp \end{pmatrix} = \begin{pmatrix} -\alpha & -1 & -1 \\ 1 & a & 0 \\ z & 0 & x-c \end{pmatrix} \begin{pmatrix} x_\perp \\ y_\perp \\ z_\perp \end{pmatrix},
\tag{6.14}
$$

where $x_\perp = x_1 - x_2$ and so on.

The leading transverse Lyapunov exponent is shown in figure 6.2 as a function of coupling strength α; where this is negative, the system is predicted to synchronize. As indicated by the figure, the synchronization manifold is unstable for small values of the coupling parameter α, but successful synchronization is achieved for intermediate values of α. This is perhaps not so surprising. More interestingly, we see that with stronger coupling, Λ becomes positive once more and the systems *desynchronize*.

In the limit of large α, the leading order balance in the equation for x_2 requires that $x_1 = x_2$. Thence,

$$
\begin{aligned}
\dot{x}_1 &= -(y_1 + z_1) \\
\dot{y}_1 &= x_1 + ay_1 \\
\dot{z}_1 &= b + z_1(x_1 - c) \\
\dot{y}_2 &= x_1 + ay_2 \\
\dot{z}_2 &= b + z_2(x_1 - c).
\end{aligned}
\tag{6.15}
$$

In other words, the diffusive coupling is equivalent to complete replacement. Complete repacement of x in coupled Rossler systems is known not to be successful for synchronization at these
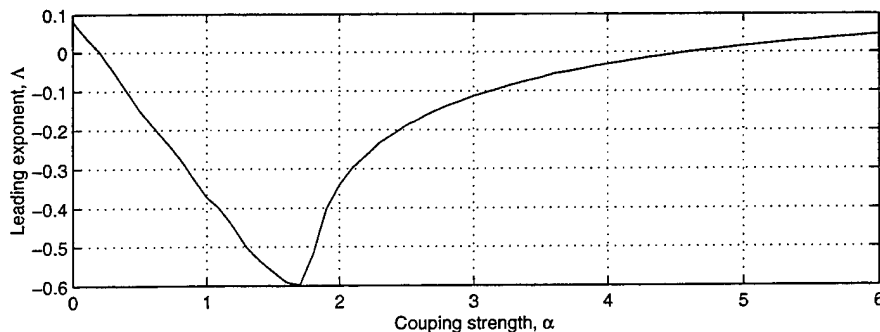
77

Figure 6.2: Strength of the leading transverse Lyapunov exponent Λ as a function of coupling strength parameter α for $a = 0.2$, $b = 0.2$ and $c = 9$.

parameter values. Hence, in this regard, the ultimate rise of Λ to positive values at larger α is expected.

Synchronization in coupled maps

In the two previous examples, the coupled system contained two elements with skew product structure; one system evolved independently of the other. Now we relax this constraint and consider a model with arbitrarily many elements that are coupled to either the whole ensemble (global coupling) or to two neighbouring elements (local coupling). Thus, we consider the global synchronization of a lattice. The particular model we choose is a coupled-map lattice which has been used by Kaneko and co-workers to explain many phenomena (Kaneko 1993).

The elements of the lattice are one-dimensional chaotic maps whose uncoupled form is $x_{n+1} = f(x_n)$. With *global coupling* of all the elements, the lattice equations become

$$x_{n+1}(i) = (1 - \epsilon)f\left[x_n(i)\right] + \frac{\epsilon}{L} \sum_{j=1}^{L} f\left[x_n(j)\right], \tag{6.16}$$

where i and j are lattice indices, L is the number of elements in the lattice, and ϵ ($0 \leq \epsilon \leq 1$) is the coupling strength. This kind of model is considered in detail in Jacobson's report elsewhere in this volume.

For strong coupling, the chaotic lattice synchronizes globally (Kaneko, 1989; Ding & Yang, 1997). This is illustrated in figure 6.3 for a lattice described by $f(x) = 1 - ax^2$ (the logistic map again).

However, below a critical coupling strength, ϵ_c, the system desynchronizes. This threshold value depends on the largest Lyapunov exponent, λ, of the uncoupled map:

$$\epsilon_c = 1 - e^{-\lambda}. \tag{6.17}$$

For coupling values just under the critical threshold, the lattice displays on-off intermittent desynchronization (Fig 6.4).
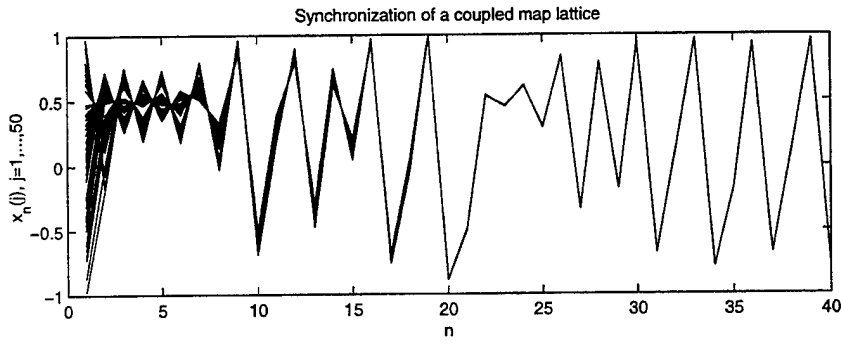
Figure 6.3: The synchronization of a globally coupled map lattice for $a = 1.9$ and $\epsilon = 0.5$ from random initial conditions lying in the range $[-1, 1]$.
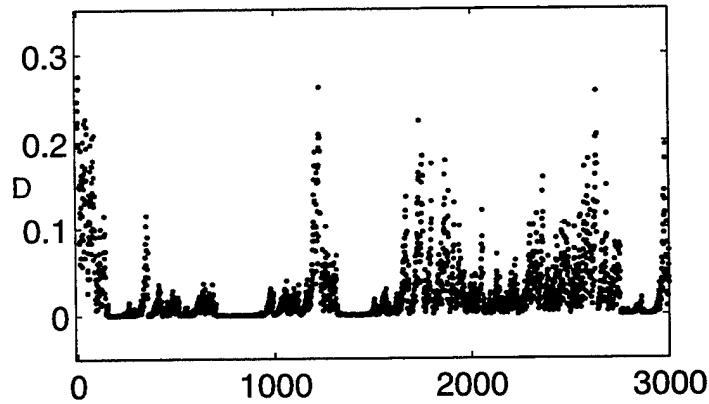

Figure 6.4: The value of $d = \frac{1}{L} \sum_{i=1}^{L} |x(i) - \bar{x}|$ as a function of n for 100 globally-coupled logistic maps with $a = 1.9$. The coupling parameter ϵ is 0.41, slightly less than $\epsilon_c = 0.43$.

One can also *locally* couple the map elements:

$$x_{n+1}(i) = (1 - \epsilon)f[x_n(i)] + \frac{\epsilon}{2}(f[x_n(i - 1)] + f[x_n(i + 1)]).$$ (6.18)

This two-way, nearest-neighbour coupling is equivalent to a discretized diffusion across the lattice.

In contrast to the global coupling case, the transverse Lyapunov exponents for local coupling are found to depend on the lattice size L. Synchronous chaos is only found in systems consisting of fewer than a critical number of elements L_m, with the maximum system size depending on the behavior of the individual map. Specifically, the leading transverse Lyapunov exponent can be shown to be

$$\Lambda = \lambda + \ln[1 - \epsilon + \epsilon \cos(2\pi/L)]$$ (6.19)

(Ding & Yang, 1997), which imples that the maximal lattice size is given by the largest integer $L < L_m$, where

$$L_m = 2\pi \left[\cos^{-1} \left(\frac{e^{-\lambda} - 1 + \epsilon}{\epsilon} \right) \right]^{-1}.$$ (6.20)

For example, when $a = 2$, $\lambda = \ln 2$ and the maximal system size is at most 6 (occuring for $\epsilon = 1$).

The origin of this limitation is that desynchronization sets in through a "long-wave" instability. Hence the only option for stable synchrony is to exclude the unstable range of wavenumbers by introducing a minimum wavenumber via the finite dimension of the lattice. When this is not possible, the coupled map lattice shows a wide range of spatio-temporal complexity as shown, for example, in figure 6.5 (see also Kaneko, 1993).

This figure shows anything but synchronization. But neither does it show a collection of chaotically evolving, independent elements. Instead there is a mixture of spatially local order and confined regions of chaos. This is, of course, how one would like to imagine the spatially extensive natural systems that we deal with, which is why coupled map lattices and their relatives remain so popular.

A model of interhemispheric teleconnections

Finally, we turn to a GFD application of the synchronization theory (Duane, 1997). The meteorlogical basis of this model is an observed correlation between weather systems in the midlatitudes of the northern and southern hemispheres. Such correlations have been termed "teleconnections" by Bjerknes (1966). One of the important properties of such teleconnections is that they may be mediated by atmospheric Rossby waves. As a result, the connection between the hemispheric midlatitudes cannot be strong: Rossby waves propagating in midlatitudes, where winds are predominantly westerly, cannot traverse the equatorial regions because they become evanescent in regions of eastward flow (this can be understood from the linear dispersion relation of Rossby waves, see Duane's article). Nevertheless, the equatorial
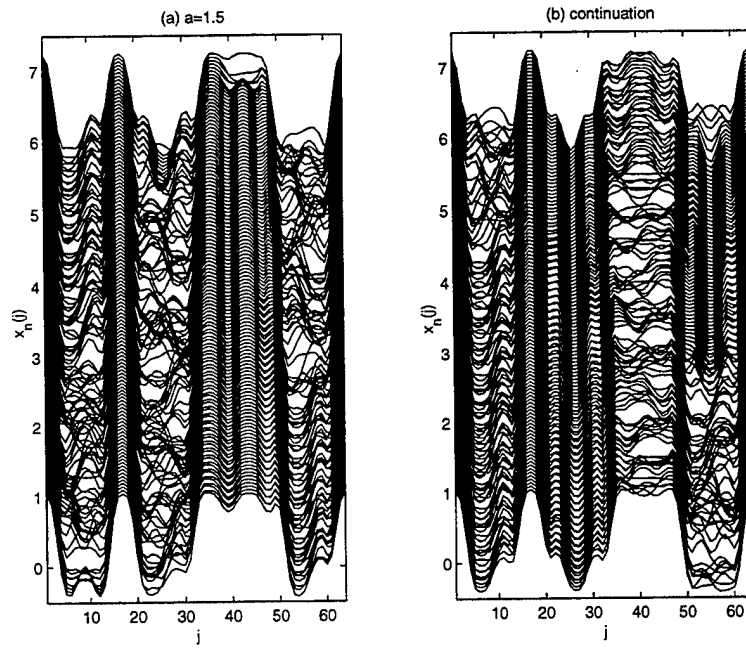
Figure 6.5: Evolution of a locally coupled map lattice for $a = 1.5$ and $\epsilon = 0.5$. Panel (b) is a continuation of (a).

81

eastward winds are observed to be occasionally interrupted by localized weather patterns with internal, westward flow. Rossby waves then propagate through the narrow "ducts" that these patterns create, coupling the two midlatitudinal regions.

An important property of this coupling is that it takes a finite amount of time for the Rossby waves to propagate through the ducts. Thus one hemisphere does not immediately experience the effect of conditions in the other, but there is a delay.

We attempt to rationalize the correlation suggested by observations in terms of chaotic synchronization. We consider two Lorenz '63 systems $\{x, y, z\}$ and $\{x_1, y_1, z_1\}$ coupled through an auxiliary variable s:

$$
\begin{aligned}
\dot{x} &= \sigma(y - x) \\
\dot{y} &= r(x - s) - y - (x - s)z \\
\dot{z} &= -\beta z + (x - s)y \\
\dot{x}_1 &= \sigma(y_1 - x_1) \\
\dot{y}_1 &= r(x_1 + s) - y_1 - (x_1 + s)z_1 \\
\dot{z}_1 &= -\beta z_1 + (x_1 + s)y_1.
\end{aligned}
\tag{6.21}
$$

If we select

$$
s = c(x - x_1),
\tag{6.22}
$$

where c is the coupling strength ($0 \leq c \leq 1$), then the system (6.21) synchronizes. This simple model suggests that an explanation of this kind is possible. But (6.22) assumes that the coupling takes immediate effect.

One can generalize the model to allow a time lag in the coupling. In particular, one can replace (6.22) with the differential equation,

$$
\dot{s} = \Gamma\left[-s + c(x - x_1)\right],
\tag{6.23}
$$

where Γ is the time scale on which s relaxes. In the limit of $\Gamma \to \infty$, one adiabatically eliminates s through the relation (6.22), and so the system reduces to the case above.

For the more general situation using (6.23) with Γ finite, a range of synchronization results is found. For sufficiently large Γ, the systems still synchronize (as verified by a direct computation of the trasverse stability exponent, see figure 6.6), but as Γ is reduced, the stability of the synchronization manifold is lost. Instead, the system displays on-off intermittent desynchronization (figure 6.6, panels (b) and (c)). This sort of desynchronization is characterized by episodic bursts of wild departure from the synchronization manifold, after which the system returns to synchrony for some macroscopic length of time. This kind of behavior is the result of the synchronization manifold becoming slightly unstable as the time lag is increased. A trajectory of the coupled system may wander near or on the manifold for long periods of time before encountering conditions which cause it to desynchronize.

Though perfect synchrony can be lost for the time-lagged coupling, there remains a close correlation between the two subsystems as a result of the on-off intermittency. Duane observes similar effects in more complicated, though still relatively low-order, atmospheric models. In fact, the observed correlation between weather patterns at midlatitude in either hemisphere is far from precise (decribed further by Duane). But whether this reflects an origin that can be described by the on-off synchronization of two coupled, low-order systems is far from clear.
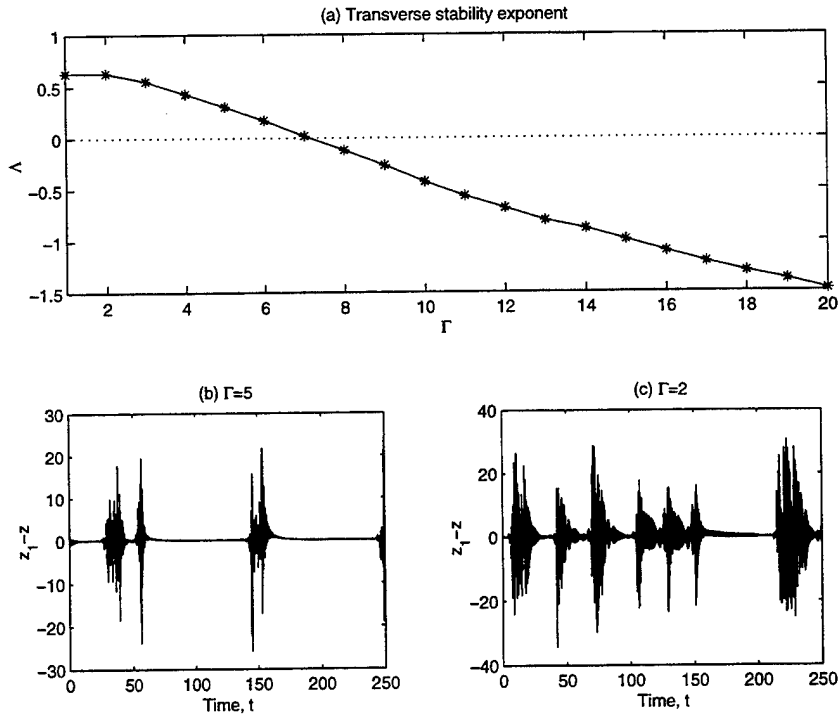
Figure 6.6: Synchronization of the coupled Lorenz systems (6.21) and (6.23). Panel (a) shows the transverse stability exponent against relaxation rate Γ. Panels (b) and (c) illustrate the intermittent synchronization that appears when the synchronization manifold loses stability, for $\Gamma = 5$ and $\Gamma = 2$ respectively. The other parameters are $c = 1$, $r = 28$, $\sigma = 10$ and $b = 8/3$.
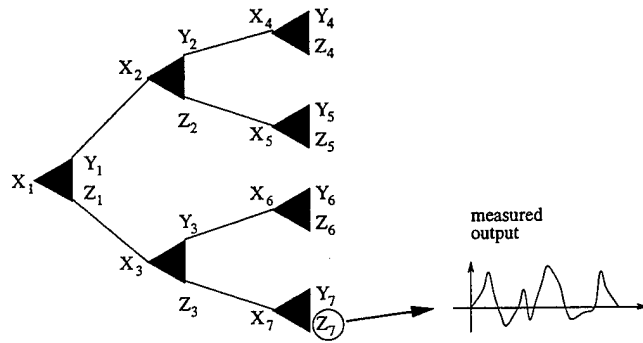
Figure 6.7: Coupling scheme for the seven Lorenz '84 systems.

6.2 Reconstructing the dynamics of coupled systems

We now turn to the issue of reconstruction. In particular, we ask the fundamental question of whether the dynamics of the full network can be inferred from a finite-length time series of just one variable from one subsystem. To answer the question we turn to metaphorics: we use a relatively simple network of coupled low-order dynamical systems to assess conventional reconstruction techniques.

We take a model proposed by Lorenz (1991; see also von Hardenberg *et al.*, 1997) . that consists of seven elements coupled through the network illustrated in figure 6.7. The coupling scheme represents some kind of cascade through subsystems of different scales, and can be extended to much larger systems. The cascade is meant to reflect some sort of analogy with turbulence (but it is clearly ludicrous to imagine that there is any real correspondence).

Each uncoupled element is a Lorenz '84 system, with parameters set such that individually each subsystem is chaotic. The equations of motion for the jth system are

$$
\left.
\begin{array}{rcl}
\dot{X}_j &=& -(Y_j^2 - Z_j^2) - a(X_j - F) + U_j \\
\dot{Y}_j &=& X_j(Y_j - bZ_j) - (Y_j - G) + V_j \\
\dot{Z}_j &=& X_j(bY_j + Z_j) - Z_j + W_j
\end{array}
\right\} \text{ for } j = \{1, 2, \cdots, 7\},
\tag{6.24}
$$

in which the coupling variables are

$$
\left.
\begin{array}{rcl}
U_{2j} &=& -cY_j \\
U_{2j+1} &=& -cZ_j \\
V_j &=& c(X_{2j} - 1) \\
W_j &=& c(X_{2j+1} - 1)
\end{array}
\right\} \text{ for } j = \{1, 2, 3\},
\tag{6.25}
$$

and the parameters are set to $a = 0.25$, $b = 4$, $F = 8$ and $G = 1$. We allow the coupling strength, c, to vary.

Poincaré sections for three different values of c are shown in figure 6.8. For small coupling, the section looks similar to the uncoupled case. But as the coupling strength increases, the section becomes less reminiscent of a low-order dynamical system; the appearance becomes
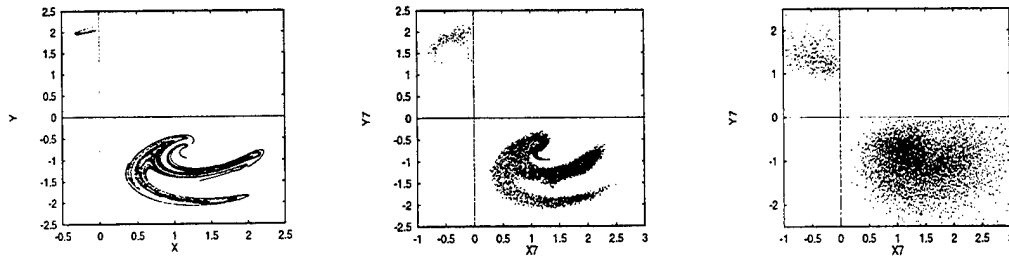
84

Figure 6.8: Poincaré maps in an X, Y plane for one member of the networked Lorenz systems of Fig. 6.7 and Eqs. (6.24) and (6.25). An isolated system ($c = 0$) is depicted in the left panel. In the middle panel, the systems are weakly coupled ($c = 0.1$). The right panel shows a map for strongly coupled systems ($c = 1.0$). Adapted from von Hardenberg (1996; *Thesis of Laurea*).

"noisier". This is presumably reflecting the fact that as we increase the coupling, the signal from each element becomes more characteristic of the entire system rather than an individual member. However, for low coupling strength, the signal from one of the subsystems has a strong, low-dimensional character and is relatively weakly influenced by the remainder of the high-dimensional network. This feature of the signal spells disaster for standard dimensional reconstruction techniques as we now illustrate.

The correlation dimension D_2 of one Lorenz '84 subsystem with these parameters values is estimated to be $D_2 \approx 2.19$. However, the coupled system has a dimensionality of something more like 15. We attempt to estimate this high dimensionality by taking the output from the seventh subsystem, $Z_7(t)$, as shown in figure 6.7. This signal provides synthetic data to test the reconstruction.

The standard time-embedding techniques using the time series of Z_7 lead to estimates of the correlation dimension as a function of the embedding dimension as shown in figure 6.9. This correlation dimension displays a slow convergence with embedding dimension and may seem to indicate rather lower values of D_2, especially for low coupling strengths ($D_2 \approx 5$ is suggested for $c = 0.1$); this is the effect of the superficial, low-dimensional character of the time series. This character masks the "jitter" due to the coupled network and hides the true dimensionality. The jitter actually leads to the very slow rise of D_2 beyond the initial levelling off. The correct conclusion to draw from figure 6.9 is that the computation simply does not converge.

This result implies that standard dimensional estimates may be misleading if the system in question is weakly coupled to other nonlinear systems. More specifically, one should exercise some care in interpreting the plots of D_2; the apparent convergence at low values is totally false, and the method simply fails to give an answer.

If we construct a signal using the output from more than one subsystem, the standard
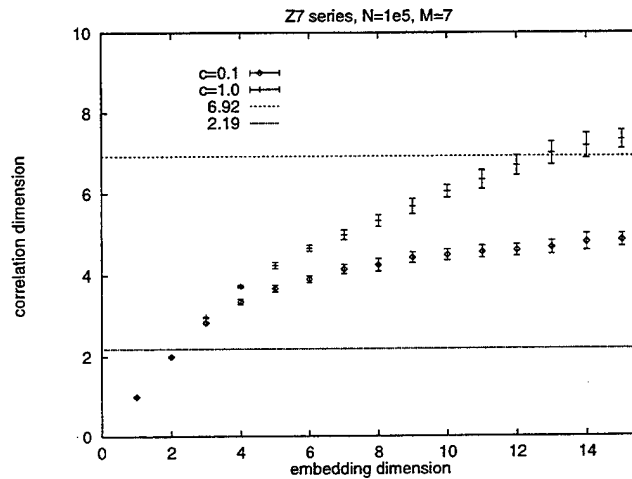
85

Figure 6.9: Correlation dimension estimates versus embedding dimension for the system (6.24),(6.25) with three values of the coupling coefficient c. The time delay is 0.025. Adapted from von Hardenberg (1996; *Thesis of Laurea*).

reconstruction techniques fare better. For example, if we use the signal $\sum_{l=1}^{7} Z_l(t)$ (*cf.* Lorenz, 1991), the estimated correlation dimension clearly shows no convergence as a function of embedding dimension over the range shown in figure 6.9. Hence, given more information about the network, it seems likely that we will not be deceived into hypothesizing the existence of low-dimensionality.

However, there is a serious problem in taking the reconstruction any further. Basically, the coupled system has so large a dimension that the time series that is actually needed to estimate D_2 is prohibitively long for any application or reasonable computation (as mentioned in lecture 3, we estimate that the length of time series needed for the current example is 2.5×10^{13} if the measurements are spaced apart by time intervals of 0.025, the delay used for the embedding in figure 6.9).

All this raises the question of how useful reconstruction really is. Clearly, for a complicated (possibly coupled) system, it is simply useless and prone to lead to spurious results. Some other method for exploring the underlying dynamics is evidently necessary.

Despite this failure, the structure of figure 6.9, with its two characteristic slopes separated by a "knee" is intriguing, and possibly conveys some information. Perhaps, as speculated by Lorenz, the shape can be used to measure some property of the inividual subsystem. But exactly what is not clear. Some systems consisting of many elements do show what one could describe as "extensive" properties: statistical measures such as correlation dimension scale approximately linearly with system size, suggesting that each subsystem can be described by a characteristic dimension. Perhaps this characteristic dimension can be extracted from figure 6.9 in some fashion.

6.2.1 Filtering a fast subsystem

Given the failure of reconstruction to estimate the correlation dimension, we consider it a bleak possibility that we might ever rebuild the structure of a complex system from a limited sampling of its dynamics. This calls for a change of perspective. The one we adopt is suggested by the arguments mentioned above, namely that in "extensive" systems, the subsystems are characterized by certain properties: Even though we cannot reconstruct the entire system, can we ignore most of its complicated components and instead determine the dynamics of a single subsystem?

This alternative approach has the advantage that, if successful, we can then "filter" out the most complicated ingredients of the problem (that we might never understand anyway), and focus on the pieces that might elementally control the phenomenon in question. Indeed, a frequently encountered feature of natural systems is variability on multiple timescales, with the fastest timescales corresponding to turbulence. Yet we commonly believe that it is the slower (or longer) scales that describe the essential features of many geophysical and astrophysical phenomena, with turbulence playing a more minor role (such as providing the source of damping via energy cascade to the dissipation scale). Can we isolate these slower scales and understand them independently of the turbulence?

A partial answer to this question comes from looking at a simple system consisting of two coupled elements with different timescales. In particular, by using tools such as the "finite-size" Lyapunov exponent, we can estimate some properties of the slow subsystem even if the faster subsystem is not resolved or stochastic (Boffetta *et al.* 1998).

Finite-Size Lyapunov Exponents (FSLE)

We define the finite-size Lyapunov exponent (Aurell *et al.* 1996) in terms of the growth of a finite error in a trajectory lying on the attractor of the system. Let $T_r(\delta)$ denote the time taken for an error with initial size δ to grow to a size $r\delta$. For example, $T_2(\delta)$ is the "error-doubling time" if we start with error δ. Then, the FSLE is given as

$$\lambda(\delta) = \frac{1}{\langle T_r(\delta) \rangle} \ln r, \tag{6.26}$$

where the angular brackets denote an ensemble average over many realizations.

Evidently, when $\delta \to 0$ and the initial error becomes infinitesimal, $\lambda(\delta) \to \lambda_{max}$, the leading, conventional Lyapuonv exponent. But as δ becomes large, the error becomes comparable to the size of the attractor itself. At this stage, the error can no longer continue to amplify exponentially; it becomes constrained by the attractor's geometry. Thus we expect the finite-size Lyapunov exponent to behave in the manner illustrated in figure 6.2.1.

In practice, the exponent is computed by taking two systems that in phase space are initially δ apart, and evolving them foward in time until the difference between them exceeds $r\delta$. This introduces a further technicality concerning the *direction* of the initial error, and not just its size, δ. If we begin from some arbitrary finite error in the initial point in phase space, then there is also an immediate convergence to the attractor. But the finite-size Lyapunov exponent is a measure of error growth on the attractor itself, and so the initial relaxation
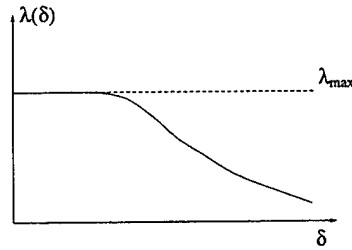
Figure 6.10: The FSLE as a function of δ

should be filtered out somehow. This amounts to taking the initial error to be aligned with the most unstable direction. Practically, we begin the computation of the two orbits from an error of size $\delta_{min} \ll \delta$, and then begin the construction of $\lambda(\delta)$ once the error amplifies through δ. Provided the relaxation to the attractor is sufficiently rapid, δ is then aligned as required.

Coupled maps

We illustrate the finite-size Lyapunov exponents using a pair of coupled maps:

$$x_s(n+1) = (1 - \epsilon)f_s(x_s) + \epsilon g[x_s, x_f] \mod 1 \qquad (6.27)$$
$$x_f(n+1) = (1 - \epsilon)f_f(x_f) + \epsilon g[x_s, x_f] \mod 1 \qquad (6.28)$$
$$f_s = e^{\lambda_s} x_s \mod 1$$
$$f_f = e^{\lambda_f} x_f \mod 1$$
$$g = \cos[2\pi(x_s + x_f)]. \qquad (6.29)$$

Two sample orbits to this system, starting from nearby initial conditions, are shown in figure 6.11.

We compute two trajectories for these maps from an initial condition of $\delta(1) = \delta_{min} = 10^{-9}$. This generates a sequences of growing errors, $\delta(1) \to \delta(2) \to \delta(3)...$, from which locate values of δ and $r\delta$, then read off their integral temporal separation. The ensemble average of repeated computations of this kind then provides the data needed to compute $\lambda(\delta)$. An example of $\lambda(\delta)$ is shown in figure 6.12.

For small δ, the exponent falls close to the Lyapunov exponent of the fast subsystem, λ_f. Evidently, the doubling of a small error is controlled by the fast subsystem. However, for larger errors, the exponent converges to values nearer the Lyapunov exponent of the slow subsystem, λ_s. This reflects the dominance of the slow dynamics in controlling the larger error growth. There is a natural explanation of this effect: as δ grows from the original, initial error, δ_{min}, the slow subsystem barely evolves over the periods over which small errors amplify. Hence the error grows mainly due to the effect of the chaotic dynamics of the fast subsystem. Eventually, however, the error in the fast subsystem reaches a maximum due to geometrical constraints. At this stage, the growth of the error becomes dominated by the slower growth of the other subsystem.
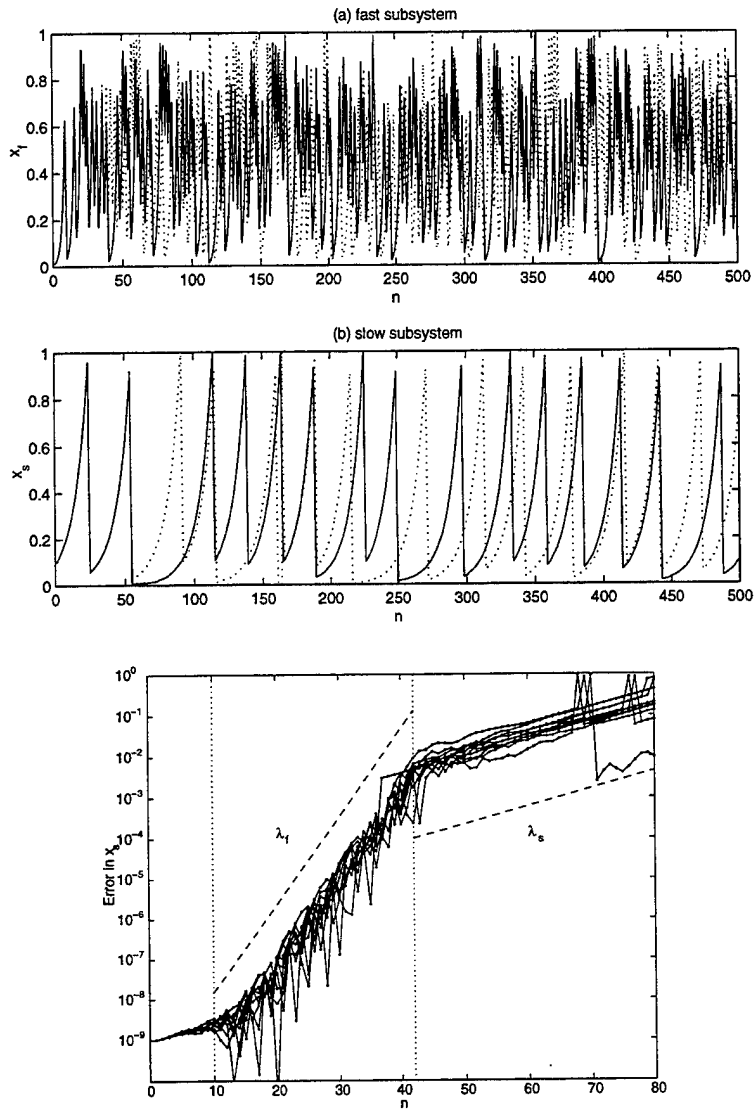
88

Figure 6.11: Time series of (a) x_f and (b) x_s for the coupled maps (6.27)-(6.29). In panel (c) we show the growth of an error of 10^{-9} for ten realizations of the system. The error growth is divided into three regimes; for $n < 10$, there is an initial relaxation onto the attractor. For $10 < n < 42$ the error grows roughly exponentially with the larger Lyapunov exponent, λ_f. Finally, for $n > 42$, the error develops according to the slow dynamics with exponent λ_s.
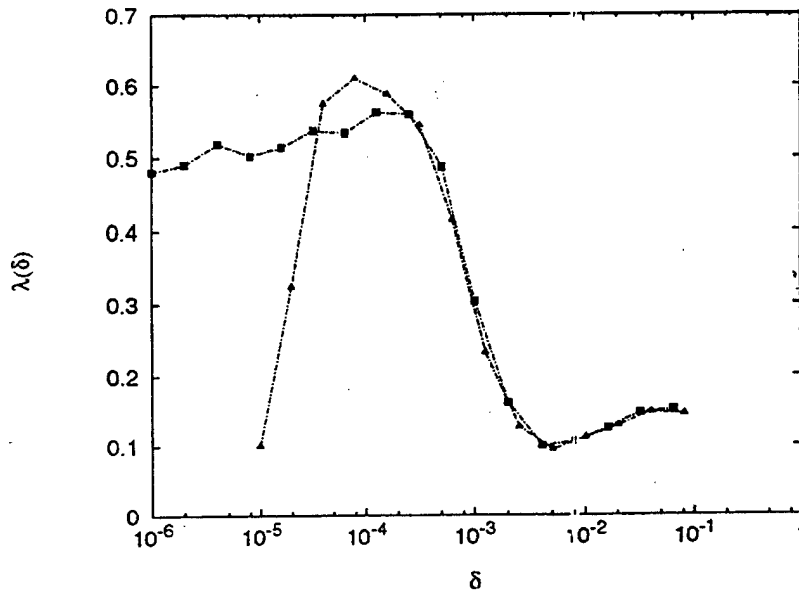
89

Figure 6.12: FSLE as a function of δ for the coupled maps (6.27)-(6.29), with $r = 2$, $\lambda_s = 0.1$ and $\lambda_f = 0.5$, and $\epsilon = 2 \times 10^{-3}$. Errors are measured in terms of the differences in x_s between two solutions, and 10^4 realizations were used to compute the ensemble average of $T_2(\delta)$. Note that the system is driven by the fast subsystem for small values of δ and by the slow subsystem for larger values. The case shown by triangles indicates the results if the initial perturbation is not aligned with the unstable direction; that is, if $\delta_1 = 10^{-5}$, the smallest value of δ for which we plot λ. (Adapted from Boffetta *et al.* 1998.)

The effect is illustrated in panel (c) of figure 6.11, which shows error development for ten realizations of the coupled system. The initial relaxation to the attractor is evident for $n < 10$. Subsequently, the error amplifies roughly exponentially, first with the Lyapunov exponent of the fast subsystem, and then with that of the slow subsystem.

Also shown in Fig. 6.12 are results computed by taking initial perturbations that were not aligned with the unstable direction. This gives a qualitatively different graph in which the convergence to λ_f at small δ is not apparent. Here, then, the relaxation from the initial condition masks the error growth due to the fast subsystem.

Nevertheless, in both cases shown in the figure, the large-error growth is dominated by the dynamics of the slow subsystem and this can be extracted easily from the results. This gives us hope that we can, with suitable technology, filter the fast subsystem, and measure quantities such as λ_s directly. However, from an experimental perspective, the extraction of information pertaining to the fast subsystem is probably impossible: it is unlikely that under experimental conditions we can resolve the growth of a small error, even if we could unmask the small$-\delta$ behaviour of $\lambda(\delta)$ from the obscuration due to intial relaxation.

The situation becomes even worse when the fast subsystem has high dimension. We illustrate this in figure 6.13 which shows the results for $\lambda(\delta)$ when we replace the fast subsystem in (6.28) by stochastic noise. For the stochastically forced system, the exponent rises to ever higher values as we lower δ. At larger error, however, we still observe the dominance of the slow system and can again measure λ_s.

Computing the FSLE from a Time Series

Experimentally, we do not have access to the equations or solutions from controlled initial conditions. Instead, we must measure some characteristic quantity and build a phase space through an embedding procedure. Then we can attempt to construct finite-size Lyapunov exponents by finding segments of the time series in which the system passes through the same neighbourhood of phase space. That is, we locate two portions of the trajectory that fall close to each other. These segments are analogous to solutions with close-by initial conditions, and we may then define error growth from the differences in the subsequent evolution.

By way of illustration, consider the coupled Lorenz equations,

$$\dot{x}_s = -\sigma(x_s - y_s) \tag{6.30}$$

$$\dot{y}_s = -x_s y_s + (r + \epsilon z_f) x_s - y_s \tag{6.31}$$

$$\dot{z}_s = x_s y_s - b z_s \tag{6.32}$$

and

$$\dot{x}_f = -a\sigma(x_f - y_f) \tag{6.33}$$

$$\dot{y}_f = a(-x_f y_f + r x_f - y_f) \tag{6.34}$$

$$\dot{z}_f = a(x_f y_f - b z_f). \tag{6.35}$$

Thus the fast subsystem acts to perturb the Rayleigh number of the slow subsystem, much as one might envision experimental noise or small-scale turbulence.
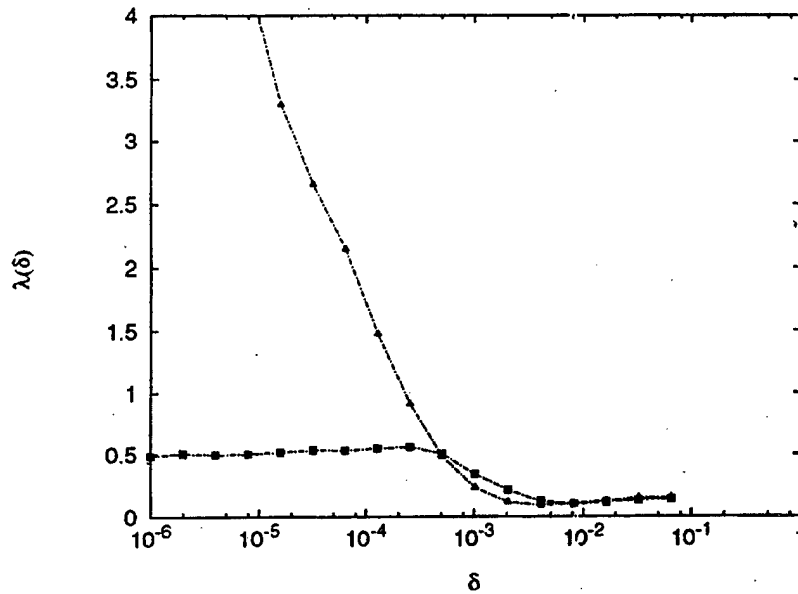
91

Figure 6.13: Finite-size Lyapunov exponents for the map (6.27) with x_f a random variable uniformly distributed in [0,1] (shown by filled triangles). Again, $r = 2$, $\lambda_s = 0.1$, and $\epsilon = 2 \times 10^{-3}$. Errors are measured in terms of the differences in x_s between two solutions, and 10^4 realizations were used to compute the ensemble average of $T_2(\delta)$. For comparison, the filled squares show the computation for the deterministic version of the system. (Adapted from Boffetta *et al.* 1998.)
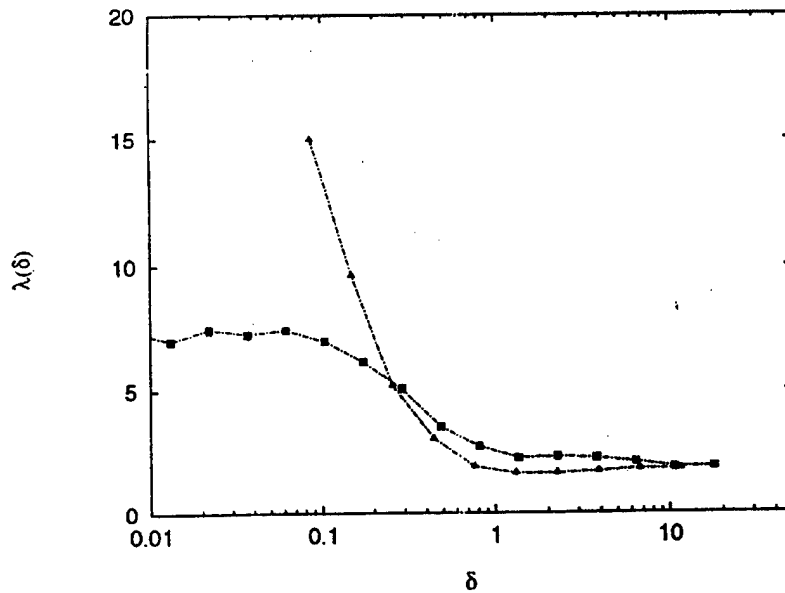
Figure 6.14: The FSLE as a function of δ obtained from the time series for the coupled Lorenz system with $\epsilon = 0.05$, $r = 45.92$, $\sigma = 16$ and $b = 4$. The parameter $a = 5$ and so $\lambda_s \approx 1.5$ and $\lambda_f = 5\lambda_s \approx 7.5$. The filled triangles show results for a three dimensional embedding with time delay of 0.02 and 5×10^5 points. The filled squares show the result from directly computing the exponent from initial-value solutions to the equations. (Adapted from Boffetta et al. 1998.)

The factor of a on the right-hand side of (6.33)-(6.35) can be removed on rescaling time in those equations, in which case we recover the Lorenz model for the fast subsytem. Thus, given the Lyapunov exponent of the Lorenz model, λ_s (which is also the exponent for the uncoupled slow subsystem), we can immediately read off the fast subsystem's exponent: $\lambda_f = a\lambda_s$.

We now evolve the system and generate synthetic data from the output of the slow sub-system. With the usual embedding procedures and the identification of segments of the time series that can be used to monitor error growth, we compute the finite-size Lyapunov exponents shown in figure 6.14. Also shown is the exponent computed directly from solutions to the equations.

Because the experimental procedure necessarily involves an embedding, the results for $\lambda(\delta)$ depend on the dimension of the embedding space, M. Importantly, as shown in figure 6.14, we appear to be able to resolve the convergence to λ_s once the embedding dimension exceeds that of the slow subsystem. From a practical perspective, this suggests that the procedure is useful.

There is also some suggestion that $\lambda(\delta)$ converges to λ_f at small δ, when the embedding space is as large as that of the full system (in figure 6.14, the emdebbing space is too small to observe convergence at small δ). But this again is obscured by our inability to aligne δ

with the direction of maximum error growth. And if the fast system is of high dimension, it is unlikely that time series will ever be of sufficient length to achieve this convergence. Hence this facet of the construction is not that useful.

6.3 Prediction and the utility of FSLEs

If we knew all of the properties of a system at a particular instant, then we could, in principle, evolve the system forwards in time and determine its state at any future moment. Practically, however, we do not know every detail of a system and our computations are imprecise. This means that there is always an uncertainty in the initial position of our system, be it either from our ignorance or our impecision. This uncertainty constitutes an error in following the system that amplifies and eventually wrecks our prediction of the future state. In other words, predictability is determined by the initial uncertainty and how this error grows.

For chaotic systems, we measure predictability in terms of a "prediction time", $t_\sigma(\delta)$, that depends on the initial error, δ, and a tolerance, σ, that we allow in the observations. From our definition (6.26), we estimate

$$t_\sigma = \frac{1}{\lambda(\delta)} \ln \frac{\sigma}{\delta}, \qquad (6.36)$$

with $r = \sigma/\delta$. Therefore, the finite-size Lyapunov exponents can be interpreted alternatively as giving the prediction time.

Previously, some studies used the leading, conventional Lyapunov exponent in place of $\lambda(\delta)$ in the estimate of the prediction time in (6.36). However, the usual Lyapunov exponent measures the growth rate of an error averaged over all time, or equivalently over the whole of the attractor. But the development of an error varies significantly over the attractor and therefore at different instants in time (in fact, errors can still magnify even for systems with negative Lyapunov exponents). Consequently, the conventional Lyapunov exponent is not always very useful in estimating the predictability time; it is more naturally determines by the finite-size exponents.

These remarks were essentially made by Lorenz (1996) in the context of predictability of

atmospheric motions. Lorenz used the model equations,

$$\frac{dX_k}{dt} = -X_{k-1}\left(X_{k-2} - X_{k+1}\right) - X_k - \frac{hc}{b}\sum_{j=1}^{J} Y_{j,k} \tag{6.37}$$

$$\frac{dY_{j,k}}{dt} = -cbY_{j+1,k}\left(Y_{j+2,k} - Y_{j+1,k}\right) - cY_{j,k} + \frac{hc}{b}X_k \tag{6.38}$$

with

$$
\begin{aligned}
k &= 1,\dots,K \\
j &= 1,\dots,J \\
X_{k-K} &= x_{k+K} = X_k \\
Y_{j-J,k} &= Y_{j,k-1} \\
Y_{j+J,k} &= Y_{j,k+1},
\end{aligned}
$$

where h, c and b are all parameters. Rough meaning is given to the variables in these equations by identifying the index k as referring to a set of longitudinal sectors at a given latitude, and j as reflecting a finer subdivision of each sector. Thus, the quantities X_k refer to some slowly varying atmospheric quantity, whilst the variables $Y_{j,k}$ represent some small-scale fields.

The growth of errors in the system (6.37)-(6.38) follows a pattern much like the coupled maps or Lorenz systems used above: the growth of a small error is dominated by the fast dynamics of the small-scale subsystems; larger error development is controlled by the large-scale subsystems.

Lorenz likened the dynamics of this coupled system to more complicated models of atmospheric phenomena such as the El Nino Soutern Oscillation (ENSO). The role of the slow system is played by the upper layer of the ocean, as X_k models sea-surface temperature; this responds rather slowly to atmospheric forcing due to the ocean's high heat capacity. But the atmospheric weather systems that migrate overhead, and which constitute the other part of the coupled climate system, vary much more quickly and on shorter scales; these are the fast subsystems.

The important feature of the coupled system is that the large-error growth, being dominated by slow dynamics, is relatively mild. Thus, although the prediction time of the atmospheric systems may be very short, there is some hope for predictability of the slower subsystems. ENSO itself is often characterized by sea surface temperatures, and models that attempt to predict the onset of these events exploit that data. Thus part of the success of those models may hinge on the predictability of the slow scales. Essentially, what may happen is that the atmospheric weather patterns are filtered out; they influence the dynamics of the large scales only through a weakly coupled, random forcing.

Lecture 7

Coherent Structures

Until now, we have discussed aspects of the dynamics of low-dimensional deterministic systems, extending our understanding to coupled and forced models. Chaotic behavior, unpredictability and bifurcations have been some of our companions in the journey.

Another crucial issue in nonlinear dynamics, that has been discarded until now, concerns the formation of "order," or of "structures," from the disordered background filling the universe. Why individual, ordered structures exist, is not a trivial question. It is so nontrivial, that nobody really knows the answer. Although some people - from time to time - have claimed to have discovered the deep truth underlying the formation of coherent patterns, no fully satisfactory answer to this question is available. For example, it is not even clear whether there are a few universal mechanisms of pattern formation, that are active in different systems. Or whether every specific case is different from any other, and each mechanism has its individuality and does not play any role in other context. Nonetheless, the issue of pattern formation is perhaps one of the deepest, and the one that touches us most directly in all science. After all, we are coherent patterns ourselves (at least sometimes), possessing the curious attitude to order our perceptions of the world around us, and to try to order and control the world itself...

7.1 Types of coherent structures

In nature, there are several different types of coherent patterns. For example, mechanisms of pattern formation are present in many reaction-diffusion systems (see the lecture notes by Fauve in a previous GFD volume for a thorough discussion of this issue).

Here, we are concerned with simple coherent structures that are present in fluid systems, such as rapidly rotating fluids and magnetofluids. In this context, a coherent structure is a localized, individual fluid state that persists for times much longer than a local dynamical time (to be properly defined). Often, these coherent structures are associated with the presence of an external ordering field, that makes the system anisotropic and induces an inverse cascade (from small to large scales) of some relevant dynamical quantities. The structures that form are often stationary solutions of the equations governing the system dynamics, and they usually live as localized entities emerging from a turbulent background.

Some examples of such coherent structures are:

- Localized nonlinear waves (e.g. solitons) arising from equations like the Korteweg-de-Vries equation, $\eta_t + c\eta_x + a\eta\eta_x + b\eta_{xxx} = 0$, or the sine-Gordon equation, $\phi_{tt} - c\phi_{xx} = a\sin\phi$. Here, subscripts indicate partial derivatives.

- Coherent jets, that are formed either as free fluid streams (e.g., the jet stream in the high atmosphere), or as boundary currents due to the presence of differential rotation and rigid boundaries (e.g., the Gulf Stream).

- Coherent vortices, which form spontaneously in rotating turbulent flows, and contain most of the energy and circulation of the system.

- Coherent flux tubes, which emerge as coherent concentrations of current in anisotropic magnetohydrodynamical flows.

This lecture and the following one are devoted to the discussion of coherent vortices and flux tubes. Coherent vortices are spectacular entities whose presence is revealed in any turbulent fluid flow that is subject to strong rotation, or in any conducting fluid immersed in an external magnetic field. Geophysical and astrophysical examples of energetic coherent vortices include the Great Red Spot on Jupiter, and similar spots on other giant gaseous planets; Gulf Stream rings arising from meandering instabilities of that jet; Meddies, mesoscale Mediterranean eddies generated by the instability of the salty outflow from the Mediterranean Sea into the Atlantic Ocean; atmospheric blocking, a big coherent vortex bound to the topography; mid-latitude atmospheric cyclones; the winter stratospheric polar vortex; "plasmoids" generated in the magnetopause of the Earth; galaxies in the intergalactic turbulence and star systems in interstellar space; starspots, coherent magnetic flux tubes whose best-known example is provided by Sunspots; and, possibly, coherent vortices on accretion disks.

7.2 The quasi-geostrophic approximation

To be specific, and stay simple, we study the dynamics of coherent vortices in the framework of the quasi-geostrophic (QG) approximation for a barotropic fluid. This approximation provides a simplified description of large scale oceanic flows and of shallow-layer atmospheric motions, provided nonadiabatic effects and baroclinicity can be neglected.

To derive the barotropic QG approximation, we first discuss the standard shallow-water system (for a thorough derivation see Pedlosky 1987). Call H the average vertical extent of the fluid layer, and L a typical horizontal scale of motion. For large-scale geophysical flows, H is usually much smaller than L, as the thickness of the dynamically active fluid layer is at most a few kilometers while the horizontal size of motion may reach hundreds or thousands of kilometers. In fact, we can define "large-scale" flows as those for which $\delta = H/L \ll 1$.

In the limit of $\delta \to 0$, for a layer of constant density ρ, the *shallow-water approximation* can be introduced. This approximation assumes hydrostatic support in the vertical direction

and then explicitly factors out the dependence on z. The equations of motion then become

$$\frac{\partial u}{\partial t} + u\frac{\partial u}{\partial x} + v\frac{\partial u}{\partial y} - fv = -g\frac{\partial \eta}{\partial x}, \tag{7.1}$$

$$\frac{\partial v}{\partial t} + u\frac{\partial v}{\partial x} + v\frac{\partial v}{\partial y} + fu = -g\frac{\partial \eta}{\partial y}, \tag{7.2}$$

$$p = \rho g(h - z) + p_0 \tag{7.3}$$

and

$$w = (h_0 - z)\left(\frac{\partial u}{\partial x} + \frac{\partial v}{\partial y}\right) + u\frac{\partial h_0}{\partial x} + v\frac{\partial h_0}{\partial y}, \tag{7.4}$$

where $\mathbf{v} = (u, v, w)$ is velocity, p is pressure, g is the acceleration of gravity, and f is the Coriolis parameter. Also, $\eta(x, y, t)$ is the free surface, and $h_0(x, y)$ describes the topography of the bottom.

The shallow-water potential vorticity is defined as

$$q_{sw} = \frac{\omega + f}{h}, \tag{7.5}$$

where $\omega = v_x - u_y$ is the relative vorticity, and $h = H + \eta - h_0$ is the total layer depth. The potential vorticity q_{sw} is conserved in the absence of forcing and dissipation:

$$\frac{D}{Dt}\left(\frac{\omega + f}{h}\right) = 0, \tag{7.6}$$

where D/Dt is the material (Lagrangian) derivative.

In the limit of strong rotation, circulations at the Coriolis frequency are faster than any other motions in the system and $f \ll U/L$. Hence the Rossby number $\epsilon = U/fL \ll 1$ (U being a velocity scale). The shallow water equations can then be expanded in powers of ϵ. This produces the quasi-geostrophic approximation and corresponds to filtering the fast modes of the system (gravity waves).

We expand the shallow-water expression for potential vorticity and keep only terms of $O(\epsilon)$:

$$q' = \omega' - \frac{\eta'}{R^2} + h_0', \tag{7.7}$$

where the primed variables are dimensionless (e.g., $\omega = U\omega'/L$). Here $R^2 = (L_R/L)^2$, where $L_R = \sqrt{gH}/f$ is the barotropic Rossby radius of deformation. Furthermore, we assumed $h_0' = h_0/H$ to be of the order of the Rossby number.

To a similar order of approximation, the expression for D/Dt becomes $D/Dt = \partial/\partial t + \mathbf{u} \cdot \nabla$ where $\mathbf{u}$ is the shallow-water geostrophic velocity, and is given by $\mathbf{u} = (-\partial\psi/\partial y, \partial\psi/\partial x)$. The geostrophic stream-function ψ is related to the free-surface elevation η by

$$\psi = \frac{\eta g}{f}, \tag{7.8}$$

which in dimensionless form becomes $\psi' = \eta'$. Hence, the potential vorticity q' can be expressed as

$$q' = \nabla^2\psi' - \frac{\psi'}{R^2} + h_0'. \tag{7.9}$$

Then conservation of potential vorticity in the (barotropic) QG approximation can be stated as:

$$\frac{\partial q'}{\partial t} + [\psi', q'] = 0 \tag{7.10}$$

where $[A, B]$ is the Jacobian operator $A_x B_y - A_y B_x$.

In the above discussion, we have considered the Coriolis parameter f to be constant. But this frequency actually varies with latitude. On a spherical planet, the local value of the Coriolis parameter is $f = 2\Omega \sin\phi$ where Ω is the rotation rate of the system and ϕ is the local latitude. If we consider motions which do not extend over a broad range of latitudes, then it is justified to take a reference value for ϕ (say, ϕ_0) and to take $f = f_0 = 2\Omega \sin\phi_0$ as a constant. For motions with large scale meridional extent, however, the variation of the Coriolis parameter with latitude can no longer be discarded. The first order approximation used to correct for this effect is the so-called "beta-plane" approximation. By Taylor-expanding f and keeping only the first order term, one obtains

$$f = 2\Omega \sin\phi_0 + 2\Omega \cos\phi_0(\phi - \phi_0) = f_0 + \beta y \tag{7.11}$$

with $\beta = 2\Omega \cos\phi_0/R_e$ and $y = R_e(\phi - \phi_0)$. Here R_e is the radius of the Earth.

In the quasi-geostrophic approximation it is assumed that $\beta \ll f_0/L$. More specifically, the dimensionless β parameter, defined as $\beta' = \beta L^2/U$, is assumed to be of the order of the Rossby number. One can then rewrite the potential vorticity as $q' = \nabla^2\psi' - \psi'/R^2 + \beta'y + h_0'$. The conservation of potential vorticity reads (for convenience, from now on we skip the primes)

$$\frac{\partial}{\partial t}\left(\nabla^2\psi - \frac{\psi}{R^2}\right) + [\psi, \nabla^2\psi + h_0] + \beta\frac{\partial\psi}{\partial x} = 0. \tag{7.12}$$

If there is neither topography ($h_0 = 0$), beta-effect ($\beta = 0$, also called the f-plane), nor free surface ($L << L_R$, i.e. $\frac{1}{R^2} \to 0$) the QG equation reduces to the two-dimensional Euler equation,

$$\frac{\partial}{\partial t}\nabla^2\psi + [\psi, \nabla^2\psi] = 0. \tag{7.13}$$

We organize our discussion of coherent structures by first considering the dynamics of turbulence in the dissipative version of the two-dimensional Euler equation. Then we continue on to describe the modifications introduced when we deal with the added ingredients in the QG approximation. The discussion spans two lectures.

7.3 2D Turbulence

The two-dimensional Euler equations admit an infinite number of conserved quantities. Two quadratic invariants that are of particular importance are the kinetic energy,

$$E = 1/2 \int (\nabla \psi)^2 dx dy, \qquad (7.14)$$

and the enstrophy,

$$Z = 1/2 \int (\nabla^2 \psi)^2 dx dy . \qquad (7.15)$$

The Euler equations are non-dissipative (i.e., conservative). In most systems, however, dissipation is present, and to be consistent with a dissipative world we have to include this physics in the QG approximation. The standard form is a Newtonian dissipation term, $D_N = \nu \nabla^2 \omega$, that is added to the right-hand-side of the Euler equation. Alternatively, Rayleigh friction takes the form $D_R = -K\omega$ (this represents, for example, bottom friction). *Hyperviscosity* provides a general expression for dissipation, $D_s = (-1)^{s-1}\nu_s \nabla^{2s}\omega$, and includes both the standard Newtonian case ($s = 1$) and Rayleigh friction ($s = 0$). In numerical simulations, a hyperviscous dissipation with $s > 1$ is often used. This approach, although artificial, attempts to confine the effects of dissipation to very small scales, and so allows us to reach higher values of the (equivalent) Reynolds number.

The equations for freely-decaying (i.e., dissipated but not forced) 2D turbulence then read

$$\frac{\partial}{\partial t}\nabla^2 \psi + [\psi, \nabla^2 \psi] = (-1)^{s-1}\nu_s \nabla^{2s}\nabla^2 \psi. \qquad (7.16)$$

For this version of the problem, energy and enstrophy are are no longer exactly conserved, but they are almost so for sufficiently small viscosity. (In fact, one may show that the energy dissipation vanishes in the limit for $\nu \to 0$; for this reason, energy is sometimes called a "rugged invariant" of the system.)

The approximate conservation of energy and enstrophy in two-dimensional, nearly inviscid systems has some important consequences, which are best appreciated in the comparison with 3D turbulence.

In nearly inviscid three-dimensional turbulence, energy is the only approximate invariant, which we may write as

$$E = \int \mathcal{E}(k)dk, \qquad (7.17)$$

where $\mathcal{E}(k)$ is the spectral energy density. The image of 3D turbulence is then associated with the celebrated "cascade" of energy to small length scales; energy injected into the system at long wavelengths becomes channeled down to small wavelengths by nonlinear interactions. Thus, the large "energy-bearing eddies" feed motions of increasing fine scale until energy is ultimately dissipated on the "dissipation scale". The range of motion between these two limits
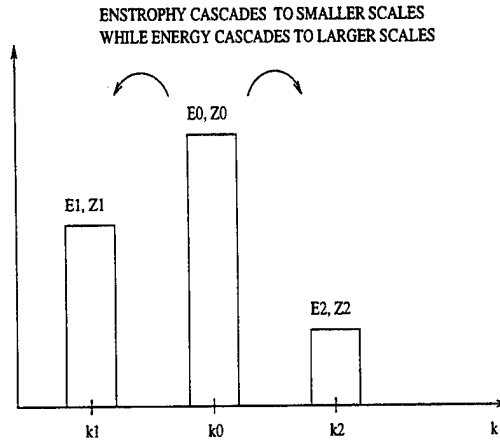
100

Figure 7.1: Energy and Enstrophy Cascades in 2D Turbulence

is the "inertial range". For isotropic turbulence, one finds that $\mathcal{E} \sim k^{-5/3}$ in the *Kolmogorov scaling* suitable for the inertial range.

In two dimensions, on the other hand, enstrophy is also approximately conserved, and it may be written as

$$Z = \int \mathcal{Z}(k)dk = \int k^2 \mathcal{E}(k)dk. \tag{7.18}$$

Now, consider a fluid element of scale k_0 transfering energy and enstrophy into the scales k_1 and k_2 (see figure 7.1). Energy and enstrophy conservation require that

$$\mathcal{E}(k_0) = \mathcal{E}(k_1) + \mathcal{E}(k_2) \qquad \text{and} \qquad k_0^2\mathcal{E}(k_0) = k_1^2\mathcal{E}(k_1) + k_2^2\mathcal{E}(k_2). \tag{7.19}$$

Thus

$$\mathcal{E}(k_1) = \frac{k_2^2 - k_0^2}{k_0^2 - k_1^2}\mathcal{E}(k_2). \tag{7.20}$$

For example, if $k_1 = k_0/2$ and $k_2 = 2k_0$, then we observe that $\mathcal{E}(k_1) = 4\mathcal{E}(k_2)$. In other words, more energy is transfered to larger scales than to smaller ones. But similar arguments indicate that $\mathcal{Z}_1 \equiv k_1^2\mathcal{E}(k_1) = k_2^2\mathcal{E}(k_2)/4 = \mathcal{Z}_2/4$, and so enstrophy is channeled primarily in the opposite direction.

Thus, the simultaneous conservation of energy and enstrophy induces a "direct" cascade (i.e., from large to small scales) of enstrophy and an "inverse" cascade (from small to large scales) of kinetic energy (see e.g. Kraichnan & Montgomery 1980). This suggests that in a two-dimensional fluid (or, a fluid which is subject to strong rotation), larger and larger structure

101

forms, in association with the flow of energy to small wavenumbers. Indeed, numerical simulation and laboratory experiments have revealed the formation of strong, long-lived vortices that contain most of the energy and the enstrophy of the system and live much longer than typical circulation times (defined, for example, as the typical rotation time of a particle inside a vortex). The qualitative appearance of 2D turbulence is thus a random, low-energy background turbulent field intermittently punctuated by strong individual vortices (McWilliams 1984 and 1990).

Simulation and experiments have also offered us a picture of the typical evolution of freely-decaying 2D turbulence. Beginning from a random vorticity field (with energy localized over a narrow band in wavenumber) there is a brief phase of strong energy dissipation, followed by a period of vortex generation, during which small vortices are generated by the inverse cascade. After the first burst of vortex formation, the dynamics becomes characterized by vortex-vortex interactions. Three significant types of interaction occur: long-range interactions between well-separated, isolated vortices (that can be approximately modelled by systems of point vortices), temporary dipolar pairing between neighbouring vortices of opposite sign, and strong inelastic interactions between closely spaced vortices of the same sign. The inelastic interaction between vortices of similar sign frequently leads to vortex mergers. Consequently, the number of vortices decreases and their typical sizes increase. This generates a vortex population with a broad distribution of size and circulation. At very late times, for systems with zero average vorticity in periodic or bounded domains, the inverse energy cascade and mergers ultimately result in a single vortex dipole with the largest spatial scale allowed. This dipole is usually characterized by a very small "nonlinearity", $[\psi, \nabla^2 \psi] \approx 0$, and it decays slowly due to dissipation.

Figure 7.2 shows the vorticity field in a representative numerical simulation of freely-decaying 2D turbulence. The vorticity is shown at intermediate times when many vortices are still present.

7.4 Properties of individual vortices

Broadly speaking, a coherent vortex is a region of circulating flow that keeps its identity for times much longer than the local eddy turnover time T_Z, which can be defined as $T_Z \approx Z_v^{-1/2}$ where Z_v is the local average enstrophy. Although the formation of coherent vortices has often been associated with the inverse energy cascade, there is - up to now - no fully satisfactory explanation of why coherent vortices form in rapidly rotating fluids. The formation of coherent vortices is probably the most important topic of 2D turbulence; it is reassuring that new generations of fluid mechanicians still have room to study interesting issues.

Given that we do not know why vortices form, we can nevertheless study what their properties are. But first we need a sensible definition of the vortices themselves; simply identifying persistent circulating motions as vortices is not a very precise definition.

One way of parameterizing the complex structure of 2D turbulence is based on the definition of the Okubo-Weiss parameter, Q, which measures the relative contribution of the squared strain S^2 and of the squared vorticity ω^2. More specifically, $Q = Q(x, y, t) = S^2 - \omega^2$, where $S^2 = S_n^2 + S_s^2$, $S_n = \partial_x u - \partial_y v$ and $S_s = \partial_x v + \partial_y u$; here S_n and S_s are the normal and

shear components of strain, respectively.

Regions dominated by rotation are called elliptic, and are characterized by $Q < 0$. Regions that are dominated by strain and deformation are termed hyperbolic and have $Q > 0$. The value of Q can be thought of as defining the behavior of advected particles in the *frozen* velocity field: regions with $Q > 0$ are characterized by local exponential divergence of nearby particles, while regions with $Q < 0$ are characterized by an approximately constant separation between nearby particles. Of course, this does not bear any direct information on the chaotic or regular nature of the trajectories of advected particles in the evolving field, but the idea is occasionally useful.

The relevance of the Okubo-Weiss parameter Q may be further understood by applying the divergence operator to the incompressible Navier-Stokes equation in the limit of vanishing viscosity, or for a statistically stationary situation where forcing and damping balance each other. One obtains in this case

$$\nabla^2 p = -\frac{1}{2}Q \tag{7.21}$$

where p is the pressure. This diagnostic equation is valid for all time and it provides a link between the value of Q and the local nature of the flow field.

Based on the values of Q, three main regions can be identified in 2D turbulence:

- Vortex cores, which are characterized by strong negative values of Q.

- Strain cells surrounding the vortices, which are characterized by large positive values of Q.

- The background, where Q fluctuates between small positive and negative values. Depending on the sign of Q, the background field may be further divided into non-coherent elliptic and hyperbolic patches.

The core of coherent vortices is thus characterized by the strong dominance of rotation over strain, and is is associated with a region where Q assumes strongly negative values. The edge of a coherent vortex can then be defined as the innermost contour for which $Q = 0$.

From a Lagrangian viewpoint, there is a significant difference between a vortex core and the external field. Inside vortex cores, the fluid motion is essentially laminar and particle trajectories are regular. This can be quantified by considering the relative dispersion between pairs of nearby particles, which is defined as the average, squared distance between two particles that were initially released close to one another. Inside a vortex, nearby particles display a very small relative dispersion along the radial direction (Provenzale, 1999). Along the azimuthal direction, though, the differential rotation of the vortex induces a relative dispersion that grows linearly in time. Outside vortices, on the other hand, one observes exponentially growing separations between nearby particles.

Coherent vortices in barotropic turbulence can therefore be interpreted as islands of regular Lagrangian dynamics in a chaotic background. It is interesting to note that these regular islands are not fixed in space and time; they wander chaotically through the turbulent field and have finite lifetime. The lack of chaoticity inside the vortices indicates that Lagrangian

transport is very weak there. Instead, mixing occurs on a diffusive time scale determined by the combined action of viscosity and differential rotation inside the vortex.

Another important property of coherent vortices is that their boundaries act as relatively impermeable barriers to mixing: there is almost no exchange of particles across the periphery of an isolated vortex. Thus, particles inside a coherent vortex tend to remain there for long times, and to be transported with the vortex motion.

This behavior of coherent vortices can be understood by noting that a strong vorticity gradient is present at the vortex edge. In two-dimensional turbulence, relative vorticity is a material invariant when forcing and dissipation are absent. In the presence of forcing, dissipation or weak three-dimensional effects, vorticity is not exactly conserved and fluid particles can cross contours of constant vorticity. But if the perturbing effects are weak, particles cannot significantly change their vorticity "label". Thus, regions of uniform or gently variable vorticity can be easily traversed by fluid particles, but regions of large vorticity gradient act as transport barriers.

Thus, mixing in vortices can be very slow and particles often become bound there. To some degree this remains true even during vortex interactions, because the cores of the interacting vortices can remain relatively intact during the interaction. However, mixing can be accelerated by strong vortex interactions which substantially disrupt the structure of the core. This happens, for example, in vortex mergers; when one vortex is much larger than the other it tears the weaker vortex apart into sheared filaments (see the next lecture). Any particles that were contained in the weaker vortex become thrown out into the chaotic background, or are entrained into the surviving structure.

The general picture of 2D turbulence that emerges is thus a low-energy background field, over which strong vorticity concentrations move and interact with one another. These coherent structures dominate the dynamics of the system, and undergo both long-range, elastic interactions and strongly inelastic processes such as straining and merging. These coherent vortices keep their identity for long times, and can be defined as regions of laminar motion where fluid particles are trapped, even though they are immersed in a turbulent sea of disorganized motion. The vortices themselves follow chaotic trajectories in the flow, and from time to time they release the fluid entrained in them during strong interactions.
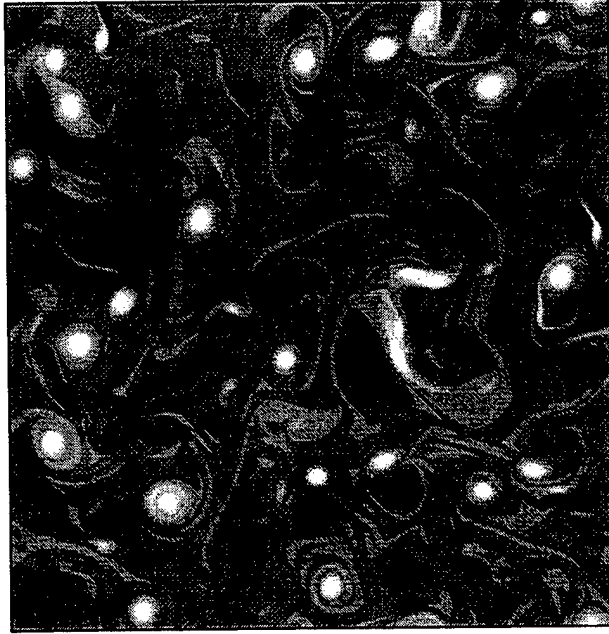
Figure 7.2: Numerical simulation of freely decaying, two-dimensional turbulence. Shown is the vorticity at time $t = 10$. The simulation began from an initially random vorticity field characterized by the energy spectrum $E(k) = E_0 k^6/(2k_0 + k)^{18}$ and random Fourier phases. Here $k_0 = 30$ and E_0 is a normalization factor which is fixed by requiring the initial average energy $E/L^2 = \frac{1}{L^2} \int E(k)dk = 0.5$. Boundary conditions are periodic, in a square box with size $L = 2\pi$. For this simulation, a pseudospectral code with standard 2/3 dealiasing and resolution 512^2 grid point has been used. The time integration is performed by a third-order Adams-Bashforth scheme and dissipation is provided by a biharmonic term $D = -\nu_2 \nabla^4 \nabla^2 \psi$ with $\nu_2 = 5 \cdot 10^{-8}$.

Lecture 8

Dynamics of Coherent Vortices

The coherent vortices that spontaneously emerge in rotating fluids do not live in isolation, as they interact both with each other and with the turbulent background that surrounds them. We now consider some of the processes that affect the life of a vortex, and explore the properties of an ensemble of vortices in 2D turbulence. A simplified, low-order model based on a point-vortex approximation will also be discussed. Then, we explore the fate of coherent vortices in baroclinic fluids on a rotating planet with a free surface, and in magnetohydrodynamics (MHD).

8.1   When vortices collide

As described in the previous lecture, the coherent vortices of 2D turbulence experience both long-range elastic interactions when they are widely separated, and strong inelastic interactions when they become close to each other. The long-term evolution of freely-decaying turbulence is largely dictated by the inelastic processes, in particular, by vortex merging.

Most of our knowledge of what happens when vortices collide comes from numerical simulation. A particularly important case is the interaction of vortices with the same sign. When such vortices come within a critical distance of each other they occasionally merge into one object, or sometimes survive as separate entities. On other occasions, a vortex becomes torn asunder by the other, and the victor entrains part of the remnants in a vortical feast. But essentially, interaction is a complicated phenomenon with intricate details and many outcomes (Dritschel 1995).

We can crudely classify interactions of this kind according to the ratio of the vortex radii, R_2/R_1, and by the initial distance that separates them, Δ. When the vortices have about the same strength, and $R_1 \approx R_2$, the interaction is largely symmetrical. Then, if their initial separation is not too large, the vortices wrap around each other to form a new entity. Simultaneously, filaments are shed from the newly created vortex that preserve its balance of angular momentum. This is "complete merger". If the initial separation is larger, however, the two vortices survive, but parts of their structure are stripped off during the interaction. These filaments can become lost in the background, or wind around the interacting vortices, adding

106

to their strength.

For larger disparities in the size of the vortices, *straining out* can occur. This means that the straining field created by the larger of the two vortices is large enough to significantly distort the structure of the weaker vortex whilst the larger vortex remains relatively undisturbed. If the initial separation is not that great, the smaller vortex is completely destroyed; for larger separations, a remnant sometimes remains intact.

In both cases, the surviving vortices can entrain the fluid stripped off their competitors. If the entrained fluid is quite large, we might call this "partial merger". Both this cannibalization and the complete mergers lead to the gradual attrition of smaller vortices in favour of larger ones. Thus, inexorably, the number of vortices decreases in time as their size increases; ultimately only a few remain, to be dissipated by viscosity and friction.

Usually, mergers occur relatively quickly, and the whole process lasts only a few eddy turnover times. However, even if a complete merger happens, the fluid particles belonging to the two individual vortices do not truly mix until much later times; the filamentation created by interaction remains distinct until the fluid eventually intermingles through viscous diffusion.

8.2 Evolution of vortex statistics

Due to the processes of merging and straining, the total number $N(t)$ of vortices present in a 2D turbulent field varies with time. In particular, due to mergers and straining out, $N(t)$ decreases. Note that it is not immediately obvious that vortex interactions should act in this way: if the vorticity filaments shed by the merging vortices were underwent a secondary instability that "wraps them up", then new vortices could be generated. In principle, there is no obvious reason why this seeding of new vortices might overwhelm the effects of mergers and straining and lead to statistics in which $N(t)$ increased with time. However, there are some crude scaling arguments, described below, that suggest otherwise, and which agree with what is seen in numerical simulation and with experiments.

First, let us assume that only the energy remains constant during a merging process. Since the domain size is constant, the number of vortices in the domain must be inversely proportional to the square of the average distance λ between two vortices. Then, by dimensional arguments, we take λ to be proportional to the product of time and a speed determined from the (constant) energy: $\lambda = t\sqrt{E}$. Consequently,

$$N(t) \propto \frac{1}{\lambda^2} \propto \frac{1}{Et^2}. \tag{8.1}$$

Thus, $N(t) \propto t^{-2}$.

However, direct numerical simulation of 2D turbulence suggest, in fact, that the number of vortices decreases much more slowly than this. Low-resolution simulations (Weiss & McWilliams 1993) indicate that the number of vortices decreases as a power law, $N(t) \propto t^{-\xi}$, with $\xi \approx 0.72$. This result can be rationalized by supposing that energy is not the only conserved quantity during a merging process. Suppose instead that the peak vorticity, ζ_{ext}, is also constant during merger. The energy per unit area is given by $\epsilon = \zeta_{ext}^2 a^2$, where a is the

107

average radius of the vortices. The total energy is then given by

$$E = N\zeta_{ext}^2 a^4. \tag{8.2}$$

Now suppose that $N(t)$ can be written in the form,

$$N(t) = l^{-2}g(t/\tau), \tag{8.3}$$

where $l = \sqrt{E}/\zeta_{ext}$ and $\tau = \zeta_{ext}^{-1}$. If the function g has power-law form, $g \propto t^{-\xi}$, then, in order to satisfy (8.2), the average vortex radius, a, and circulation, Γ, must be given by

$$a \propto t^{\xi/4} \qquad \Gamma \propto \xi_{ext}a^2 \propto t^{\xi/2}. \tag{8.4}$$

This argument does not provide the form of $N(t)$, but it does predict the time dependence of $a(t)$ and $\Gamma(t)$, given $N(t)$. Should we observe such scalings in the numerical simulation, then, presumably, the argument is self-consistent and roughly correct.

The above relationships were indeed observed from the numerical simulations at times beyond the era of vortex formation (Weiss *et al.* 1993). A repetition of the simulations at much larger Reynolds number and higher resolution has provided similar results, indicating that the scaling behavior seems to be a robust property of freely-decaying 2D turbulence (Bracco *et al.*, in preparation). It remains to identify what theoretical arguments could justify a power-law form of $N(t)$, and to understand what determines the value of the scaling exponent, ξ.

8.3 Systems of point vortices

Systems of point vortices represent an extreme form of vortex-dominated flows. Here, vorticity is concentrated in point-like singularities which move due to their mutual advection, and the fluid between the singularities is completely passive. The description of 2D turbulence in terms of point vortices can be obtained by discarding viscosity and supposing that the vorticity is concentrated in a set of singular points, ideally representing the intense coherent structures discussed above. As we indicate below, the partial differential equations describing the motion of the fluid are then replaced by ordinary differential equations determining the positions of the point vortices (see Aref (1983) for a review). Note that, in this approach, the individual vortices do not have internal degrees of freedom, and are characterized by their (constant) circulation and (evolving) position. More complex expansions, based for example on modelling each vortex as a constant elliptical patch of vorticity, have also been introduced.

Formally, point vortices are singular solutions of the two-dimensional Euler equations. In a system of N point vortices, the vorticity distribution is given by

$$\omega(\mathbf{x}) = \sum_{j=1}^{N} \Gamma_j \delta(\mathbf{x} - \mathbf{x}_j). \tag{8.5}$$

The stream function due to a point vortex centred at $\mathbf{x}_j$ with a circulation Γ_j is given by

$$\nabla^2 \psi_j = \Gamma_j \delta(\mathbf{x} - \mathbf{x}_j). \tag{8.6}$$

If $G(\mathbf{x}, \mathbf{x}_j)$ is the solution of $\nabla^2 G = \delta(\mathbf{x} - \mathbf{x}_j)$ (that is, the Green function of the Laplacian in the relevant geometry), then

$$\psi_j(\mathbf{x}) = \Gamma_j G(\mathbf{x}, \mathbf{x}_j). \tag{8.7}$$

The Eulerian velocity components at $\mathbf{x}$ due to the jth vortex are then

$$u_j(\mathbf{x}) = -\frac{\partial \psi_j}{\partial y} = -\Gamma_j \frac{\partial}{\partial y} G(\mathbf{x}, \mathbf{x}_j) \tag{8.8}$$

and

$$v_j(\mathbf{x}) = +\frac{\partial \psi_j}{\partial x} = +\Gamma_j \frac{\partial}{\partial x} G(\mathbf{x}, \mathbf{x}_j). \tag{8.9}$$

In the point-vortex approximation, each vortex moves due to the velocity field generated by the other vortices. Thus, the coordinates of the ith vortex, (x_i, y_i), evolve according to

$$\frac{dx_i}{dt} = -\sum_{j \neq i} \Gamma_j \frac{\partial G_{ij}}{\partial y_i} \tag{8.10}$$

and

$$\frac{dy_i}{dt} = +\sum_{j \neq i} \Gamma_j \frac{\partial G_{ij}}{\partial x_i}, \tag{8.11}$$

where $G_{ij} = G(\mathbf{x}_i, \mathbf{x}_j)$.

A system of point vortices is a Hamiltonian system. The Hamiltonian is given by

$$H(\mathbf{x}_i) = -\frac{1}{2} \sum_{i \neq j} \sum_{j=1}^{N} \Gamma_i \Gamma_j G(\mathbf{x}_i, \mathbf{x}_j) \tag{8.12}$$

and the evolution of (x_i, y_i) is obtained from

$$\Gamma_i \frac{dx_i}{dt} = +\frac{\partial H}{\partial y_i} \quad \text{and} \quad \Gamma_j \frac{dy_i}{dt} = -\frac{\partial H}{\partial x_i}. \tag{8.13}$$

Note that, in equation (8.13), the canonically conjugate variables are x_i and y_i. That is, the space coordinate y_i plays the role usually performed by linear momentum.

Each vortex represents a degree of freedom in the Hamiltonian system (two dimensions in phase space, in the terminology of Hamiltonian dynamics, not dissipative dynamical systems); with N vortices, there are N degrees of freedom and $2N$ dimensions in phase space. Note, also, that the form of the point-vortex Hamiltonian is quite peculiar, as there is no kinetic term and only the interaction energy (related to the distance between vortices) enters its expression.

A system of point vortices can have several invariants of the motion, other than the energy. Clearly, the total circulation $\sum_j \Gamma_j$ is constant, but this does not constitute a dynamical

invariant (circulation is automatically conserved by the point-vortex form of the vorticity). Linear momenta for point vortices are traditionally defined as

$$P = \sum_i \Gamma_i y_i \quad \text{and} \quad Q = \sum_i \Gamma_i x_i. \tag{8.14}$$

Similarly, angular momentum is defined as

$$I = \sum_i \Gamma_i (x_i^2 + y_i^2). \tag{8.15}$$

Depending on the boundary conditions used, linear and angular momenta can be invariants of the system. The existence of these conserved quantities introduces important constraints on the dynamics of point vortices. If the system has N_0 independent conserved quantities, the motion of $N \leq N_0$ vortices is regular and the maximum Lyapunov exponent in the $2N$-dimensional phase space is zero. But the motion of $N > N_0$ point vortices is in general chaotic, with a positive maximum Lyapunov exponent (see Aref, 1983).

On the infinite plane, the Green's function is

$$G(\mathbf{x}_i, \mathbf{x}_j) = \frac{1}{2\pi} \ln r_{ij}^2, \tag{8.16}$$

where

$$r_{ij}^2 = (x_i - x_j)^2 + (y_i - y_j)^2. \tag{8.17}$$

Substitution of equation (8.16) into equations (8.10) and (8.11) gives

$$\frac{dx_i}{dt} = -\sum_{j \neq i} \frac{\Gamma_j}{2\pi} \frac{y_i - y_j}{r_{ij}^2} \tag{8.18}$$

and

$$\frac{dy_i}{dt} = +\sum_{j \neq i} \frac{\Gamma_j}{2\pi} \frac{x_i - x_j}{r_{ij}^2}. \tag{8.19}$$

For this system, in the case of a non-zero total circulation, there are three independent conserved quantities, namely the energy, the angular momentum, and one component of the linear momentum. Thus, if the number of point vortices is less than or equal to three, the motion is regular; but if there are more than three vortices, chaotic motion is possible and is generally observed for generic initial conditions.

Vortices having the same sign undergo a bounded motion on the infinite plane. In this case, vortices cannot get too far or too close to each other due to the simultanous conservation of energy and angular momentum. By contrast, if vortices on the infinite plane have opposite signs, unbounded motion can occur, due to the formation of dipoles that travel off to infinity.

110

Another important case is that of periodic boundary conditions (motion on a torus). In this case, angular momentum is not conserved. For a periodic domain the Green's function is given by (Weiss & McWilliams 1991)

$$G(\mathbf{x}_i, \mathbf{x}_j) = \sum_{m=-\infty}^{\infty} \ln \left[\frac{\cosh(x_i - x_j - 2\pi m) - \cos(y_i - y_j)}{\cosh(2\pi m)} \right] - \frac{(x_i - x_j)^2}{2\pi}. \qquad (8.20)$$

The velocity of the ith vortex is then determined by substituting equation (8.20) into equations (8.10) and equation (8.11). This gives

$$\frac{dx_i}{dt} = - \sum_{j=1, j \neq i}^{N} \Gamma_j \sum_{m=-\infty}^{\infty} \frac{\sin(y_i - y_j)}{\cosh(x_i - x_j - 2\pi m) - \cos(y_i - y_j)} \qquad (8.21)$$

and

$$\frac{dy_i}{dt} = \sum_{j=1, j \neq i}^{N} \Gamma_j \sum_{m=-\infty}^{\infty} \frac{\sin(x_i - x_j)}{\cosh(y_i - y_j - 2\pi m) - \cos(x_i - x_j)}. \qquad (8.22)$$

Systems of N vortices on the periodic domain have been used to model the properties of 2D turbulence, primarily in studying the trajectories of individual vortices subject to long-range elastic interactions with the other vortices. In systems of a large number of point vortices, the motion of each individual vortex can be decomposed into periods of quasi-random motion, associated with the mean velocity field generated by the vortex ensemble, and rare, but long, quasi-ballistic flights generated by the temporary coupling of two opposite-sign vortices into a dipole. A dipole travels rapidly across the domain, until it is destroyed by a close encounter with another vortex (Weiss *et al.*, 1998). .

The main drawback of point-vortex systems as models of turbulence is the absence of inelastic interactions such as vortex mergers, which play a crucial role in the evolution. An attempt to introduce a parameterization of mergers was given by Carnevale *et al.* (1991). In this approach, it is assumed that the vortices evolve according to (8.10)-(8.11) whilst they are all well separated. But if two same-sign vortices come within a certain distance of each other, then they "merge" according to the following prescription: Consistent with indications from numerical simulation of 2D turbulence (as discussed in the previous section), it is assumed that during a merger both energy and peak vorticity are conserved. By contrast, circulation is not conserved during the merger because of dissipation. Therefore, during the merging of two same-sign vortices *with equal amplitude* (the case considered by Carnevale *et al.*), the peak vorticity, ζ, and vortex radii, a, satisfy

$$\zeta_3 = \zeta_1 = \zeta_2 \qquad (8.23)$$

and

$$a_3^4 = a_1^4 + a_2^4, \qquad (8.24)$$

111

where the subscript 3 refers to the vortex created by the merging of vortices 1 and 2. The critical distance below which two vortices, with radii a_1 and a_2, merge is fixed at

$$d_c = 3.3 \left(\frac{a_1 + a_2}{2} \right),$$

(8.25)

which is suggested from simulations.

By using this approach, Carnevale *et al.* were able to reproduce the statistical behavior of the population of extended vortices in 2D turbulence. Because the system takes the form an evolving population of point vortices interrupted by instantaneous mergers, Carnevale *et al.* coined the term "Punctuated Hamiltonian Dynamics" to describe it, much as biologists refer to one possible scenario for the evolution of species. But, leaving aside this pleasant analogy, we learn that the point-vortex metaphor, with its artifice of merging appears to reproduce some of the gross aspects of two-dimensional turbulence.

8.4 Effects of a free surface, β, and baroclinicity

We now discuss the fate of coherent vortices when the effects of the free surface, planetary rotation and baroclinicity cannot be neglected.

Let us first consider the role of the free surface and the $\beta-$effect in a barotropic fluid. We recall the equation for barotropic quasi-geostrophic (QG) turbulence:

$$\frac{\partial q}{\partial t} + [\psi, q] = D,$$

(8.26)

where the potential vorticity q is given by

$$q = \nabla^2 \psi - \frac{\psi}{R^2} + \beta y$$

(8.27)

and $D = (-1)^{s-1} \nu \nabla^{2s} \nabla^2 \psi$ is the dissipation term.

The potential vorticity equation (8.26) describes the evolution of q as a result of the velocity field prescribed by ψ. But that streamfunction is related to the potential vorticity through (8.27). However, as we have seen for freely decaying two-dimensional turbulence, the dynamics is dominated by the interaction of coherent vortices. Thus the kinds of solutions that we are interested in are those for which q is approximately composed of a sum of well separated, localized vortices:

$$q \sim \sum_j q_j.$$

(8.28)

Each of the q_j closely corresponds to the solution for an isolated vortex. In that circumstance we can approximately write ψ as a sum over the streamfunctions associated with each of these vortices:

$$\psi \sim \sum_j \psi_j.$$

(8.29)

112

Thus, an approximate equation for the motion of the jth vortex is given by

$$\frac{\partial q_j}{\partial t} + [\psi_j, q_j] \sim - \sum_{l, l \neq j} [\psi_l, q_j], \qquad (8.30)$$

if we ignore dissipation, and because the vorticity of the objects is more localized than the streamfunction. This equation describes how the vortex evolves under the combined influence of the others; the right-hand side models vortex interactions. Importantly, the interaction is mediated by the streamfunctions, and so to understand the effects of the free surface and β we must explore how the corresponding terms modify ψ. But

$$\psi = \int \int G(\mathbf{x}, \mathbf{x}') q(\mathbf{x}', t) d\mathbf{x}', \qquad (8.31)$$

where $G(\mathbf{x}, \mathbf{x}')$ denotes the Green function of the Laplacian. Hence, the key to understanding the new terms lies in how they modify the structure of the Green function.

If the Rossby deformation radius, R, is infinite and $\beta = 0$, equations (8.26) and (8.27) reduce to those for 2D turbulence with $q = \nabla^2 \psi$. In this case the Green's function for the system is a solution to

$$\nabla^2 G = \delta(\mathbf{x} - \mathbf{x}_j) = \delta(r), \qquad (8.32)$$

for which $G \propto \ln r$ on the infinite plane (see equation (8.16)). If R is finite (but β still zero), then

$$\nabla^2 G - \frac{G}{R^2} = \delta(r). \qquad (8.33)$$

This Green function has the form $G \propto \ln r$ for $r < R$, and $G \propto \exp(-r/R)$ for $r \geq R$. The exponential decay of the Green's function at large r reflects a "shielding" effect by the free surface. As a result, vortex interactions become spatially more localized (see, for example, the report by Mockett elsewhere in this volume). For the same reason, the presence of a free surface slows down the inverse cascade at scales larger than R; at the larger scales, nonlinear couplings are weakened. At scales smaller than R, on the other hand, the dynamics remains basically that of 2D turbulence. Coherent vortices thus form and grow by merging until they reach a scale of order R. After this stage, the evolution becomes very slow because the different vortices interact much more weakly with each other. This is illustrated in figure 8.1, which shows the result of a numerical simulation. This picture should be compared with the corresponding figure 7.2 in lecture 7. The comparison shows that vortices in the fluid with a free surface are more numerous and smaller, as expected from the reduction in interactions and therefore mergers.

The latitudinal variation of the planetary rotation, modelled by $\beta \neq 0$, has a more significant influence (see, for example, Rhines 1975 and 1979; McWilliams 1984). In particular, the β-term introduces an upper scale $L_\beta = (U/\beta)^{1/2}$, above which the inverse energy cascade is actually inhibited. (Here, U is again a typical velocity scale which is determined by the dynamics.) The essential reason behind this arrest of the cascade is that, on sufficiently long

scales, the β–effect dominates any nonlinearity, and the fluid equations become practically linear. These linear equations describe Rossby waves.

The length L_β is called the Rhines scale, and above it Rossby waves dominate the dynamics; usually, coherent vortices cannot grow larger than L_β. Even below the Rhines scale, β-plane vortices live for shorter times than their f-plane counterparts. This is because, in general, isolated monopoles on the β-plane emit Rossby waves and undergo zonal and meridional motion. Thus they decay through *radiation*, even without viscosity. Nevertheless, coherent vortices still form and persist for relatively long times. As such, they still exert a significant influence on the dynamics of the flow.

A representative simulation with $\beta \neq 0$ and $r \to \infty$ is shown in figure 8.2. This picture is to be compared with figures 7.2 and 8.1. The most obvious feature of the case with β is that there are significantly fewer vortices, but there is also large-scale structure that we associate with the Rossby waves.

When we add both β and finite R at the same time, there is in some sense a mixture of the two effects of these terms: there is both shielding and Rossby-wave radiation. Interestingly, the free surface can partially shield the destructive effects of differential planetary rotation, leading to vortices that can live for very long times in fluids with both β and a free surface. But otherwise, the overall dynamics remains much the same.

Finally, we briefly discuss the role of baroclinic effects. For baroclinic QG flow another form of potential vorticity must be used. The conservation of QG potential vorticity in a stratified flow takes the form

$$\frac{\partial q}{\partial t} + [\psi, q] = D \tag{8.34}$$

and

$$q = \frac{\partial^2 \psi}{\partial x^2} + \frac{\partial^2 \psi}{\partial y^2} + \frac{\partial}{\partial z} \frac{f^2}{N^2} \frac{\partial}{\partial z} \psi, \tag{8.35}$$

where N is the Brunt-Vaisala frequency given by

$$N^2 = -\frac{g}{\rho} \frac{d\rho}{dz}. \tag{8.36}$$

For constant N, the z coordinate can be rescaled as $z' = (N/f)z$ so that q can then be written as

$$q = \nabla_{3D}^2 \psi \tag{8.37}$$

where ∇_{3D}^2 is the three-dimensional Laplacian. In this system, the Green's function for the infinite plane takes the form $G \propto 1/r$. Once again this leads to interactions that are more localized than in two-dimensional turbulence, and prolongs the run down of a freely decaying system.

The dynamics of stratified QG turbulence has been numerically studied by several authors (e.g. McWilliams 1989; McWilliams & Weiss 1994; McWilliams, Weiss & Yavneh 1994).

114

The simulations show that an initially random vorticity field organizes itself into well-defined coherent vortices, similarly to what happens in 2D turbulence. The vortices initially take the form of three-dimensional, ellipsoidal vorticity concentrations, reminiscent of ocean structures (for example, the Meddies). These vortices undergo long-range elastic interactions with each other, and occasional inelastic interactions (such as mergers and straining), much like their two-dimensional counterparts. A new feature present in this system, however, is that vortices on different vertical levels tend to align into columnar structures, when they become sufficiently close to each other. As a result, freely-decaying systems display some tendency to evolve to a final state composed of two tall columns of opposite vorticity, somehwat analogous to the final dipolar state observed for 2D turbulence. Although the stratified case has been explored less thoroughly than the barotropic one, one can safely conclude that, here too, there is a robust tendency to form coherent vortices, which then dominate the system evolution.

8.5   Magnetic vortices

Up to now, we have considered a purely hydrodynamical situation, where electromagnetic forces do not play any role. In most astrophysical flows, however, magnetic effects cannot be discarded. In keeping with the attitude of staying as simple as possible (and sometimes even simpler than that), here we mention the issue of vortex formation in two-dimensional incompressible magnetohydrodynamics.

If the conducting fluid is incompressible, and it is subject to a strong constant magnetic field along z (the ordering field that we discussed in Lecture 7), one can make the following approximations to the full equations of MHD:

$$\partial_z \to 0, \quad w = 0, \quad B_z = \text{constant}$$

where w is the fluid velocity and B_z is the magnetic field in the z direction. Thus, the only dynamical variables left are the velocity, $\mathbf{u} = (u, v)$, and magnetic field, $\mathbf{B}_h = (B_x, B_y)$, in the (x, y) plane. Both $\mathbf{u}$ and $\mathbf{B}_h$ are divergenceless, and can be expressed as

$$u = -\frac{\partial \psi}{\partial y} \ , \quad v = \frac{\partial \psi}{\partial x} \tag{8.38}$$

and

$$B_x = -\frac{\partial a}{\partial y} \ , \quad B_y = \frac{\partial a}{\partial x}, \tag{8.39}$$

where ψ is the stream function and a is the magnetic potential. The vorticity is given as usual by $\omega = \nabla^2 \psi$. Analogously, the only relevant component of the current, $\mathbf{j} = \nabla \times \mathbf{B}$, is that in the z direction, and is given by $j = \nabla^2 a$.

The evolution equations for the flow take the form,

$$\partial_t \nabla^2 \psi + [\psi, \nabla^2 \psi] - [a, \nabla^2 a] = \nu \nabla^2 \nabla^2 \psi$$

115

and

$$\partial_t a + [\psi, a] = \eta \nabla^2 a,$$

where we have introduced a Newtonian viscosity ν and a resistivity η. These equations are intriguing. Imagine, for example, if we discarded the term $[a, \nabla^2 a]$ in the first equation (the Lorentz force). Then, one is left with standard 2D turbulence, with the addition of a passive scalar field a which is advected by the flow, with no feedback on the flow itself. This is similar to the *kinematic dynamo problem* in which one studies whether a given velocity field can amplify an embedded, passive magnetic field. However, by turning on the term $[a, \nabla^2 a]$, the skew-product asymmetry is broken and the advected field a feeds back on the advecting field. In fact, this term amplifies rapidly in turbulent fluids, and the system becomes dominated by the magnetic effects.

For zero viscosity and resistivity, 2D-MHD has three quadratic invariants, namely the total energy (E), the square of the magnetic potential (A), and the cross-helicity (H). These are

$$E = \frac{1}{2} \int (u^2 + v^2) dx dy + \frac{1}{2} \int (B_x^2 + B_y^2) dx dy,$$

$$A = \int a^2 dx dy$$

and

$$H = \int u B_x + v B_y dx dy.$$

Note that, in this system, enstrophy is not conserved. This induces severe modifications in the turbulent cascades. In particular, in 2D-MHD, energy flows from large to small scales (as in 3D turbulence), and it is the magnetic potential that undergoes an inverse cascade from small to large scales.

Numerical integrations of 2D-MHD have indicated the formation of strong vorticity sheets (Biskamp *et al.* 1990), but no kinetic vortices. However, the current field develops localized structures that one might call "magnetic vortices". In other words, the current plays a similar role to that played by vorticity in the simpler hydrodynamical case (Kinney *et al.* 1995).

The details of the dynamics of 2D-MHD are very complex, depending, for example, on the initial ratio between kinetic and magnetic energy and on the cross-correlation between the fluid velocity and the magnetic field. Nevertheless, it is clear that coherent structures do play a crucial role in this system as well. But here, we deal with coherent magnetic flux tubes rather than with vortices, and these magnetic coherent structures are reminiscent (to the eye of the believer) of the coherent magnetic flux tubes associated with sunspots.
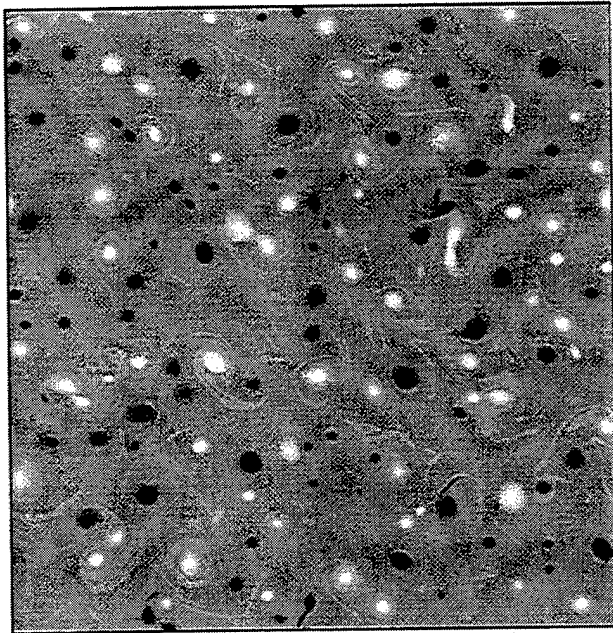
Figure 8.1: Numerical simulation of freely decaying, two-dimensional turbulence with $R = 0.2$ and $\beta = 0$. Shown is the vorticity field at $t = 10$. The numerical scheme is described in the caption to figure 7.2.
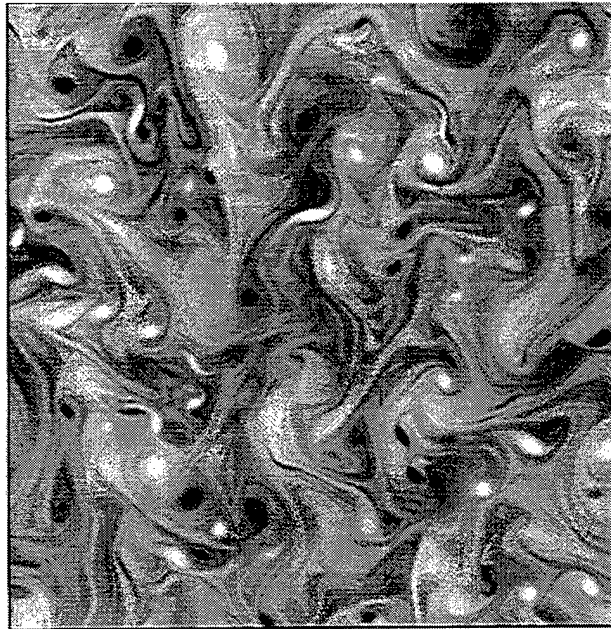
Figure 8.2: Numerical simulation of freely decaying, two-dimensional turbulence with $\beta = 10$ and $R \to \infty$. Shown is the vorticity field at $t = 10$. The numerical scheme is described in the caption to figure 7.2.

Lecture 9

Floats, Balloons, and Planets

With a final effort, we consider what happens to particles that are transported by a fluid flow. If the tracers are passive (that is, they do not feed back on the advecting fluid), then we are in the presence of another skew-product system, where the driver is the Eulerian flow and the driven system is represented by the advected tracers.

9.1 Chaotic advection

How can we model the motion of a particle advected by a flow? Let us first suppose that the particle under study is passive, point-like and it has a vanishing inertia with respect to the advecting fluid. That is, it is a passive fluid particle. The equations of motion for such a particle are obtained by equating the Lagrangian velocity and the Eulerian fluid velocity at the particle position, i.e.

$$\frac{d\mathbf{x}}{dt} = \mathbf{V}(t) = \mathbf{u}(\mathbf{x}, t), \tag{9.1}$$

where $\mathbf{x}(t) = (x(t), y(t))$ is the particle position at time t, $\mathbf{V}(t)$ is its Lagrangian velocity, and $\mathbf{u}(\mathbf{x}, t)$ is the Eulerian velocity at point $\mathbf{x}$ and time t. For simplicity, we have assumed a two-dimensional velocity field.

For two-dimensional incompressible flows, such as those discussed in Lectures 7 and 8, the Eulerian velocity may be expressed in terms of a stream function $\psi(x, y, t)$. In this case, equation (9.1) becomes

$$\frac{dx}{dt} = -\frac{\partial\psi}{\partial y} \quad ; \quad \frac{dy}{dt} = \frac{\partial\psi}{\partial x} \quad . \tag{9.2}$$

Equation (9.2) formally defines an Hamiltonian system with one degree of freedom, described by the canonically conjugate variables x and y. Here, the stream function ψ plays the role of the Hamiltonian and the phase space of the system is the physical plane (x, y) (see e.g. Ottino, 1989). For stationary stream functions, system (9.2) is integrable, the particles follow the streamlines and particle trajectories are regular. When the stream function is time-dependent (for example, periodic in time), the system becomes non-integrable. In this case,

chaotic particle trajectories are in general expected and the Lagrangian motion may become highly irregular even if the Eulerian dynamics is simple. This type of behavior is known as *chaotic advection*, and it has been shown to be of some use in the description of particle advection in flows dominated by one or a few structures, such as an isolated vortex, a simple jet or a single wave train.

One classic example of chaotic advection in a two-dimensional flow was studied by Solomon and Gollub (1988). They considered a time-dependent stream function representing simplified convection cells

$$\psi = A \cos x \cos \left(y + B \sin \Omega t \right).$$

If the stream function ψ is constant in time ($B = 0$) particles are constrained to stay within the cell in which they start. For $B \neq 0$ it is found that particles cross cell boundaries and undergo dispersion processes similar to those observed in turbulent flows. At short times, the mean square displacement $A^2 = < [\mathbf{x}(t) - \mathbf{x}(0)]^2 >$ of a particle ensemble increases as t^2 (ballistic motion), while on long times the motion becomes Brownian-like and $A^2 \propto t$. Examples of *anomalous* diffusion, with $A^2 \propto t^\alpha$ with $\alpha \neq 1$ at large times have also been reported.

Chaotic advection has been studied in several other flows of geophysical interest, ranging from modulated travelling waves (Weiss & Knobloch 1989), to models of the Gulf Stream (Samelson 1992) and low-resolution general circulation models of the atmosphere (Pierrehumbert & Yang 1992). The main lesson that we can learn from this approach is that even simple Eulerian flows can generate unpredictable, Brownian-like particle trajectories and strong particle dispersion. This leads to potentially serious difficulties when trying to relate Eulerian and Lagrangian statistics, and to reconstruct Eulerian flows from Lagrangian measurements. Also, we see that we do not need turbulent flows and high-dimensional stochastic processes to generate particle dispersion, as a simple time-periodic wavetrain can generate it.

9.2   Dynamics of advected impurities

In the previous section we have assumed that the advected particles have vanishing inertia with respect to the advecting fluid. Complications arise when the advected particles have finite relative inertia or size, as in the case of dust grains, gas bubbles and the floats and balloons used as Lagrangian tracers in the ocean and the atmosphere. In this case, Newton's laws have to be used, and we must equate the particle acceleration to the force per unit mass acting on the particle. The simplest expression for the equations of motion of an advected particle with finite inertia (an *impurity*) then becomes

$$\frac{d^2 \mathbf{x}}{dt^2} = \delta \frac{D\mathbf{u}}{Dt} - \gamma \left(\frac{d\mathbf{x}}{dt} - \mathbf{u} \right) + \mathbf{g}(1 - \delta).$$

where

$$\delta = \frac{\rho_f}{\rho_p}$$

120

is the ratio of fluid density ρ_f to the density of the impurity ρ_p,

$$\gamma = \frac{9}{2} \left(\frac{a}{L}\right)^{-2} Re^{-1}$$

is the coefficient of the Stokes drag term, and

$$\frac{D}{Dt} = \frac{\partial}{\partial t} + \mathbf{u} \cdot \nabla \ .$$

For two-dimensional incompressible flows,

$$\mathbf{u} = (u, v) \ ; \ \ u = -\frac{\partial \psi}{\partial y} \ , \ \ v = \frac{\partial \psi}{\partial x}.$$

The left-hand-side of equation (9.2) represents particle acceleration. The first term on the right-hand-side represents the force that the fluid would exert on a fluid particle placed at the position of the impurity, weighted by relative inertia. The second term is the Stokes drag, and it models the friction that the fluid exerts on a particle moving with a velocity that is different from the local fluid velocity. Here, a is the radius of the particle, L is a typical length scale of the flow, and Re is the Reynolds number. γ^{-1} represents the time constant for the equilibration of the velocity of the tracer with the flow velocity. Finally, the third term represents the buoyancy force acting on the impurity.

This system has been considered by Stommel (1949) as a simplified model for the fall of heavy particles in a two-dimensional vertical plane. Consider x in the horizontal direction and y pointing vertically downward. Thus, $\mathbf{g} = (0, g)$. By discarding the particle acceleration $d^2\mathbf{x}/dt^2$ and considering very heavy particles, $\delta \to 0$, the system reduces to

$$\frac{dx}{dt} = -\frac{\partial \psi}{\partial y} \ , \ \ \frac{dy}{dt} = \frac{\partial \psi}{\partial x} + g$$

which can be recast in a stream function form by introducing $\phi = \psi + gx$.

For example, if $\psi = \psi_0 \sin x \sin y$, it can be shown that, depending on their initial position and velocity, some of the heavy particles can be trapped forever in recirculation regions of the flow. However, as shown by Maxey (1987), this result is spurious: if one includes the particle acceleration, no permanent trapping is possible and the fate of all heavy particles is to fall, sooner or later.

For horizontal flows, buoyancy is absent and particles are not constrained to fall under gravity. In such cases, the dynamics of the particles can depend crucially on whether they are light ($\delta > 1$), or heavy ($\delta < 1$). For example, Crisanti et al (1992) studied fluid laden with particles of finite δ, using the model streamfunction of Solomon & Gollub: $\psi = A \cos x \cos (y + B \sin \Omega t)$. When $B = 0$ and the flow is steady, they showed that light particles converge to the elliptic fixed points at the center of the advection cells. Heavy particles, on the other hand, are pushed outside regions of closed streamlines (as their inertia is larger than that of fluid particles) and undergo chaotic motion associated with a strange attractor in the four-dimensional phase space, $(x, y, dx/dt, dy/dt)$. For time-dependent stream functions ($B \neq 0$), the picture

is more complicated and light particles can also display chaotic dynamics. In general, however, it remains true that heavy particles are pushed outside coherent structures with closed streamlines.

Note that system (9.2) is dissipative, and thus phase-space volumes shrink with time. This implies that the long-term evolution of the system takes place on a set of measure zero in the full phase space. This is a major difference with respect to the dynamics of fluid particles, described by a Hamiltonian system for which the Liouville theorem holds. Note, also, that system (9.2) is an extension of the model used for fluid particles, to which it reduces for $\delta = 1$ and $a \to 0$ (though this is a singular limit as the order of the equation changes).

Finally, we recall that even though interesting results can be obtained with a simple system such as (9.2), the equations of motion for finite-size, finite-inertia particles are extremely complicated, as they depend, for example, on the shape of the particle itself. It is only in the case of very small spherical particles, that the equations of motion take a manageable form that can be derived from Newton's second law of motion (see Maxey & Riley (1983) for a fairly complete discussion of the dynamical equations for small spherical impurities in non-rotating systems and Tanga *et al* (1996) for the rotating case). Even in this case, however, terms known as the added mass, the Basset history term, the Faxen corrections, and the lift all participate in reminding us that the world is more complicated than we would like. Insisting in the Walsh cottage tradition of not dealing too heavily with the *accidenti*, we have decided not to talk about these complications here.

9.3 Dust in the spots

The presence of an overall rotation of the system induces new effects in the dynamics of heavy impurities. In a rotating frame, the equations of motion for an advected impurity become

$$\frac{d^2\mathbf{x}}{dt^2} = \delta\frac{D\mathbf{u}}{Dt} - \gamma\left(\frac{d\mathbf{x}}{dt} - \mathbf{u}\right) + \mathbf{g}(1-\delta) - 2\Omega \times \left(\frac{d\mathbf{x}}{dt} - \delta\mathbf{u}\right) + |\Omega|^2 r(1-\delta)\hat{\mathbf{r}}, \qquad (9.3)$$

where we have introduced the relative Coriolis and centrifugal accelerations which are present in a rotating reference frame; here Ω is the angular velocity of the system.

As a consequence of rotation, when heavy particles are spinning inside a coherent vortex in a rotating reference frame, they are subject to two main opposing forces: the centrifugal force, which pushes the heavy particles outside the region of closed isolines, and the Coriolis force, which - for an overall cyclonic rotation of the reference frame - pushes the particles to the right of the direction of motion. Thus, the Coriolis force pushes heavy impurities out of cyclonic vortices and it pushes them toward the center of anticyclonic vortices. Thus, in rotation-dominated systems for which the Coriolis force is stronger than the centrifugal term, heavy impurities can concentrate in the cores of anticyclonic vortices (Tanga *et al.* 1996, Provenzale 1999), in complete contrast to the nonrotating case for which heavy impurities are always ejected from coherent vortices,

Can all this be of some use in explaining the formation of planets? First, we must mention how people think of planet formation. The *nebular hypothesis* by Kant and Laplace was based

122

on the conjecture that the solar system formed from a flattened gas cloud. Until now, this has survived as a basically correct explanation, and it has been further elaborated by realizing that stars condense from an interstellar medium composed by gas and an admixture of solid particles called interstellar dust. As the central star contracts, it leaves around it material that contains a significant portion of the initial angular momentum of the system. In this nebula, centrifugal forces balance the stellar gravity in the radial direction and a disk forms. This is a Keplerian disk, because it is dominated by the gravity of the central star. The disk is dusty, and the dust settles toward the midplane, until it forms - in a process whose details are still poorly understood - small protoplanetary objects called planetesimals. Later on, the planetesimals start feeling the gravity of each other, cluster together to form larger objects, and the true planets are finally formed.

A crucial problem in this scenario, however, is to reconcile the time scales for growth by accumulation of objects of the size of Jupiter, and the estimated lifetime of the gaseous nebula itself. In particular, there is a lack of standard mechanisms for building planetesimals between the centimeter-sized grains formed by agglomeration and sticking, and the larger objects capable of efficiently triggering gravitational instability.

At this point, vortices enter the scene, much as the Cavalry always appeared in old, politically incorrect movies. Since coherent vortices are so common in rotating fluids, we could imagine that there are vortices in the rotating nebula. This hypothesis seems natural to fluid dynamicists, but has not been appreciated by astrophysicists, as they claimed that the strong shear present on Keplerian disks can easily destroy any incipient coherent structure. And, apart from the shear, there are several other effects (compressibility, magnetic fields, and so forth) that can complicate the picture.

In an attempt of dealing with just one problem at a time, Bracco *et al* (1998) have explored whether coherent vortices can survive in incompressible Keplerian disks. That is, whether the Keplerian shear is really able to prevent the formation of vortices. The system dynamics is governed by the standard equation for barotropic turbulence:

$$\frac{\partial}{\partial t}\nabla^2\psi + [\psi, \nabla^2\psi] = \nu\nabla^2\nabla^2\psi, \tag{9.4}$$

where a Newtonian viscosity has been added. The initial conditions at time $t = 0$ are given by

$$\psi = \psi_{Kep} + \psi', \tag{9.5}$$

where $\nabla\psi_{Kep} \propto r^{-3/2}$ represents the unperturbed Keplerian disk, and ψ' is a perturbation to the Keplerian flow.

Numerical simulation of this system indicates that weak perturbations are destroyed by the shear of the Keplerian flow. If the initial perturbations are large enough, however, coherent vortices can form even in the presence of the strong shear (see figure 9.1). Interestingly enough, only anticyclonic vortices can form, since cyclonic vortices are more readily destroyed by the shear. This is at least partly because the local, Keplerian vorticity gradient is *negative* (if we consider a local Cartesian coordinate system centerd at some particular radius). But cyclonic vortices rotate against this Keplerian background and so become sheared out. Anticyclones,

123

however, are reinforced by the background, and so they may survive if they are of sufficient initial strength.

In general, the presence of vortices is also determined by the interplay of two limiting space scales. The smaller one, L_ν, is the scale associated with dissipative effects; below it, vortices cannot form as the nonlinear terms are overwhelmed by dissipation. The larger scale, L_{out}, is determined by the shear; above L_{out}, vortices are destroyed by the shear. Thus, vortices can exist only in the range between these two scales, and this requires that $L_\nu \ll L_{out}$. In conclusion, it is possible to obtain coherent anticyclonic vortices on Keplerian disks only if there are large enough initial perturbations on the Keplerian flow and the viscosity is small enough. Given this, coherent vortices happily form, and lead to what have been called *spotted disks*, by analogy with sunspots.

Given that vortices can form on (barotropic) Keplerian disks, the remainder of the metaphor for planet formation in vortices follows naturally. The dust grains in the solar nebula are very heavy, being characterized by $\delta \approx 10^{-8}$. For these impurities, the concentration mechanism discussed above is at work, and, if the rotation of the nebula is sufficiently rapid, the Coriolis force can overcome the centrifugal force of the vortices; as a consequence, the dust grains are pushed into the cores of the anticyclonic vortices (Barge & Sommeria 1995, Tanga *at al* 1996, Bracco *et al* 1998). Potentially, this leads to a relatively rapid accumulation of matter into vortex cores, and the birth of planetesimals.

Explicit numerical simulation of dust grain dynamics verifies this image; see figure 9.2. Moreover, the computations confirm that the process effectively concentrates the heavy particles and therefore expedites the formation of planetesimals. Hence, we can say that the spots on the disk are dusty.

The fact that vortices may have played a role in the formation of the solar system is, of course, appealing to the palate of the nonlinear dynamicist. However, the world is as usual more complicated than we depict it, and in this discussion we have for example discarded important effects such as compressibility of the gas in the disk and magnetic fields. But, just as a note, we report that preliminary simulations based on the (compressible) thin-layer aproximation indicate that vortices should be able to form in weakly compressible disks as well (Bracco *et al.* 1999).

Conclusion

We started these lecture notes by considering the motion of a dust grain in a stratified atmosphere. And we concluded them, by discussing the dynamics of dust grains in the primordial solar nebula. In the process of passing from dust to dust, we have enjoyed an exploration of some intriguing mysteries. Nothing more should be desired, nor expected. And it is not allowed in such a short summer program.

Figure 9.1: Vorticity field evolving from a perturbed Keplerian disk in the incompressible, barotropic approximation. A pseudo-spectral code with Newtonian viscosity $\nu = 5 \times 10^{-5}$ and resolution 512^2 grid points has been used. The initial mean kinetic energy of the Keplerian disk is $E_{Kep} = 0.5$ and the mean perturbation energy is $E' = 4 \times 10^{-3} E_{Kep}$. The time shown is $t = 8$. (Adapted from Bracco et al)
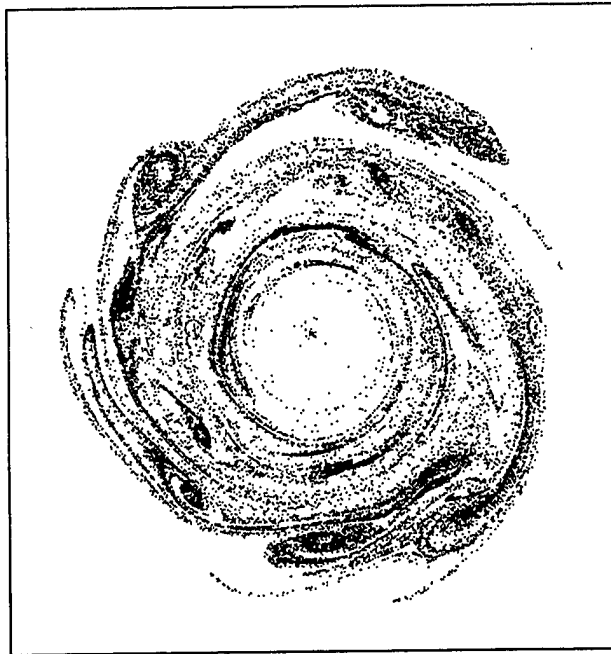
Figure 9.2: Distribution of dust grains in the perturbed Keplerian disk shown above. The particles were initially released uniformly in the disk. (Adapted from Bracco *et al.*)

Bibliography

[1] H. AREF, *Integrable, chaotic, and turbulent vortex motion in two-dimensional flows*, Ann. Rev. Fluid Mech., 15 (1983), pp. 345–389.

[2] E. AURELL, G. BOFFETTA, A. CRISANTI, G. PALADIN, AND A. VULPIANI, Phys. Rev. Lett., 77 (1996), p. 1262.

[3] N. J. BALMFORTH, M. MARTENS, A. PROVENZALE, E. A. SPIEGEL, C. TRESSER, AND C.-W. WU, *Red spectra from white and blue noise*, Proc. Roy. Soc. London B, to appear, (1998).

[4] P. BARGE AND J. SOMMERIA, *Did planet formation begin inside persistent gaseous vortices?*, Astron. Astrophys., 295 (1995), pp. L1–L4.

[5] R. BENZI, G. PARISI, A. SUTERA, AND A. VULPIANI, Tellus, 34 (1982), p. 10.

[6] R. BENZI, A. SUTERA, AND A. VULPIANI, J. Phys. A, 14 (1981), p. L453.

[7] D. BISKAMP, H. WELTER, AND M. WALTER, Phys. Fluids B, 2 (1990), p. 3024.

[8] J. BJERKNES, Tellus, 18 (1966), p. 820.

[9] G. BOFFETTA, A. CRISANTI, F. PAPARELLA, A. PROVENZALE, AND A. VULPIANI, *Slow and fast dynamics in coupled systems: A time series analysis view*, Physica D, 116 (1998), pp. 301–312.

[10] A. BRACCO, P. H. CHAVANIS, A. PROVENZALE, AND E. A. SPIEGEL, *Particle aggregation in a turbulent keplerian flow*, Phys. Fluids A, submitted, (1998).

[11] A. BRACCO, A. PROVENZALE, E. A. SPIEGEL, AND P. YECKO, *Spotted disks*, in Theory of black hole accretion disks, M. Abramowicz, G. Björnsson, and J. Pringle, eds., Cambridge University Press, 1999.

[12] A. R. BULSARA AND L. GAMMAITONI, *Tuning into noise*, Physics Today, (1996), pp. 39–45.

[13] G. F. CARNEVALE, J. C. MCWILLIAMS, Y. POMEAU, J. B. WEISS, AND W. R. YOUNG, *Evolution of vortex statistics in two-dimensional turbulence*, Phys. Rev. Lett., 66 (1991), pp. 2735–2737.

[14] P. CESSI, *A simple box model of stochastically forced thermohaline flow*, J. Phys. Oceanog., 24 (1994), pp. 1911–1920.

[15] J. G. CHARNEY AND J. G. DEVORE, *Multiple flow equilibria in the atmosphere and blocking*, J. Atmos. Sci., 36 (1979), pp. 1205–1216.

[16] A. CRISANTI, M. FALCIONI, A. PROVENZALE, P. TANGA, AND A. VULPIANI, *Dynamics of passively advected impurities in simple two-dimensional flow models*, Phys. Fluids A, 4 (1992), pp. 1805–1820.

[17] M. DING AND W. YANG, *Stability of synchronous chaos and on-off intermittency in coupled map lattices*, Phys. Rev. E, 56 (1997), pp. 4009–4016.

[18] P. G. DRAZIN, *Nonlinear Systems*, University Press, Cambridge, 1992.

[19] D. G. DRITSCHEL, *A general theory for two-dimensional vortex interactions*, J. Fluid Mech., 293 (1995), pp. 269–303.

[20] G. S. DUANE, *Synchronized chaos in extended systems and meteorological teleconnections*, Phys. Rev. E, 56 (1997), pp. 6475–6493.

[21] J.-P. ECKMANN AND D. RUELLE, Physica D, 56 (1992), p. 185.

[22] W. FERREL, *The motions of fluids and solids relative to the earth's surface*, Math. Monthly, 1 (1859), pp. 140–147,210–216,300–307,366–372,397–406.

[23] A. M. FRASER AND H. L. SWINNEY, Phys. Rev. A, 33 (1986), p. 1134.

[24] H. GHIL AND S. CHILDRESS, *Topics in Geophysical Fluid Dynamics*, Springer, New York, 1987.

[25] P. GRASSBERGER AND I. PROCACCIA, Physica D, 9 (1983), p. 189.

[26] G. HADLEY, *Concerning the cause of the general trade winds*, Phil. Trans., 39 (1735), pp. 58–63.

[27] K. KANEKO, *Chaotic but regular posi-nega switch among coded attractors by cluster-size variation*, Phys. Rev. Lett., 63 (1989), pp. 219–223.

[28] ———, ed., *Theory and applications of coupled map lattices*, Nonlinear science: Theory and applications, John Wiley & Sons, West Sussex, England, 1993.

[29] H. KANTZ AND T. SHREIBER, *Nonlineat Time Series Analysis*, Cambridge University Press, Cambridge, 1997.

[30] R. KINNEY, J. C. MCWILLIAMS, AND T. TAJIMA, *Coherent structures and turbulent cascades in two-dimensional incompressible magnetohydrodynamic turbulence*, Phys. Plasmas, 2 (1995), pp. 3623–3639.

[31] R. H. KRAICHNAN AND D. MONTGOMERY, *Two-dimensional turbulence*, Rep. Prog. Phys., 43 (1980), pp. 547–619.

[32] E. N. LORENZ, *Deterministic nonperiodic flow*, J. Atmos. Sci., 20 (1963), pp. 130–141.

[33] ——, *The local structure of a chaotic attractor in four dimensions*, Physica D, 13 (1984), p. 90.

[34] ——, *Can chaos and intransitivity lead to interannual variability?*, Tellus, 42A (1990), pp. 378–389.

[35] ——, *Dimension of weather and climate attractors*, Nature, 353 (1991), pp. 241–244.

[36] ——, *Predictability: A problem partly solved*, in Proc. Seminar on Predictability, vol. 1, ECMWF, Reading, Berkshire, UK, 1996.

[37] M. R. MAXEY, *The motion of small spherical particles in a cellular flow field*, Phys. Fluids, 30 (1987), pp. 1915–1928.

[38] M. R. MAXEY AND J. J. RILEY, *Equation of motion for a small rigid sphere in a nonuniform flow*, Phys. Fluids, 26 (1983), pp. 883–889.

[39] B. MCNAMARA AND K. WIESENFELD, Phys. Rev. A, 39 (1989), p. 4854.

[40] J. C. MCWILLIAMS, *The emergence of isolated coherent vortices in turbulent flow*, J. Fluid Mech., 146 (1984), pp. 21–43.

[41] J. C. MCWILLIAMS, *Statistical properties of decaying geostrophic turbulence*, J. Fluid Mech., 198 (1989), pp. 199–230.

[42] J. C. MCWILLIAMS, *The vortices of two-dimensional turbulence*, J. Fluid Mech., 219 (1990), pp. 361–385.

[43] J. C. MCWILLIAMS AND J. B. WEISS, *Anisotropic geophysical vortices*, Chaos, 4 (1994), pp. 305–311.

[44] J. C. MCWILLIAMS, J. B. WEISS, AND I. YAVNEH, *Anisotropy and coherent vortex structures in planetary turbulence*, Science, 264 (1994), pp. 410–413.

[45] D. W. MOORE AND E. A. SPIEGEL, *A thermally excited nonlinear oscillator*, Astrophys. J., 143 (1966), pp. 871–887.

[46] C. NICOLIS, Tellus, 34 (1982), p. 1.

[47] A. R. OSBORNE, A. D. KIRWAN, A. PROVENZALE, AND L. BERGAMASCO, Physica D, 23 (1986), p. 75.

[48] A. R. OSBORNE AND A. PROVENZALE, Physica D, 35 (1989), p. 357.

[49] E. OTT, *Chaos in dynamical systems*, Cambridge University Press, Cambridge, Great Britain, 1993.

[50] E. OTT, T. SAUER, AND J. A. YORKE, *Coping with Chaos*, Wiley, New York, 1994.

[51] J. M. OTTINO, *The kinematics of mixing: stretching, chaos and transport*, Cambridge University press, Cambridge, 1989.

[52] N. H. PACKARD, J. P. CRUTCHFIELD, J. D. FARMER, AND R. S. SHAW, *Geometry from a time series*, Phys. Rev. Lett., 45 (1981), pp. 712–715.

[53] L. M. PECORA AND T. L. CARROLL, *Synchronization in chaotic systems*, Phys. Rev. Lett., 64 (1990), pp. 821–824.

[54] L. M. PECORA, T. L. CARROLL, G. A. JOHNSON, D. J. MAR, AND J. F. HEAGY, *Fundamentals of synchronization in chaotic systems, concepts, and applications*, Chaos, 7 (1997), pp. 520–543.

[55] J. PEDLOSKY, *Geophysical Fluid Dynamics*, Springer, New York, 1987.

[56] R. T. PIERREHUMBERT AND H. YANG, *Global chaotic mixing on isentropic surfaces*, J. Atmos. Sci., 50 (1992), pp. 2462–2480.

[57] N. PLATT, E. A. SPIEGEL, AND C. TRESSER, *The intermittent solar cycle*, Geophys. Astrophys. Fluid Dyn., 73 (1993), pp. 147–161.

[58] N. PLATT, E. A. SPIEGEL, AND C. TRESSER, *On-off intermittency: A mechanism for bursting*, Phys. Rev. Lett., 70 (1993), pp. 279–282.

[59] Y. POMEAU AND P. MANNEVILLE, *Intermittent transition to turbulence in dissipative dynamical systems*, Comm. Math. Phys., 74 (1980), p. 189.

[60] A. PROVENZALE, *Transport by coherent barotropic vortices*, Ann. Rev. Fluid Mech., 31 (1999), pp. 55–93.

[61] ——, *Transport by coherent barotropic vortices*, Ann. Rev. Fluid Mech., 31 (1999), pp. 55–93.

[62] A. PROVENZALE, L. A. SMITH, R. VIO, AND G. MURANTE, *Distinguishing between low-dimensional dynamics and randomness in measured time series*, Physica D, 58 (1992), pp. 31–49.

[63] A. PROVENZALE, B. VILLONE, A. BABIANO, AND R. VIO, *Intermittency, phase randomization and generalized fractal dimensions*, Intern. J. Bifurc. Chaos, 3 (1993), pp. 729–736.

[64] A. PROVENZALE, R. VIO, AND S. CRISTIANI, Astrophys. J., 428 (1994), p. 591.

[65] S. RAHMSTORF, *On the fresh-water forcing and trasnport of the atlantic thermohaline circulation*, Climate Dynamics, 12 (1996), pp. 799–811.

[66] P. B. RHINES, *Waves and turbulence on a beta-plane*, J. Fluid Mech., 69 (1975), pp. 417–443.

[67] ——, *Geostrophic turbulence*, Ann. Rev. Fluid Mech., 11 (1979), pp. 401–441.

[68] M. G. ROSENBLUM, A. S. PIKOVSKY, AND J. KURTHS, *Phase synchronization of chaotic oscillators*, Phys. Rev. Lett., 76 (1996), pp. 1804–1807.

[69] R. M. SAMELSON, *Fluid exchange across a meandering jet*, J. Phys. Oceanog., 22 (1992), p. 431.

[70] L. A. SMITH, Phys. Lett. A, 133 (1988), p. 283.

[71] T. H. SOLOMON AND J. P. GOLLUB, *Chaotic particle transport in time-dependent rayleigh-bénard convection*, Phys. Rev. A, 38 (1988), pp. 6280–6286.

[72] C. SPARROW, *The Lorenz equations: bifurcations, chaos and strange attractors*, Springer, Berlin, 1982.

[73] H. STOMMEL, *Trajectories of small bodies sinking slowly through convection cells*, J. Mar. Res., 8 (1949), pp. 24–29.

[74] ——, *Thermohaline convection with two stable regimes of flow*, Tellus, 13 (1961), pp. 224–230.

[75] F. TAKENS, Lecture Notes in Matematics, 898 (1981).

[76] P. TANGA, A. BABIANO, A. PROVENZALE, AND B. DUBRULLE, *Forming planetesimals in vortices*, ICARUS, 121 (1996), pp. 158–170.

[77] J. THEILER, S. EUBANK, A. LONGTIN, B. GALDRIKIAN, AND J. B. FARMER, Physica D, 58 (1992), p. 77.

[78] J. THOMSON, *On the grand currents of atmospheric circulation*, Phil. Trans. Roy. Soc. A, 183 (1857), pp. 653–684.

[79] J. VON HARDENBERG AND A. PROVENZALE, *Dynamics of forced and coupled systems*, in Proceedings of the International School of Physics "Enrico Fermi", G. C. Castagnoli and A. Provenzale, eds., no. 133, IOS Press, Amsterdam, 1997, pp. 161–176.

[80] J. G. VON HARDENBERG, F. PAPARELLA, N. PLATT, A. PROVENZALE, E. A. SPIEGEL, AND C. TRESSER, *Missing motor of on-off intermittency*, Phys. Rev. E, 55 (1997), pp. 58–64.

[81] J. B. WEISS AND E. KNOBLOCH, *Mass transport and mixing by modulated travelling waves*, Phys. Rev. A, 40 (1989), p. 2579.

[82] J. B. WEISS AND J. C. MCWILLIAMS, *Nonergodicity of point vortices*, Phys. Fluids A, 3 (1991), pp. 835–844.

131

[83] ——, *Temporal scaling behaviour of decaying two-dimensional turbulence*, Phys. Fluids A, 5 (1993), pp. 608–621.

[84] J. B. WEISS, A. PROVENZALE, AND J. C. MCWILLIAMS, *Lagrangian dynamics in high dimensional point vortex systems*, Phys. Fluids, (1998).

[85] J. A. WHITEHEAD, *Thermohaline ocean processes and models*, Ann. Rev. Fluid Mech., 27 (1995), pp. 89–113.

132

Effects of Discreteness in Solitonic Excitations:
A Future Challenge or just Numerical Observations?

P. Kevrekidis

Abstract

In this study we will focus on the significant effects of discreteness in solitons as they appear in a number of physical applications (material dislocations , charge density waves fluxons in arrays of Josephson junctions and many others). We will primarily be interested in the discrete version of the Sine-Gordon equation and on the kink and breather-like solutions of it (however we will give extensions of our results to other systems such as the ϕ^4 or the double sine-Gordon (DSG)).Numerical Results will be presented that will explicitly demonstrate the vital role of discreteness in altering the continuum- like picture and in producing entirely new features in the problem such as internal shape modes of the solutions , pinning due to the Peierls-Nabarro barrier , emission of radiation or Brownian motion of the kink when driven by the fluctuations.We will also attempt to investigate the stability of these structures (kinks and breathers) using the Evans functions and Nyquist Theory techniques as well as to trace the very rich dynamics of the interactions of such structures (i.e. k-k or k-$\bar{k}$ interactions as well as breather-breather or breather-image collisions). In view of the dramatic effects of discreteness in the continuum description we are going to introduce an appropriate technique for discretizing continuum systems for computational purposes.Whenever possible the results of our numerical simulations will be compared with the relevant existing theories.

The full report is available on the web at `http://www.whoi.edu/gfd/`.

Data Assimilation in Chaotic Systems

Mark S. Roulston

1   Introduction

Data assimilation is a crucial component of numerical weather prediction (NWP) schemes. It is the method by which the initial conditions for the model are determined. NWP models are obviously not perfect models of the atmosphere but if they were then the accuracy of the initial conditions would be the sole factor determining the forecast skill of the model.

Data assimilation involves using time series of observations over the recent past to estimate the state of the system at the present moment. Simply using the observations taken at the present moment is not enough because firstly these observations will contain errors and secondly these observations are incomplete. That is, there is not an observation of every relevant variable at every model gridpoint.

Data assimilation methods can be placed into two categories. Sequential methods such as *nudging* integrate the model forward in time with extra non-physical forcing terms which push the model towards the observations. If the model is linear (which NWP models are not) then it can be shown that the optimal nudging scheme takes the form of a *Kalman filter*. Variational methods seek to minimize a cost function which is the measure of the misfit between the model and observations over the assimilation period. Variational methods are regarded as the "next generation" of assimilation schemes and they are now used operationally.

An important distinction between sequential schemes and the variational method is that the model is used as a strong constraint and thus the trajectory that results from assimilation (called the analysis) must be a valid trajectory of the model. This is not so in sequential methods in which observations are essentially blended with the model. This means that if the aim of assimilation is to validate the model the variational method is to be preferred. In this paper only variational based assimilation schemes will be considered.

In section 2 the adjoint method will be described. The Lorenz model will then be used to illustrate the problem of multiple minima when assimilating into strongly nonlinear models. The problem of data assimilation in strongly nonlinear systems has been addressed by several researchers [Stensrud and Bao, 1992, Miller et al., 1994, Pires et al., 1996, Evensen, 1997]. As with this previous work the Lorenz model will be used as a simple example. However, the previous work has assumed that the system and the model are identical. In this work the case when the model is not an exact copy of the system will also be considered. The Quasi Static Variational Algorithm (QSVA) [Pires et al., 1996] will be explained and simple but effective improvement to this method will be outlined. The modified and standard QSVA algorithms will be compared in section 5.

134

2 Variational data assimilation and the adjoint method

As the name suggests variational data assimilation uses a variational method to find the model state at time $t = 0$ which leads to the best fit between the model and observations over the period $0 < t < T$. "Best fit" is usually means the minimum mean square error but other cost functions (or *objective* functions) can be used. The computational efficiency of the variational method is greatly aided by the existence of a means to calculate the gradient of the cost function in the space of initial conditions which is only slightly more computationally expensive than calculating the cost function itself. This is done by integrating the model equations forward in time and then integrating the *adjoint* version of the model backwards in time.

Consider a time-discrete dynamical model, $\mathbf{M}$, which can be written as

$$\mathbf{x}_{t+1} = \mathbf{M}(\mathbf{p}, \mathbf{x}_t) \tag{1}$$

where $\mathbf{p}$ is a vector of model parameters and $\mathbf{x}_t$ is the state of the model at time t. An *objective* function, J, which is a measure of the misfit between the model and the actual observations is now introduced. The goal is to minimize the objective function, J, under the constraint given by Eq. 1. This can be done using the method of undetermined multipliers. Thus the function that must be minimized is

$$L = J + \sum_{t=0}^{T} \lambda_t'(\mathbf{x}_{t+1} - \mathbf{M}(\mathbf{p}, \mathbf{x}_t)) \tag{2}$$

where λ_t is the vector of undetermined multipiers and a prime denotes the transpose. Differentiation of Eq. 2 with respect to λ_t recovers the original model equation. Differentiation of Eq. 2 with respect to $\mathbf{x}_t$ gives

$$\frac{\partial J}{\partial \mathbf{x}_t} - \left(\frac{\partial \mathbf{M}(\mathbf{p}, \mathbf{x}_t)}{\partial \mathbf{x}_t}\right)' \lambda_t + \lambda_{t-1} \tag{3}$$

Eq. 3 can be rearranged to give

$$\lambda_{t-1} = \left(\frac{\partial \mathbf{M}(\mathbf{p}, \mathbf{x}_t)}{\partial \mathbf{x}_t}\right)' \lambda_t + \mathbf{G}_t \tag{4}$$

where

$$\mathbf{G}_t = -\frac{\partial J}{\partial \mathbf{x}_t} \tag{5}$$

Eq. 4 is sometimes called the *adjoint* equation. Notice that it can be solved by integrating it backwards in time forced by the forcing function $\mathbf{G}_t$e The initial condition for λ is $\lambda_N = \mathbf{0}$. It will be shown below that this initial condition will result in the vector λ_0 being equal to the negative of the gradient of the objective function with respect to the initial condition, $\mathbf{x}_0$. First J is differentiated with respect to the initial condition, $\mathbf{x}_0$, to obtain

$$\frac{\partial J}{\partial \mathbf{x}_0} = -\sum_{t=0}^{T} \left(\frac{\partial \mathbf{x}_t}{\partial \mathbf{x}_0}\right)' \mathbf{G}_t \tag{6}$$

The matrix of partial derivatives in Eq. 6 must now be evaluated. This can be done by induction as follows.

$$\frac{\partial \mathbf{x}_t}{\partial \mathbf{x}_0} = \frac{\partial \mathbf{M}(\mathbf{p}, \mathbf{x}_{t-1})}{\partial \mathbf{x}_0} = \frac{\partial \mathbf{M}(\mathbf{p}, \mathbf{x}_{t-1})}{\partial \mathbf{x}_{t-1}} \frac{\partial \mathbf{x}_{t-1}}{\partial \mathbf{x}_0} \tag{7}$$

Taking the transpose of Eq. 7 gives

$$\left(\frac{\partial \mathbf{x}_t}{\partial \mathbf{x}_0}\right)' = \left(\frac{\partial \mathbf{x}_{t-1}}{\partial \mathbf{x}_0}\right)' \left(\frac{\partial \mathbf{M}(\mathbf{p}, \mathbf{x}_{t-1})}{\partial \mathbf{x}_{t-1}}\right)' = \left(\frac{\partial \mathbf{x}_t}{\partial \mathbf{x}_0}\right)' \mathcal{M}'_{t-1} \tag{8}$$

In the last step the matrix $\mathcal{M}_t$ has been introduced for convenience. This matrix is defined as

$$\mathcal{M}'_t = \left(\frac{\partial \mathbf{M}(\mathbf{p}, \mathbf{x}_t)}{\partial \mathbf{x}_t}\right)' \tag{9}$$

Substitution of Eq. 8 into Eq. 6 gives

$$\frac{\partial J}{\partial \mathbf{x}_0} = -\sum_{t=0}^{T} \mathcal{M}'_1 \mathcal{M}'_2 ... \mathcal{M}'_{t-1} \mathbf{G}_t \tag{10}$$

It will now be shown that λ_0 is equal to the negative of the expression given in Eq. 10. First Eq. 4 is rewritten as

$$\lambda_{t-1} = \mathcal{M}'_t \lambda_t + \mathbf{G}_t \tag{11}$$

Thus λ_{t-2} can be expressed as

$$\lambda_{t-2} = \mathcal{M}'_{t-1} \lambda_{t-1} + \mathbf{G}_t \tag{12}$$

Substituting for λ_{t-1} in Eq. 12 using Eq. 11 gives

$$\lambda_{t-2} = \mathcal{M}'_{t-1}(\mathcal{M}'_t \lambda_t + \mathbf{G}_t) + \mathbf{G}_{t-1} \tag{13}$$

This process can be continued to obtain an expression for λ_0.

$$\lambda_0 = \sum_{t=0}^{T} \mathcal{M}'_1 \mathcal{M}'_2 ... \mathcal{M}'_{t-1} \mathbf{G}_t = -\frac{\partial J}{\partial \mathbf{x}_0} \tag{14}$$

where the last step can be made by comparison with Eq. 10. Once the undetermined multipliers have been determined the gradient of the cost function with respect to the parameters, $\mathbf{p}$, can also be calculated.

$$\frac{\partial L}{\partial \mathbf{p}} = -\sum_{t=0}^{T} \lambda'_t \frac{\partial \mathbf{M}(\mathbf{p}, \mathbf{x}_t)}{\partial \mathbf{p}} \tag{15}$$

The gradients with respect to the initial conditions and the parameters can be combined to give $\nabla J = [-\lambda_0, \partial L/\partial \mathbf{p}]$ enabling the best combination of parameters and initial condition to be found. For this work the optimization was performed with an iterative Newton method from the IDL package. However, this requires the storage of the Hessian matrix. Real NWP models have around 10^4 variables and thus the Hessian matrix is unfeasibly large. Conjugate-gradient methods are usually employed for such large models [Navon and Legler, 1987].

In the above derivation a general cost function was used. A specific cost function, namely the mean square error, will now be considered. Let $\mathbf{H}$ be the *observation matrix* which relates the state of the system, $\mathbf{x}$, to the observations that would be made if the system were in the state $\mathbf{x}$. That is, if the system is in state $\mathbf{x}$ the vector of observations is given by $\mathbf{Hx}$. If $\mathbf{y}_t$ is the vector of actual observations at time t then the mean square error cost function is given by

$$J = \frac{1}{2} \sum_{i=0}^{T} (\mathbf{y}_i - \mathbf{Hx}_i)'(\mathbf{y}_i - \mathbf{Hx}_i) \tag{16}$$

Thus $\mathbf{G}_t$ is given by

$$\mathbf{G}_t = -\frac{\partial J}{\partial \mathbf{x}_t} = \mathbf{H}'(\mathbf{y}_t - \mathbf{Hx}_t) \tag{17}$$

To keep computational expense down when the adjoint method is used with large NWP models the forward model described by Eq. 1 is linearized about the basic trajectory. If the basic trajectory is written as $\bar{\mathbf{x}}_t$ and the deviation from this trajectory is written as $\mathbf{x}_t'$ then the linearization of Eq. 1 can be written as

$$\mathbf{x}_{t+1}' = \mathbf{L}(\bar{\mathbf{x}}_t)\mathbf{x}_t' \tag{18}$$

The linear model $\mathbf{L}$ is referred to as the *Tangent Linear Model* or TLM. The adjoint model given by Eq. 4 is also linearized about the trajectory $\bar{\mathbf{x}}_t$. The linearized adjoint model will be referred to as the ADJM.

3   The Lorenz model

As with previous work in this area the Lorenz model will be used as toy nonlinear system with which to test ideas.

The equations of the Lorenz model can be written in matrix form as

$$\frac{dX}{dt} = -\sigma(X - Y) \tag{19}$$

$$\frac{dY}{dt} = rX - Y - XZ \tag{20}$$

$$\frac{dZ}{dt} = XY - bZ \tag{21}$$

where σ, r and b are parameters of the model. The Lorenz model can be written in discrete form as

$$\begin{bmatrix} X_{t+1} \\ Y_{t+1} \\ Z_{t+1} \end{bmatrix} = \begin{bmatrix} 1 - \sigma\tau & +\sigma\tau & 0 \\ r\tau & 1 - \tau & -X_t\tau \\ Y_t\tau & 0 & 1 - b\tau \end{bmatrix} \begin{bmatrix} X_t \\ Y_t \\ Z_t \end{bmatrix} \tag{22}$$

where τ is the length of the time step used in integrating the model. The TLM of Eq. 22 is given by

$$\begin{bmatrix} X'_{t+1} \\ Y'_{t+1} \\ Z'_{t+1} \end{bmatrix} = \begin{bmatrix} 1 - \sigma\tau & +\sigma\tau & 0 \\ (r - \bar{Z}_t)\tau & 1 - \tau & 1 - \bar{X}_t\tau \\ \bar{Y}_t\tau & \bar{X}_t\tau & 1 - b\tau \end{bmatrix} \begin{bmatrix} X'_t \\ Y'_t \\ Z'_t \end{bmatrix} \tag{23}$$

Where an overbar denotes the trajectory about which the model is linearized and a prime denotes the deviation from this trajectory.

Using Eq. 9 the adjoint form of Eq. 22 is

$$\mathcal{M}'_t = \begin{bmatrix} 1 - \sigma\tau & (r - Z_t)\tau & Y_t\tau \\ \sigma\tau & 1 - \tau & X_t\tau \\ 0 & -X_t\tau & 1 - b\tau \end{bmatrix} \tag{24}$$

To illustrate a major problem in variational assimilation in chaotic systems a set of "observations" was generated using the Lorenz model by running it with the standard parameters ($\sigma = 10, r = 28, b = 8/3$) and taking the X component only as the observed variable, this corresponds to $\mathbf{H} = [1, 0, 0]$. The MSE cost function defined in Eq. 16 was then calculated as a function of error in the initial value of the Y coordinate. The results when the cost function was evaluated over periods of 1, 2, 4 and 10 dimensionless time units are shown in Fig. 1. For short periods the cost function is smooth and has a single, global minimum in the vicinity of the true initial condition. However, as the time period is increased local minima appear and the cost function becomes pathological for longer assimilation periods. Clearly finding the global minimum of the cost function when the assimilation time is 10 units is a daunting task. There are methods, such as simulated annealing and genetic algorithms, which could be tried but exploiting the option of controlling the cost function would seem to be the best line of attack.

4 Quasi Static Variational Assimilation

Quasi Static Variational Assimilation (QSVA) was introduced by Pires *et al.* [Pires et al., 1996]. The QSVA algorithm can be outlined as follows:-

1. Start with an initial guess of the state of the system and let the initial assimilation time be $n = \Delta$.
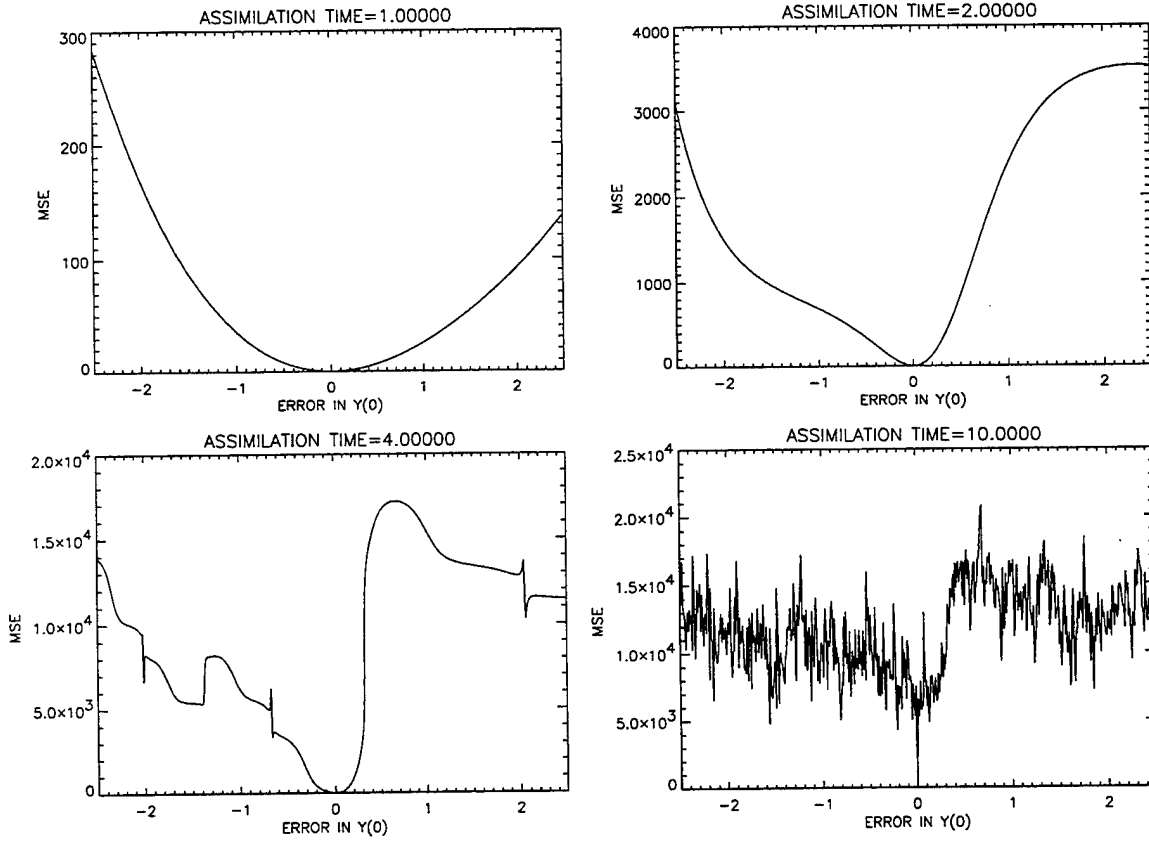
Figure 1: The MSE cost function in the Lorenz model as a function of error in the initial value of the Y coordinate. The function becomes increasingly pathological as the assimilation period is increased.

2. Minimize the MSE over the assimilation period $t = 0$ to $t = n$ to produce a new estimate of the state of the system at time $t = 0$.

3. Increase n to $n + \Delta$ and repeat step 2 until $n = T$.

The aim of the QSVA algorithm is to keep the estimate of the state of the system at time $t = 0$ in the basin of the global minimum, even as the local minima appear. In this algorithm Δ is a preset parameter. How should Δ be chosen? In their experiments with the Lorenz model Pires *et al.* used a value of $\Delta = 0.2/\tau$ where τ is the model time step. The most efficient value of Δ will depend on the particular system under consideration and also the region of phase space which the system is in at the time. In some regions of their phase space nonlinear systems can be well approximated by linear models and in these regions assimilation can be performed over relatively long periods. In other regions the assimilation period must be increased more slowly to remain in the basin of the global minimum. Thus a simple modification of the QSVA algorithm is proposed. In the modified algorithm Δ can be adapted so this modified algorithm will be refered to as *Adaptive Quasi Static Variational Assimilation* or AQSVA. The criteria for choosing the assimilation period will be that the model can "shadow" the observations over the assimilation period. The shadowing time T_s will be taken to mean that $\|\mathbf{Hx}_t - \mathbf{y}_t\| < \varepsilon$ for all $t \leq T_s$.

The AQSVA algorithm is as follows:-

1. Start with an initial guess of the state of the system. Integrate the model until either $t = T$ in which case $T_s = T$ or until $\|\mathbf{Hx}_t - \mathbf{y}_t\| \geq \varepsilon$ in which case T_s is the shadowing time.

2. Minimize the MSE over the period $t = 0$ to $t = T_s$ to produce a new estimate of the state of the system at time $t = 0$.

3. Unless $T_s = T$ or T_s is no longer increasing return to step 1.

The parameter ε must be chosen. It should be large enough to allow for experimental noise but it should be small enough such that the tangent linear model is valid. Since the TLM has a single quadratic minimum in the MSE cost function.

5   A comparison of QSVA and AQSVA

A series of numerical experiments was performed to compare the accuracy and efficiency of the standard QSVA algorithm and the modified AQSVA version. The Lorenz equations with parameters $\sigma = 10$, $r = 28$ and $b = 8/3$ were used as the system. The Lorenz equations were also used as the model into which the observations were assimilated. A perfect model and imperfect model were considered. Perfect model refers to the case when the parameters of the model were the same as those for the system while in the imperfect case the value of r in the model was changed from 28 to 30. In all the experiments only the X variable of the system was "observed". In some of the experiments noise was added to the observed values of X. This noise was uncorrelated and Gaussian with a standard deviation of 0.2. The full assimilation period in each experiment was 5.00 time units.

Perfect model/noise free	QSVA	AQSVA	Standard
Computational expense	36316	16460	41300
Shadowing time	5.00	5.00	0.42
Error in x_0	10^{-5}	3×10^{-4}	4.3

Table 1: Perfect model without observational noise.

Perfect model/noise s.d. = 0.2	QSVA	AQSVA	Standard
Computational expense	54912	17674	42700
Shadowing time	5.00	4.94	1.17
Error in x_0	0.12	0.12	5.8

Table 2: Perfect model with observational noise.

The results of the experiments are shown in Tables 1-4. Each table was constructed by averaging the results of 10 experiments with different initial conditions. All the initial conditions lay on the attractor of the system. As well as the QSVA and AQSVA algorithms standard MSE minimization was also included in the experiments. That is when an attempt was made to minimize MSE over the entire assimilation period from the initial first guess. The computational expense of each of the methods was measured in terms of integration steps. That is, forward integration steps of the TLM plus backward integration steps of the ADJM.

In the case of perfect models the accuracy of the AQSVA algorithm is comparable with the QSVA algorithm. Although the accuracy of the final estimate for the initial condition is slightly worse when using AQSVA this inaccuracy is much less than the inaccuracy in this estimate caused by adding noise to the observations. Both algorithms can find model trajectories that shadow the observations to the end of the assimilation period with the exception of one of the ten AQSVA cases without noise. Standard MSE minimization always performs very poorly. This isn't suprising given the fact that for an assimilation period of 5 time units the cost function has many local minima in which the optimization algorithm can become trapped. The most important difference between QSVA and AQSVA is the computational expense. AQSVA is typically about half as expensive as QSVA.

For the imperfect model making a direct comparison between the QSVA and AQSVA algorithms is complicated by the fact that they are essentially attempting to do different things. While the QSVA algorithm is trying to minimize the MSE over the entire assimilation

Imperfect model/no noise	QSVA	AQSVA	Standard
Computational expense	109940	25402	46000
Shadowing time	0.11	1.58	0.25
Error in x_0	9.28	2.60	3.90

Table 3: Imperfect model without observational noise.

Imperfect model/noise s.d. =0.2	QSVA	AQSVA	Standard
Computational expense	125028	15683	48400
Shadowing time	0.11	1.39	0.30
Error in x_0	27.6	2.66	4.34

Table 4: Imperfect model with observational noise.

period the AQSVA algorithm stops as soon as shadowing breaks down. This difference is reflected in the shadowing times which the algorithms achieve. QSVA shadowing times are never very long because in its efforts to fit the model to observations at later times the algorithm sacrifices a good fit for earlier times. The AQSVA algorithm does not make this sacrifice and it thus achieves shadowing times an order of magnitude longer than QSVA. AQSVA also obtains better estimates for the state of the system at the beginning of the assimilation period. Again AQSVA is several times cheaper computationally than QSVA. In the imperfect model case the computational saving of AQSVA is even higher than for the perfect model because AQSVA never assimilates to the end of the assimilation period.

The reason for the cheapness of AQSVA compared to QSVA can be explained as follows. In some parts of phase space the model is close to linear and thus MSE can be minimized over relatively large time periods without secondary minima becoming a problem. However, in QSVA the value of Δ is determined by the regions of phase space where the model is most nonlinear and where the assimilation period must be increased slowly. If this limiting value of Δ is used in all regions of phase space the algorithm is less efficient than AQSVA where the value of Δ can be varied, taking a large value when the model is well approximated by the TLM and a small value when it is not.

When data assimilation is being used to obtain an estimate of the state vector at time $t = T$ to initialize a forecast it is of no use if the AQSVA algorithm stops short of $t = T$. In this case the AQSVA can be run from the point when shadowing breaks down, using the estimate of the state vector at $t = T_s$ as the initial estimate for the next run of the AQSVA algorithm. This procedure can be repeated until a sequence of discontinuous trajectories has been constructed which shadow the observations for the complete assimilation period.

6 AQSVA in a system with dynamical noise

In the previous section imperfect model was taken to mean that the parameters of the model were not the same of those of the system. Another way in which a model can be imperfect is by lacking extrinsic forcing terms which are present in the system. To investigate this effect stochastic forcing terms were added to the Lorenz equations of the system. Thus the system

142

became

$$\frac{dX}{dt} = -\sigma(X - Y) + W_X(t) \tag{25}$$

$$\frac{dY}{dt} = rX - Y - XZ + W_Y(t) \tag{26}$$

$$\frac{dZ}{dt} = XY - bZ + W_Z(t) \tag{27}$$

where $W_{X,Y,Z}$ represent uncorrelated gaussian noise with zero mean and variance $w^2 = 25.0$. Again the X coordinate of the system was the observed variable. The AQSVA algorithm was then used to find a shadowing trajectory of the model which had the same parameters as the system but lacked the stochastic forcing terms. A typical result is shown in Fig. 2.

The thin solid line is the X coordinate of the system with stochastic forcing. The dashed line is the X coordinate of the model when the actual initial condition is used. Note that in this case the trajectoroy of the model deviates from the observations after about 3 time units. The thicker solid line is the trajectory found using the AQSVA algorithm. This trajectory shadows the stochastically forced system for about 6 time units even though the forcing terms were missing. The reason for this is that in the Lorenz system the relatively small forcing terms are only important when the system is close to a decision point in phase space. At such a point a small perturbation can determine which of the two unstable fixed points the system will orbit. A slight change in the state of the system at $t = 0$ can "fake" the effect of this forcing.

7 An alternative cost function

As described above one of the main problems with the MSE cost function in strongly nonlinear systems is the existence of many local minima in addition to the global minimum. Perhaps an alternative approach to the problem is to use a different cost function. The length of time for which the model can shadow the observations would seem to be a reasonable measure of the validity of the model. The shadowing time, T_s, can be written as follows.

$$T_s = \sum_{i=0}^{T} \prod_{k=0}^{i} \mathcal{H}(\varepsilon^2 - r_k^2) \tag{28}$$

where $\mathcal{H}$ is the Heaviside step function and $r_k = \|\mathbf{y}_k - \mathbf{H}\mathbf{x}_k\|$.

Note that the step function is zero if the distance between the model and observations exceeds ε. Also note that each term in the sum over time contains a product of all the step functions up to that time, thus if any term is zero all the terms that follow it are zero. Equation 28 does not have a continuous derivative which can be used to force the adjoint equation. The step function can be replaced by a smooth approximation of a step function, $\mathcal{K}$. A *pseudo-shadowing time* can now be defined as
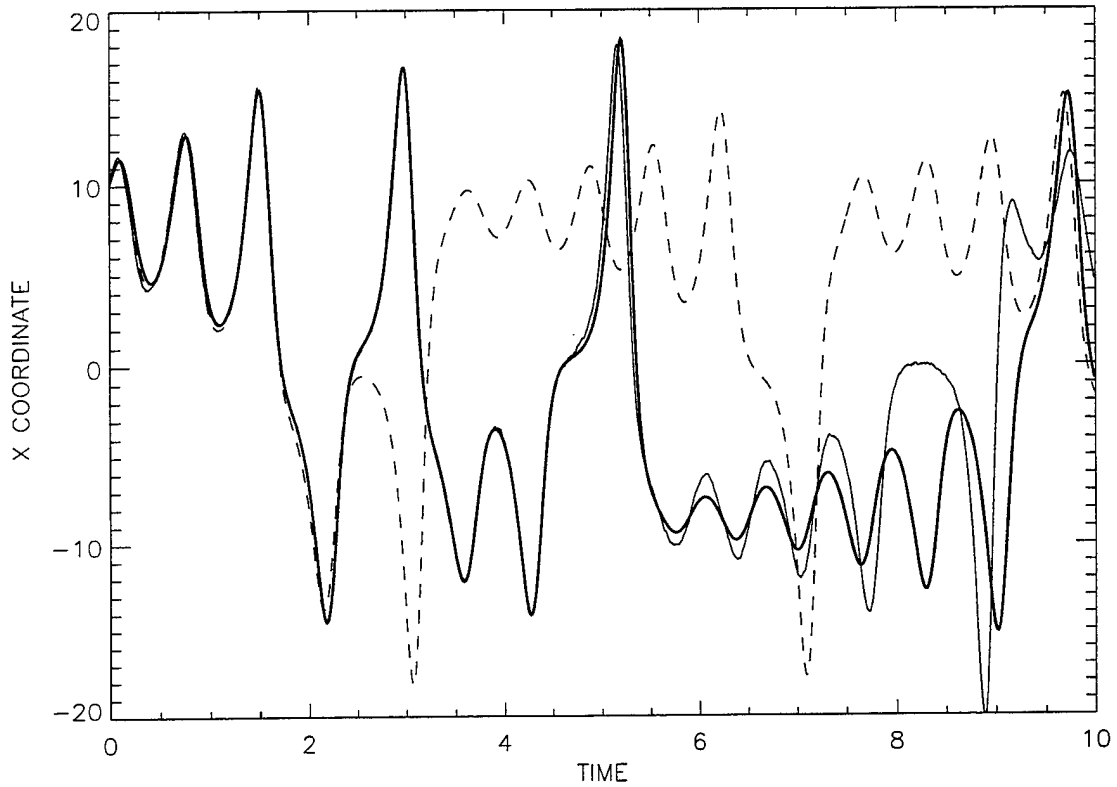
Figure 2: Assimilation in the presence of dynamical noise. The thin solid line is the X coordinate of the system with dynamical noise. The dashed line is the X coordinate of the model with identical parameters to the system and initialized with the same initial state but without the stochastic forcing terms. The thick solid line (which overlies the thin solid line until about 6 time units) is the X coordinate of the model without the dynamical forcing terms after the thin solid line was assimilated into it.

$$T_s^* = \sum_{i=0}^{T} \prod_{k=0}^{i} \mathcal{K}(\varepsilon^2 - r_k^2) \tag{29}$$

If the cost function is defined as $J = -T_s^*$ the forcing term for the adjoint equation is given by

$$\mathbf{G}_t = -\frac{\partial J}{\partial \mathbf{x}_t} = \frac{2\mathbf{H}'(\mathbf{y}_t - \mathbf{H}\mathbf{x}_t)}{\mathcal{K}(\varepsilon^2 - r_t^2)} \left[\frac{d\mathcal{K}}{dr_t^2}\right]_{\varepsilon^2 - r_t^2} \sum_{i=t}^{T} \prod_{k=0}^{i} \mathcal{K}(\varepsilon^2 - r_k^2) \tag{30}$$

A possible form of the function $\mathcal{K}$ is

$$\mathcal{K}(z) = \left\{ \begin{array}{ll} 0 & z < -\beta \\ -\frac{1}{4\beta^3}z^3 + \frac{3}{4\beta}z + \frac{1}{2} & -\beta \leq z \leq +\beta \\ 1 & z > +\beta \end{array} \right\} \tag{31}$$

In numerical experiments using the Lorenz model the alternative cost function described by Eqs. 30 and 31 did not produce estimates of the initial state as accurately as AQSVA. This may be because the model used was always very similar to the system, even in the "imperfect" model experiments. The pseudo-shadowing cost function may be an effective way to maximize shadowing time in models which are not structurally the same as the systems they are modeling.

8 Summary

The QSVA algorithm introduced by Pires *et al.* [Pires et al., 1996] has been slightly modified to include adaptive increments in the assimilation time determined by the models ability to shadow observations. The adaptive QSVA (AQSVA) algorithm was compared with the conventional QSVA using the Lorenz equations as a simple system-model combination. The AQSVA method was found to be more computationally efficient than standard QSVA.

An alternative to the MSE cost function based on shadowing time was proposed although it was not determined what practical advantages this *pseudo-shadowing* cost function may have over AQSVA.

145

References

[Evensen, 1997] Evensen, G. (1997). Advanced data assimilation for strongly nonlinear dynamics. *Mon. Wea. Rev.*, 125:1342–1354.

[Miller et al., 1994] Miller, R. N., Ghil, M., and Gauthiez, F. (1994). Advanced data assimilation in strongly nonlinear dynamical systems. *J. Atmos. Sci.*, 51:1037–1056.

[Navon and Legler, 1987] Navon, I. and Legler, D. (1987). Conjugate-gradient methods for large-scale minimization in meteorology. *Mon. Wea. Rev.*, 115:1479–1502.

[Pires et al., 1996] Pires, C., Vautard, R., and Talagrand, O. (1996). On extending the limits of variational assimilation in nonlinear chaotic systems. *Tellus A*, 48:96–121.

[Stensrud and Bao, 1992] Stensrud, D. and Bao, J.-W. (1992). Behaviors of variational and nudging assimilation techniques with a chaotic low-order model. *Mon. Wea. Rev.*, 120:3016–3028.

Towards a Non-Linear Model for Spicules

Aaron C. Birch

1   Introduction

Spicules are approximately 7,000 km high jets of hot plasma seen on the sun extending from the chromosphere into the lower corona. Each jet lasts roughly ten minutes and then disappears. These jets have been previously discussed in the literature (for example, see [Hasan and Venkatakrishnan, 1981], [Athay, 1984], and [Umurhan et al., 1998]); there is no consensus on the driving mechanism. This paper follows the approach of Umurhan, Tao, and Spiegel ([Umurhan et al., 1998]) who suggested that spicules are a non-linear effect of overstable acoustic modes.

There are two main parts to this work. The first is to write down an eigenvalue equation that can be numerically solved to obtain frequencies and growth rates for the various oscillation modes, considered as infinitesimal perturbations to a background state, of a chromosphere-like layer. The second part is to use the results of the linear stability problem to derive a non-linear equation to describe the time evolution of the layer.

The main outline of the paper is as follows: Section 2 contains a brief outline of the basic structure of the sun and spicules. Section 3 describes the time scales involved in the problem. The basic equations that will be used to describe the plasma are introduced in Section 4 and linearized in Section 5. Section 6 contains a discussion of the energy equation and Newton's law of cooling. Section 7 discusses the various background atmospheres around which the linearization is done. The boundary conditions for the problem are described in Section 8. Results for the case of the isothermal and polytrope background are shown in Sections 9 and 10. Sections 11 and 12 develop the amplitude equation. The remaining sections discuss the conclusions and possibilities for future work.

2   A Brief Review of Spicules and The Sun

The sun has radius of 7×10^5 km. The inner 20% by radius is where the nuclear burning takes place and is responsible for energy generation. The region below 70% of the solar radius is called the radiative zone, in this region energy is carried outwards by radiation. Above the radiative zone and extending to the surface is the convection zone, where as the name implies energy is carried outwards mainly by convection. The top of the convection zone, known as the photosphere, produces most of the visible light we see. At the top of the photosphere the temperature, which decreases steadily outwards from the core, reaches its minimum of about 6,000 K. Above the photosphere is the chromosphere, a layer roughly 4,000 km thick, in which

147

the temperature increases with height from the photospheric value to approximately 10,000 K while the density and pressure are steadily decreasing. At the top of the chromosphere the temperature starts increasing very rapidly with height, up to the two million degrees of the corona.

The surface of the photosphere shows two main spatial scales of convection. The smaller of these scales is the granule scale, which is 1000 km. Granules are up-drafts of hot plasma, with thin boundaries of down-going cooler plasma. The larger length scale is due to supergranules, each of which contains approximately 1,000 granules. Supergranules, like granules, consist of a widespread warm up-welling surrounded by thin lanes of cooler down-drafts. The flow due to the supergranular structure sweeps granules, as well as magnetic flux, towards the boundaries between supergranules. As a result the magnetic field above the supergranule lanes can be up to 2000 G, compared to the usual background of a few gauss. Spicules tend to occur above these supergranule lanes. As a result, it is suggested that the formation of spicules is related to the presence of the magnetic field.

Spicules can be seen in $H\alpha$, the 660 nm spectral line of hydrogen, images of the solar limb as well as of the disk. In limb images they appear as extended, much taller than they are wide, bright regions. They are seen to extend to heights of 7,000 to 10,000 km above the photosphere and last for roughly ten minutes (e.g. [Suematsu et al., 1995]).

3 Time Scales

The time scales involved in the problem determine what physics needs to be included when describing the chromosphere. As only the fundamental modes of waves in a chromosphere-like layer are considered the length scale is taken to be the height of the chromosphere, 4,000 km. The sound speed is approximately 10 $\frac{km}{s}$. 200 G is taken as the magnetic field strength. The important times are the sound speed transit time, the Alfvén wave transit time, and resistive diffusion time, the viscous damping time, and the rotation period. In the expressions for these times L is the length scale, c_s is the sound speed, c_a is the Alfvén speed, and η is the resistivity. The expressions and values for these times are then:

$$T_{sound} = \frac{L}{c_s} = 400s$$

$$T_{Alfvén} = \frac{L}{c_a} = 200s$$

$$T_{resist} = \frac{L^2}{\eta} = 10^7 years$$

T_{sound} is the time for a vertically pressure perturbation to cross the layer, $T_{Alfvén}$ is the time for a vertically propagating magnetic field disturbance to cross the layer. The resistive

diffusion time T_{resist} is the time scale for the decay of magnetic field due to finite conductivity. Because the resistivity of the chromosphere is so small compared to the length scale in the problem, the resistive diffusion term will be neglected in the MHD equations in the next section. The viscous diffusion time is the time for a velocity perturbation to decay in the absence of other effects. It is not clear what value to use for the viscosity, perhaps turbulent viscosity is important. The rotation period is a approximately a month, so rotation is not a large effect on waves with periods of minutes, of order the sound or Alfvén wave transit times.

4 MHD equations

The standard ideal MHD equations are used to describe the plasma. ρ is the density, P is the pressure, $\vec{v}$ is the velocity, $\vec{J}$ is the current, $\vec{B}$ is the magnetic field, $\vec{E}$ is the electric field, T is the temperature. These quantities are functions of time and space. C_v is the heat capacity at constant volume and is considered fixed. R is the gas constant. The equations are:

$$\frac{\partial \rho}{\partial t} + \nabla \cdot (\rho \vec{v}) = 0 \tag{1}$$

$$\rho \frac{d\vec{v}}{dt} = -\nabla P + \rho g \hat{z} + \frac{1}{c} \vec{J} \times \vec{B} \tag{2}$$

$$\frac{\partial \vec{B}}{\partial t} = -\nabla \times \vec{E} \tag{3}$$

$$C_v \rho \frac{dT}{dt} + P \nabla \cdot \vec{v} = Q(T, \rho) \tag{4}$$

$$P = R\rho T \tag{5}$$

$$\vec{J} = \frac{c}{4\pi} \nabla \times \vec{B} \tag{6}$$

$$\vec{E} = -\vec{v} \times \vec{B} \tag{7}$$

Equation 1 is the usual continuity equation, expressing the fact that there are no sources or sinks of mass in the problem. Conservation of momentum is expressed by Equation 2. The forces on the right hand side are the pressure gradient, gravity, and the Lorentz force.

Gravity is assumed to act only the in the $+\hat{z}$ direction. Equation 3 is the usual Faraday's Law. Conservation of energy is given by Equation 4, the function Q gives the rate at which energy is injected into (or removed from) the fluid at a given point and is in principle a function of temperature and density. The equation of state is assumed to be that for an ideal gas and is given in Equation 5. Equation 6 is the pre-Maxwell prescription for the current. The displacement current is assumed to be negligible, so this set of equation is not expected to be valid at high frequencies. The final equation gives the electric field in terms of the magnetic field. It arises from Ohm's law and the infinite conductivity assumption of Ideal MHD. If the conductivity σ is infinite then in the frame of reference moving with the fluid the current $\vec{J} = \sigma(\vec{E} + \vec{v} \times \vec{B})$ must be zero, from which a relation between $\vec{E}$ and $\vec{B}$ is obtained. Once Q is specified this set of equations, along with boundary conditions and initial conditions, gives a complete description of the time evolution of the system.

5 Linearization

In order to study the linear stability problem the MHD equations must be linearized around a background state. In this work only the two dimensional plane-parallel problem is studied, x describes the horizontal direction, z describes the vertical. The background state is assumed static. Gravity and the background magnetic field are assumed to be constant and in the $\hat{z}$ direction. The background pressures is given by P_0, the density by ρ_0, and field by $B_0\hat{z}$. The variables $P, \rho, \theta, \vec{v} = (U, W)$, $\vec{B} = (B_x, B_z)$ describe the perturbations to the pressure, density, temperature, velocity, and magnetic field respectively. The perturbations are assumed to have the form $f(z) \exp i(kx - \omega t)$. The linearized equations, given below, along with a prescription for boundary conditions and a background state then constitute a linear eigenvalue problem for the complex frequency ω.

$$-i\omega\rho + W\rho' + \rho_0(ikU + W') = 0$$

$$-i\omega U = -\frac{ikP}{\rho_0} + \frac{iB_0{}^2}{4\pi\rho_0\omega}(-k^2U + U'')$$

$$-i\omega W = -\frac{P'}{\rho_0} + g\frac{\rho}{\rho_0}$$

$$C_v\rho_0(-i\omega\theta + WT_0') + P_0(ikU + W') = Q(\theta, \rho, T_0, \rho_0)$$

$$\frac{P}{P_0} = \frac{\rho}{\rho_0} + \frac{\theta}{T_0}$$

The real part of ω gives the frequency of the mode and the imaginary part is the growth rate. The linearization makes it clear the the magnetic field causes only a force in the horizontal direction and is only due to motions in the horizontal direction. Motion along the background field is not affected at all. Note now that the function Q, which originally was a function of the total T and ρ must now be considered a function of both the background and perturbation values of these quantities. In order to further simplify these equations a form of Q must be chosen.

6 Heating Function

As mentioned earlier the function Q describes that rate at which heat is added or removed from the plasma as a function of its temperature and density. The chromosphere, to a good approximation, is optically thin (e.g. [Syrovat-skii and Zhugzhda, 1968]). Optically thin perturbations can be described by Newton's law of cooling: $Q(\theta, \rho) = -q\rho_0 C_v \theta$ ([Spiegel, 1957]). In general q is a function of the background state. For this work only the case in which q is a constant is considered. For q constant and no flow the non-linearized heat equation is:

$$\frac{\partial T}{\partial t} = -q(T - T_0)$$

For the case $q > 0$ deviations in the temperature T from the background value T_0 decay with a time scale of $\frac{1}{q}$. If $q < 0$ then any temperature perturbation is unstable, growing exponentially with time scale $\frac{-1}{q}$. In general, though not always, $q > 0$ has the effect of damping waves that produce temperature perturbations, and $q < 0$ increases the growth rate of waves that produce temperature perturbations.

7 Background State

In addition to the function Q the background state also must be specified. The full problem of heating in the chromosphere is unsolved. As a result it is not clear what the appropriate background model is. For lack of a better model, the three simplest temperature profiles are examined: a constant, a linear function of depth, and a quadratic function of depth. All three of these background temperatures can be obtained from the diffusion equation, with constant thermal conductivity κ and heating rate h,

$$-\kappa \frac{\partial^2 T}{\partial z^2} = h$$

For the case $h = 0$ a linear temperature profile is obtained, of which the constant profile is a special case. For nonzero h a parabolic profile is obtained. In all cases gravity is assumed to be constant and the equations of state is that of an ideal gas. A further assumption, for the sake of simplicity, is that the background state is in hydrostatic equilibrium. This assumption is probably not good for the chromosphere.

7.1 Isothermal Atmosphere

For the case of T constant,

$$\frac{dP}{dz} = g\rho = \frac{gP}{RT}$$

With the definition of the scale height $H = \frac{RT}{g}$, $P(z)$ has the form $\tilde{P}\exp\frac{z}{H}$, where $\tilde{P}$ is the pressure at $z = 0$. The scale height H is the distance it takes for the density and pressure to increase by a factor e. It is reasonable the this distance increases with temperature and decreases with increasing strength of gravity, g. It can be shown that this atmosphere is always convectively stable.

7.2 Polytrope Atmosphere

Suppose $T = \beta z + \alpha$. For $\beta \neq 0$, α can be made zero by choice of coordinates. Then:

$$\frac{dP}{dz} = g\rho = \frac{gP}{R\beta z}$$

The solution of which is $P(z) = \tilde{P}(\frac{z}{z_s})^{(\frac{g}{R\beta})}$. Here $\tilde{P}$ is the value of P at $z = z_s$. z_s has the units of length and is put in only to make the units look correct. The definition of $m = \frac{g}{R\beta} - 1$ is commonly used. With this definition $P(z) = \tilde{P}(\frac{z}{z_s})^{m+1}$ and $\rho(z) = \tilde{\rho}(\frac{z}{z_s})^{m}$. This atmosphere is known as a polytrope and can be either convectively stable or unstable depending on the relationship between m and $\gamma = \frac{C_p}{C_v}$. For $m < \frac{1}{\gamma-1}$ the atmosphere is unstable, while for $m > \frac{1}{\gamma-1}$ it is not. The instability arises from the combination of the stratification with gravity.

7.3 Constant Heating

For the case of $h \neq 0$ the temperature has the form $\frac{-h}{2\kappa}z^2 + \beta z + \alpha$. Again by change of coordinates α can be made zero. By the same method as in the previous two sections the pressure profile of this atmosphere is found to be $P(z) = \tilde{P}(\frac{z}{\beta - \frac{h}{2\kappa}z})^{(\frac{g}{R\beta})}$. This atmosphere is more interesting then the previous two. In the other cases the temperature and pressure both increase with depth. With constant non-zero heating there is the possibility of having the temperature decrease with depth. This feature makes this atmosphere more like the chromosphere than the previous two.

8 Boundary Conditions

Boundary conditions must be specified in order to complete the formulation of the linear stability problem. The linearized version of the equations are fourth order in space. As a result four boundary conditions are required. The traditional boundary condition that the

vertical velocity, W, vanish on the top and bottom of the layer is used. This condition ensures that the mechanical part of the energy flux across the boundary is zero.

Two more boundary conditions are required. Limits on the possible boundary conditions on the magnetic field can be found be requiring that the Poynting vector $\vec{S} = \vec{E} \times \vec{B}$ at the boundary be parallel to the boundary. The result of the calculation is that for $k \neq 0$ either B_x or B_z must be zero on the boundary. The physical meaning of these boundary conditions requires some discussion.

The basic problem of selecting boundary conditions for this problem is that the boundaries do not correspond to clear physical boundaries, but rather have been selected arbitrarily. In order to deduce the physical meaning of the various boundary conditions on $\vec{B}$ it is necessary to make assumptions about what is outside the layer in which the eigenvalue problem is to be solved.

8.1 $B_x = 0$

For the case $k \neq 0$ the boundary condition $B_x = 0$ is equivalent to $U' = 0$ which is a statement of no stress on the boundary. In particular U is allowed to be nonzero on the boundary. Another point of view is that if the magnetic perturbation to the field outside the layer is required to be vertical, then $B_x = 0$ on the boundary implies that no surface currents are allowed, as can be seen by the standard Ampere's law argument. In order to maintain $\nabla \cdot \vec{B} = 0$ there would have to be a vertical perturbation to the field outside the layer to match the perturbation inside.

8.2 $B_z = 0$

The boundary condition $B_z = 0$ is equivalent to considering the outside of layer to be a perfect conductor with fixed field $B_0 \hat{z}$ in it. As a result of $\nabla \cdot \vec{B} = 0$, B_z must vanish at the boundary. A consequence of this condition is that for $k \neq 0$ the horizontal velocity must vanish at the boundary. The can be understood in terms of line pinning. Any horizontal motion along the boundary would drag field lines with it, this motion is therefore not allowed as the field lines are stuck into the boundary and cannot move.

9 Polytrope Atmosphere

The problem of the stability of adiabatic motions ($q = 0$) in a polytrope atmosphere without magnetic field is well understood (e.g. [Lamb, 1925]). The adiabatic problem with magnetic field has been studied in the case of a complete polytrope, i.e. a polytrope that extends from $z = 0$ to $z = \infty$ (e.g. [Bogdan and Cally, 1997]) as well as for a generic polytrope layer (e.g. [Kaplan and Petrukhin, 1965]). The case without magnetic field but including heat transfer by conduction rather than Newton's law of cooling has been previously studied (e.g. [Lou, 1990]), as has the case of particular spatially dependent cooling times $\frac{1}{q}$ (e.g. [Macdonald and Mullen, 1997], [Spiegel, 1964]). There are few generalizations than can be obtained from these studies besides that the existence of unstable modes depends sensitively

153

on the exact form of heat transfer that is used. In this study only the case where the cooling time is independent of depth is considered.

9.1 Non-Dimensionalization

For the polytrope background atmosphere it is convenient to non-dimensionalize the MHD equations by scaling the pressure, density and velocity perturbations by the background pressure, density, and adiabatic sound speed at the bottom of the layer. The length scale, z_s, is the distance from the height where the density is zero to the bottom of the layer. In all of the calculations for polytrope atmospheres shown here the layer is chosen to extend from $z = 0.1$ to $z = 1$. A result of this scaling is that the dimensionful frequency is given by $\frac{\omega c}{z_s}$ where c is the adiabatic sound speed. For the values assumed for the chromosphere this implies that the dimensionful frequency is $\frac{1}{400}$ Hz times the dimensionless frequency. The dimensionful horizontal wavenumber is given by $\frac{k}{z_s}$ where k is the dimensionless horizontal wave number.

9.2 Results

The results of numerical calculations, done in terms of the dimensionless variables, of the frequencies and growth rates for the fundamental acoustic and gravity modes are shown for a sample stable polytrope in Figure 1 and for an unstable polytrope in Figure 2, in both cases without magnetic field. The first figure shows that both the acoustic and gravity wave branches have zero growth rate as one would expect for a stable atmosphere. The gravity wave frequency goes to zero with decreasing wavenumber. The acoustic wave has a minimum frequency, this would be this case even in an infinitely thick layer though the actual minimum would be different. The second figure shows that the acoustic mode has zero growth rate and has a dispersion relation much like that for the stable atmosphere. The gravity mode is completely different, however. The gravity mode is not oscillatory in time at all, rather it grows exponentially.

If magnetic field is added to the problem, but the adiabaticity of the oscillations is maintained, a new set of features arises. The most striking feature of the magnetized polytrope, with boundary conditions $B_x = 0$ on the top and bottom of the layer, is that the magnetic field can make unstable polytropes behave in a stable way. Kaplan and Petrukhin ([Kaplan and Petrukhin, 1965]) argued that stabilization of the transverse mode by the magnetic field only occurs, in the adiabatic case, for $\frac{m+1}{m} < \gamma + \frac{B^2}{4\pi}$. This claim has not been investigated here. One example where the magnetic fields makes the layer stable is shown in Figure 3. The dotted line represents the more longitudinal mode and the solid the more transverse mode. Growth rates are not shown because they are all zero. The modes are identified by their $k = 0$ behavior. At $k = 0$ the equations separate into two decoupled eigenvalue problems, one for $U(z), \vec{B}(z)$ and one for $W(z), P(z)$. The first eigenvalue problem describes the vertically propagating Alfvén mode, which is transverse and causes no density or pressure perturbations. The second eigenvalue problem describes the vertically propagating acoustic mode, which is unaffected by the magnetic field. By starting at $k = 0$ with one of these solutions and moving up in k the behavior of each branch can be calculated.

The ability of the magnetic field to completely suppress convective instability is likely due to the reversibility of fluid parcel motions. For nonzero q as well as B_0 the unstable polytrope regains its instability. This is shown in Figure 4, again using the boundary conditions $B_x = 0$. This figure has a number of important features. As in previous plots the dashed line is for the longitudinal mode and the solid line for the transverse mode. The transverse mode is unstable for large k while the longitudinal mode is unstable for small k. this is a general feature that appears in many of the calculations shown in this paper. Another feature is that the modes come very close to crossing. As a result, resonance between the modes, despite their different physical characteristics, might be an important effect.

10 Isothermal

Adiabatic oscillations in an isothermal atmosphere in the absence of magnetic field have been studied and well understood (e.g. [Lamb, 1925]). The isothermal atmosphere is always convectively stable and supports three types of modes: the acoustic, Lamb, and the gravity waves. With the addition of the magnetic field there are only two fundamental modes, a mostly transverse and a mostly longitudinal mode.

The problem of the isothermal atmosphere with a constant magnetic field and Newton's law of cooling has been previously studied (e.g. [Babaev et al., 1995]). Babaev and coworkers considered the case of an infinite isothermal atmosphere and found analytic solutions to the linear stability problem. They found that all the modes were stable and discussed the damping rates in the limits of strong and weak magnetic field.

10.1 Non-Dimensionalisation

For the numerical calculations with isothermal atmosphere background, pressure and density perturbations are scaled by the values of background pressure and density at the middle of the layer. The velocity perturbations are scaled by the adiabatic sound speed. The scale height is used as the length scale. The calculations were done on a layer that extends from $z = -0.5$ to $z = 0.5$.

10.2 Results

The results of the calculations for the isothermal atmosphere are qualitatively similar to those of [Babaev et al., 1995] in that for $q > 0$ there are no unstable modes, as long as the boundary conditions on $\vec{B}$ are either $B_x = 0$ or $B_z = 0$. For $q < 0$, all modes are overstable. For the case $q < 0$ the fundamental longitudinal mode is most unstable for $k = 0$ while the transverse mode is most unstable for some finite k which depends on the parameters of the problem. The transverse mode is always marginally stable for $k = 0$ as the vertically propagating transverse mode does not produce temperature perturbations.

11 General Form of The Amplitude Equation

As a result of the unrealistic nature of the background atmospheres considered in this work no attempt was made at the derivation of a detailed amplitude equation. Instead the procedure of Fauve ([Fauve, 1991]) is followed in order to derive a schematic amplitude equation.

Consider the isothermal atmosphere with a background magnetic field. For $q = 0$ the fundamental longitudinal mode is marginally stable. For $q > 0$ the fundamental longitudinal mode is overstable with maximum growth at $k = 0$. Define $\epsilon = -q$ as the control parameter, which will be useful later. The amplitude $A(k, t)$ is then introduced through the equation:

$$\psi(x, z, t) = \int A(k, t)e^{ikx}\phi_k(z)dk \tag{8}$$

Where $\phi_k(z) = (\vec{v_k}(z), \vec{B_k}(z), P_k(z))$ describes the velocity, magnetic field, and density perturbation eigenfunctions associated with the fundamental longitudinal mode with horizontal wavenumber k. $\psi(x, z, t)$ then describes the behavior of these fields in time as well as space. It is important to note that the effect of modes other than the fundamental longitudinal mode is ignored. The other modes could be easily included. With the simplifying, but incorrect, assumption that $\phi_k(z) = \phi_0(z)$ Equation 8 becomes:

$$\psi(x, z, t) = \phi_0(z) \int A(k, t)e^{ikx}dk = \phi_0(z)A(x, t)$$

Thus if the amplitude $A(x, t)$ is known, the behavior of our physical fields can be found by multiplying by the eigenfunction for $k = 0$.

Fauve explains that for the case of overstable modes with most unstable wave number k the lowest order non-linear equation for the time evolution of $A(k, t)$ is

$$\frac{\partial A(k, t)}{\partial t} = (i\omega(k) + \eta(k))A(k, t) + \alpha|A(k, t)|^2 A(k, t)$$

Here $\omega(k)$ is the mode frequency as a function of k and $\eta(k)$ is the growth rate. The Fourier transform of this equation gives the time dependence of the amplitude $A(x, t)$. The Fourier transform of the linear part is straightforward and gives a linear operator involving even power of ∂_x, as only even powers of k can appear by symmetry. The non-linear part is quite complicated. In order to proceed without working out the details, the Swift-Hohenberg argument ([Manneville, 1990]) is used to show that:

$$\int |A(k, t)|^2 A(k, t)e^{ikx}dk \approx |A(x, t)|^2 A(x, t)$$

With this assumption:

$$\frac{\partial A(x, t)}{\partial t} = L(\partial_x{}^2)A(x, t) + \alpha|A(x, t)|^2 A(x, t)$$

12 Particular Form of the Amplitude Equation

In the previous section the general form of the amplitude equation was derived. In this section the linear operator $L(\partial_x{}^2)$ is obtained from the Fourier transform of $i\omega(k) + \eta(k)$. In order facilitate this computation a function of the form $\epsilon\delta + \frac{\epsilon\kappa}{1+\beta k^2}$ is fit to the numerical results for the growth rate. In addition the frequency is assumed constant, equal to ω_0. This approximation could easily be relaxed. The calculation that needs to be done then is:

$$\int (i\omega_0 + \epsilon\delta + \frac{\epsilon\kappa}{1+\beta k^2})A(k,t)\exp ikx\, dk$$

which gives:

$$(i\omega_0 + \epsilon\delta)A(x,t) + \epsilon\kappa C(x,t)$$

with

$$(1 - \beta\Delta)C(x,t) = A(x,t)$$

The complete form of the amplitude equation is then, (explicitly noting that α is order ϵ) :

$$\frac{\partial A(x,t)}{\partial t} = (i\omega_0 + \epsilon\delta)A(x,t) + \epsilon\kappa C(x,t) + \epsilon\alpha|A(x,t)|^2 A(x,t)$$

with

$$(1 - \beta\Delta)C(x,t) = A(x,t)$$

13 Conclusions

The general eigenvalue problem for the growth rates of normal modes of 2D MHD with Newton's law of cooling in a layer with a variety of boundary conditions has been set up and solved for both isothermal and polytrope backgrounds with constant vertical magnetic field. The linear stability of the different modes depends strongly on the boundary conditions as well as the background atmosphere.

For the particular case of the boundary condition $B_z = 0$ and an isothermal background atmosphere it was found the modes are always stable for $q > 0$ and unstable for $q < 0$. An amplitude equation was developed for the overstable fundamental acoustic modes for the case $q < 0$. The amplitude equation was derived with the assumption that the only important branch is the fundamental acoustic branch and by making a Swift-Hohenberg type simplification of the Fourier Transform of the nonlinear term.

14 Future Work

This work is far from complete. Viscosity of any sort has not been included. It is likely that introducing a finite viscosity would reduce the growth rates or perhaps even damp the large horizontal wave number modes. This would introduce a new horizontal length scale into the problem and would alter the amplitude equation significantly. The expansions in the eigenfunctions may have to be done around finite k instead of $k = 0$.

The issue of resonance between modes was not treated in the work, and may be an important effect. For many choices of parameters there appears to be nearly a mode crossing between the longitudinal and transverse waves.

A vast improvement in the realism of the problem could be made through the use of a more accurate background atmosphere. For both the polytrope and the isothermal atmosphere the temperature either increases with pressure and density or remains constant. The temperature of the chromosphere decreases with increasing density and pressure.

15 Acknowledgments

References

[Athay, 1984] Athay, R. (1984). The origin of spicules and the heating of the lower transition region. *ApJ*, 287:412–417.

[Babaev et al., 1995] Babaev, E., Dzhalilov, N., and Zhugzhda, Y. D. (1995). Nonadiabatic magneto-acoustic-gravity waves in a stratified atmosphere. *Astronomy Reports*, 39:211–219.

[Bogdan and Cally, 1997] Bogdan, T. and Cally, P. (1997). Waves in magnetized polytropes. *Proc. R. Soc. Lond.*, 453:943–961.

[Fauve, 1991] Fauve, S. (1991). Amplitude equations in dissipative systems. In *1991 Summer Study Program in Geophysical Fluid Dynamics: Patterns in Fluid Flow*. Woods Hole Oceanographic Institute, Woods Hole.

[Hasan and Venkatakrishnan, 1981] Hasan, S. and Venkatakrishnan, P. (1981). A time dependent model for spicule flow. *SolPhys*, 73:45–57.

[Kaplan and Petrukhin, 1965] Kaplan, S. and Petrukhin, N. (1965). The theory of convection in a polytropic atmosphere with a uniform magnetic field. *Soviet Physics - Astronomy*, 9(1):55–57.

[Lamb, 1925] Lamb, H. (1925). *Hydrodynamics*. Cambridge University Press, London.

[Lou, 1990] Lou, Y. (1990). A stability study of nonadiabatic oscillations in a background polytrope. *ApJ*, 361:527–539.

[Macdonald and Mullen, 1997] Macdonald, J. and Mullen, D. (1997). Radiative transfer effects on the stability of sound waves in a polytropic atmosphere. *ApJ*, 481:963–972.

[Manneville, 1990] Manneville, P. (1990). *Dissipative Structures and Weak Turbulence*. Academic Press, Inc., Boston.

[Spiegel, 1957] Spiegel, E. (1957). *ApJ*, 126:202.

[Spiegel, 1964] Spiegel, E. (1964). The effects of radiative transfer on convective growth rates. *ApJ*, 139:959–974.

[Suematsu et al., 1995] Suematsu, Y., Wang, H., and Zirin, H. (1995). High-resolution observations of disk spicules. i. evolution and kinematics of spicules in the enhanced network. *ApJ*, 450:411–421.

[Syrovat-skii and Zhugzhda, 1968] Syrovat-skii, S. and Zhugzhda, Y. (1968). Oscillatory convection of a conducting gas in strong magnetic field. *Soviet Physics - Astronomy*, 11(6):945–952.

[Umurhan et al., 1998] Umurhan, O., Tao, L., and Spiegel, E. (1998). Stellar oscillons. *Annals of the New York Academy of Sciences*, 867:298–305.
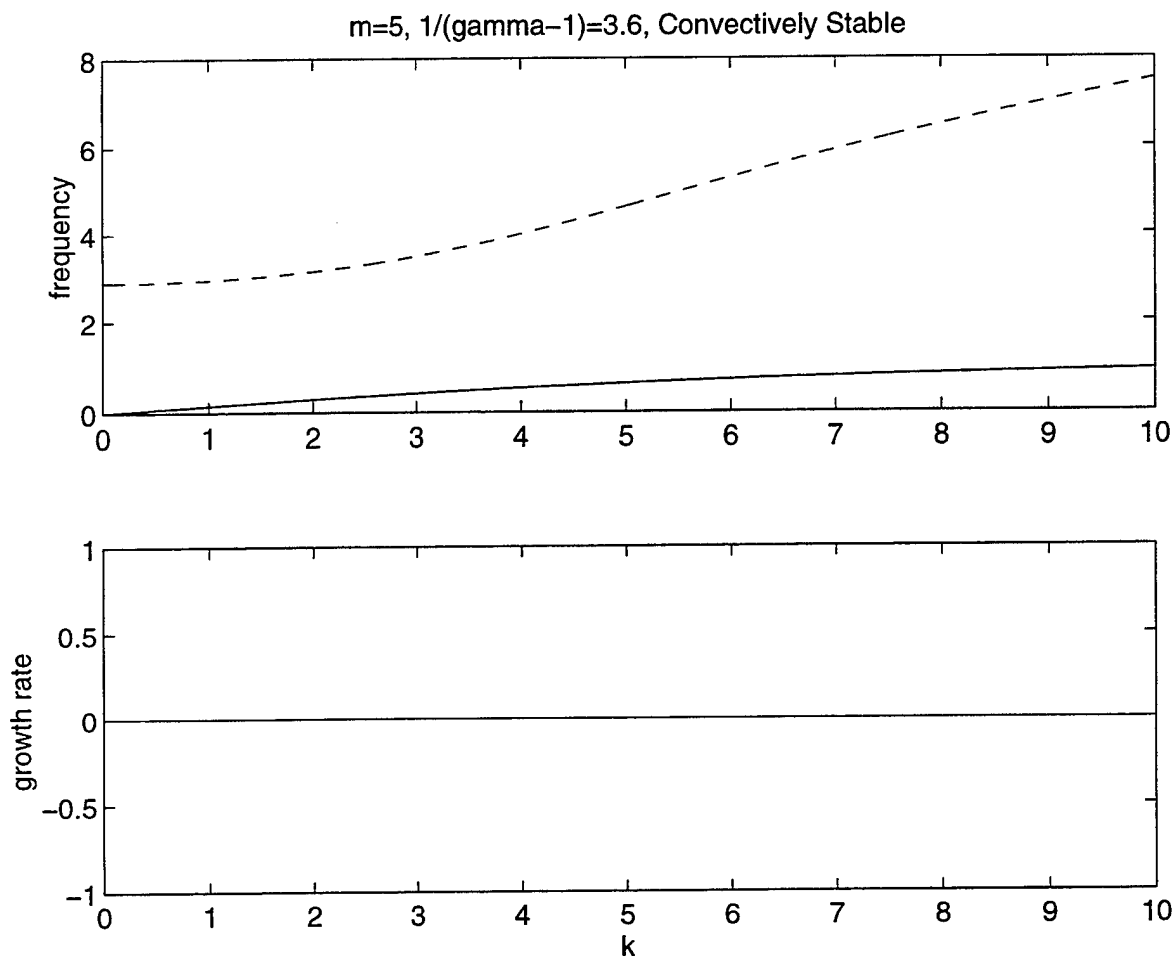
Figure 1: The dispersion relation for the fundamental acoustic, in the dashed line, and gravity mode, in the solid line, are shown for the $m = 5$, $\gamma = 1.28$, non-magnetic polytrope atmosphere. The layer extends from $z = .1$ to $z = 1$. The atmosphere is stable and the oscillations are adiabatic so the growth rate is zero for both branches.

m=1.5, 1/(gamma-1)=3.6, Convectively Unstable
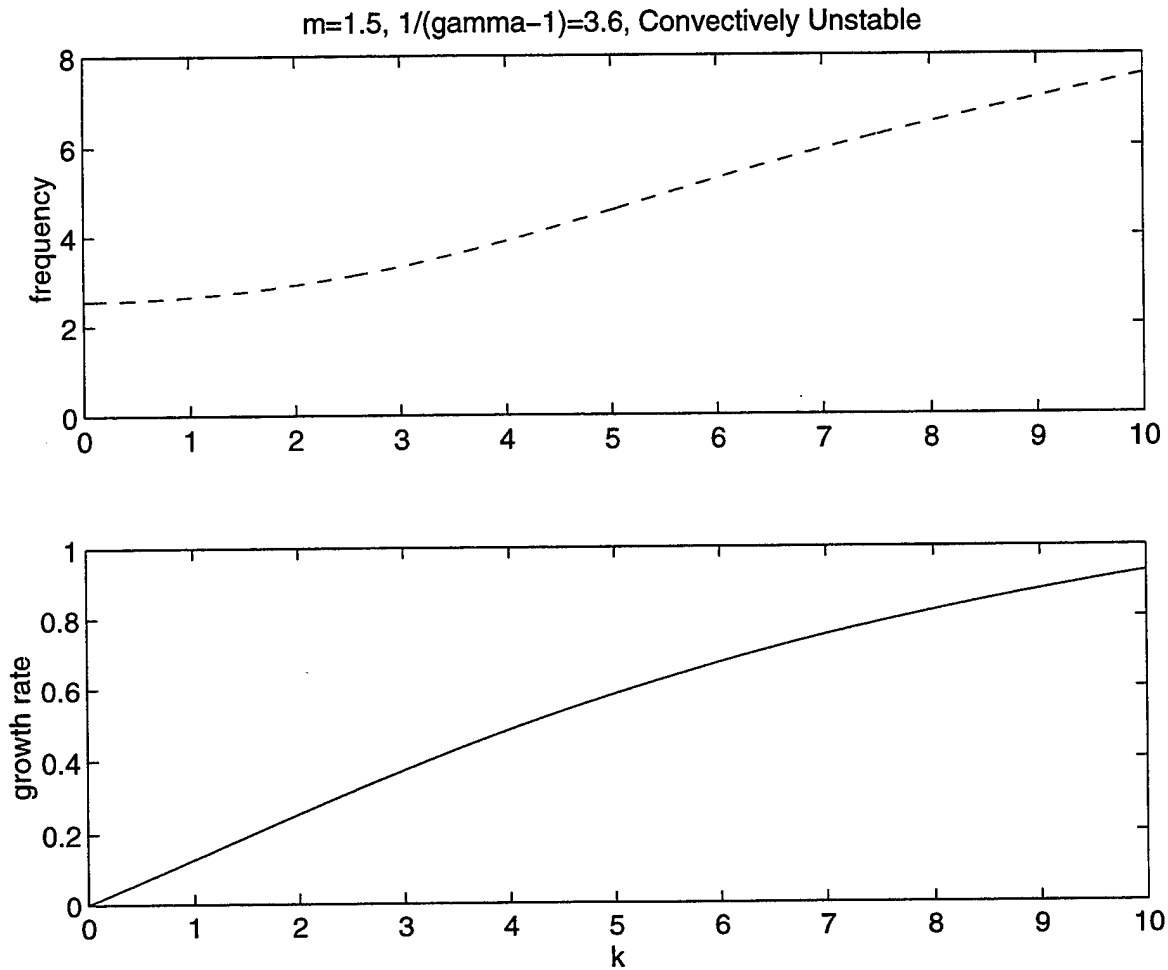
Figure 2: The dispersion relation for the fundamental acoustic, in the dashed line, and gravity mode, in the solid line, are shown for the $m = 1.5$, $\gamma = 1.28$, non-magnetic polytrope atmosphere. The layer extends from $z = .1$ to $z = 1$. The atmosphere is unstable and the oscillations are adiabatic so the growth rate is zero for the acoustic mode and positive for the gravity modes. The gravity modes have zero frequency and thus are not oscillatory in time
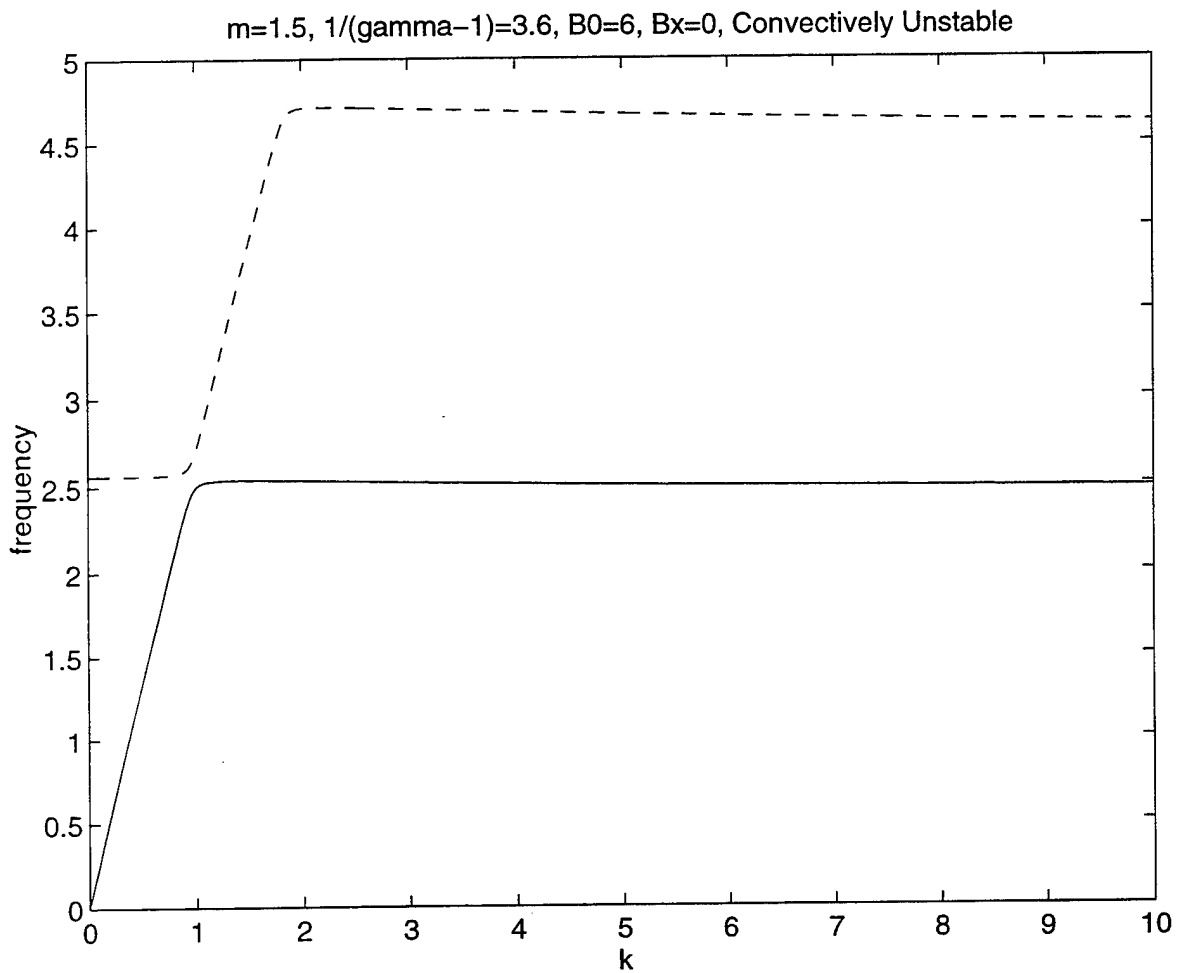
Figure 3: The dispersion relation for the fundamental longitudinal, in the dashed line, and transverse mode, in the solid line, are shown for the $m = 1.5$, $\gamma = 1.28$ magnetic polytrope. The layer extends from $z = .1$ to $z = 1$ and the magnetic boundary conditions are $B_x = 0$ on top and bottom. For this plot $q = 0$ so the oscillations are adiabatic.The growth rates are not shown because they are zero. Without magnetic field this atmosphere would be unstable, but the transverse modes are stabilized by the magnetic field.
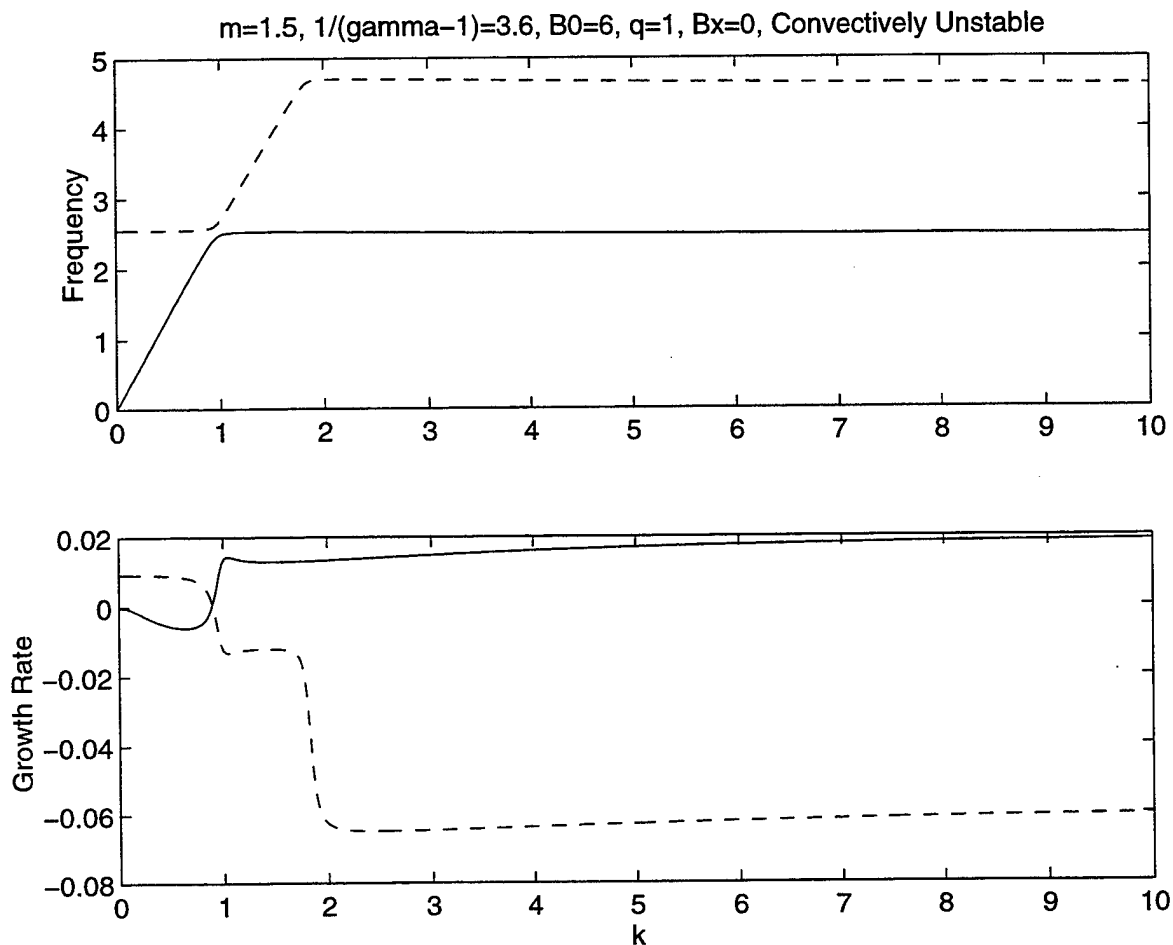
Figure 4: The dispersion relation for the fundamental longitudinal, in the dashed line, and transverse mode, in the solid line, are shown for the $m = 1.5$, $\gamma = 1.28$ magnetic polytrope. The layer extends from $z = .1$ to $z = 1$ and the magnetic boundary conditions are $B_x = 0$ on top and bottom. For this plot $q = 1$ so the oscillations are non-adiabatic. The finite cooling time makes fluid motions irreversible so the transverse modes are unstable. Even though this atmosphere is convectively unstable the transverse modes have an oscillatory component. In addition for the given B_0 and q the longitudinal mode is unstable for $k < 1$.
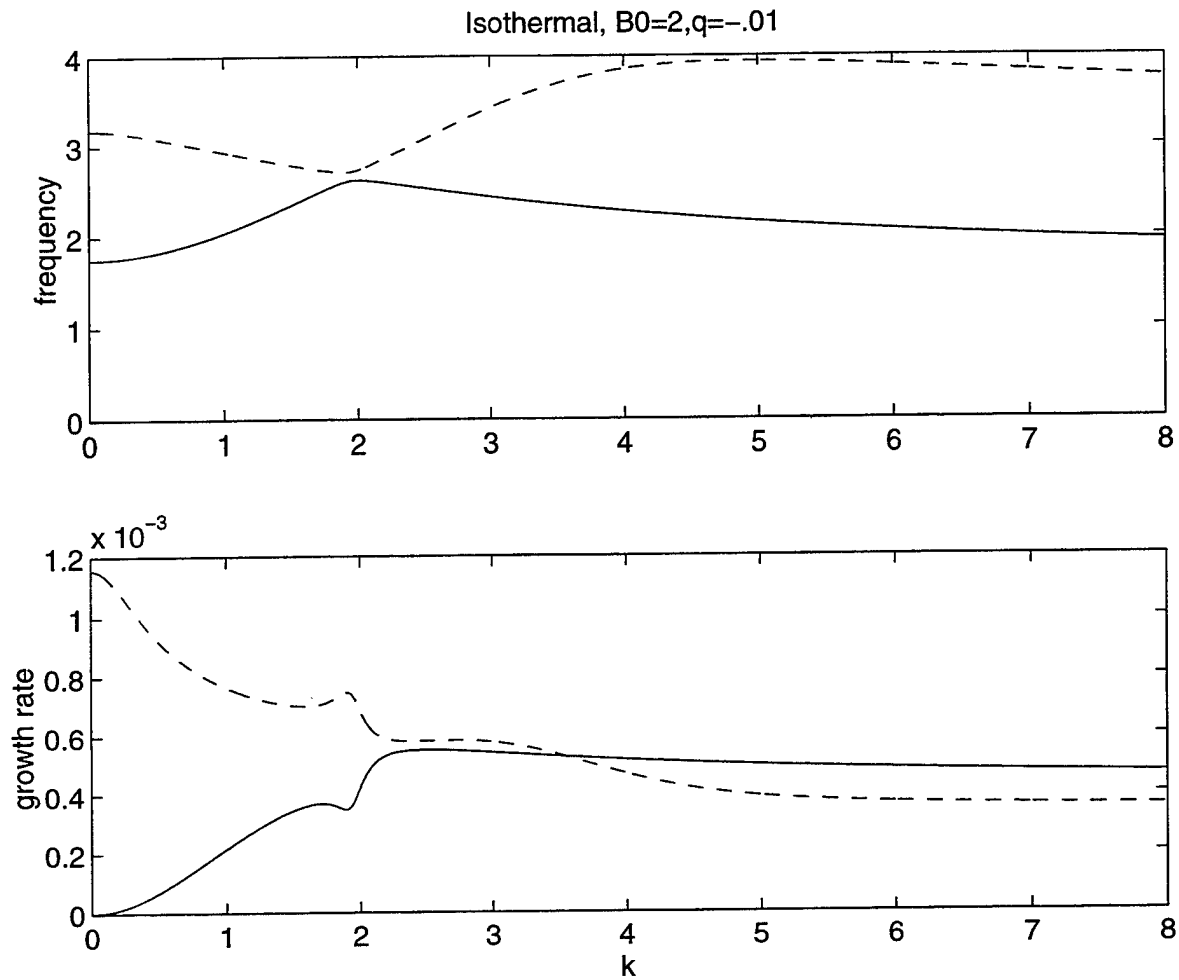
Figure 5: The dispersion relation for the fundamental longitudinal, in the dashed line, and transverse mode, in the solid line, are shown for the isothermal atmosphere. The layer extends from $z = -0.5$ to $z = 0.5$ and the magnetic boundary conditions are $B_z = 0$ on top and bottom. For this plot q is small and negative. The background magnetic field is 2 which corresponds roughly to real magnetic field of 60 gauss. The modes in this diagram almost cross, which results in small features in the growth rate near the close approach of the frequencies.

Isothermal, B0=6,q=−.01
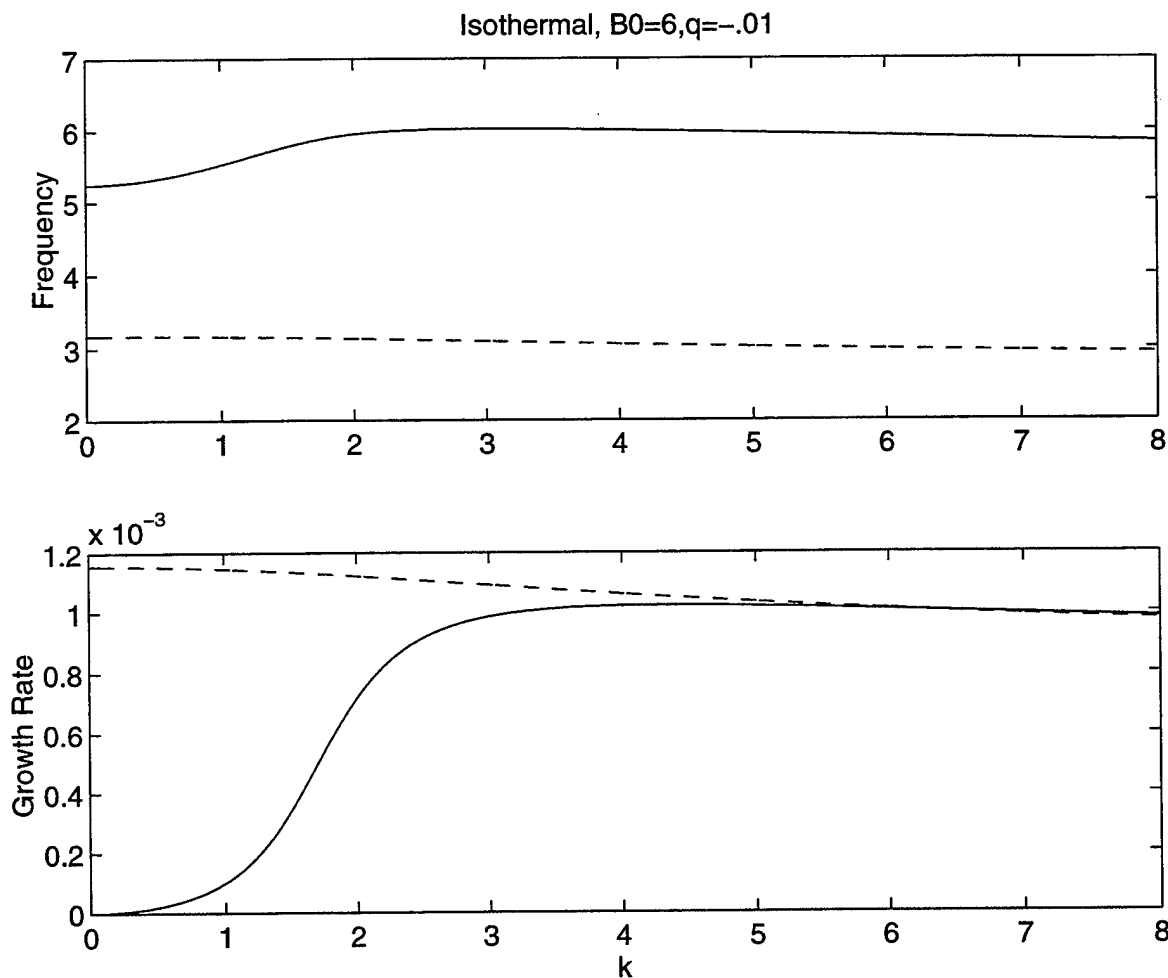
Figure 6: The dispersion relation for the fundamental longitudinal, in the dashed line, and transverse mode, in the solid line, are shown for the isothermal atmosphere. The layer extends from $z = -0.5$ to $z = 0.5$ and the magnetic boundary conditions are $B_z = 0$ on top and bottom. For this plot q is small and negative. The background magnetic field is 6 which corresponds roughly to real magnetic field of 180 gauss. In contrast with the previous diagram, for a weaker field, the modes don't come close to crossing. This is a result of the higher frequency for the $k = 0$ Alfvén mode.

Dispersion and Reconstruction

Carolyn R. Mockett

1 Introduction

Since the 1970's physical oceanographers have been using neutrally buoyant floats to make Lagrangian measurements of ocean circulation. Today the use of floats is becoming more and more common, and these measurements are regularly used to make maps of the Eulerian flow. Yet the relationship between Eulerian and Lagrangian statistics has been not been fully explored. One can approach this relationship from two directions. The first is given a certain Eulerian flow field, what can one say about the Lagrangian float trajectories? The inverse of this is given the Lagrangian float trajectories what can one say about the Eulerian flow?

There has been work on the dispersion of passive particles in 2-D turbulence. But there has not been a full exploration of the effects of β and the free surface on dispersion, both of which are factors in large scale flow in the ocean. In addition what are the direct and indirect effects of vortices on dispersion with β and a free surface? An improved understanding of dispersion in different types of flow will assist in better understanding float data.

The inverse question of starting from the Lagrangian data and attempting to reconstruct the Eulerian field is a broad topic. A simple place to start is to add a zonal flow to a turbulent background and test various factors that effect how well one succeeds in recovering the mean from Lagrangian measurements.

2 The Model

To explore both of these questions a series of numerical experiments have been carried out that integrated the equivalent barotropic quasigeostrophic equation in dimensionless form. It is given by:

$$\frac{\partial q}{\partial t} + [\psi, q] + \beta \frac{\partial \psi}{\partial x} = -\mu \nabla^6 \psi$$

The vorticity q is given by $q = \nabla^2 \psi - F\psi$, where $\nabla^2 \psi$ is the relative vorticity and $F\psi$ is the free surface term. $F = (L/L_R)^2$ where L is the length scale of the domain and $L_R = \frac{(g'H)^{\frac{1}{2}}}{f}$ is the Rossby radius of deformation. The Rossby radius gives a length scale at which the effects of rotation become important. There is no forcing so the field is freely decaying, and a hyper viscosity is used with $\mu = 5 \times 10^{-7}$.

The numerical integration is done on a doubly periodic square lattice $(0, 2\pi; 0, 2\pi)$ with 128x128 resolution. The code is pseudo-spectral with standard 2/3 dealiasing. Pseudo-spectral

means that the derivatives are done in spectral space while the the products are done in physical space. A 3rd order Adams-Bashforth scheme is used for the time-integration.

To calculate the float trajectories one needs to integrate $\dot{x} = -\frac{\partial \psi}{\partial y}$, $\dot{y} = \frac{\partial \psi}{\partial x}$. Again 3rd order Adams-Bashforth scheme is used for the time integration and the spatial interpolation of position between grid points is done with cubic spectral splines.

All the runs are started with a random Gaussian vorticity field with narrow band wave number spectrum. The initial kinetic energy spectrum is given by $E(k) = \frac{E_o k^6}{(2k_o + k)^{18}}$, where $k_o = 15$, and E_o is fixed such that the total energy $E = \int E(k)dk = 0.5$. The initial field then freely evolves. As energy cascades to larger scales vortices form. They interact, and merge, and with time there are fewer and fewer vortices since there is no forcing. Since these flows are freely decaying one must worry about their stationarity. The hope is that the flow is sufficiently stationary over the time period analyzed, during which the total energy only decreases by about 2%. One can also argue that there is no reason to believe the ocean itself is stationary.

After the vortex formation period, a 32x32 uniform grid of floats are put in the flow and passively advected. Each float measures position (x, y), velocity (u, v), the stream function ψ, and vorticity $\nabla^2 \psi - F\psi$ every $dt = .1$, from $t = 0$ to $t = 40$. Since there are periodic boundaries, the trajectories are unfolded before calculating dispersion statistics. Therefore the final area of the unfolded float trajectories can be much larger than the original 128x128 domain. The Eulerian velocity field is recorded on the same uniform grid where the floats were initially seeded. In order to have the same amount of data in the Eulerian data set as the Lagrangian, the Eulerian velocities are also recorded every $dt = .1$ for the same length of time.

The dimensional and non-dimensional scales this model corresponds to are $U \sim .2m/s$, $U^n \sim .6$, $L \sim 400\,km$, $L^n = 2\pi$, $L_\beta \sim 150\,km$, $L_\beta^n \sim 2$, $L_R \sim 70\,km$, $L_R^n \sim 1$, and $T \sim 3\,days$, $T^n = 1$. A superscript n refers to non-dimensional. The Rhines scale, $L_\beta = \sqrt{\frac{U}{\beta}}$ gives an (upper) estimate of the scale at which Rossby waves dominate over vortices.

3 Part I: Dispersion

3.1 Definitions

In order to explore the dispersion of floats there are certain statistics that are useful. To begin with absolute dispersion measures the mean square displacement of an ensemble of floats at a given time. It is defined as

$$A(t)^2 = \langle (x(t) - x(0))^2 \rangle$$

where $\langle ... \rangle$ is an average over an ensemble of floats and $x(0)$ is the initial position of a float. One can also define the dispersion coefficient by

$$D(t) = \frac{A^2}{2t}$$

167

Taylor(1921) obtained two limits for D(t) in isotropic, homogeneous,stationary turbulence

$$D \propto t \quad \text{when } t \to 0$$

$$D = \text{Const.} \quad \text{when } t \to \infty$$

This first limit is called ballistic diffusion, while the second is Brownian diffusion. Single particle diffusion is a good measure of the mean displacement of floats. But if one wants to know more specifically how floats are dispersing, it is useful to define a PDF of displacement. This is given by

$$p(d) = \frac{n(d)}{N\Delta d}$$

where $n(d)$ is the number of floats that have been displaced a distance between d and Δd, N is the total number of floats, and Δd is the width of the bin.

Another useful tool is the power spectrum. Given

$$S(\nu) = \int_0^T u'(t)e^{-i2\pi\nu t}dt$$

where $u'(t) = u(t) - \overline{u(t)}$ is for a given float or Eulerian velocity time series, and $\overline{u(t)}$ is the mean of that time series. ν is the frequency. The power spectrum $P(\nu)$ is given by:

$$P(\nu) = \frac{1}{T}[S(\nu) \cdot S^*(\nu)]$$

The spectrum was calculated for each float and then averaged over all floats. The same was done with the Eulerian data.

As a word of caution, note that all the previously defined statistics have been developed for statistically stationary processes. Since our turbulence is decaying, strictly speaking we are out of the domain of applicability of the methods and their use must be considered heuristic. However, the energy decay is very slow and as a good approximation the dynamics may be considered stationary.

Previously it has been demonstrated that the form of dispersion for passive particles in vortices is different from those in the background (Elhmaidi et al. 1993). To distinguish between these two regions one can use the Okubo-Weiss parameter $Q(x, y, t) = S^2 - \omega^2$, where S^2 is the sum of the squares of the normal and shear components of strain, and ω is the vorticity. The only problem is that strain and vorticity are very difficult to measure in the ocean with floats. Rupolo et al (1996) used low and high kinetic energy (KE) as a proxy to distinguish between floats in and out of vortices. Since the goal of this project is to explore dispersion of floats, high and low KE will be used to make this distinction. The 200 floats with the highest kinetic energy and with the lowest kinetic energy will be used for the high KE floats, and the low KE floats respectively.

3.2 The Four Cases Considered

To examine the effects of β and a free surface on dispersion the natural thing to do is look at four different cases: Case 1 ($\beta = 0, F = 0$), Case 2 ($\beta = 5, F = 0$), Case 3 ($\beta = 0, F = 30$), Case 4 ($\beta = 5, F = 30$). In order to start each case with the same kinetic energy $F\psi$ was subtracted from the initial relative vorticity field used to start Cases 1 and 2 to obtain a new vorticity field to start Cases 3 and 4. However, since the fields evolved differently Cases 3 and 4 have half the kinetic energy of Cases 1 and 2. Therefore one cannot compare the magnitude of the absolute dispersion between these two pairs, but one can compare the form of the dispersion.

3.2.1 Case 1: $\beta = 0$, $F = 0$

With $F = 0$ there is no physical limit on the size of the vortices and there are long spatial correlations . This makes it a difficult case to study since quickly the vortices grow and form large scale flow (Figure 1 b) which can bias the dispersion. Regardless of these difficulties this case presented the main features of the dispersion are as one would expect. There are comparable displacements in x and y as is evident from the dispersion coefficients (Figure 2 c). Also from the plot of the dispersion coefficient one can see that there is ballistic dispersion at small t, while relatively Brownian dispersion at large times. From the spectrum (Figure 3 a,b) one can see that there is more energy in high frequencies ($\nu \approx 1$) in the Lagrangian data than in the Eulerian data. This reflects that floats travel more rapidly through different parts of the flow than the rate at which the flow changes at a given point and the general process of formation of small space and time scales in advected tracers even for smooth Eulerian flows. When the floats are divided into high KE and low, the high KE floats have much more energy at high frequencies than the low KE floats. This is due to the fact the high KE floats are in the vortices. In addition there is a $-1/4$ slope to the high KE floats previously observed for high KE floats in the ocean (Rupolo et al. 96), which is a possible sign of anomalous diffusion (diffusion that is not Brownian).

3.2.2 Case 2: $\beta = 5$, $F = 0$

The first thing that is evident when one looks at the contours of vorticity of this case (Figure 1 c,d) is the lack of vortices. The presence of β allows Rossby waves, which have been shown to alter both the dispersion directly and through their inhibition of the formation of vortices (McWilliams 84). If β is large enough Rossby waves can eliminate vortices. The Rhines scale gets smaller as β increases, so the spatial scale over which Rossby waves dominate decreases. This case clearly is dominated by Rossby waves. From Figure 4 a,b one can see that there is much greater x-displacement than in Case 1 because of the waves. There also is a greatly repressed y-displacement since now for a float to move north or south it must cross contours of planetary vorticity. In order to conserve potential vorticity a north-south displacement requires a change in the free surface or relative vorticity to balance the change in planetary vorticity. From (Figure 4 c) one can see from the plot of the dispersion coefficient a long ballistic period until almost t=1.

To compare Eulerian statistics to Lagrangian, the energy spectrum (Figure 5 a,b) provides a good comparison. The strong peaks from the waves which are clearly visible in the Eulerian spectrum are absent in the Lagrangian. Since the floats travel with the waves they do not detect them.

It should also be noted that because there are no vortices there is little difference between high and low kinetic energy floats as seen in their spectrum (Figure 5 c,d). In this case, the only difference is that the low KE floats display some indication of the Rossby wave peaks. Thus statistics for high and low KE floats appear to differ significantly only in the presence of vortices.

3.2.3   Case 3: $\beta = 0$, $F = 30$

With the addition of the free surface the inverse cascade of energy to scales larger than L_R is slowed down. In addition interaction between vortices at distances larger than L_R is shielded, and the dynamics become more localized. This can be seen in Figure 1 e,f. The vortices are $O(L_R)$ so their movement is very slow. The slowness of the vortex movement is most evident when looking at the trajectories of the high and low KE floats (Figure 7 a,b). The high KE floats are trapped in vortices and confined to small areas, while the low KE floats are dispersing through this field of almost stationary vortices. As a consequence the x and y displacement (Figure 7 c) of the high KE floats is repressed by about 1/2 compared to the mean of all floats, and almost all of the energy is at high frequencies (Figure 8 c). For low KE floats there is a greater x, y-displacement (Figure 7 d) than the mean. On the plot of the dispersion coefficient (Figure 7 f) one also notes that there is a longer ballistic dispersion until almost $t = 1$.

For this case the Eulerian and float spectrum (Figure 8 a,b) are especially different. In fact the Eulerian spectrum has not yet leveled off. This is due to the slow motion of the vortices. For the Eulerian time series one vortex can come by and skew the mean such that the time series with the mean removed has long sections of essentially constant velocity and one or a few large jumps. As a consequence the Eulerian spectrum does not level off. With enough time several vortices would come by and the mean would begin to make sense. For this reason the memory in the Eulerian flow is especially long.

3.2.4   Case 4: $\beta = 5$, $F = 30$

This final case is the most interesting since it combines both the effects of β and the free surface, and is the most applicable to actual ocean dynamics. For this case the x-displacement (Figure 9 a) is twice as large as Case 3 ($\beta = 0, F = 30$). There also is an interesting skew PDF of x-displacement (Figure 9 c). The cause of this becomes very clear when the high KE floats are examined separately. The y-displacement (Figure 9 b) on the other hand is 2/3 less than Case 3 since now β is present. But interestingly the y-displacement is almost twice that of Case 2 ($\beta = 5, F = 0$) even though Case 2 has more kinetic energy. Therefore one can conclude that vortices must contribute to y dispersion.

For the high KE floats there is a smaller x-displacement by 2/3 than the mean, and large net westward displacement (Figure 10 c). The vortices are clearly traveling westward and are

responsible for this behavior. This can also be seen in the PDF of x-displacement which has westward migration with time (Figure 10 e). The low KE floats on the other hand have a comparable x-displacement to the mean and a slight net Eastward displacement (Figure 10 c). There is also noticeably longer ballistic period. Both have similar y displacements.

3.3   Conclusions of Part I

There are large differences between Eulerian and Lagrangian statistics. In particular there is a much longer memory in the Eulerian field, as indicated by the large power in the low-frequency components of the spectrum, which is a reflection of the different characteristics of each method of measurement. By comparing Case 2 with the other three one can also see that coherent structures alter the overall dispersion. Not only do they alter the dispersion but there are different dispersion properties for floats in vortices and those in the background in all three cases with vortices. In particular vortices decrease the ballistic period. This was seen by Elhmaidi et al. 1993 in two dimensional turbulence (Case 1) but it also evident with β and F. Separating the floats into those in and out of vortices allows one to see which are dispersing more. By comparing the displacement of low KE floats to high KE it appears that vortices contribute to dispersion by the flow they set up, but it is not the particles in the vortices (high KE) that disperse the most. It is the particles outside them (low KE) that do. This is evident from Case 3 and Case 4. For these turbulent flows high and low KE is a good proxy for distinguishing between floats that are in or out of vortices.

Finally the addition of β alters the dispersion. It greatly represses dispersion in y, and causes vortices to travel westward as well as the particles they have trapped. Vortices do assist in over coming the effects of β since there is more y dispersion in Case 4 than Case 2, even though Case 2 has more kinetic energy. The Rhines scale also plays an important role in dispersion on the β-plane. Dispersion in the x becomes almost ballistic again after a displacement near the Rhines scale, while y dispersion is essentially halted.

4   PART II: Reconstructing the Mean Flow

The second half of this research approaches the relationship between Eulerian and Lagrangian measurements from the other direction. What factors contribute to how well one can reconstruct the mean Eulerian flow from float data? Although there are numerous things one could test, one can begin with the spatial resolution of initial position of the floats, how often each float measures the flow, and the ratio of the kinetic energy of the mean flow to the kinetic energy of the eddies KE ratio=KE_{Jet}/KE_{Eddy}. One can also explore the error that is induced by how the velocity is determined, whether it is directly measured or inferred from float trajectories as is done with ALACE floats (Davis et al., 96).

In order to add a mean flow, a simple sinusoidal vorticity field is added to the initial vorticity field of Case 4 ($\beta = 5, F = 30$). The resulting velocity field is a jet in the center of the domain traveling eastward and westward flow along the top and bottom of the domain. The jet and the turbulent background are then allowed to freely evolve together before the floats are added. The resulting mean zonal velocity is no longer a sinusoid. The jet has extracted

171

some of the kinetic energy from the eddy field. Figure 11 shows example stream lines for two different strength jets. The first set of stream lines (a,b) is the most energetic case examined, KE ratio=1.4. The vortices are confined to the regions of minimum velocity. One can see from the second set (c,d) when the KE ratio=.312 there are is a much more substantial spatial and temporal variability in jet. The KE of the jet is determined from the mean Eulerian flow $\frac{1}{2}\overline{u_e^2}$, where $\overline{u_e^2}$ is averaged over all the Eulerian data. The eddy KE is found by subtracting this estimate of the KE of the jet from the total KE of the domain, $KE_{Eddy} = KE_{Total} - KE_{Jet}$.

4.1 Perfect Data

With the numerical model the floats act as perfect roving current meters measuring the exact Eulerian velocity at varying locations over time as they follow a fluid parcel. So the comparison between Eulerian data and Lagrangian is purely an issue of resolution (temporally and spatially) since both are making exact measurements. Both Eulerian and Lagrangian velocity measurements are binned in 128x8 rectangles to reconstruct the mean flow averaged over x. All the unfolded trajectories outside the initial 128x128 domain are discarded. Floats are not allowed to wrap around and continue to measure the field. This was done to emphasize one of the drawbacks of floats,that they can leave the area of interest.

Figure 12 shows two reconstructions for two different strength jets. The floats reconstruct the flow quite well, even with as few as 16 floats. But in the less energetic jet there appears to be a systematic underestimate of the peaks of the jet regardless of the number of jets. This is evident in all of the runs at the lower energies.

4.2 Imperfect Data

Since the "perfect" data works very well, we now explore what happens when the velocity is inferred from the float position data. There is a type of float used by oceanographers that are ballasted to sink to certain depth and travel with the flow untracked on the order of weeks, after which they surface and relay their location to a satellite, and then submerge again. The velocity is inferred from the where the float went down and where it next resurfaces and the time in between.

To mimic this type of flow measurements one can reconstructed u and v from trajectories in a similar manner using a centered difference scheme:

$$u(x_i) = \frac{x_{(i+1)} - x_{(i-1)}}{2\Delta t}$$

$$v(y_i) = \frac{y_{(i+1)} - y_{(i-1)}}{2\Delta t}$$

$\Delta t = .1, .4, 1, 2$ were used. The data is thinned temporally, such that $x_{(i+1)}$ and $x_{(i-1)}$ are $2\Delta t$ apart. A $\Delta t = 1$ is between once and twice an eddy turn over time depending on the strength of the mean flow. Measurements are then analyzed the same way as the "perfect" data.

To approximate the two-week period the ALACE floats are submerged, a $\Delta t = 2$ is used since a non-dimensional time unit is about three days and a centered difference has a time separation of $2\Delta t$. In Figure 13 one can see that the underestimate of the peaks of the jet is now significant. To ensure this was not due to the lack of data, there also is a plot of the "perfect" data thinned temporally by $\Delta t = 2$ to compare it to. The thinned "perfect" data actually slightly over estimates the peaks. Therefore one can conclude that this method of reconstructing the mean velocity is introducing some type of systematic error.

4.3   Energy of mean flow vs. energy of eddies

To explore whether the ratio of the kinetic energy of the mean flow to the kinetic energy of the eddies is a key factor, several runs were done with the magnitude of KE ratio varying from 1.4 to .18 . The rms error between the the Lagrangian velocity and Eulerian divided by the total rms velocity of the Eulerian mean is then plotted as a function of the KE ratio. This was calculated with all 1024 floats, 256 floats, 64 floats, and 16 floats.

For the most energetic jet there is an increase in error since the floats move quickly through the domain and there are less measurements, but as the KE ratio of the flow decreases below .7 the error begins to increase again and reaches forty percent. One will also note that with the "perfect" data (Figure 14 a)the number of floats does not seem to matter much, all the error curves lie close together.

The same procedure is applied to the reconstructed velocities. For $\Delta t = .1$ (Figure 14 b)the plot looks similar to the "perfect" data, but now there is a spreading of the error lines of different number of floats. For $\Delta t = 1$ (Figure 14 d) the whole curve flattens out and the error from the way the velocity field was reconstructed masks the error determined by the KE ratio .

4.4   Conclusions of Part II

Overall there is an underestimate of the jet strength when using float data especially as the KE ratio decreases. As the KE ratio decreases it becomes much more difficult to detect the mean and the error can rise to forty percent. The underestimate is particularly evident when the velocities are reconstructed from the trajectories using a centered difference. The longer Δt one uses to reconstruct the velocity field, the larger the underestimate. In addition the number of floats becomes much more important when the velocity is reconstructed from trajectories since each measurement contains a certain level of error. In fact if the data is "perfect" one can do basically as well with only 16 floats as 1024 floats.

5   Future Work

For the study of dispersion:

To improve the stationarity of the statistics all fours case should be re-run at higher resolution (512x512), so the friction can be decreased. This will cause less decay of the total energy and potential vorticity. One can also do runs that explore relative dispersion in all four

cases by seeding pairs of floats close together. This is something that is being done with floats in the ocean now. It would be interesting to compare the numerical data set with a real one. For the exploration of flow reconstruction from Lagrangian data:

Since reconstructing the velocities from float trajectories causes a systematic underestimate of the jet peaks the next thing to look at would be the effects of other imperfections in float measurements, like drift, finite size of a float, etc... One could also look at how well Lagrangian float measurements compare to the Eulerian ones with a north-south mean flow, and more complicated mean flows.

Acknowledgements

References

[Bartello and Holloway, 1991] Bartello, P. and Holloway, G. (1991). Passive scalar transport in β-plane turbulence. *J. Fluid Mech.*, 223:521–536.

[Davis, 1996] Davis, R. (1996). Comparison of autonomous lagrangian circulation explorer and fine resolution antartic model results in the south atlantic. *J.Geophys.Res.*, 101(C1):855–884.

[Elhmaidi et al., 1993] Elhmaidi, D., Provenzale, A., and Babiano, A. (1993). Elementary topology of two-dimensional turbulence from a lagrangian viewpoint and single-particle dispersion. *J. Fluid Mech.*, 257:533–558.

[Maltrud and Vallis, 1991] Maltrud, M. and Vallis, G. (1991). Energy spectra and coherent structures in forced two-dimensional and beta-place turbulence. *J.Fluid Mech.*, 228:321–342.

[McWilliams, 1984] McWilliams, J. (1984). The emergence of isolated coherent vortices in turbulent flow. *J. Fluid Mech.*, 146:21–43.

[Owens, 1991] Owens, W. (1991). A statistical description of the mean circulation and eddy variability in the northwestern atlantic using sofar floats. *Prog. Oceanog.*, 28:257–303.

[Provenzale, 1998] Provenzale, A. (1998). Transport by coherent barotropic vortices. *Annual Review*. in press.

[Rupolo et al., 1996] Rupolo, V., Hua, B., Provenzale, A., and Vincenzo, A. (1996). Lagrangian velocity spectra at 700 m in the western north atlantic. *Physical Oceanography*, 26(8):1591–1606.

[Taylor, 1921] Taylor, G. (1921). Diffusion by continuous movement. *Proc. Lond. Math Soc.*, 20:196–212.

[Wiess et al., 1997] Wiess, J., Provenzale, A., and McWilliams, J. (1997). Lagrangian dynamics in high-dimensional point-vortex system. *Physics of Fluids*. submitted.
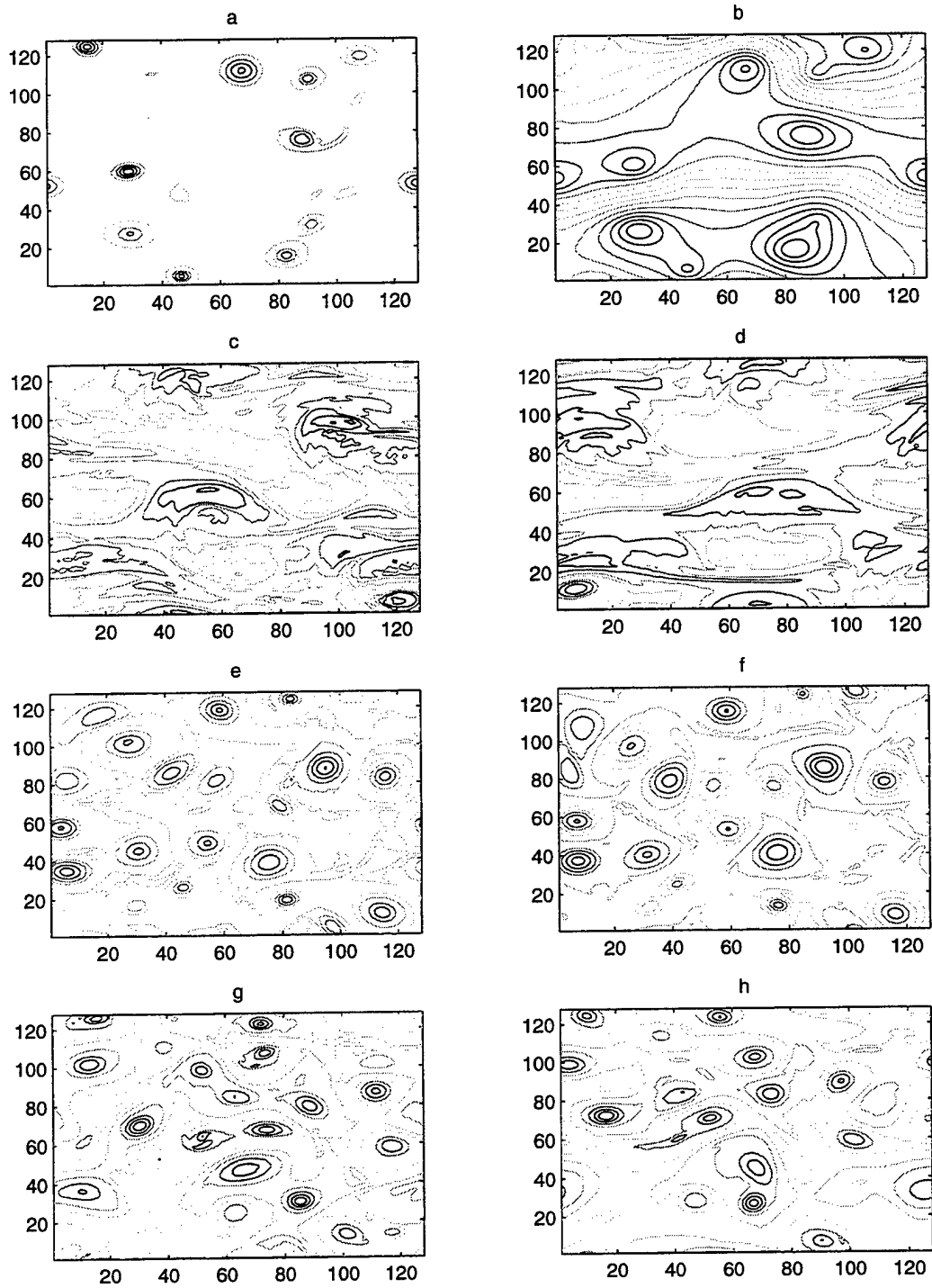
Figure 1: a) CASE 1 contours of vorticity at t=15, b) CASE 1 contours of ψ at t=15, c,d) CASE 2 contours of vorticity at t=15,20, e,f) CASE 3 contours of vorticity at t=15,20 g,h) CASE 4 contours of vorticity at t=15,20.
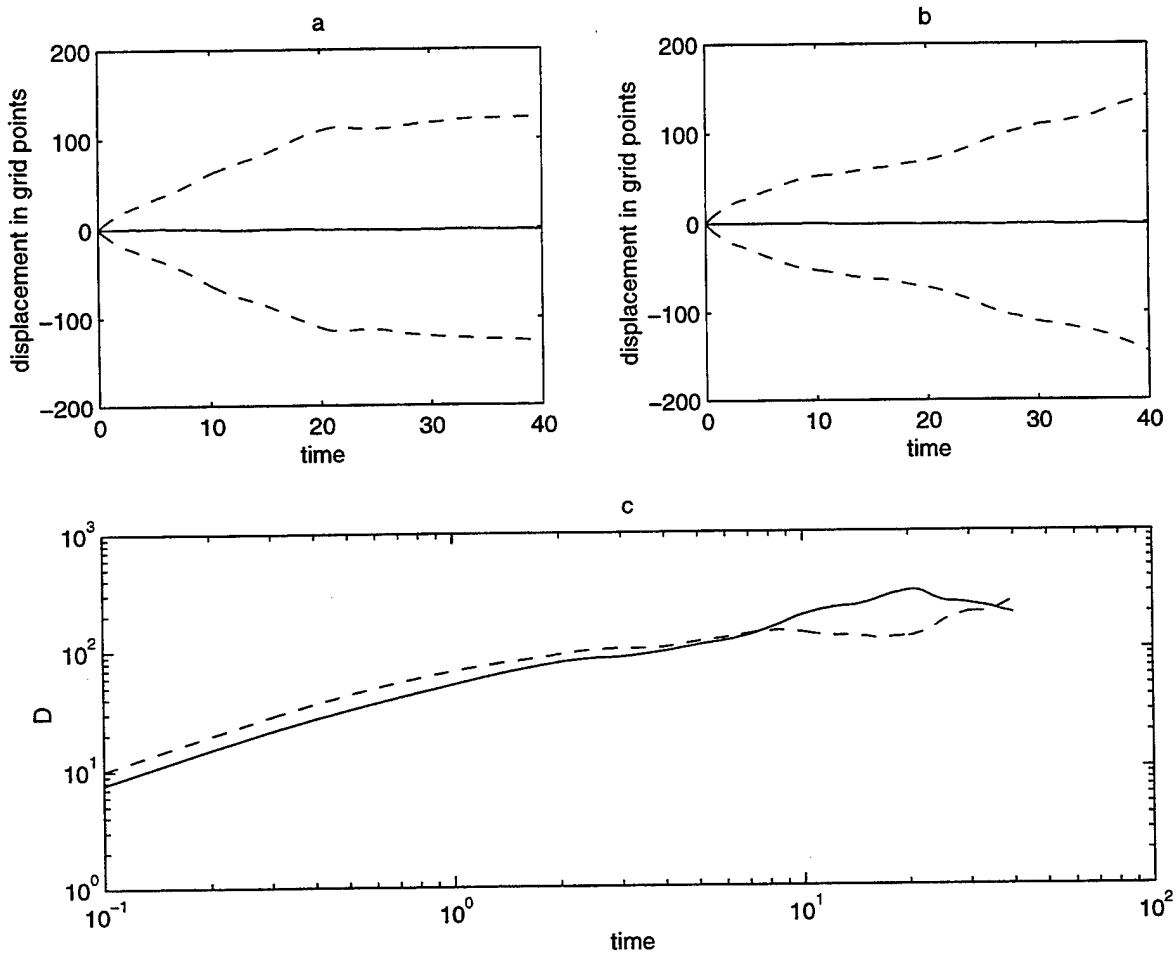
Figure 2: CASE 1 a) the solid line is the mean x-displacement, and the dashed are plus and minus A, the rms. b) the solid line is the mean y-displacement,and the dashed are plus and minus A, the rms. c) The dispersion coefficient, solid line -in x, dashed line - in y.
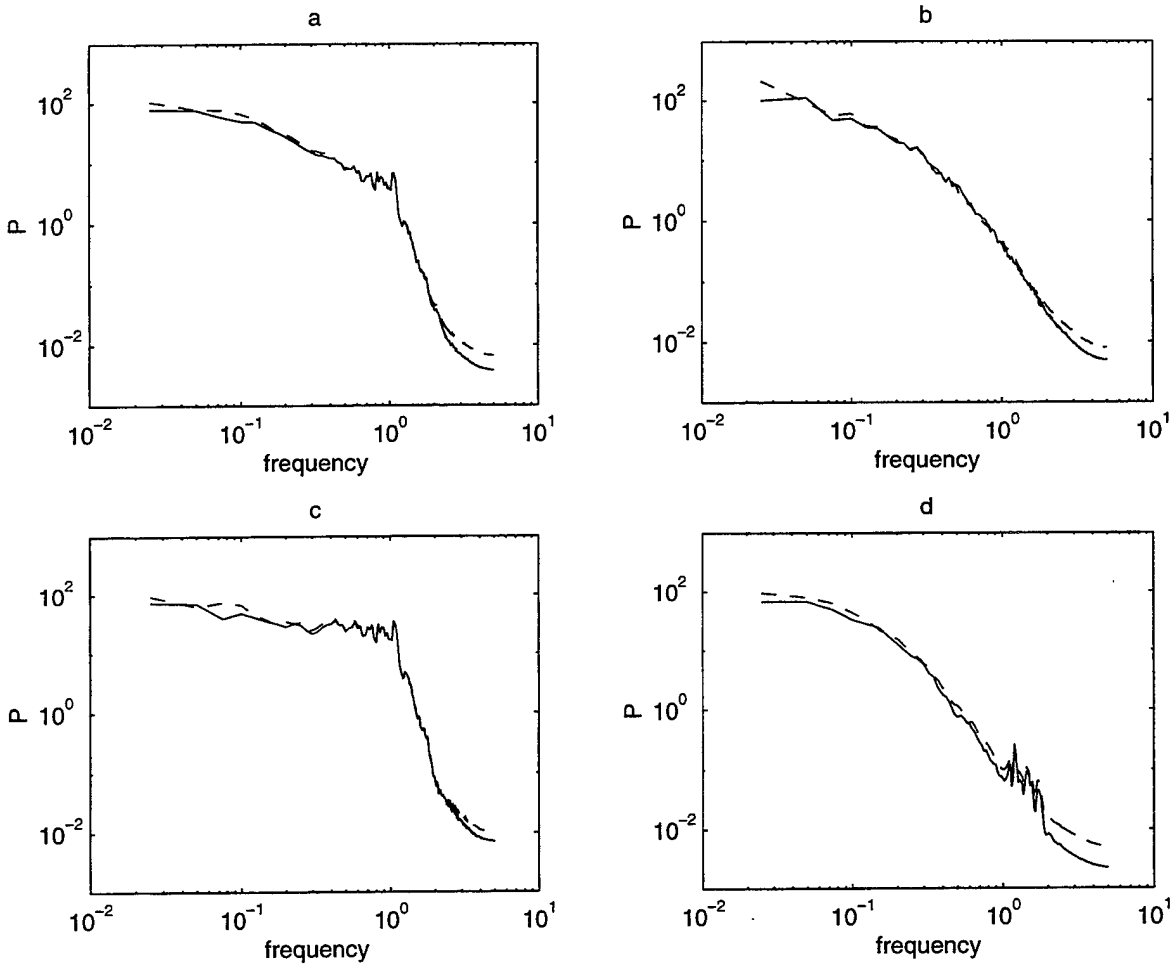
Figure 3: CASE 1 The power spectrum from u(solid), v(dashed). a) the floats. b)the Eulerian field. c) high KE floats. d) low KE floats
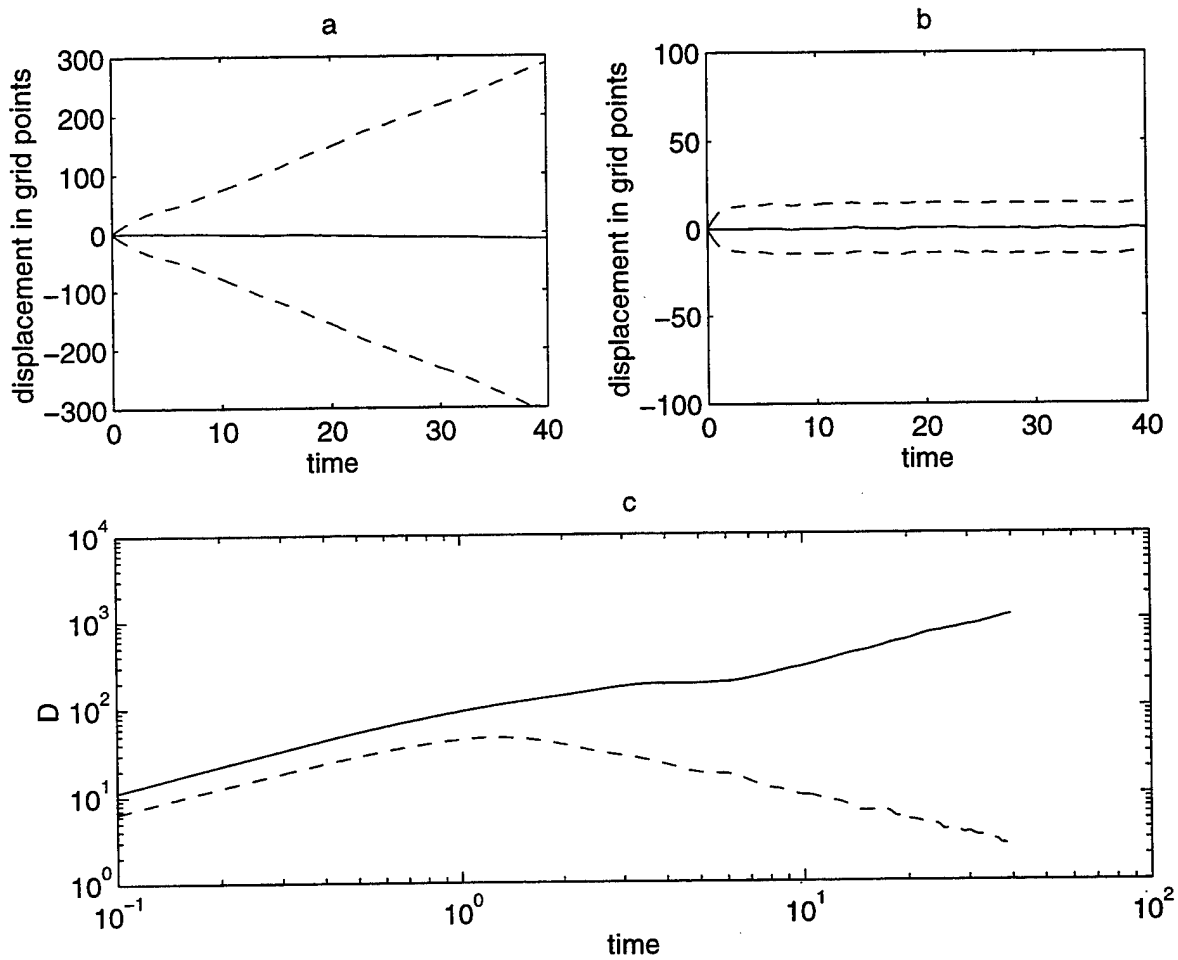
Figure 4: CASE 2 a) the solid line is the mean x-displacement, and the dashed are plus and minus A, the rms. b) the solid line is the mean y-displacement, and the dashed are plus and minus A, the rms. c) The dispersion coefficient, solid line -in x, dashed line - in y.
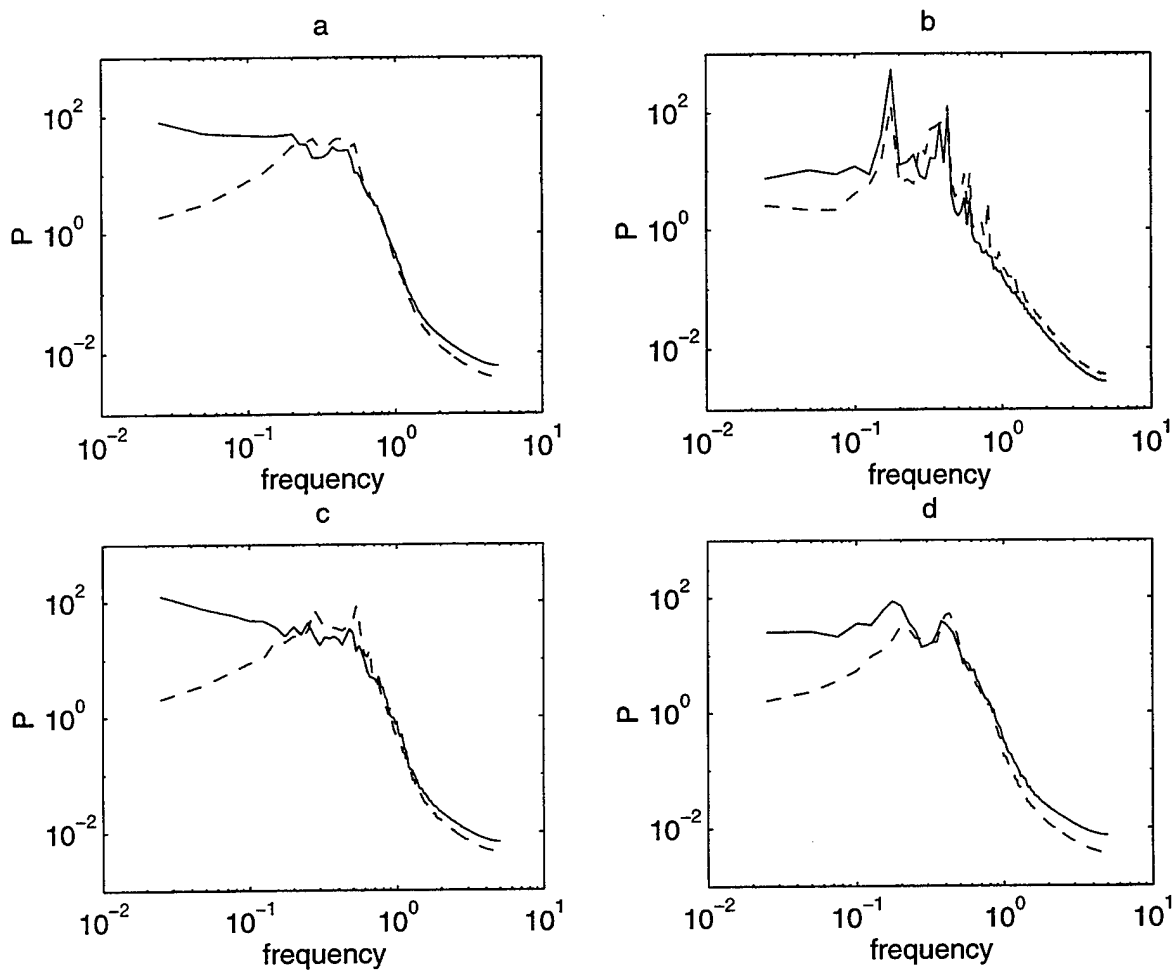
Figure 5: CASE 2 The power spectrum from u(solid), v(dashed). a) the floats. b)the Eulerian field. c) high KE floats. d) low KE floats
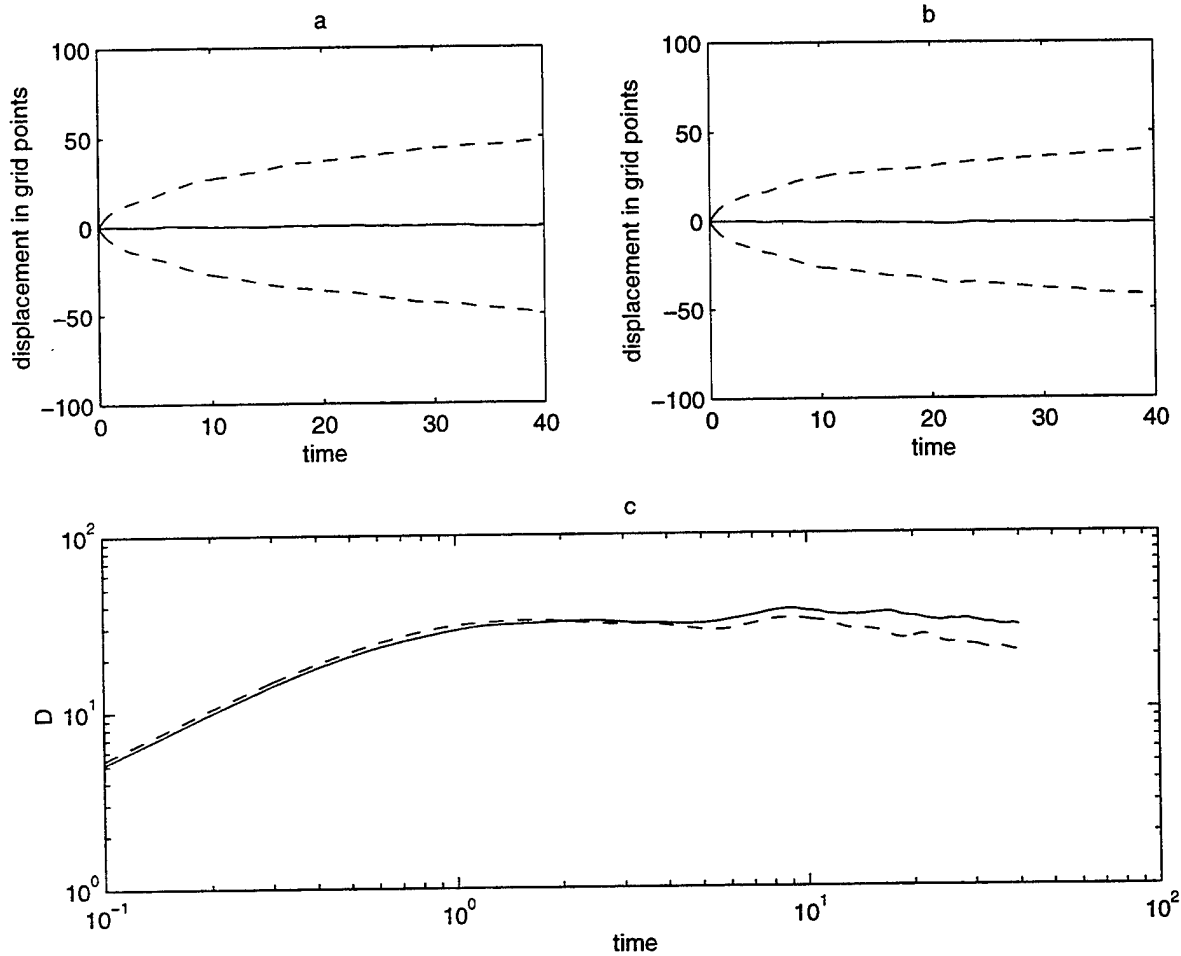
Figure 6: CASE 3 a) the solid line is the mean x-displacement, and the dashed are plus and minus A, the rms. b) the solid line is the mean y-displacement,and the dashed are plus and minus A, the rms. c) The dispersion coefficient, solid line -in x, dashed line - in y.
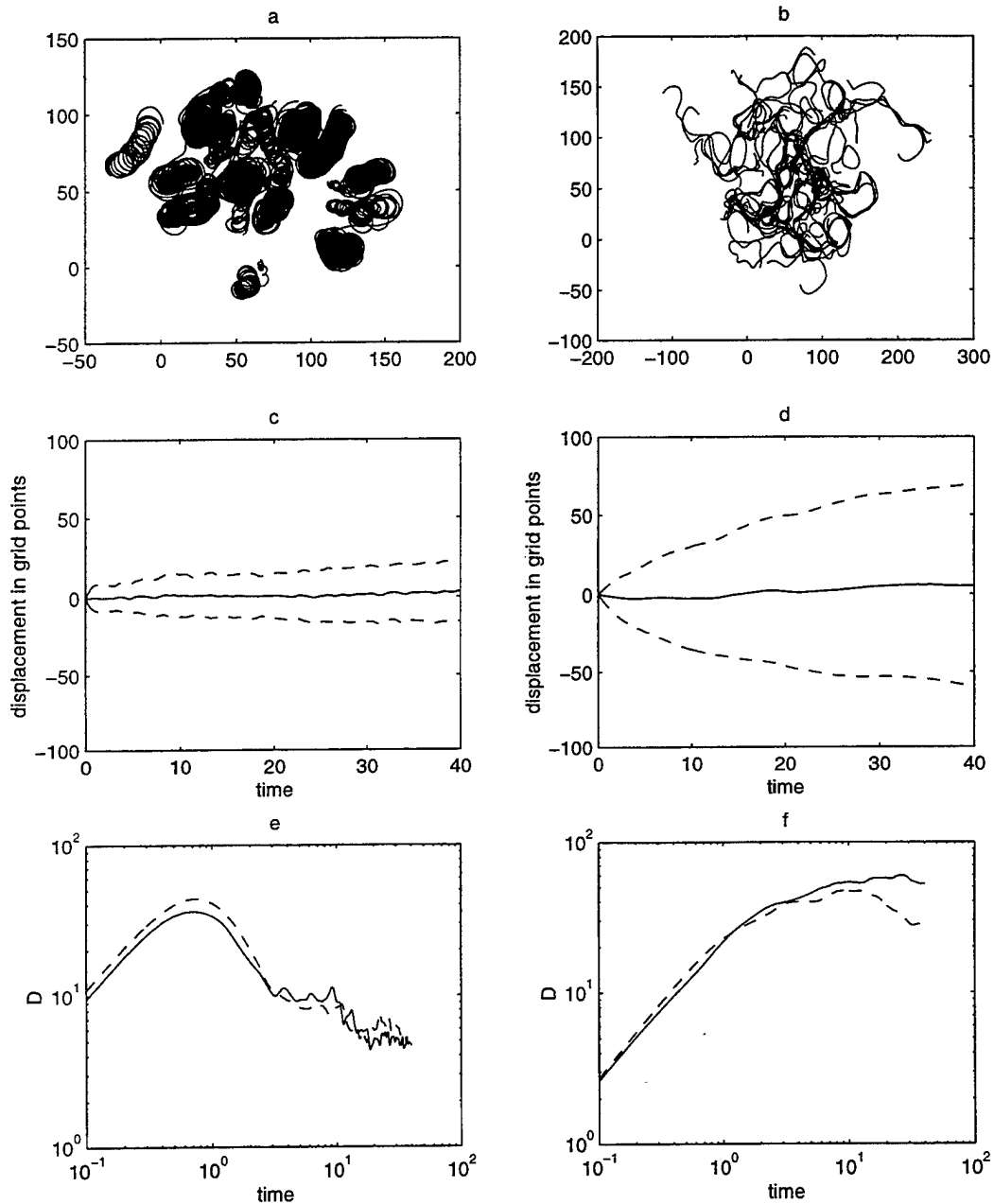
Figure 7: CASE 3 a) The trajectories of high KE floats, b) The trajectories of low KE floats, c) high KE floats: the solid line is the mean x-displacement, and the dashed are plus and minus A, the rms. d)low KE floats: the solid line is the mean x-displacement, and the dashed are plus and minus A, the rms. e) The dispersion coefficient for the high KE floats, solid line -in x, dashed line - in y. f)The dispersion coefficient for low KE floats, solid line -in x, dashed line -in y.
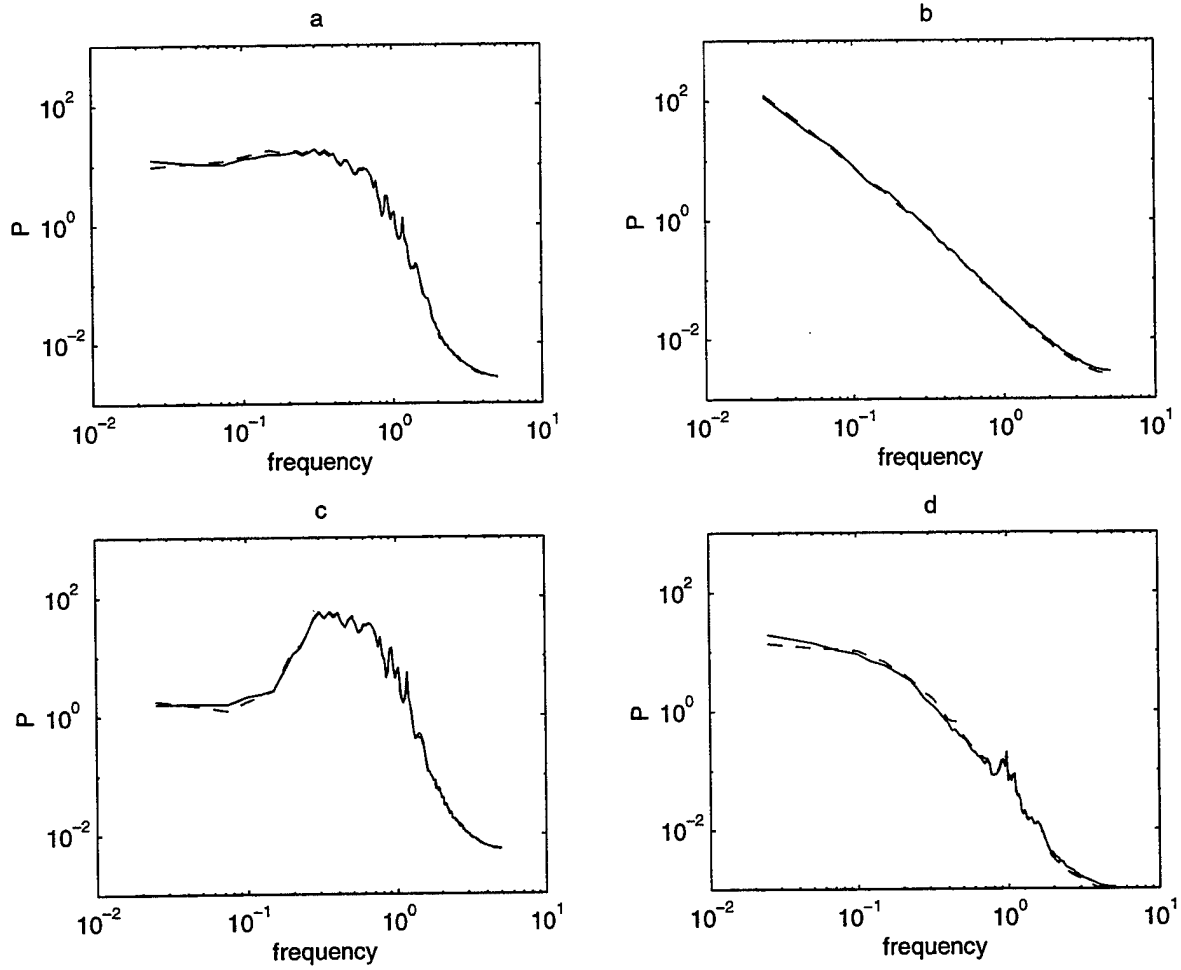
Figure 8: CASE 3 The power spectrum from u(solid), v(dashed). a) the floats. b)the Eulerian field. c) high KE floats. d) low KE floats
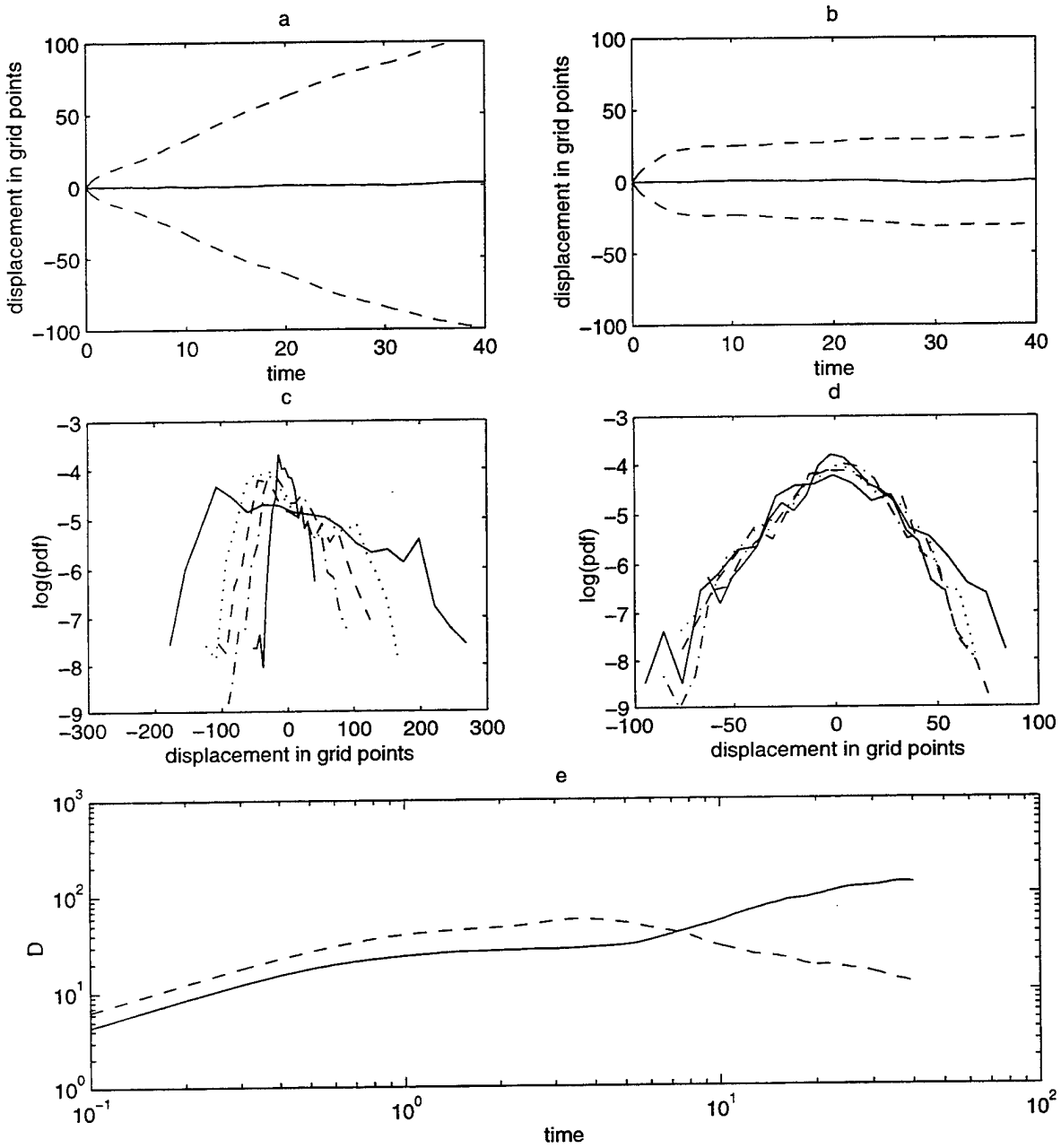
Figure 9: CASE 4 a) the solid line is the mean x-displacement, and the dashed are plus and minus A, the rms. b) the solid line is the mean y-displacement,and the dashed are plus and minus A, the rms.c) PDF of x displacement, inner solid is t=5, dashed dotted is t=10, dashed is t=15 , dotted is t=20, outer solid is t=40. d) PDF of y displacement, the lines mean the same as for the x pdf. e) the dispersion coefficient, solid - in x, dashed - in y.)

184
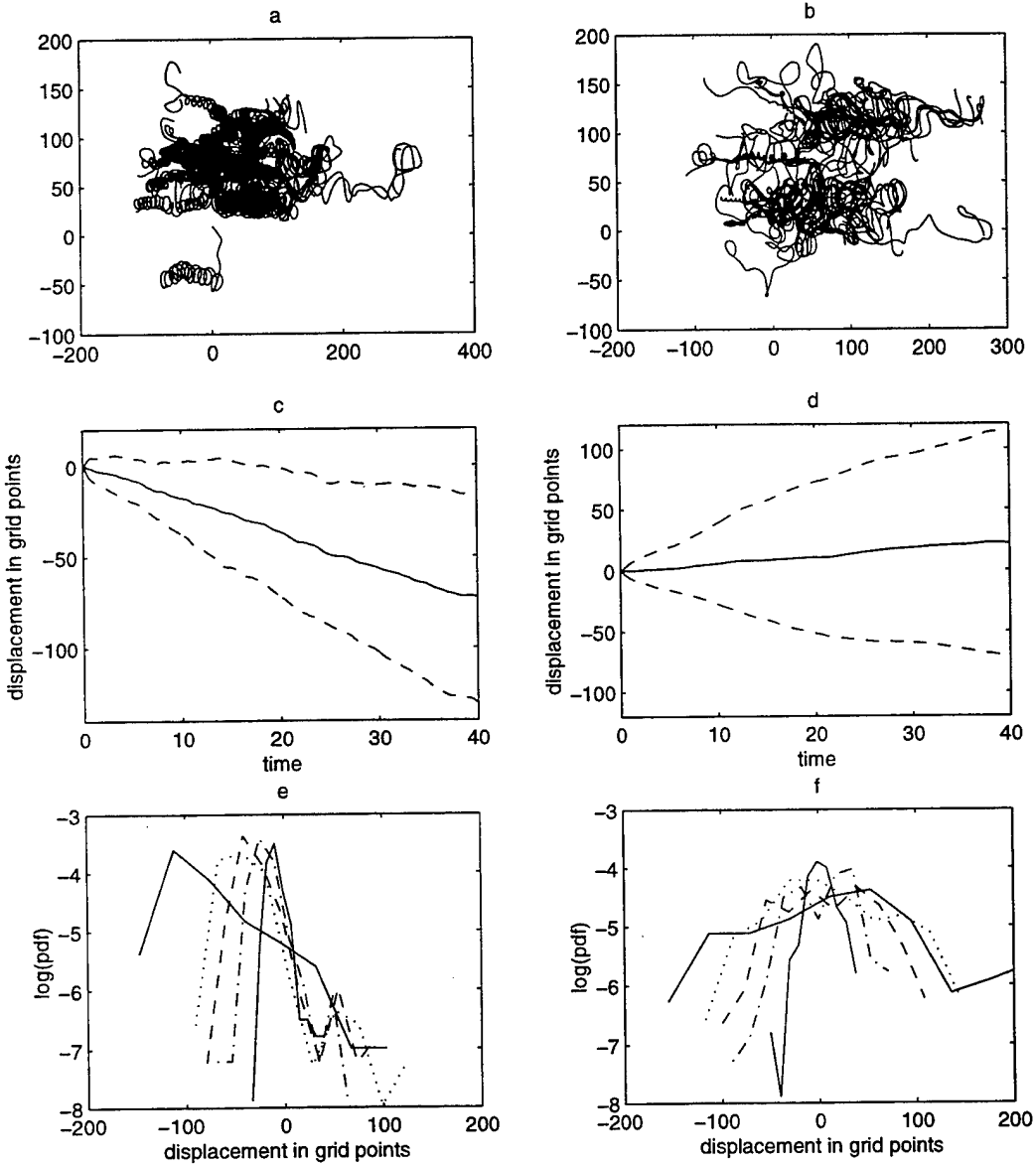
Figure 10: CASE 4 a)The trajectories of high KE floats. b) The trajectories of low KE floats. c) high KE floats: solid line is the mean x-displacement and the dashed lines are plus and minus A, the rms. d) low KE floats displacement same as c. e) high KE floats x PDF, inner solid is t=5, dashed dotted is t=10, dashed is t=15 , dotted is t=20, outer solid is t=40. f) low KE floats x PDF, same as e.

185
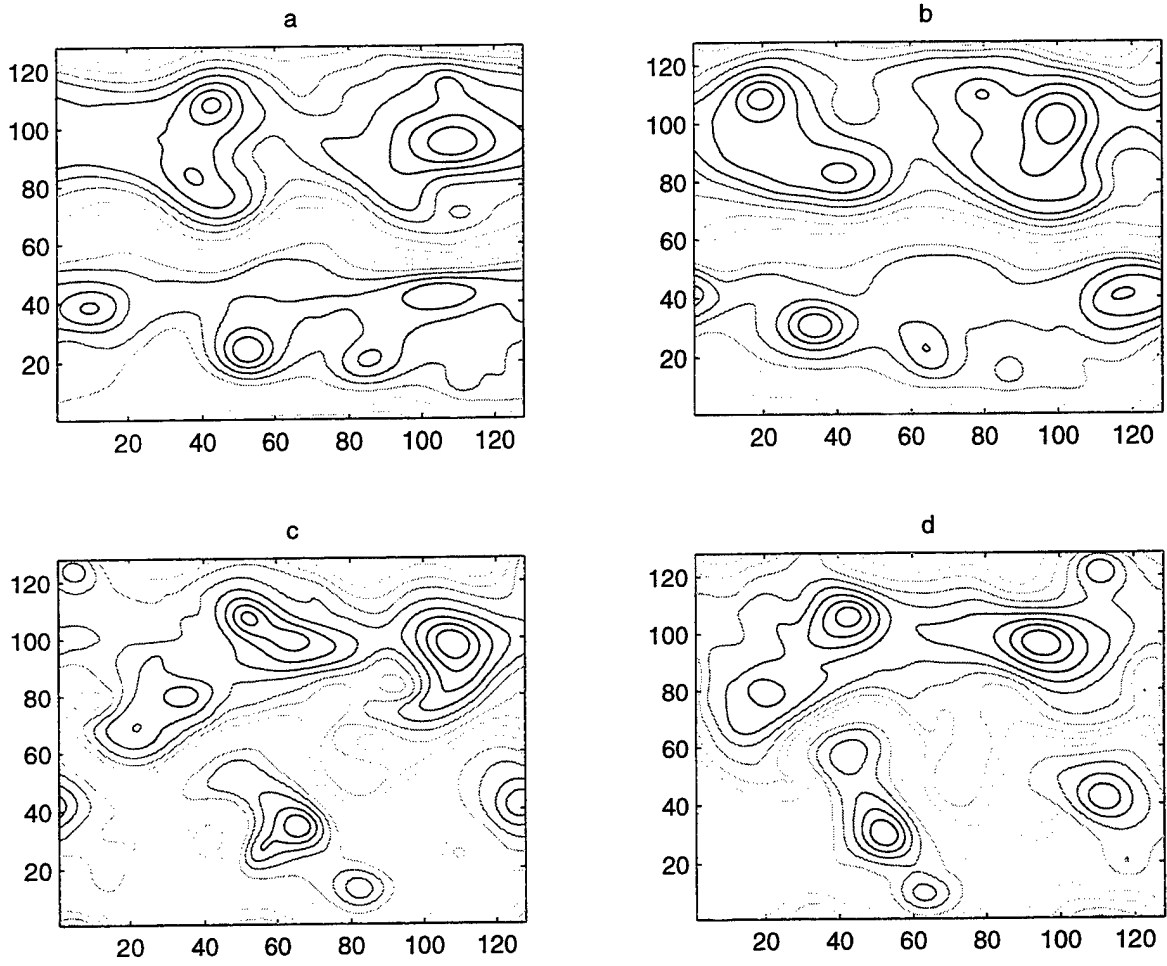
Figure 11: a,b) streamlines for KE ratio=1.4 at t=15,20. c,d) streamlines for KE ratio=.31 at t=15,20.
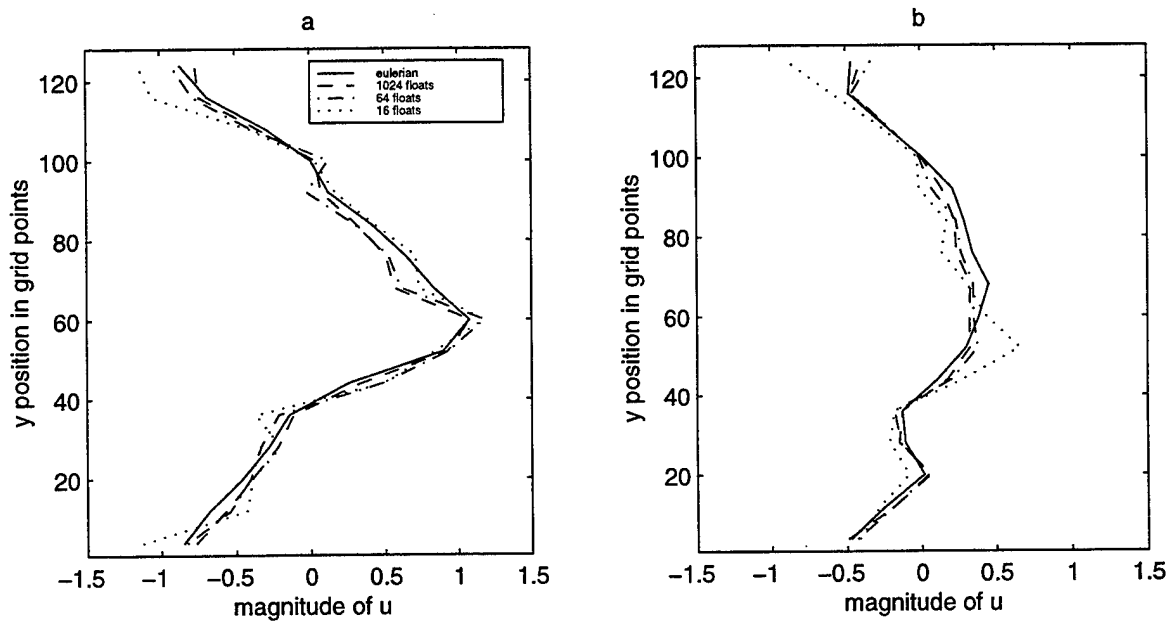
Figure 12: a) mean flow with KE ratio= 1.4 b) mean flow with KE ratio=.312
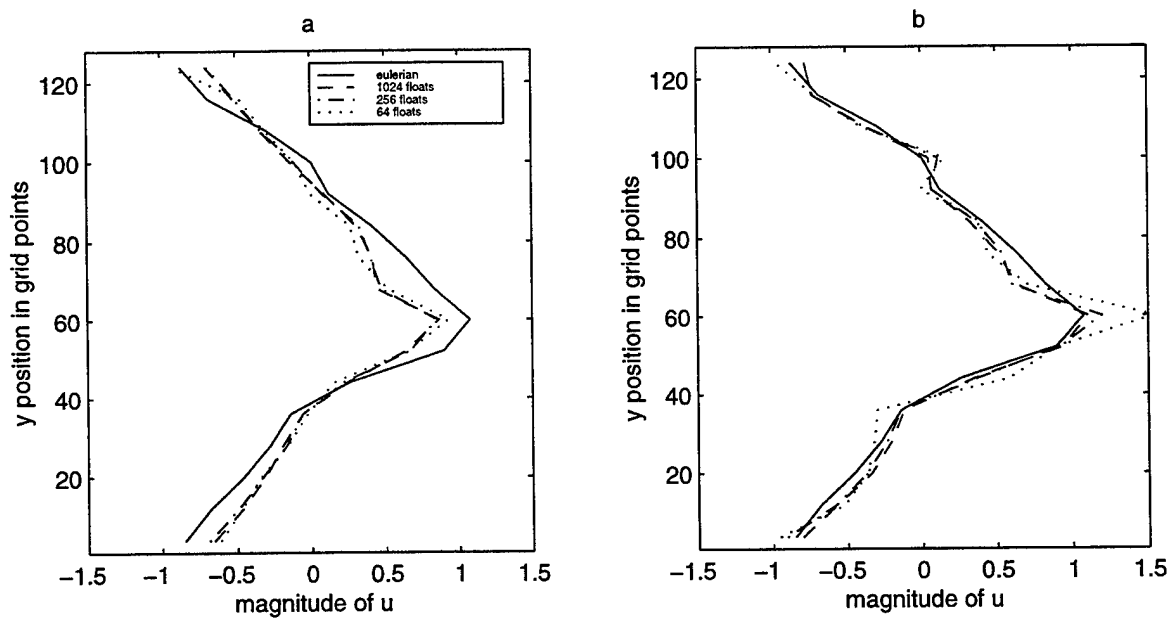
Figure 13: a) mean flow with KE ratio= 1.4 and u reconstructed from trajectories with dt=2 b) mean flow with KE ratio=.1.4 with the velocity data thinned every dt=2
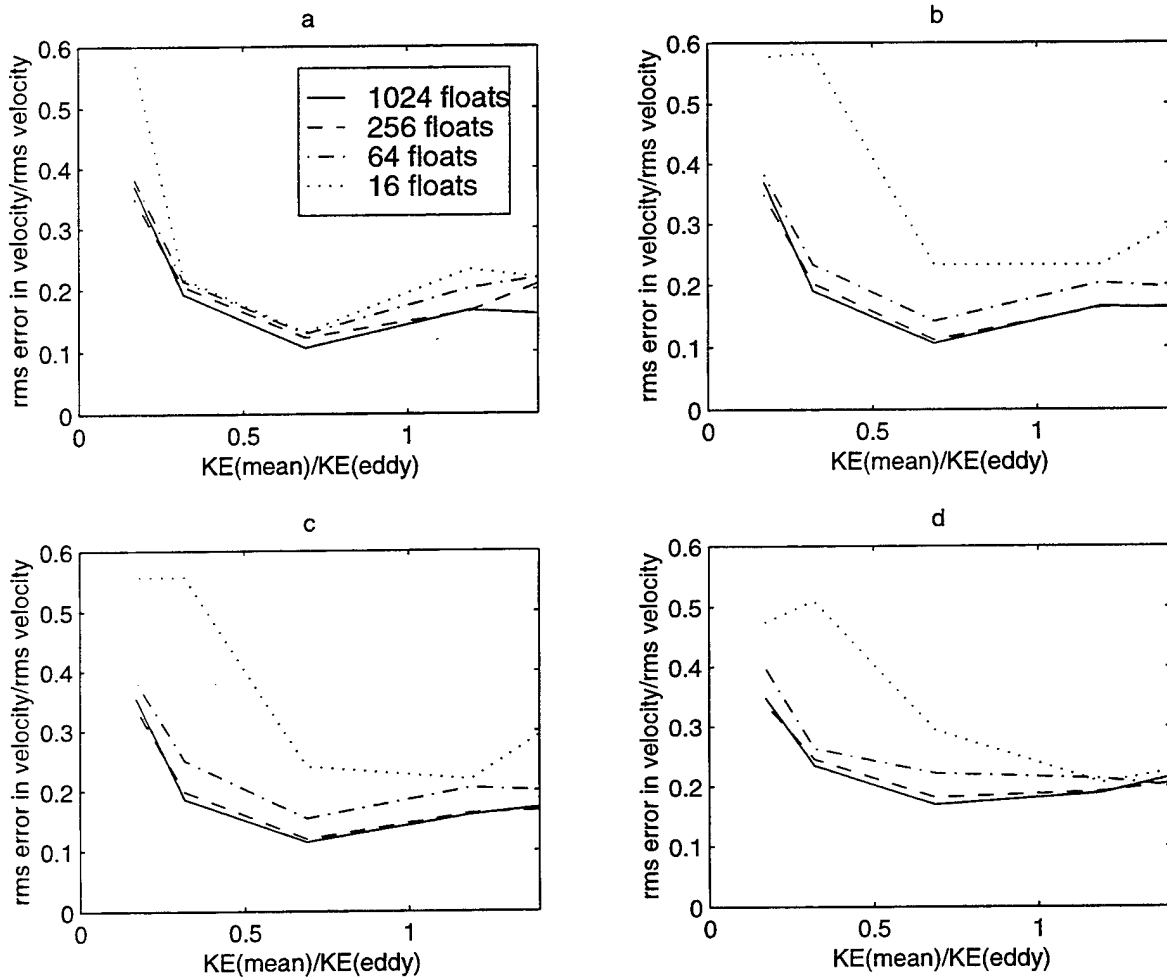
Figure 14: a) perfect data. b) reconstructed flow with dt=.1. c) reconstructed flow with dt=.4 d) reconstructed flow with dt=1

Pandora's Lattice:
Family-Synchronized States in a
Globally Coupled Logistic Map Lattice

Andrew R. Jacobson

1 Introduction

The system of interest in this study is a lattice of N globally coupled one dimensional maps. The lattice evolution is described by

$$x_{n+1}(i) = (1 - \epsilon)f[x_n(i)] + \frac{\epsilon}{N}\sum_{j=1}^{N} f[x_n(j)], \tag{1}$$

where i and j are indices of maps within the lattice, n and $n + 1$ are iteration indices, the coupling strength is ϵ, and $f(x)$ is the map function. $x_n(i)$ is the nth iteration of the ith map in the lattice. The coupling strength ϵ varies between zero and one.

All the lattices discussed in this study are constructed using logistic maps of the form

$$f(x_n) = 1 - ax_n^2. \tag{2}$$

For reference, a bifurcation diagram for this form of the logistic map is shown in Figure 1. This map has the property that any condition on the interval [-1 1] will remain on that interval under iteration of the map.

We should especially note that since the coupling term is constructed of equal contributions from each map in the lattice, there is no spatial dependence in this system.

2 Strong Coupling Limit

As the coupling strength approaches unity, we expect the lattice to tend to a fully-synchronized state. In this limit, all the maps take on the same value and follow the same evolution, which is that of a single, uncoupled logistic map.

There is a threshold coupling value for the lattice above which the system will synchronize. This critical coupling value, ϵ_c, may be computed using linear stability analysis. To do so, we rewrite the N-dimensional lattice evolution (1) in matrix form as $x_{n+1} = C f(x_n)$, where the coupling matrix C is given by
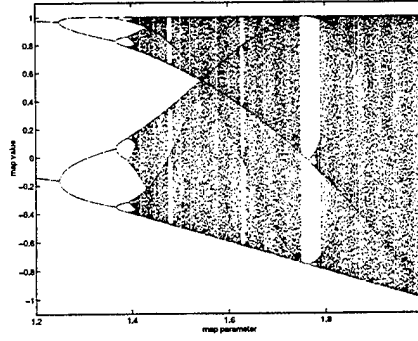
Figure 1: Logistic map bifurcation diagram.

$$\mathbf{C} = \begin{pmatrix} 1 - \epsilon + \frac{\epsilon}{N} & \frac{\epsilon}{N} & \frac{\epsilon}{N} & \cdots & \frac{\epsilon}{N} \\ \frac{\epsilon}{N} & 1 - \epsilon + \frac{\epsilon}{N} & \frac{\epsilon}{N} & \cdots & \frac{\epsilon}{N} \\ \vdots & \vdots & \vdots & \vdots & \vdots \\ \frac{\epsilon}{N} & \frac{\epsilon}{N} & \frac{\epsilon}{N} & \cdots & 1 - \epsilon + \frac{\epsilon}{N} \end{pmatrix}, \tag{3}$$

and

$$\mathbf{f}(\mathbf{x}_n) = \begin{pmatrix} f[x_n(1)] \\ f[x_n(2)] \\ \vdots \\ f[x_n(N)] \end{pmatrix}.$$

The coupling matrix C may also be written as $(1 - \epsilon)\mathbf{I}_N + \frac{\epsilon}{N}\mathbf{1}_N$, where $\mathbf{I}_N$ is the $N \times N$ identity and $\mathbf{1}_N$ is an $N \times N$ matrix of all ones.

The Jacobian matrix at iteration n is $\mathbf{J}_n = \mathbf{C}\,\mathbf{F}'(\mathbf{x}_n)$, with

$$\mathbf{F}'(\mathbf{x}_n) = \begin{pmatrix} f'[x_n(1)] & f'[x_n(1)] & \cdots & f'[x_n(1)] \\ f'[x_n(2)] & f'[x_n(2)] & \cdots & f'[x_n(2)] \\ \vdots & \vdots & \vdots & \vdots \\ f'[x_n(N)] & f'[x_n(N)] & \cdots & f'[x_n(N)] \end{pmatrix}.$$

A small perturbation $\delta\mathbf{x}$ to the synchronized state $x_i = x$ therefore evolves according to

$$\begin{pmatrix} \delta x_{n+1}(1) \\ \delta x_{n+1}(2) \\ \vdots \\ \delta x_{n+1}(N) \end{pmatrix} = \mathbf{J}_n \begin{pmatrix} \delta x_n(1) \\ \delta x_n(2) \\ \vdots \\ \delta x_n(N) \end{pmatrix}. \tag{4}$$

The leading eigenvector of the Jacobian matrix lies entirely within the synchonization manifold and represents the evolution of the manifold itself. The Lyapunov exponent corresponding to this mode, λ_1, is that of the uncoupled logistic map. As reported by Kaneko [Kaneko, 1990] and Ding and Yang [Ding and Yang, 1997], the remaining $N-1$ eigenvectors represent growth transverse to the manifold. Their Lyapunov exponents are degenerate and related to the exponent of the uncoupled map: $\lambda_2 = \lambda_3 = \cdots = \lambda_1 + \ln(1 + \epsilon)$.

This leads to a simple criterion for the appearance of full synchronization within the system. For the synchronization manifold to be attracting, we require that $\lambda_1 + \ln(1+\epsilon)$ have an absolute value less than unity. In chaotic regions of the logistic map, $\lambda_1 > 1$, and the value of the critical coupling strength is

$$\epsilon_c = 1 - e^{\lambda_1}. \tag{5}$$

3 Existence of Other Global Attractors

One application of globally coupled map lattices that is frequently mentioned is to arrays of Josephson junctions. In 1989, Weisenfeld and Hadley [Weisenfeld and Hadley, 1989] published a paper in which they report on a mutiplicity of coexistent stable solutions in coupled arrays of Josephson junctions. They found a large number (order of $(N-1)!$) of stable limit cycles within such a system, and remarked on how small white noise perturbations may induce the system to jump from one basin of attraction to another. They called this phenomenon "attractor crowding", and showed that it may also be found in a system of coupled circle maps.

Shortly thereafter, Kaneko [Kaneko, 1989, Kaneko, 1990] reported finding similar results in a globally coupled logistic map lattice. In addition, he found a rich variety of "family"-synchronized solutions. These stable solutions are global attractors for which the N maps are partitioned into k groups with N_k members each. Each of these groups is a "family", and within each family, all the maps are synchronized to one another. The term "clustering" has been used in the literature to describe these types of solutions. We wish to avoid the connotation of spatial proximity associated with this term, however.

An example of such an attractor in which the lattice falls into a two family attractor is depicted in Fig. 2. The 100 maps are partitioned unequally into the two families; the larger family has 91 members and the smaller has 9 members. Note also that as expected, the members of the smaller family are located haphazardly within the lattice. This is solely a result of the randomly chosen initial conditions.

3.1 Coexistent Global Attractors

One of the interesting features of the system (1) is that there can be mutiple global attractors coexisting at the same parameter values (Fig. 3). In practice, a lattice falls into one basin of attraction or another depending on the initial values of the maps. There is evidence that some of the basins of attraction fill a considerable portion of phase space. At $a = 1.9$ and for coupling strengths of around $\epsilon = 0.385$, we find that randomly-initialized lattices fall robustly
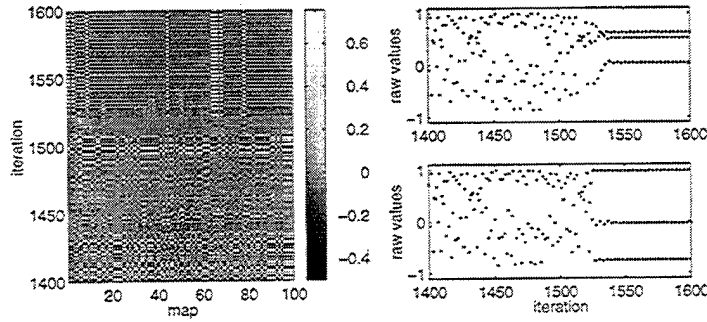
Figure 2: Transition to a two-family attractor for the globally coupled logistic map lattice at map parameter value $a=1.9$, lattice size $N=100$ and coupling strength $\epsilon = 0.385$. The maps of the lattice were initialized with random values. In this attractor, the larger family has 91 members, and the smaller family has 9. (left) Lattice-iteration diagram showing map values as a function of iteration before and after transition to the global attractor. To show contrast between families, the lattice mean at each iteration has been removed. (right, top) Time series of raw map values for map 1, which becomes a member of the smaller family. (right, bottom) Time series for map 2, a member of the larger family.

into one of three categories of two-family attractors: (i) $N_1 = 90$, $N_2 = 10$, period 3, (ii) $N_1 = 91$, $N_2 = 9$, period 3, (iii) $N_1 = 92$, $N_2 = 8$, chaotic. The attractor of Fig. 2 is of type (ii), and the attractor of Fig. 3 is of type (iii). The third return map of the chaotic attractor (Fig. 3, left panel) has an apparently fractal nature reminiscent of that of the Hénon map; as the figure is succesively enlarged, more and more lines become evident.
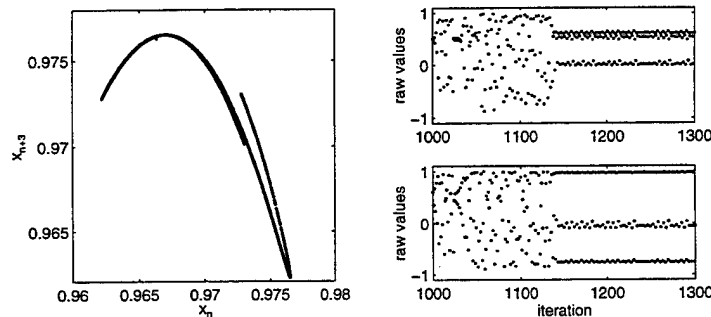
Figure 3: A second two-family attractor for a map lattice identical to that of Fig. 2. This attractor is chaotic. The larger family has 92 members, and the smaller family has 8. (left) Third return map for larger family. (right,top) Time series of raw map values for map #1, which becomes a member of the smaller family. (right, bottom) Time series for map #2, a member of the larger family.

4 Phase diagram

One of the prinicipal results of this summer's work is a refinement of the "phase portrait" presented by Kaneko [Kaneko, 1989, Kaneko, 1990]. This new diagram (Fig. 4) was created with 50 randomly initialized runs at each of 1570 points in the map parameter-coupling strength plane. The map parameter a was varied between 1.4 and 1.98 in steps of 0.02; the coupling strength ϵ was varied from 0.1 to 0.5 in steps of 0.075. There is a rectangular window at $\epsilon > 0.3$ and $a < 1.42$ for which results were not computed.
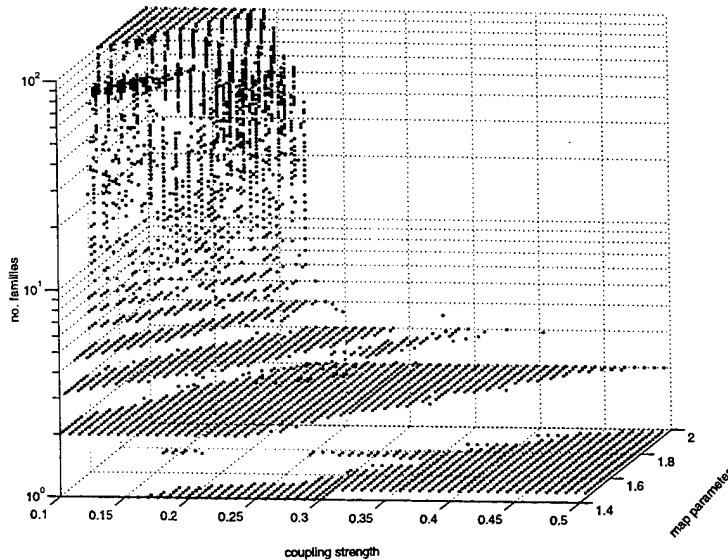
Figure 4: Number of families in statistically-stationary final states as a function of coupling strength ϵ and map parameter a. A dot at a given point means that some number of the runs at the corresponding a and ϵ values had final states with that number of families. Note that the vertical axis is logarithmic. Methodology is described in the text.

For each run, the lattice was initially iterated 300,000 times. The lattice was then further iterated until a measure of statistical stationarity was achieved, up to a maximum of another 500,000 iterations. The quantity which was monitored for stationarity was the mean of the lattice map values at each iteration. The first three statistical moments of both a short- and long-term running series of this quantity were computed. The two series were 75,000 and 300,000 iterations long respectively. For each moment, the short-term and long-term values were compared. If all three pairs of moments were equivalent to within a certain threshold, the lattice was determined to be in a state of statistical stationarity. About a quarter of the runs never achieved this measure of stationarity. Of the 5445 runs resulting in 100-family final states, 1220 failed to achieve stationarity.

Two maps were considered to be in the same family if the cumulative squared difference in map values summed over the 1000 iterations following the run to stationarity was less than

1×10^{-6}.

This method was chosen rather heuristically to see whether lattices with subcritical coupling ($\epsilon < \epsilon_c$) would robustly converge to family-synchronized solutions. The plateaus in Fig. 4, such as the set of 3-family solutions, suggest a perspective which contrasts with that of Kaneko [Kaneko, 1989, Kaneko, 1990], who drew analogies between the phase portraits of conventional thermodynamics and the final states of a globally-coupled logistic map lattice. In those works, Kaneko used a 200-map lattice with 500 randomly-initialized runs at each point, but with a much smaller time series of iterations. After discarding the first 2000 iterations, he categorized each final state using the next 500. Unfortunately, it appears that such systems can exhibit transients which are much longer than 2500 iterations.

The boundary between one-family and two-family states in Fig. 4 approximately follows the critical coupling threshold (5) for chaotic regimes of the logistic map. However, there are runs which converge to fully-synchronized states at sub-critical coupling values, and regions in which stable solutions with both one and two families appear to fill a significant fraction of phase space volume.

The period-three window around $a \simeq 1.76$ is clearly evident in the appearance of a tongue of fully-synchronized states extending to relatively low coupling values. Note also the "island" of one family states at $\epsilon \simeq 0.15$. This region of map parameter space will be explored in more detail in Section 4.1.

The lines that define the boundaries of a given plateau generally run diagonally across the ϵ-a plane. This is a manifestation of a sort of competition between the synchronizing or stabilizing influence of increased coupling and the destabilizing influence of increased map parameter. In the direction transverse to these boundaries, toward higher map parameter or lower coupling strength, there is a generally smooth increase in the number of families. This trend accelerates rapidly until a sort of "wall" is encountered. At this point, the number of families increases quickly until the limit of full desynchronization is reached. The abrupt changes and the complexity of the results in this region of rapid desynchronization suggest that a more finely-grained exploration of parameter space might help to uncover hidden detail and structure.

4.1 Two-dimensional Sections

A more refined study of the distribution of stationary final states was performed for three representative map parameter values: $a = 1.9$, $a = 1.76$, and $a = 1.5$. For these sections, 200 independent runs with randomly-chosen initial conditions were used, and an empirical attempt was made to distinguish between different solutions. Each stationary state was categorized by the number of families in the solution, and by information about each of its families. Each family time series of 1000 iterations was characterized by its mean, its variance, and its periodicity if it had one.

For most of the parameter space domain explored in this manner, the number of distinct solutions found is nearly as large as the number of initial conditions used. If the methods used to distinguish between solutions work as intended, then this is good evidence of attractor crowding [Weisenfeld and Hadley, 1989]. There is a tendency for there to be fewer unique

solutions at higher values of the coupling strength.
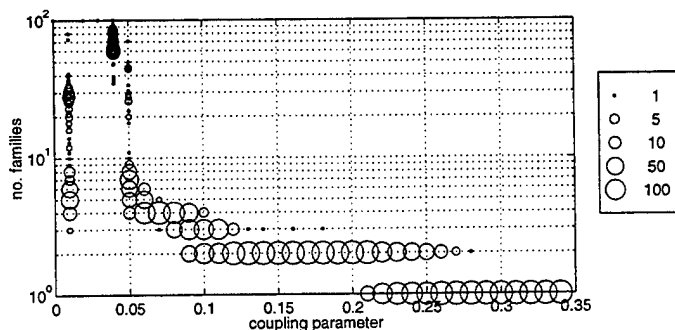
Figure 5: Two-dimensional slice through the parameter space of Fig. 4 at $a = 1.5$. The size of the symbol as given by the key is the number of randomly-initialized runs out of 200 which manifested the given number of families in their stationary final states. For clarity, runs with 100-family results have been portrayed with the smallest symbols.
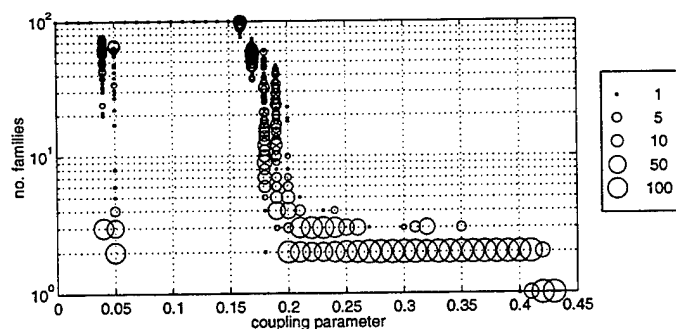
Figure 6: Same as Fig. 5 but at $a = 1.9$.

The existence of simultaneous stable solutions and the general trend for a greater number of families as the coupling strength is reduced is evident in Fig. 5. It is surprising to see that after the complete desynchronization limit is reached at $\epsilon = 0.04$, there is a window at $\epsilon = 0.01$ in which a host of family-synchronized solutions becomes apparent once more. In this window, solutions with 4-7 families and 26-30 families are apparently more prevalent.

The same general features are evident at $a = 1.9$ (Fig. 6). The critical coupling value of 0.4225 [Ding and Yang, 1997] is empirically confirmed here; of the 200 runs at $\epsilon = 0.43$, all had fully-synchronized stationary states. The desynchronization wall occurs near the higher coupling value of $\epsilon = 0.19$, and the window of low-coupling family-synchronized solutions occurs between $\epsilon = 0.04$ and $\epsilon = 0.05$. Once more, there is evidence for a bimodal distribution of number of families in final states in this window, with peaks at around $k = 3$ and $k = 60$. A conjecture concerning the existence of this window at low coupling values will be presented
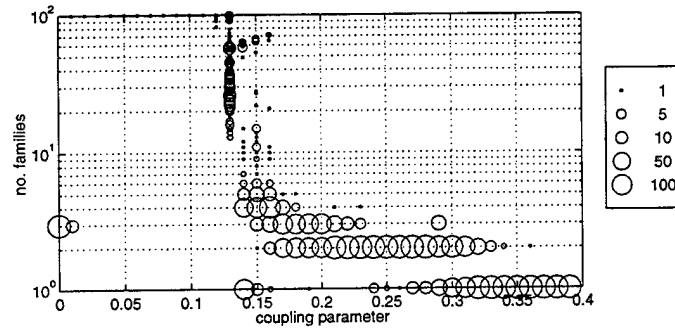
Figure 7: Same as Fig. 6 but at $a = 1.76$. This is in the period-three window of the uncoupled logistic map.

A section through the period-three window (Fig. 7) reveals features which appear to be qualitatively different. As one would expect, at zero coupling only three-family solutions are found. At $\epsilon = 0.01$, there are a few three-family solutions, with the remainder being completely desynchronized. There is a peculiar structure to the desynchronization wall between $\epsilon = 0.13$ and $\epsilon = 0.16$, in which some preference for 60-70 family solutions is shown. Fully-synchronized solutions persist to much lower coupling strengths, and the "island" of one-family states (Sec. 4 and Fig. 4) is clearly evident. Of the three sections which were analyzed in this fashion, this is the only one for which fully-synchronized solutions coexist with final states having three and more families.

It should be noted that during this study, we never found a solution in which member families had differing periodicities. For instance, if one family was period-12, all members were. If one was chaotic, all families were chaotic.

5 Simplified Dynamics

To develop a better understanding of the dynamics at play here, it is instructive to retreat momentarily from the full complexity of the 100-dimensional lattice of fully chaotic maps. In this section, we discuss the dynamics of much smaller lattices of non-chaotic maps. In particular, we will be dealing with regions of the logistic map in which uncoupled maps fall uniquely onto stable period-two or period-four attractors.

5.1 Period-Two Maps

From about $a = 0.74$ to $a = 1.24$, the uncoupled logistic map manifests a single stable solution, that of a period-two oscillator (Fig. 1). There is also an unstable fixed point at $(-1 + \sqrt{1 + 4a})/2a$. Considering both stable and unstable solutions, there are three periodic points of the map. Bifurcation diagrams can be constructed for a lattice with some given

Condition	Map 1	Map 2
1	X_{low}	X_{low}
2	X_{low}	X_{fixed}
3	X_{low}	X_{high}
4	X_{fixed}	X_{fixed}
5	X_{fixed}	X_{high}
6	X_{high}	X_{high}

Table 1: Combinations of initial conditions for two-map lattice in the period two window.

number of maps by considering all the unique possible combinations of solutions as a function of number of periodic points and number of maps. Since position within the lattice is unimportant for globally-coupled systems, we are interested in the number of unique combinations and not the number of permutations. For instance, with the three periodic points coded as X_{high}, X_{fixed}, and X_{low}, there are six unique combinations for a two-map system (Table 1).

Each combination forms an initial condition for the tracing of one branch of a bifurcation diagram. The procedure involves starting just above $\epsilon = 0$ with the maps partitioned according to one combination of the periodic points. Since the coupling strength is non-zero, we expect that the values of the periodic points will have shifted by some small amount. Using Newton's method for zero finding with initial guesses given by the uncoupled periodic points, we determine the actual values of the periodic points for that branch at the given coupling strength. The Jacobian matrix is also computed, and from its eigenvalues we determine whether the particular solution is stable or unstable at that coupling strength. The procedure is continued for an incrementally larger value of ϵ with the just-determined periodic points as the initial guesses.

In Fig. 8(a), we see the results of tracing all six possible branches. The results from both maps in the lattice are plotted. The solid horizontal lines at the top and bottom represent fully-synchronized states, in which both maps are oscillating in phase between the two stable periodic points. The top line corresponds to condition #6 of Table 1 and the bottom line to condition #1. The horizontal dashed line in the center of the plot represents condition #4, the fully-synchronized condition in which both maps are started at the fixed-point. The two stable curving branches represent condition #3, in which one map is initialized at each of the two periodic points. This is an out-of-phase state. As the coupling strength is increased, the maps feel each other to a greater extent and consequently, the periodic points are drawn together. Eventually, this solution becomes unstable. The remaining unstable curving branches represent conditions #2 and #5, for which one map is initialized at the fixed point and the other at one of the two periodic points.

The diagram becomes more involved in Fig. 8(a), for which we have four maps in the lattice and more than twice as many possible combinations of initial conditions. Of the 15 branches traced in this diagram, only 9 are new. There are six combinations which effectively reduce to a two-map lattice. Two more stable branches are generated, depicted by the solid lines
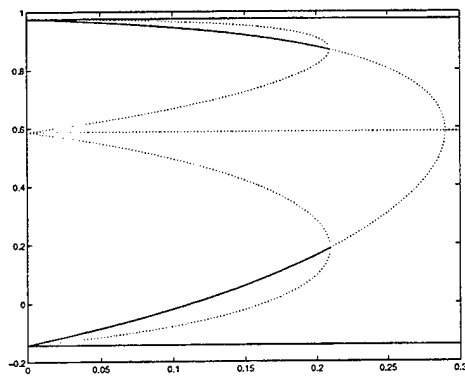
(a) Two-map lattice
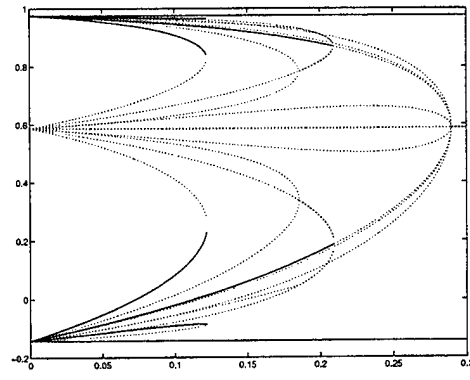
(b) Four-map lattice
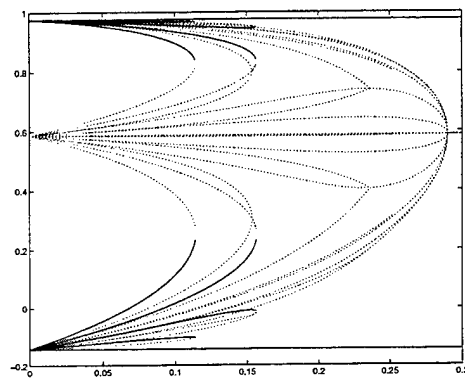
(c) Five-map lattice
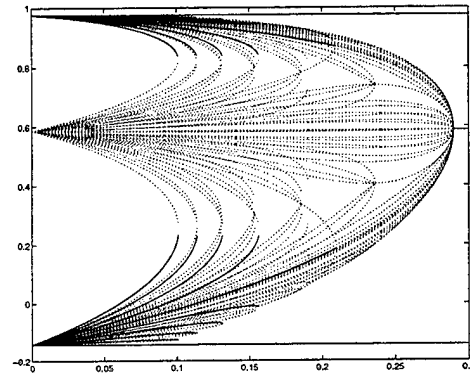
(d) Ten-map lattice

Figure 8: Bifurcation diagrams for lattices of varying size when the map parameter $a = 1.2$ is in the period-two window. Stable solutions are depicted with a solid line, unstable solutions with a dashed line. In all cases, the horizontal axis represents coupling strength ϵ.

terminating at around $\epsilon = 0.12$. These represent the partitioning of one map into one periodic point and three into another. We see already the emergence of multiple stable solutions.

With five maps, an equipartition solution is not possible. The stable out-of-phase solutions shown in Fig. 8(c) are of two sorts: a partitioning of 1:4 into the periodic points, and a 2:3 partitioning. The 1:4 solution becomes unstable at a lower coupling value than the more balanced 2:3 solution.

Finally with the ten maps of Fig. 8(c) we see one way in which attractor crowding might develop. As the number of maps increases, the number of stable solutions at low ϵ increases.

5.2 Period-Four Maps

Between $a = 1.24$ and $a = 1.36$, the uncoupled logistic map is characterized by a single stable period-four solution (Fig. 1). The fixed point of the map persists as an unstable solution, and the period-two points are also solutions. This means that there are seven initial conditions in which to partition the maps to find each branch of the bifurcation diagram.

The bifurcation diagrams of Fig. 9 are characterized by a compression and repetition of the period-two map bifurcation diagrams. This additional complexity yields a further set of stable solutions at low coupling strengths.

(a) Two-map lattice   (b) Four-map lattice
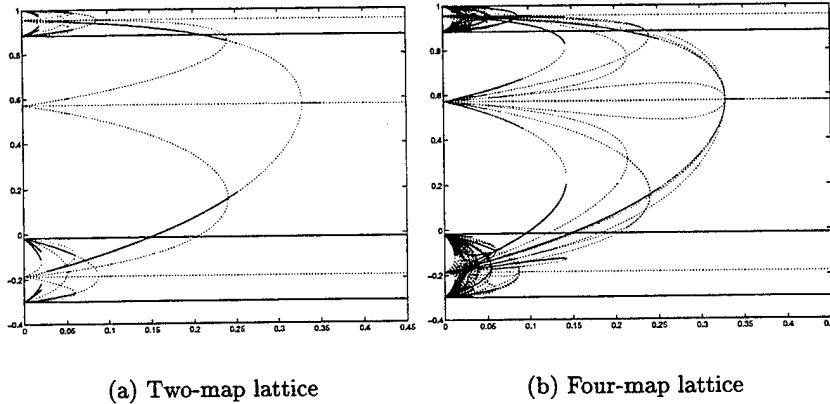
Figure 9: As in Fig. 8, but for map parameter $a = 1.3$ in the period-four window.

6 Stability of Two-Family Solutions

When a lattice assumes a stable family-synchronized solution, its dynamics are vastly simplified. The dynamics of an N-map lattice evolving as k families may simply be written as a k-dimensional map. For instance, let $k = 2$ with families x and y of size N_x and N_y respectively. If we define $N_x/N = \alpha$ and $N_y/N = 1 - \alpha$, then the system evolution at iteration i may be written as

$$
\begin{aligned}
x_{i+1} &= (1 - \epsilon)f(x_i) + \epsilon S_i \\
y_{i+1} &= (1 - \epsilon)f(y_i) + \epsilon S_i,
\end{aligned}
$$

where the mean field is

$$
S_i = \alpha f(x_i) + (1 - \alpha)f(y_i).
$$

(6)

This leads to the determination of criteria for the linear stability of a two-family system. A perturbation $\xi(n)$ to each map $x(n)$ and a perturbation $\eta(m)$ to each map $y(m)$ evolve according to

$$
\begin{aligned}
\xi(n)_{i+1} &= (1-\epsilon)f'(x_i)\xi(n)_i + \epsilon\sigma_i \\
\eta(m)_{i+1} &= (1-\epsilon)f'(y_i)\eta(m)_i + \epsilon\sigma_i,
\end{aligned}
$$
with
$$
\sigma_i = \alpha f'(x_i)\sum_{n=1}^{N_x}\xi(n)_i + (1-\alpha)f'(y_i)\sum_{m=1}^{N_y}\eta(m)_i. \tag{7}
$$

If all the maps within each family are subject to the same perturbation (i.e., $\xi(n) = \xi$ and $\eta(n) = \eta$), then the problem reduces to that of dynamics within the synchronization manifold. The more intriguing question, however, involves the remaining stability exponents, which are transverse to the synchronization manifold and thus describe the linear stability of the two-family state. If we assume that σ_i is identically zero, then we can search for two cases: either $\sum_{n=1}^{N_x}\xi(n) = 0$ and $\eta(m) = 0$, or $\xi(n) = 0$ and $\sum_{m=1}^{N_x}\eta(m) = 0$. The first case gives

$$
\xi(n)_{i+1}/\xi(n)_i = (1-\epsilon)f'(x_i), \tag{8}
$$

and the second

$$
\eta(m)_{i+1}/\eta(m)_i = (1-\epsilon)f'(y_i). \tag{9}
$$

The stable regime of one particular two-family solution is depicted in Fig. 10. The initial solution is period-three. The bifurcation which occurs from $\epsilon = 0.334$ to $\epsilon = 0.321$ is shown in detail in Fig. 11.
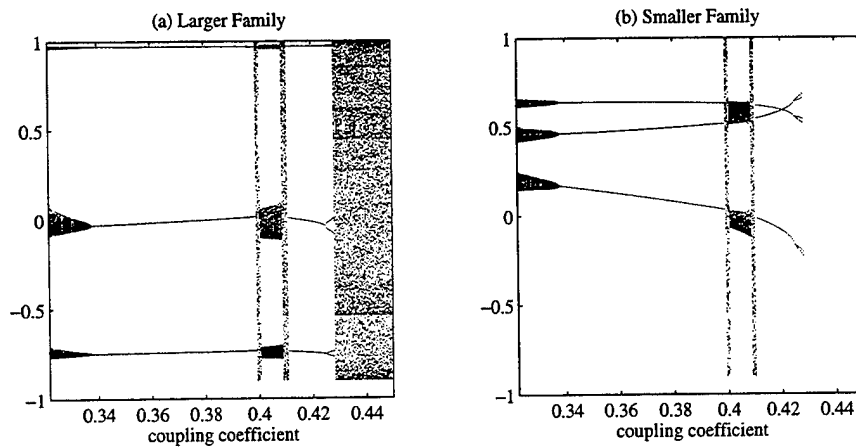
Figure 10: Bifurcation diagram for a particular solution as a function of coupling parameter ϵ. This is a two-family (10 and 90 members) period-three solution generated at $a = 1.9$ and $\epsilon = 0.388$. At each successive value of the coupling parameter, the lattice was initialized with the stationary final state of the lattice from the previous coupling parameter value. (a) Larger family. (b) Smaller family. For $\epsilon > \epsilon_c$ at about 0.4225, the lattice is fully synchronized and only one family exists.

7 Acknowledgements

References

[Ding and Yang, 1997] Ding, M. and Yang, W. (1997). Stability of synchronous chaos and on-off intermittency in coupled map lattices. *Phys. Rev. E*, 56(4):4009–4016.

[Kaneko, 1989] Kaneko, K. (1989). Chaotic but regular posi-nega switch among coded attractors by cluster-size variation. *Phys. Rev. Lett.*, 63(3):219–223.

[Kaneko, 1990] Kaneko, K. (1990). Clustering, coding, switching, hierarchical ordering, and control in a network of chaotic elements. *Physica D*, 41:137–172.

[Ott, 1993] Ott, E. (1993). *Chaos in Dynamical Systems*. University Press, Cambridge.
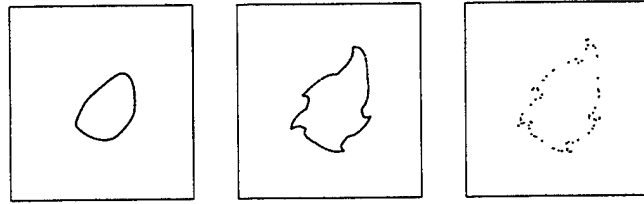
(a) $\epsilon = 0.334$ (b) $\epsilon = 0.33$ (c) $\epsilon = 0.3292$
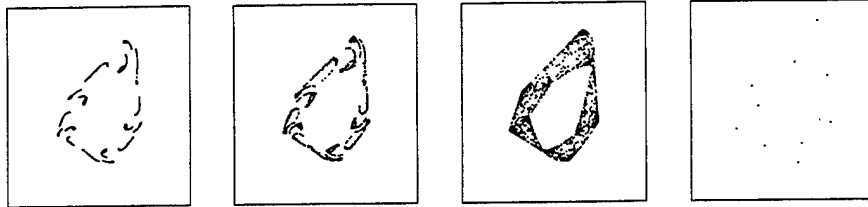
(d) $\epsilon = 0.3286$ (e) $\epsilon = 0.32855$ (f) $\epsilon = 0.328$ (g) $\epsilon = 0.327$

(h) $\epsilon = 0.3268$ (i) $\epsilon = 0.3264$ (j) $\epsilon = 0.321$

Figure 11: Third return map for break up of the two-family solution of Fig. 10. The smaller family third returns are plotted on the horizontal axis and those of the larger family on the vertical. Panels depict succesively smaller coupling strengths. Linear stability is lost at about $\epsilon = 0.322$.

[Weisenfeld and Hadley, 1989] Weisenfeld, K. and Hadley, P. (1989). Attractor crowding in oscillator arrays. *Phys. Rev. Lett.*, 62(12):1335–1338.

Hill's Horseshoes:
Chaos in a Forced System

Claudia Pasquero

1   Introduction

To describe the basic mechanism of the ocean circulation, Stommel [Stommel, 1961] proposed a simple model that takes in account of the difference in density at different latitudes: he considered a box at the equator with temperature T_E and salinity S_E and a box at the pole with temperature T_P and salinity S_P.

Due to the different incoming heat fluxes and the different evaporation rates, a water flux (that he supposed to occur in pipes connecting the two boxes) that reduces the gradients between the two boxes is necessary. In terms of the adimensionalized difference in temperature x and salinity y, the equations that describe this model are:

$$\begin{cases} \dot{x} = \tau(1 - x) - |q|x \\ \dot{y} = \nu - |q|y \end{cases}$$

where $q = \mu(x - Ry)$ is the adimensionalized water flux, considered proportional to the density difference between the two boxes (which is given in terms of x and y through a linear equation of state); ν describes the constant salinity flux at the surface of the ocean and τ is related to the relaxation time scale of the ocean to the atmospheric temperature. (A constant salinity flux and a restoring temperature are often referred to as "mixed boundary condition").

This system is equivalent to a second order differential equation for the flux q:

$$\ddot{q} = -\frac{\partial V}{\partial q} - (\tau + 3\mu|q|)\dot{q}$$

where the potential is:

$$V(q) = \mu^2 \frac{q^4}{4} + \mu\tau \frac{|q|q^2}{3} - \mu(\tau - \nu R)\frac{|q|q}{2} - \tau R\nu q$$

and the term containing the first time derivative of the flux can be considered as a nonlinear dissipation. Since the shape of the potential is a double well (fig. 1), it is clear that there are three fixed points, and that only two of them (q_S and q_T) are stable. (The same approach to the Stommel model is described in [Thual and McWilliams, 1992]).
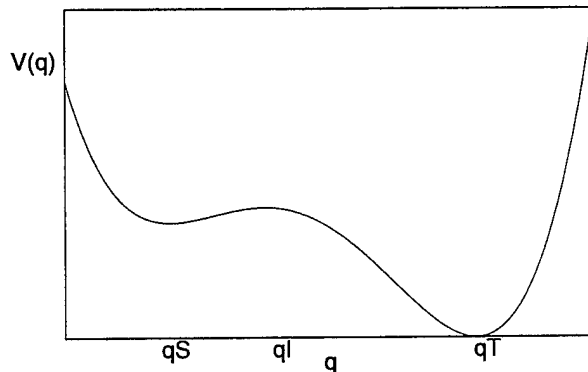
Figure 1: Potential of the Stommel model: q_S, q_I and q_T are three steady states for the water flux q.

More complicated potential (with a larger number of steady states) can be obtained by including different features, like a vertical structure in the boxes or the effect of the surface wind-driven circulation. Since variability in the intensity of the water flux has been proposed to explain some obervational data from the ocean and multiple equilibria have been obtained in numerical models, we address a question on the way the various states can interact. This kind of variations can be due to an internal variability or to an external forcing acting on the system. In this study we only deal with this second case: we will consider a double well potential whose shape changes periodically in time and we will study the different kinds of possible solutions.

2 A forced system

We are intersted in a system such as:

$$\begin{cases} \ddot{x} = -\frac{\partial V}{\partial x} - \mu \dot{x} \\ V = V(x, \lambda), \qquad \qquad \text{where} \quad \lambda = \lambda(t) \end{cases} \tag{1}$$

One of the systems that can be described in this way is the well known three dimensional model of the Rayleigh-Benard convection due to Lorenz [Lorenz, 1963]: Marzec & Spiegel [Marzec and Spiegel, 1978] showed that it can be described as the motion of an idealized dissipated particle in a simmetric double well potential $V(x) = \frac{x^4}{4} - \lambda \frac{x^2}{2}$ that varies in time: $\dot{\lambda} = -\epsilon g(x, \lambda)$. Poyet [Poyet, 1980] showed that in the limit of small ϵ, the variation of λ becomes periodic in time.

Since we are interested in a variation in the potential that is due to an external forcing that does not receive any feedback from the system in consideration, we will use the same kind of skew-product coupling and let λ vary in time as a periodic function:

$$\lambda(t) = \lambda_0 + \lambda_1 \sin \omega t$$
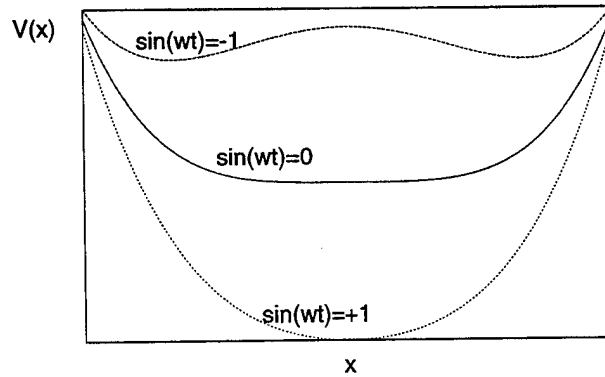
Figure 2: Variation of the shape of the potential subjected to the periodic forcing described in the main text: the stability properties of the fixed points change with time, every half a period of the forcing.

Therefore, the second order equation (1) becomes

$$\ddot{x} = -x^3 - (\lambda_0 + \lambda_1 \sin \omega t)x - \mu\dot{x} \tag{2}$$

This equation is a particular case of a general class of equations that have an explicit dependence of time (Hill's equations) and in particular it is a non linear damped Mathieu equation. The non dissipative case ($\mu = 0$) describes the separatix crossing problem in a Hamiltonian system. The linear case (without the x^3 term) has solutions that, in some "resonance tongues" in the parameter space (λ_0, λ_1), are unbounded (the amplitude of the periodic solutions grows to infinity), both in non dissipated and dissipated cases. Hsu [Hsu, 1977] and Fauve [Fauve, 1991] studied the non linear equation in the case of small amplitude forcing ($\lambda_1 \ll \lambda_0$). We want to focus on the case of large amplitude fluctuations of the forcing ($\lambda_1 > \lambda_0$) such that λ can vary sign with time, leading to variations in the stability properties of the fixed points (for this reason we can consider $\lambda_0 = 0$), and, eventually, chaotic behavior.

3 Numerical results

In order to integrate numerically equation (2), we write it as a system of two first order equations:

$$\begin{cases} \dot{x} = y \\ \dot{y} = -x^3 - \lambda(t)\, x - \mu y \end{cases} \tag{3}$$

where x and y can be seen as the position and the velocity of the idealized particle in the potential, respectively.

In fig. 3 time series of the x variable for different values of the parameters are plotted. If the time scale of the forcing is very large, the system has time to react to the "adiabatic"
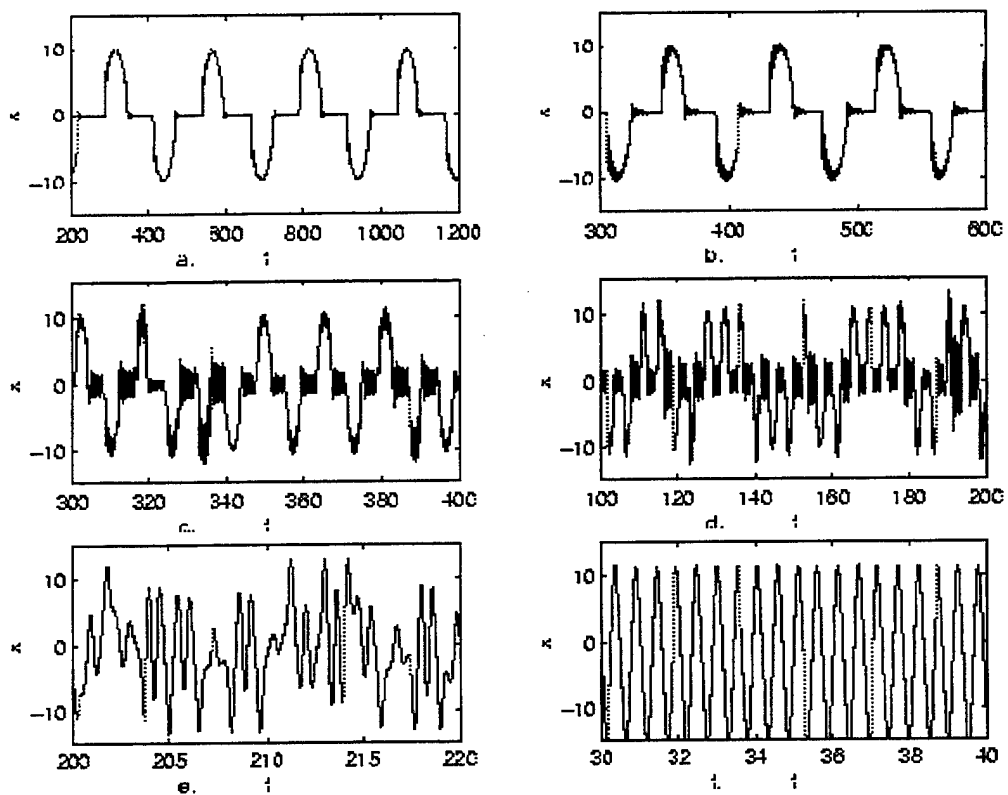
Figure 3: Time series of the x variable obtained integrating system (3) with $\lambda_0 = 7$, $\lambda_1 = 100$, $\mu = 0.3$ and **a.** $\omega = 0.05$, **b.** $\omega = 0.15$, **c.** $\omega = 0.8$, **d.** $\omega = 1.5$, **e.** $\omega = 4$, **f.** $\omega = 15$
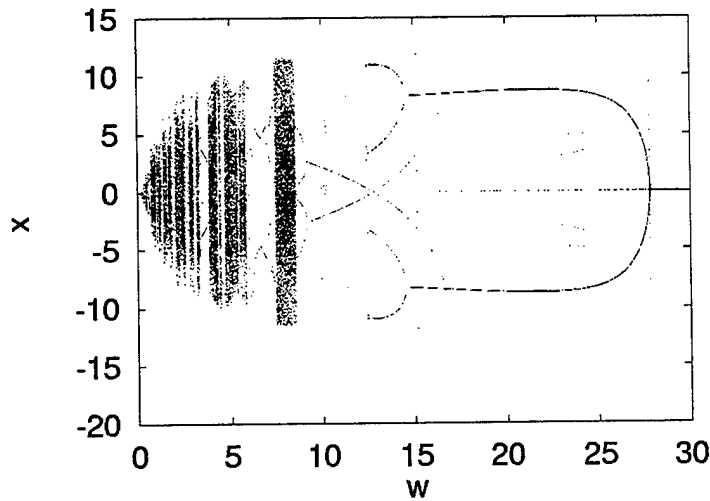
Figure 4: Bifurcation diagram when varying the time scale of the forcing ω. $\lambda_0 = 7$, $\lambda_1 = 100$, $\mu = 0.3$

variations and the solution will be periodic, passing from the middle fixed point to one of the two others, in a regular way, every $\Delta t = \pi/\omega$.

When the frequency of the forcing, compared to the dissipative time scale, increases, the oscillations of the solution around each fixed point will have larger amplitude and at a certain value (when the two time scales become comparable) chaotic motion appears, leading to irregular alternance of the position of the solution in the phase space between the two simmetric wells, according to the phase at the time in which the middle point looses its stability. If the forcing frequency becomes very large (such that $\omega/\mu >\sim 100$) the chaotic regime ends and the solutions become again periodic: in this case the system does not have time to react to the forcing because it has a strong inertia and it feels only a mean potential without fluctuations. In the large regime where chaos occurs (as it can be seen in the bifurcation diagram, fig. 4) there are windows where periodic behavior is restored and period doubling bifurcations may occur.

In fig. 3 attractors corresponding to these different type of solutions are shown: on the vertical axis the temporal dependence, through λ, is stressed. The motion along that axis is independent on the behavior of the solution, and in this sense the plot in fig. 3 are not attractors in the phase space but, more properly, projections of a four dimensional autonomous system phase space, where the variation of λ is written in term of an oscillator, using a new variable ν:

$$\begin{cases} \dot{\lambda} = \omega\nu \\ \dot{\nu} = -\omega\lambda \end{cases}$$

207

c.
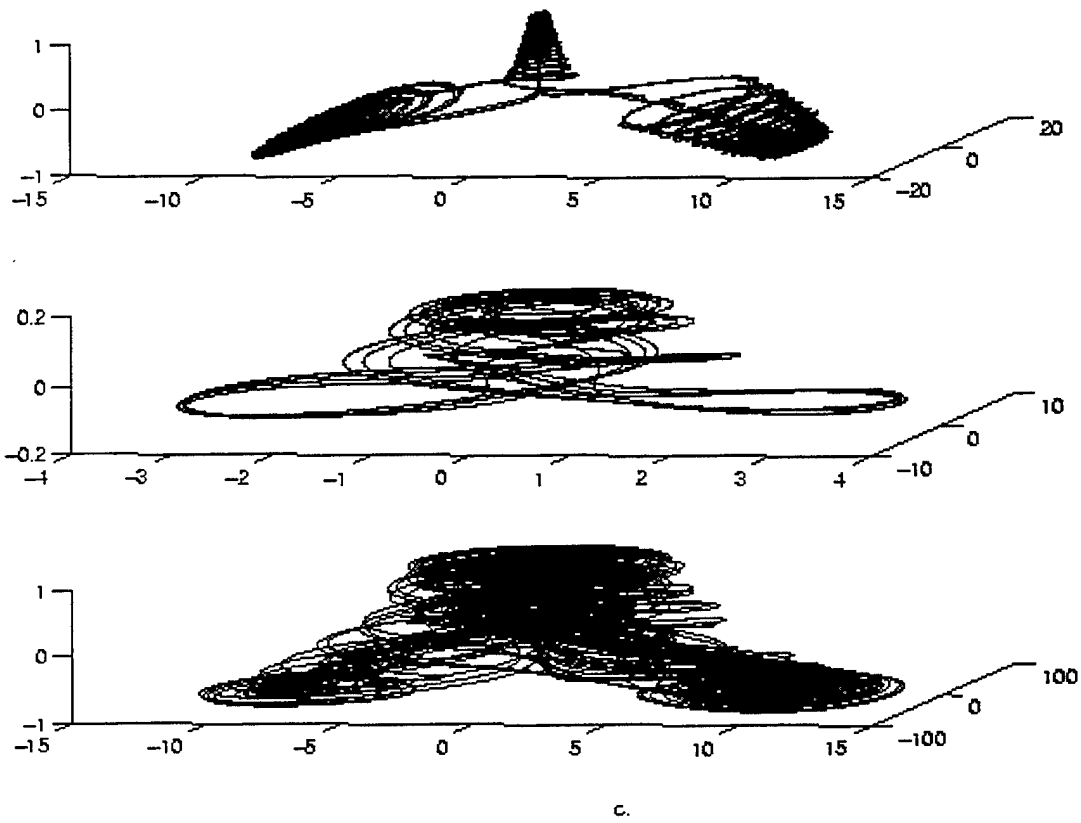
Figure 5: Trajectories in x,y,λ space by integration of the system (3) with $\lambda_0 = 7$, $\lambda_1 = 100$, $\mu = 0.3$ and **a.** $\omega = 0.15$, **b.** $\omega = 0.825$, **c.** $\omega = 1.2$

208

The approach of the autonomous system is not useful in our case because these two new differential equations represent by themselves a Hamiltonian system and the linearization around its fixed point ($\lambda = 0$, $\nu = 0$) is not a good approximation when, as in our case, the oscillations have a finite amplitude and therefore the trajectory in its phase space is far from the origin.

4 Shil'nikov theory

Since the plots of our attractors remind the structure of the Shil'nikov homoclinic orbit, let's try to see if we can use the same approach to study our system.

Theorem (Shil'nikov [Shil'nikov, 1965]):

consider the system

$$\begin{cases} \dot{x} = \rho x - \omega y + P(x,y,z) \\ \\ \dot{y} = \omega x + \rho y + Q(x,y,z) \\ \\ \dot{z} = \lambda z + R(x,y,z) \end{cases}$$

where P,Q,R are C^r functions ($1 \leq r \leq \infty$) vanishing together with their first derivatives at the origin $0 = (0,0,0)$. Let us assume that one of the orbits, denoted by Γ_0, leaves the origin and returns to it as $t \to +\infty$. Then, if $\lambda > -\rho > 0$ every neighbourhood of the orbit Γ_0 contains a denumerable set of unstable periodic solutions of saddle tipe.

In other words, if the dynamics in the neighbourhoods of a fixed point of a system can be described in term of an oscillation towards it along the stable manifold (x,y plane) and an exponential divergence from it on the unstable direction (z) (see the sketch of a homoclinic orbit approaching the fixed point in fig. 4a), the exact law, derived by the linear approximation, that describes the dynamics in that region tell us (see [A. Arneodo and Tresser, 1981] and [A. Arneodo and Tresser, 1985]) that a line on the Poincaré section on the plane Σ_0 orthogonal to the local stable manifold will be deformed in a spiral on the plane Σ_1 orthogonal to the local unstable manifold. When reinjecting points from Σ_1 to Σ_0 with a rigid motion (defined by an arbitrary translation and rotation) it can be seen that the initial line has been folded in a spiral. This motion can be represented by a two dimensional map of Σ_0 into itself: for each line it is a topological horseshoe. Arneodo et al. [A. Arneodo and Tresser, 1985] showed that this map, in the limit of infinite dissipation, can be reduced to a one dimensional map and that the number of unstable periodic solutions increases as approaching the homoclinc orbit.

This theorem proves the existence of infinitely many periodic orbits in a large class of three dimensional differential equation. It is a usefool approach because the linearized system can be solved analitically, but in our case it cannot be straight used because of the lack of an unstable direction: therefore, the linearization of the system around the fixed points simply represents a rigid rotation, and nothing more, as we can see in the next section.
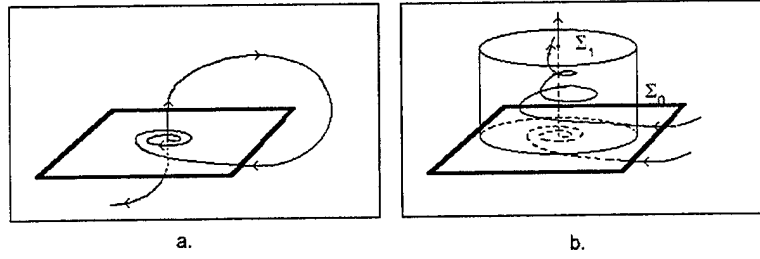
Figure 6: a. Homoclinic orbit. b. The sections Σ_0 and Σ_1.

5 Linear Stability Analysis

The full system is:

$$\begin{cases} \dot{x} = y \\ \dot{y} = -\mu y - x^3 - a\sin\omega t\, x \end{cases} \qquad (4)$$

In order to find its steady states, we set the time derivatives to zero: the point $z_0 = (x_0, y_0) = (0,0)$ is always a fixed point, while to other fixed points $z_{1,2} = (\pm\sqrt{-a\sin\omega t}; 1)$ appears only when $\sin\omega t < 0$.

The linear stability analysis around the fixed point z_0 shows that its stability properties change with time. The linearized version of system (4) around z_0 is:

$$\begin{cases} \dot{x} = y \\ \dot{y} = -\mu y - a\sin\omega t x \end{cases} \qquad (5)$$

The eigenvalues that describe the evolution of a linear perturbation close to this point can be found by solving the characteristic equation:

$$\begin{vmatrix} -\lambda & 1 \\ -a\sin\omega t & -\mu - \lambda \end{vmatrix} = \lambda^2 + \mu\lambda + a\sin\omega t = 0$$

Therefore the eigenvalues are

$$\lambda_{\pm} = -\frac{\mu}{2} \pm \frac{\mu}{2}\sqrt{1 - \frac{4a}{\mu^2}\sin\omega t}$$

The real part of the eigenvalues is negative for $\sin\omega t > 0$ and the fixed point is stable (while it is unstable for $\sin\omega t < 0$). Let's study the behaviour of the solution in his vicinity (when it is stable). The eigenvetors corresponding to λ_+ and λ_- are $z_+ = (1, \lambda_+)$ and $z_- = (1, \lambda_-)$, respectively. Let's notice that they are function of time.

Any vector $z(t = t_0) = (x(t_0), y(t_0))$ can be written as a linear combination of the two eigenvectors calculated at the same time t_0

$$z(t = t_0) = c_+(1, \lambda_+) + c_-(1, \lambda_-)$$

and the constants c_+, c_- can be easily determined:

$$\begin{cases} c_+ + c_- = x(t_0) \\ \lambda_+ c_+ + \lambda_- c_- = y(t_0) \end{cases} \qquad \begin{cases} c_+ = \frac{y(t_0) - \lambda_- x(t_0)}{\lambda_+ - \lambda_-} \\ c_- = \frac{-y(t_0) + \lambda_+ x(t_0)}{\lambda_+ - \lambda_-} \end{cases}$$

Assuming that the dissipation μ is small ($\mu^2 \ll a$) we can consider the eigenvalues as $\lambda_\pm = -\frac{\mu}{2} \pm i\nu(t)$, where $\nu(t) = \frac{\mu}{2}\sqrt{\frac{4a}{\mu^2}\sin \omega t - 1}$, therefore the coefficients c_+ and c_- are conjugates and they can be written as

$$c_+ = c = \frac{x(t_0)}{2} + i\frac{-y(t_0) - x(t_0)\mu/2}{2\nu}.$$

and $c_- = \bar{c}$.

Since $\frac{dz_\pm}{dt} = \lambda_\pm z_\pm$, the general solution is

$$z(t) - z_0 = (x(t) - x_0, y(t) - y_0) = cz_+ e^{\lambda_+} + \bar{c}z_- e^{\lambda_-}$$

and it can be seen that the imaginary parts vanish while the real parts of the equation gives:

$$\begin{aligned}
\begin{pmatrix} x \\ y \end{pmatrix} = & \ e^{-\mu t/2}\left\{ \left[x(t_0)\begin{pmatrix} 1 \\ -\mu/2 \end{pmatrix} + \frac{y(t_0) + x(t_0)\mu/2}{\nu}\begin{pmatrix} 0 \\ \nu \end{pmatrix} \right] \cos \int_{t_0}^{t} \nu(\tau)d\tau \right. \\
& \left. - \left[-\frac{y(t_0) + x(t_0)\mu/2}{\nu}\begin{pmatrix} 1 \\ -\mu/2 \end{pmatrix} + x(t_0)\begin{pmatrix} 0 \\ \nu \end{pmatrix} \right] \sin \int_{t_0}^{t} \nu(\tau)d\tau \right\}
\end{aligned} \qquad (6)$$

As a first approximation, instead of $\int_{t_0}^{t} \nu(\tau)d\tau$ we can use a mean frequency, easily obtained from the shape of the potential: since $\sin(\omega t)$ is varying from zero to 1 and back to zero when z_0 is stable, let's use its mean value 1 in the linearized equation and remove the dissipation term: we obtain

$$\ddot{x} = -ax$$

that is the equation for a linear oscillator whose frequency is $\sqrt{a}$.

With this approximation system (6) becomes

$$\begin{cases} x(t) = e^{-\mu t/2}\left[x(t_0)\cos\sqrt{a}(t - t_0) + \frac{y(t_0) + x(t_0)\mu/2}{\sqrt{a}}\sin\sqrt{a}(t - t_0) \right] \\ y(t) = e^{-\mu t/2}\left[y(t_0)\cos\sqrt{a}(t - t_0) - \left(\frac{y(t_0) + x(t_0)\mu/2}{2\sqrt{a}}\mu + x(t_0) \right)\sqrt{a}\sin\sqrt{a}(t - t_0) \right] \end{cases}$$

And finally, since $\mu \ll a$,

$$\begin{cases} x(t) = e^{-\mu t/2} \left[x(t_0) \cos \sqrt{a}(t - t_0) + \frac{y(t_0)}{\sqrt{a}} \sin \sqrt{a}(t - t_0) \right] \\[2mm] y(t) = e^{-\mu t/2} [y(t_0) \cos \sqrt{a}(t - t_0) - x(t_0)\sqrt{a} \sin \sqrt{a}(t - t_0)] \end{cases} \tag{7}$$

The same procedure can be applied to $z_{1,2}$: the linearization around these two fixed points leads to:

$$\begin{cases} \dot{x} = y \\[2mm] \dot{y} = -\mu y + 2a \sin \omega t \, x \end{cases} \tag{8}$$

The linear stability analysis of these fixed points gives:

$$\begin{vmatrix} -\lambda & 1 \\[3mm] 2a \sin \omega t & -\mu - \lambda \end{vmatrix} = \lambda^2 + \mu \lambda - 2a \sin \omega t = 0$$

Therefore the eigenvalues are

$$\lambda_\pm = -\frac{\mu}{2} \pm \frac{\mu}{2}\sqrt{1 + \frac{8a}{\mu^2} \sin \omega t}$$

As expected, since $\sin \omega t < 0$, the points are stable (when they exist!).

We can derive the solutions around these points following exactly the same procedure as before, the only difference being that we need to replace ν with $\nu' = \frac{\mu}{2}\sqrt{-1 - \frac{8a}{\mu^2} \sin \omega t}$.

To obtain the approximated frequency of the oscillations around these fixed points we write the non dissipative linearized equation when $\sin \omega t = -1$:

$$\ddot{x} = -2ax$$

that is a linear oscillator with frequency $\sqrt{2a}$.

The system that describes the approximated solutions around $z_{1,2}$ is:

$$\begin{cases} x(t) = x_{1,2} + e^{-\mu t/2} \left[x(t_0) \cos \sqrt{2a}(t - t_0) + \frac{y(t_0)}{\sqrt{2a}} \sin \sqrt{2a}(t - t_0) \right] \\[2mm] y(t) = e^{-\mu t/2} [y(t_0) \cos \sqrt{2a}(t - t_0) - x(t_0)\sqrt{2a} \sin \sqrt{2a}(t - t_0)] \end{cases} \tag{9}$$

212
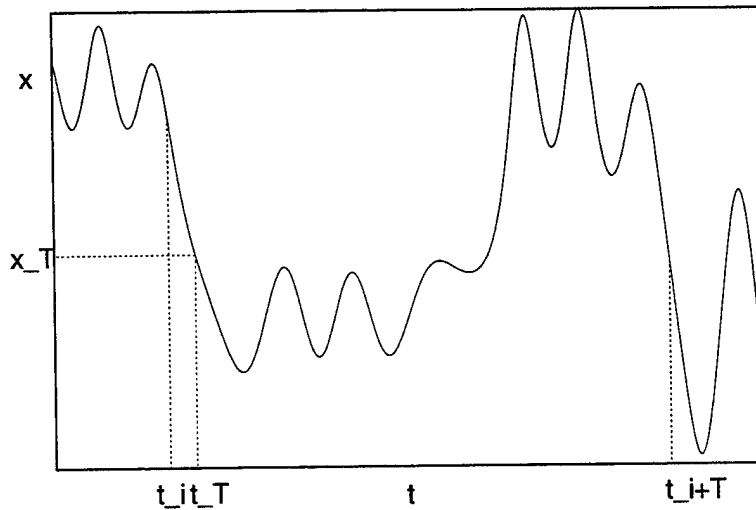
Figure 7: Sketch of a time series: in the time interval between t_i and t_T the linear approximation around the fixed point ($x_0 = 0$) is not valid

6 Construction of a two dimensional map

To connect the two systems (7 and 9) we need to integrate each of them for the period in which the solution is close to them, that, in first approximation (supposing that the solution quick passes from one to the other) can be considered half of the period of the variation of the potential: π/ω. But the relative motion is simply a rigid rotation plus an exponential contraction determined by the dissipative term. Clearly it does not represent the complicated behaviour that we saw in the numerical results. The missing key is due to the fact that we cannot consider the jump between one state to the other to be instantaneous: according to the initial state at the time in which the stability properties vary (any time that $\sin \omega t$ is equal to zero), the linear approximation is valid for a different time interval. In fig. 6 a time series has been sketched: at the time t_i, $\sin \omega t$ becomes negative and the position of our idealized particle in the potential is pretty far from the origin, therefore, before its behavior being well represented by the linear approximation around z_0, it has to go closer to the origin. At the time t_{i+1} the phase is such that the value of x is quite small, and it is in a range where the linear approximation is already valid. In order to keep this crucial difference, we define a threshold x_T (here it is the middle point between x_0 and x_1) in the position of the particle, and we apply the linearized version of our system in the time interval $\Delta t = \pi/\omega - t_T$ in which $|x| < x_T$. In a rude approximation, we calculate t_T by considering an exponential decay towards the stable fixed point:

$$x(t_T) = x_T = x(t_i)e^{-\mu(t_T - t_i)/2}.$$

The corresponding velocity will be

$$y(t_T) = y(t_i)e^{-\mu(t_T - t_i)/2}.$$

213

The same procedure is applied in the neighborhoods of $z_{1,2}$: when, at the time $t_i + \pi/\omega$, the middle state becomes unstable, the "delay" time is given by

$$t_T = \frac{2}{\mu} \ln \frac{|x_{i+1} - x_{1,2}|}{x_T}$$

and the corresponding velocity is

$$y(t_T) = y(t_i)e^{-\mu(t_T - t_i)/2}$$

where x_{i+1} and y_{i+1} are position and velocity at time t_{i+1}.

The full two dimensional map is therefore:

$$t_T = max(0, \frac{2}{\mu} ln \frac{|x_n|}{x_T}) \qquad \Delta t = \frac{\pi}{\omega} - t_T$$
$$x_{n,eff} = x_n e^{-\mu t_T/2} \qquad y_{n,eff} = y_n e^{-\mu t_T/2}$$

$$\begin{cases} x_{n+1} = e^{-\mu\Delta t/2} \left[x_{n,eff} \cos \frac{\sqrt{a}\Delta t}{2} + \frac{y_{n,eff}}{\sqrt{a}} \sin \frac{\sqrt{a}\Delta t}{2} \right] \\ y_{n+1} = e^{-\mu\Delta t/2} \left[y_{n,eff} \cos \frac{\sqrt{a}\Delta t}{2} - x_{n,eff}\sqrt{a} \sin \frac{\sqrt{a}\Delta t}{2} \right] \end{cases} \qquad (10)$$

$$t_T = max(0, \frac{2}{\mu} ln \frac{|x_{n+1} - x_{1,2}|}{x_T}) \qquad \Delta t = \frac{\pi}{\omega} - t_T$$
$$x_{n+1,eff} = (x_{1,2} + x_{n+1})e^{-\mu t_T/2} \qquad y_{n+1,eff} = y_{n+1} e^{-\mu t_T/2}$$

$$\begin{cases} x_{n+2} = x_{1,2} + e^{-\mu\Delta t/2} \left[(x_{n+1,eff} - x_{1,2}) \cos \frac{\sqrt{2a}\Delta t}{2} + \frac{y_{n+1,eff}}{\sqrt{2a}} \sin \frac{\sqrt{2a}\Delta t}{2} \right] \\ y_{n+2} = e^{-\mu\Delta t/2} \left[y_{n+1,eff} \cos \frac{\sqrt{2a}\Delta t}{2} - (x_{n+1,eff} - x_{1,2})\sqrt{2a} \sin \frac{\sqrt{2a}\Delta t}{2} \right] \end{cases} \qquad (11)$$

In this map, we will decide whether use x_1 or x_2 at any iteration according to the sign of the outgoing value x_{i+1} from the map that decsribes the behavior close to z_0.

In fig. 8a. the spiral has been obtained by putting a straight line in the map (10), while fig. 8b. represents a successive iteration trough the map (11).

If we pick an initial condition and we let the system evolve according to the described equations, we will obtain a time series that represents the variation of the position x every half a period π/ω. It can be seen (fig. 9) that, with different parameters values, we can obtain solutions corresponding to steady solutions, limit cycles or chaotic motion exactly as in the full system. The general behavior of the solutions of the full system is therefore well detected by this approximation. In fig. $10a, b$ the stroboscopic map for a particular choice of the parameters corresponding to chaotic motion is shown: the position in the phase space (x, y) is

214
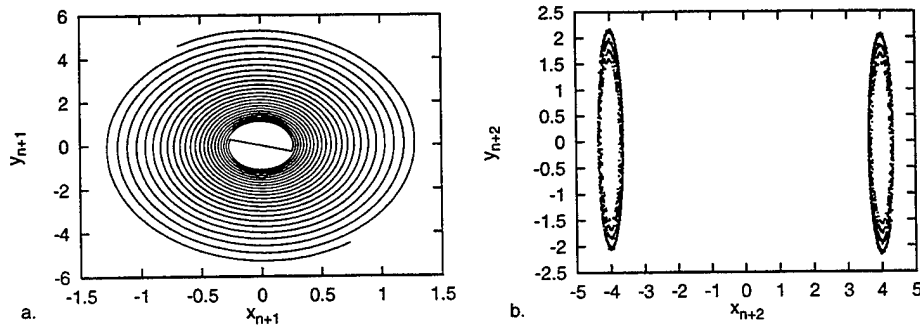
Figure 8: Effect of **a.** map (10) on a straight line $y = 4x$ and **b.** map (11) on the spiral shown in panel **a.**

taken every period $2\pi/\omega$, when $\sin \omega t$ becomes negative and positive respectively.

If we consider the two spirals in fig. 10b as a one dimensional line, we can label each point on them with a different value of a parameter α that describes the curve: in fig. 6 the return map of the interval of the α−axis into itself is shown: the line $\alpha_{n+1} = \alpha_n$ cuts the graph of the map many times with a slope greater than one; hence these intersections correspond to unstable periodic orbits. With other parameters the number of intersections can increase, and our impression is that, if we are able to demonstrate that it becomes infinit, the birth of chaos can be anticipated.

7 Acknowledgments

I would like to thank Ed Spiegel, whom I did this work with, who gave me advises and ideas day by day, and from whom I learned how to approach research work. It has been very pleseant to work with you, Ed. I say thanks to the GFD organization for giving me the possibility to came here this summer and all the staff that I always found available for any kind of questions and supports that I needed. And thank you, all fellows and people that helped me.

References

[A. Arneodo and Tresser, 1985] A. Arneodo, P.H. Coullet, E. S. and Tresser, C. (1985). Asymptotic chaos. *Physica D*, 14:327–347.

[A. Arneodo and Tresser, 1981] A. Arneodo, P. C. and Tresser, C. (1981). Possible new strange attarctors with spiral structure. *Commun. Math. Phys.*, 79:573–579.

[Fauve, 1991] Fauve, S. (1991). In *Summer Study Program in geophysical Fluid Dynamics: Patterns in Fluid Flow*, Woods Hole. Woods Hole Oceanographic Institute.
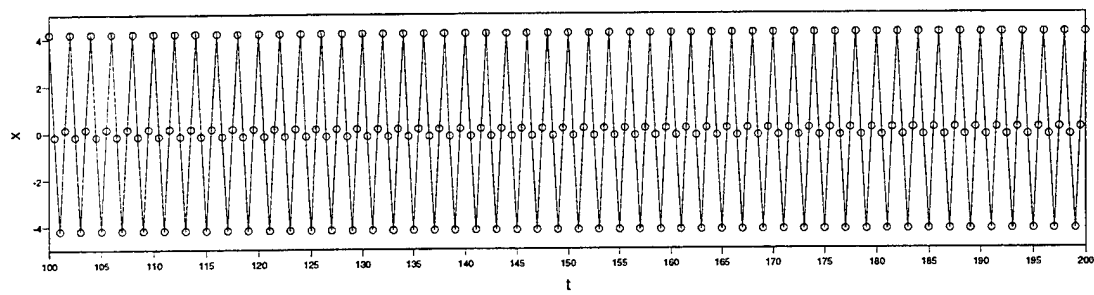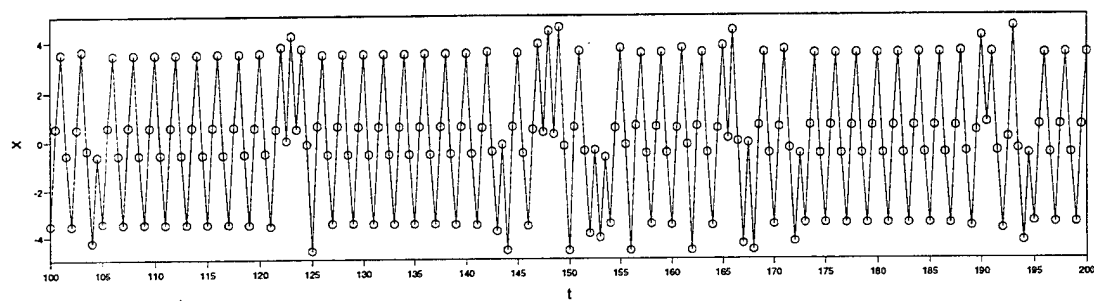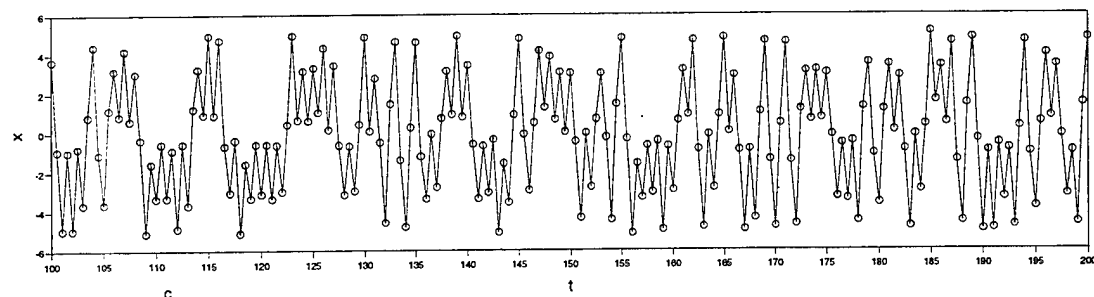
Figure 9: Time series of the variable x from the map $(10 + 11)$ with $a = 16.$, $\omega = 0.2$ and **a.** $\mu = 0.35$; **b.** $\mu = 0.2255$; **c.** $\mu = 0.15$.

216
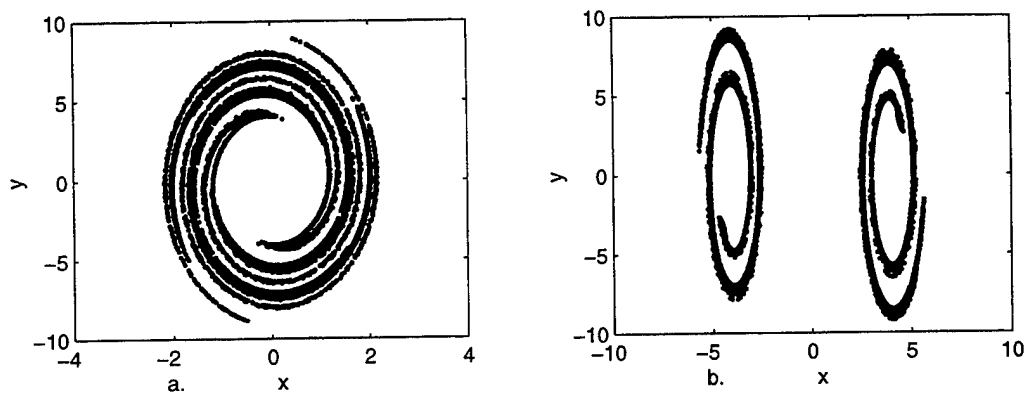
Figure 10: Stroboscopic map (from 10+11) when $\sin \omega t = 0$ while it is **a.** decreasing and **b.** increasing.
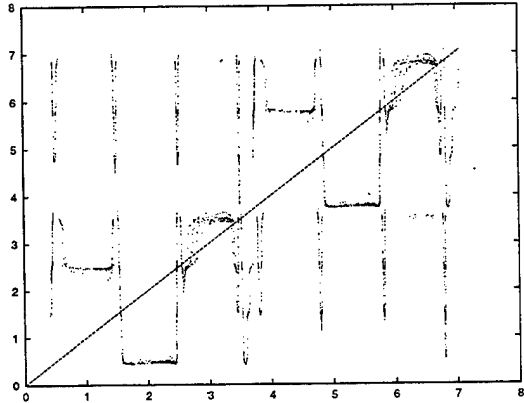
Figure 11: Return map of the interval in α into itself

217

[Hsu, 1977] Hsu, C. S. (1977). On nonlinear parametric exitation problems. *Adv. in Applied Mechanics*, 17:245–303.

[Lorenz, 1963] Lorenz, E. (1963). Deterministic nonperiodic flow. *J. Atmos. Sci.*, 20:134–141.

[Marzec and Spiegel, 1978] Marzec, C. J. and Spiegel, E. A. (1978). *J. of Applied Math.*

[Poyet, 1980] Poyet, J.-P. (1980). *Time-dependent convection*. PhD thesis, Columbia Univeristy.

[Shil'nikov, 1965] Shil'nikov, L. P. (1965). A case of the existence of a countable number of periodic motions. *Sov. Math. Dokl.*, 6:163–166.

[Stommel, 1961] Stommel, H. (1961). Thermohaline convection with two stable regimes of flow. *Tellus*, 13(2):224–230.

[Thual and McWilliams, 1992] Thual, O. and McWilliams, J. (1992). The catastrophe structure of thermohaline convection in a two-dimensioal fluid model and a comparison with low-order box models. *Geophys. Astrophys. Fluid Dynamics*, 64:67–95.

Forecasting improvement via optimal choice of sites for observations: a toy model

Sarah Dance

1 Introduction

Oceanic and atmospheric processes can be described as nonlinear dynamical systems. These systems often display a chaotic sensitivity to initial conditions, i.e. trajectories which have close initial conditions in phase space may diverge rapidly in forward time. Since no observable can be measured exactly, it is not possible to know the true state of the system at any given time. Hence, even using a perfect model, it would seem that trying to predict future states accurately is futile. However, it is certainly not true that all directions in phase space are unstable to perturbations. By identifying the most unstable directions and improving the accuracy of measurements at the corresponding locations in physical space, a strategy for forecast improvement can be developed.

Storm tracks are an example of a nonlinear system displaying regions of perturbation growth and damping. In the winter, for example off the East coast of the USA, there are large air temperature gradients between the land and the sea. These give rise to large density gradients and the area becomes unstable to baroclinic instabilities. Further downstream, density gradients are much smaller so perturbations are dissipated. Intuitively, at least some unstable directions in phase space may be expected to correspond to unstable regions in physical space.

Another example of a natural nonlinear system displaying chaotic dynamics is the ocean circulation. The western boundary current and its offshore extension are unstable to small perturbations which grow and form eddies. These eddies affect the flow downstream. Away from the boundaries and strong interior fronts the system is often stable and the eddies dissipate.

In the ocean, observations are very scarce due to the difficulty in making them. Predictability techniques, such as those described later, could be of particular use here in choosing the optimal sites for these measurements. There is also a choice of the kind of measurements to be made. For example, is it better to use lagrangian floats or make a series of observations at a fixed location? Perhaps more sophisticated predictability techniques could be used to answer this question.

The aim of this project was to identify an optimal measurement strategy in a toy model with some qualitatively similar features to a natural system. Unstable directions in phase space were found using different techniques. Simulated forecasts were then carried out based on an approximate system and additional observations of the true system taken at locations determined using information about the most unstable directions. These forecasts were compared

with each other, with the evolution of the true system, and with the evolution of the approximate system unconstrained by additional observations. This work examines a system described by a nonlinear one-dimensional PDE; Lorenz and Emmanuel [Lorenz and Emmanuel, 1998] carried out a similar analysis using coupled ODEs.

2 The Model PDE

The model PDE is given by

$$u_t + \beta u u_x + \lambda u + \alpha u_x + \nu(x) u_{xx} + \mu u_{xxx} + \gamma u_{xxxx} = 0 \tag{1}$$

for $0 \leq x < 2\pi$ with periodic boundary conditions and

$$\nu(x) = \nu_0 H(x) \text{ where } H(x) = \begin{cases} 1 & \text{if } 0 \leq x < \frac{2\pi}{5} \\ 0 & \text{if } \frac{2\pi}{5} \leq x < 2\pi \end{cases}$$

This is a modified version of Benney's equation. Here there are two extra terms: a linear advection term and a damping term. A spatial dependence in the coefficient of u_{xx} has been introduced so that there is an area in the domain which is unstable to perturbations and damping elsewhere. Benney's equation can be used to describe motion of thin liquid films and has also arisen in plasma instabilities. It has been shown to admit pulse-like solutions [Balmforth et al., 1997].

Fig. 1 shows a sample trajectory of the system (1) obtained by numerical integration. There are two regimes evident: a vigorous regime (e.g. from $t = 0$ to $t = 15$ or $t = 25$ to $t = 35$) where there are large disturbances in the unstable region, and a quiet regime (e.g. near $t = 20$ or $t = 40$) where the disturbances are much smaller. Nonlinear effects cause some disturbances to move to the left.

An energy equation for (1) is given by

$$\frac{1}{2} \frac{\partial}{\partial t} \int_0^{2\pi} u^2 dx = \nu_0 \int_0^{2\pi/5} (u_x)^2 dx - \gamma \int_0^{2\pi} (u_{xx})^2 dx$$

Note that the only positive contributions to the right-hand-side come from the interval $[0, 2\pi/5]$ where $\nu = \nu_0$.

The parameter values used throughout the rest of this discussion are: $\lambda = 6.4 \times 10^{-2}$, $\beta = 2.0$, $\nu_0 = 1.7 \times 10^{-2}$, $\alpha = 5.0 \times 10^{-2}$, $\mu = 1.0 \times 10^{-5}$, $\gamma = 8.3 \times 10^{-5}$

These parameters were chosen so that growth was significant in the unstable region of the domain and was damped as the disturbances moved into the stable region. The damping was sufficiently small to allow perturbations to grow again on re-entering the unstable region.

Simple estimates of the intrinsic time-scales of the system may be obtained by considering a linearisation about the zero state. Assuming $\nu = \nu_0$ over the whole domain, trying a solution of the form $u \propto e^{ikx + (\sigma - i\omega)t}$ and neglecting nonlinear terms gives:

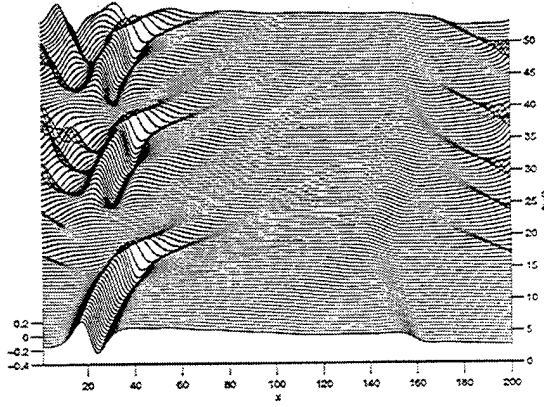$$\sigma = -\lambda + \nu k^2 - \gamma k^4, \quad \omega = \alpha k - \mu k^3$$

220

Figure 1: A segment of a trajectory of equation (1) The equation was solved numerically using a 200 point grid. Here the x-axis is labelled by grid point. Each curve represents the state of the system at a particular instant in time. Time progresses into the paper, with each curve separated by 0.5 time units. The $u(x)$ scale is on the left.

For the chosen parameters $\sigma(k)$ has a maximum at $k = \sqrt{102} \simeq 10$. So in the growing region of the domain, for a wavenumber $k = 10$, estimates of the growth rate and phase speed are $\sigma = 0.8$ and $c = 0.05$ respectively.

3   Predictability Techniques

In this section the techniques used to find the unstable directions are described. These methods include an empirical approach (Ensemble vector analysis) and more quantitative techniques based on a linearised system (Singular vector and Lyapunov vector analysis). The discussion takes place in a general setting with the system described by

$$\dot{X} = f(X)$$

with $X \in U^{\text{open}} \subseteq \mathbb{R}^n, f : U \to \mathbb{R}^n$

3.1   Ensemble Vectors

Ensemble vectors (EV) provide one way of estimating the most unstable directions along a given trajectory as given by an empirical approach. Note that this name is not in common use in the predictability literature. Fig. 2 shows a chosen fiducial (reference) trajectory in phase space. Let this trajectory be given by $X_{ref}(t)$. To find an ensemble vector take a ball of initial conditions of a given (small) radius δ around the reference initial condition, $X_{ref}(0)$. Pick an ensemble of points randomly distributed on this ball and flow them forward under the full nonlinear PDE (1) for time t_{opt}, the optimisation time. (t_{opt} is generally taken to be the same as the forecast period.) The hope is that the trajectory the furthest away from

221
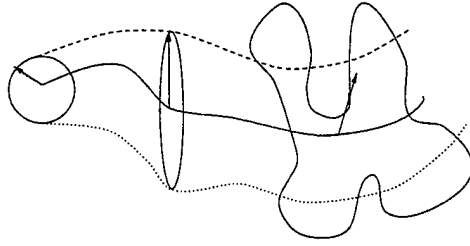
Figure 2: A fiducial trajectory is shown as a solid line. The evolution of a ball of initial conditions about the reference initial condition is depicted, with the arrows representing the instantaneous maximum growth directions. Two other trajectories with initial conditions a distance δ from the fiducial initial condition are shown as dotted and dashed lines.

the reference trajectory at optimisation time has experienced growth aligned with the most unstable direction. Let this trajectory be given by $\tilde{X}(t)$. The ensemble vector is defined by

$$EV = \kappa \left(\tilde{X}\left(t_{opt} \right) - X_{ref}\left(t_{opt} \right) \right)$$

where κ is a normalising factor, chosen so that $\|EV\| = 1$.

Note that for the purposes of this project the Euclidean norm was used to measure distances in phase space. Any other norm could have been used. It is clear that the unstable directions calculated are norm dependent. There is some debate over which norm is the best measure of trajectory divergence, see [Smith, 1995].

3.2 Singular Vectors and Lyapunov Vectors

These techniques are based on linearising the system about a reference trajectory.

Recall

$$\dot{X} = f(X)$$

with $X \in U^{\text{open}} \subseteq \mathbb{R}^n, f : U \to \mathbb{R}^n$.

Consider a small perturbation x of the state X. For sufficiently small times t the evolution of the perturbation can be described by the linear approximation

$$\dot{x} = Df(X(t))x \tag{2}$$

This equation can be written in integral form

$$x(t) = L(t, t_0)x(t_0).$$

Given an inner product $< \cdot, \cdot >$, define the perturbation norm at time t by

$$\|x(t)\|^2 = \langle x(t), x(t) \rangle = \langle x(t_0), L^*Lx(t_0) \rangle$$

where L^* is the adjoint of L. In the case that L is a real matrix, $L^* = L^T$, the transpose of L.

L^*L is often referred to as the Oseledec operator. It is clearly a symmetric operator. It follows that all its eigenvalues σ_i^2 are real and there exists an orthonormal basis of eigenfunctions v_i which satisfy

$$L^*L v_i(t_0) = \sigma_i^2 v_i(t_0)$$

Note that the eigenvalues may be repeated and the basis of eigenfunctions may not be unique.

At a future time t, these eigenfunctions evolve to $v_i(t) = L v_i(t_0)$ and

$$LL^* v_i(t) = \sigma_i^2 v_i(t)$$

Assuming that the basis of eigenfunctions is complete (in the tangent space of perturbations), any perturbation can be written as a linear combination of eigenvectors.

$$x(t) = \sum_i c_i v_i(t)$$

It follows that

$$\max_{x(t_0) \neq 0} \left(\frac{\|x(t)\|^2}{\|x(t_0)\|^2} \right) = \sigma_1^2$$

where σ_1^2 is the largest eigenvalue of L^*L. (For simplicity, we have assumed that the eigenspace corresponding to σ_1 is one dimensional.)

Maximum energy growth over the interval (t_0, t) is associated with the largest eigenvalue and the corresponding eigenvectors of L^*L and LL^*: $v_1(t_0)$ at initial time and $v_1(t)$ at optimisation time.

It is useful to have a name for these eigenvectors. In the predictability literature there are many conflicting definitions in use. In order to avoid any confusion here, define

Singular vectors (SV) as the eigenvectors of L^*L e.g. $v_1(t_0)$ is the initial perturbation which will have grown the most at optimisation time.

Lyapunov vectors (LV) as the eigenvectors of LL^* e.g. $v_1(t) = L v_1(t_0)$ represents the orientation at time t, of the vector which experiences maximum growth over the chosen optimisation time t.

3.2.1 Relationship to 'Normal' Mode Analysis

Normalised eigenmodes ξ_i of $Df(X(t))$ with eigenvalues λ_i give rise to solutions $\xi_i e^{\lambda_i(t-t_0)}$ of the linear perturbation equation (2). Operator L is not usually *normal* so that in general $\langle \xi_i, \xi_j \rangle \neq \delta_{ij}$ If the initial disturbance is a linear combination of the eigenmodes then the fastest growing eigenmode will eventually dominate the solution, so for sufficiently large t

$$LV = eigenmode \times phase\ factor.$$

It is possible to have decaying eigenmodes, but transient growth in the Lyapunov vectors. This is due to the lack of orthogonality in the eigenmodes. An example of this phenomenon is given in [Smith et al., 1997].
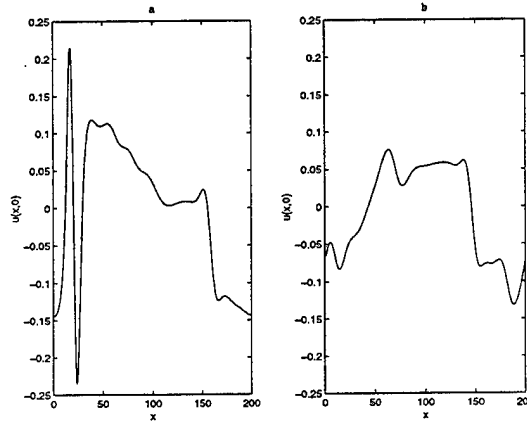
Figure 3: Panel (a) shows the initial condition (I) from the vigorous regime. Panel (b) shows the initial condition (II) from the quiet regime.

4 Results – unstable directions

Equation (1) was solved numerically using fourth-order Runge-Kutta time-stepping and centered differences in space on a 200 point grid. The linear forward tangent propagator L was calculated by linearising the numerical scheme about a fiducial trajectory and computing its effect on basis vectors. The SV and LV were calculated using matlab.

An alternative calculation for systems with a large number of variables is to code the adjoint model (see [Talagrand and Courtier, 1987]) and then use a power method to calculate the eigenvectors and eigenvalues. This was attempted here, but the results were found to be very bad due to the slow convergence of the power method.

Two sets of initial conditions were used to generate the fiducial trajectories (see Fig. 3): I) a representative from the vigorous regime of the equation and II) a representative from the quiet regime.

A plot of first singular exponents i.e. $\log(\sigma_1/t)$, is given in Fig. 4. Panel (a) (initial condition I) appears to indicate that the rescaled first singular value is asymptoting to some constant, although this is not so clear from Panel (b) (initial condition II). This constant is less than the simple scale estimate in Section 2, mainly because here the unstable region occupies only part of the domain. The differences between Panel (a) and Panel (b) indicate that the transient growth rate is highly dependent on the region of phase space from which the initial condition is taken. The following theoretical asymptotic relation links the first singular value, σ_1 to the first Lyapunov exponent, l_1 (see [Palmer, 1996] for further details).

$$l_1 = \lim_{t_{opt} \to \infty} \left[\frac{1}{t_{opt}} \log \sigma_1 \right]$$

The SV and LV are given in Figs. 5, 6, 7 and 8. Note that the unstable directions are localised to the unstable region of the domain. For the initial condition coming from the more

224
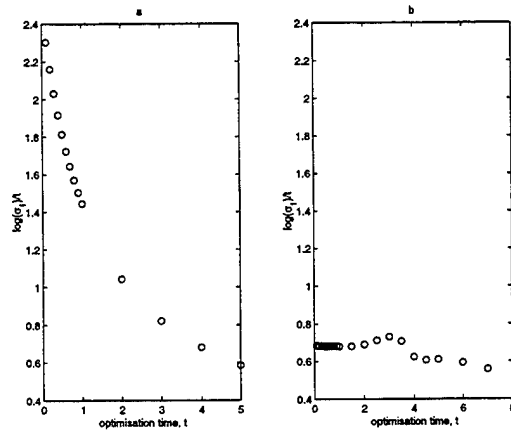
Figure 4: Rescaled singular values for (a) initial condition I, (b) initial condition II. These values provide an estimate of the fastest growth rates.

vigorous regime (I) the basic forms of the SV and LV do not change over time. The peaks broaden, but remain in the same location in physical space. For the initial condition coming from the quiet regime (II) the SV and LV show more variation with time. This may be due to faster movement of smaller disturbances through the unstable region, or to differences in evolution of the distinct steep gradients initially present in and near the unstable region.

Fig. 9 shows EV for both initial conditions, chosen from ensembles of six randomly distributed initial conditions a distance δ from the fiducial trajectory. Unlike the SV and LV the EV are not localised. Since the ensembles contained only six members there is no guarantee that the EV are in fact aligned with the most unstable directions. A larger sample and hence more computational work would be needed in order to find the EV with a greater probability of alignment with the true maximal growth direction.

5 Forecasting

Starting from an exact initial condition for a fiducial trajectory, an initial condition for a forecast trajectory is obtained by perturbing the value at each grid point with white noise of a specified maximum amplitude. Grid points are chosen at which to make 'additional measurements' using information obtained via the predictability techniques described earlier. The exact details of this choice are explained in Fig. 10. At the chosen grid points the perturbed initial condition is reset to the exact values of the fiducial initial condition. The system is then integrated forward to obtain a forecast trajectory. A forecast time of 5.0 time units was chosen since this is approximately the time taken for a large peak to grow to maximum amplitude in the growing region of the domain.

As a comparison, another strategy was also used to reset points. This was done by picking points randomly from the unstable region of the domain.
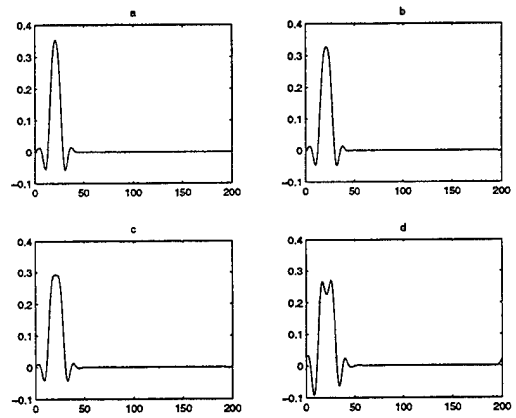
Figure 5: Singular vectors for initial condition I a) optimisation time 0.3, b) optimisation time 0.5, c) optimisation time 1.0, d) optimisation time 5.0
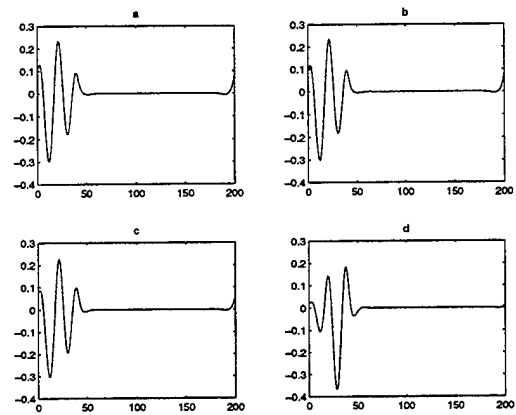

Figure 6: Singular vectors for initial condition II a) optimisation time 0.3, b) optimisation time 0.5, c) optimisation time 1.0, d) optimisation time 5.0
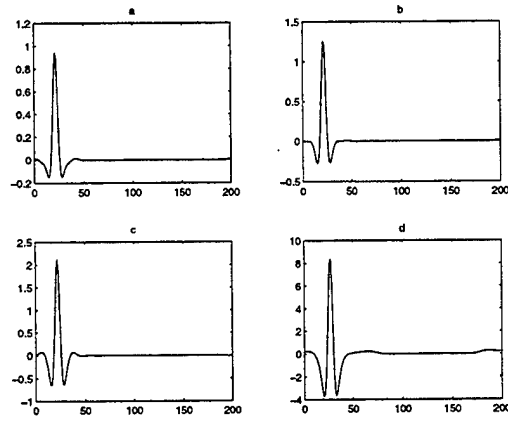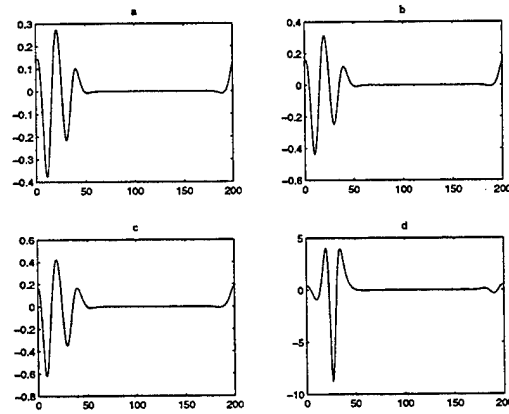
Figure 7: Lyapunov vectors for initial condition I a) optimisation time 0.3, b) optimisation time 0.5, c) optimisation time 1.0, d) optimisation time 5.0
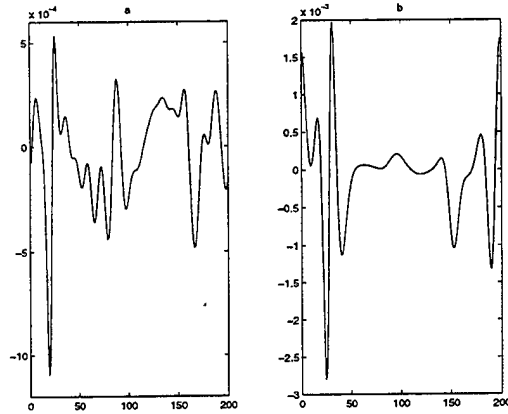

Figure 8: Lyapunov vectors for initial condition II a) optimisation time 0.3, b) optimisation time 0.5, c) optimisation time 1.0, d) optimisation time 5.0

227

Figure 9: Ensemble vectors with optimisation time 0.3 a) initial condition I, b) initial condition II
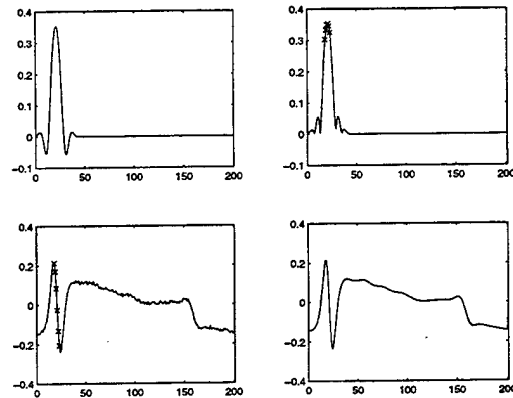
Figure 10: The plot on the top left shows an example singular vector. The absolute values of the components of this vector were taken (top right) and sorted by size. The grid points corresponding to the largest were selected (the first six are marked as x). At these grid points the values of the perturbed initial condition were reset to the exact values (bottom left) as given by the true initial condition (bottom right).
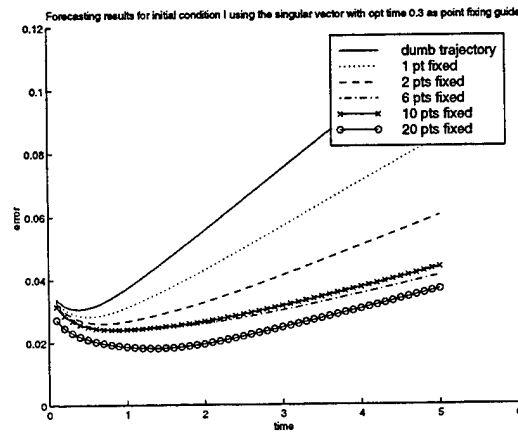
Figure 11: Variation of error with number of points reset. Note that the error is measured in Euclidean norm so that the true trajectory would be represented by the zero line on this plot. The 'dumb' trajectory corresponds to the perturbed initial condition with no points reset. Maximum initial pointwise perturbation size $= 1.0 \times 10^{-2}$

A brief experiment was carried out to determine the number of points to fix in order to achieve a reasonable improvement over the forecast from the 'dumb' trajectory (the perturbed trajectory with no points reset to their exact values). The results for initial condition I with maximum initial pointwise perturbation 1.0×10^{-2} using the singular vector with optimisation time 0.3 as point resetting guide are given in Fig. 11.

For the initial condition from the vigorous regime it was found that six points were necessary to give a good result (Fig. 12). Note that since the SV did not change much with optimisation time, the first six points selected for resetting were identical for experiments using the SV associated with different optimisation times. The same is true for the LV. All the strategies employed offered an improvement over the dumb trajectory. The strategy employing the SV gave the best results.

With a larger noise amplitude of 1.0×10^{-1} the results from resetting points using SV were still good initially. However, Fig. 13 shows that eventually the errors become comparable with those for the dumb trajectory. This is after 5 or 6 e-folding times (approximated using the growth rates given in Fig. 4 so the perturbed trajectory will be so far away from the fiducial trajectory in phase space that the linear approximation is no longer relevant. Here SV are no longer valid tools.

For the initial condition from the quiet regime (II) it was more difficult to get good results. Fig. 14 shows results from resetting twelve points at initial time. One explanation for this disparity of results between the two initial conditions is that it is easier to follow the movement of a peak along a trajectory than it is to predict which small perturbation will grow in a transition between the quiet and the vigorous regimes of the equation.
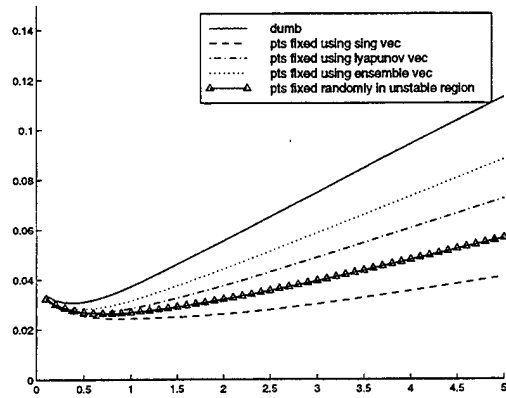
Figure 12: Forecasting results with initial condition I, time against error measured in Euclidean norm. Maximum pointwise initial perturbation size $= 1.0 \times 10^{-2}$
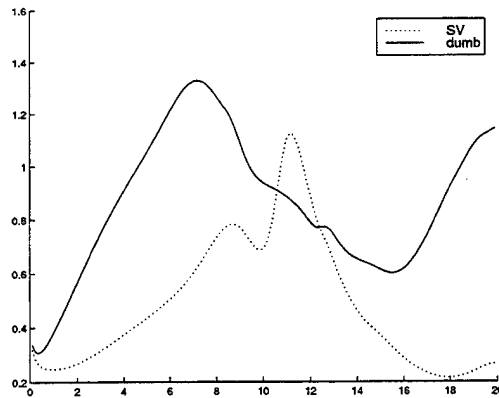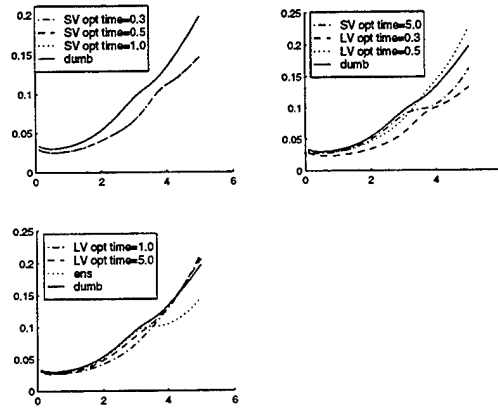

Figure 13: Forecasting results with initial condition I, time against error measured in Euclidean norm. Maximum pointwise initial perturbation size $= 1.0 \times 10^{-1}$

Figure 14: Forecasting results with initial condition II, time against error measured in Euclidean norm. Maximum pointwise initial perturbation size $= 1.0 \times 10^{-2}$

5.1 Climatology

Suppose there is no data from the present time. A climatology can be constructed by averaging all past data. The climatology and results obtained using the climatology as the initial trajectory are given in Fig. 15. The results are fairly poor. One contributing factor is that the climatology initial condition lies in a different region of phase space to the other initial conditions studied here.

6 Conclusions

The form of the SV and LV depends on

1. the initial conditions

2. the optimisation time

Further study needs to be done in order to make this dependence more precise. For example, it has been suggested that the peak of the singular vector might correspond to the largest gradient in the initial condition. This hypothesis has not yet been tested.

In a more realistic scenario it would be necessary to calculate the most unstable directions from a noisy set of data rather than from the true initial conditions. The noisy data is likely to be less smooth than the true initial condition. If the unstable directions do have a strong dependence on the gradients in the initial condition then smoothing algorithms will have to be employed.

In general, singular vectors produced the best forecasting results. The common sense approach of picking random points in the unstable region also seemed to work quite well. The quality of the forecasting results is dependent on the fiducial trajectory – whether the initial condition lay in the vigorous or the quiet regime. The results indicate that in the quiet regime
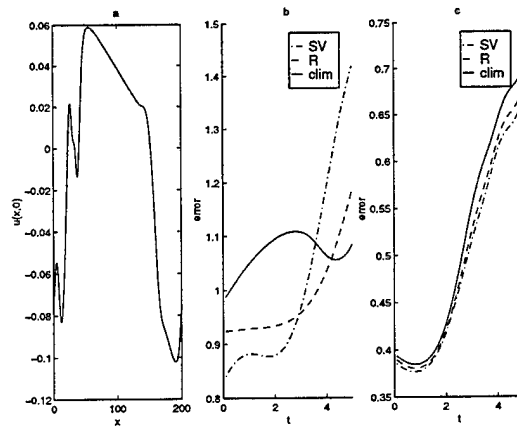
Figure 15: a) shows the initial condition for the climatology, b) and c) show forecasting results with six points reset using SV and random selection in the unstable region (R) as point picking guide. b) shows the results with initial condition I, c) shows the results with initial condition II

the most unstable direction changes rapidly along the fiducial trajectory, thus making it much harder to predict which perturbations will grow the most in the transition to the vigorous regime. This would suggest that having more accurate measurements for more than just the initial time would also be an interesting variant of the technique to study.

For practical applications it may be the case that a more accurate forecast is required only at certain locations in physical space (for example an oil rig in the middle of the ocean). For such instances forecast improvement may be offered by using a weighted norm to calculate the unstable directions (these will be different from those calculated using the Euclidean norm).

The SV and LV are only a valid tool for time-scales when the perturbed trajectories are still sufficiently close to the fiducial trajectory. The development of techniques which can follow the evolution of the most unstable directions over longer time-scales would be very valuable.

7   Acknowledgments

References

[Balmforth et al., 1997] Balmforth, N. J., Ierley, G., and Worthing, R. (1997). Pulse dynamics in an unstable medium. *SIAM J. Appl. Math.*, 57(1):205–251.

[Lorenz and Emmanuel, 1998] Lorenz, E. N. and Emmanuel, K. A. (1998). Optimal sites for supplementary weather observation: Simulation with a small model. *J. Atmos. Sci.*, 55:399–414.

[Palmer, 1996] Palmer, T. N. (1996). Predictability of the atmosphere and oceans: from days to decades. *NATO ASI Series*, 1(44).

[Smith, 1995] Smith, L. A. (1995). Accountability and error in ensemble forecasting. *ECMWF Proceedings of Seminar on Predictability*.

[Smith et al., 1997] Smith, L. A., Ziehmann, C., and Fraedrich, K. (1997). Uncertainty dynamics and predictability in chaotic systems. *Quart. J. Roy. Meteorol. Soc.*, 123:1–30.

[Talagrand and Courtier, 1987] Talagrand, O. and Courtier, P. (1987). Variational assimilation of meteorological observations with the adjoint vorticity equation. I: Theory. *Quart. J. Roy. Meteorol. Soc.*, 113:1311–1328.

Mathematical and Analog Modeling
of Lava Dome Growth

Amy Shen

1 Introduction

Lava domes are masses of solid rock that are formed when molten lava erupts slowly from a vent. The traveling distance and speed of a lava flow depends on the effusion rate, the fluidity of the lava, the volume erupted, the channel geometry, and the obstructions in the path of flow. Between 1980 and 1986, Mount St. Helens built a lava dome approximately 1,000 feet high and 3,500 feet in diameter. The burning, crushing, and other effects associated with lava flows can cause extensive damage. As lava domes spread slowly, they typically do not endanger human life, however, they can destroy permant structures.

Lava domes are the simplest type of lava flow. If the lava is sufficently viscous, it will pile up above the vent to form a dome. Usually such lava is composed of high-silica andesite and dacite. To minimize the damage of lava flows to human resources, numerous studies have been performed over the past 100 years. The central goal of these studies is to predict flow growth and the eruption state. Due to the difficulty of obtaining field measurements, labarotary simulation provides a good alternative approach to obtaining data. As lava often shows a non-Newtonian behavior with a finite yield stress, appropriate materials for these laboratory studies should posses such rheological characteristics. For isothermal studies, slurries, consisting, for example, of water and kaoline, have been used with some success. However, more realistically, the role of cooling at the lava surface exerts an important influence on flow structure and morphology. Griffiths, Fink and other resarchers[5−9] studied the morphology of the dome surface in recent years, and in so doing, took the surface cooling and the solidification of the lava into account. In particular, experiments and a scaling analysis that yielded approximate radius and height profiles evolving with time were performed.[2,7,8]

The work presented here is based on the hypothesis that the flowing lava can be modeled as a Bingham fluid. Following some theoretical preliminaries, an isothermal model is presented and a thin layer theory is applied. Analytical and experimental results are then compared. The results from the isothermal model proposed here fit quite well with our experimental data. Later, the surface cooling of the flow is taken into account through a depth averaged temperature field. Analytical and numerical results show some qualitatively different flow features compared to the isothermal case. Further, spreading of kaoline and PEG600 wax mixture, which is a slurry that has a highly temperature dependent viscosity and yield stress under cold water is studied in the laboratory.

2 Theoretical Preliminaries

We consider a lava flow that occupies a region $\mathcal{R}$ of three-dimensional Euclidiean space. The basic variables of the theory are

ϱ	mass density,
v	particle velocity,
T	Cauchy stress tensor,
g	gravitational acceleration,
ε	specific internal energy,
q	heat flux vector,
η	specific entropy,
θ	(absolute) temperature.

We assume that the medium is incompressible, so that

$$\operatorname{div} v = 0; \tag{1}$$

this being the case, it is useful to introduce the extra stress S and the pressure, defined so that

$$S = T + p\mathbf{1}, \qquad p = -\tfrac{1}{3}\operatorname{tr} T. \tag{2}$$

Clearly, S, so defined, is traceless.

The basic variables satisfy the field equations

$$\left.\begin{aligned} \varrho\dot{v} &= -\operatorname{grad} p + \operatorname{div} S + \varrho g, \\ S &= S^{\mathsf{T}}, \\ \varrho\dot{\varepsilon} = S\cdot D - \operatorname{div} q \quad &\left(D = \tfrac{1}{2}(\operatorname{grad} v + \operatorname{grad} v^{\mathsf{T}})\right), \end{aligned}\right\} \tag{3}$$

which express linear momentum balance, angular momentum balance, and energy balance, as well as the field inequality

$$\varrho\dot{\eta} \geq -\operatorname{div}\left(\frac{q}{\theta}\right), \tag{4}$$

which expresses entropy imbalance. Note that $\dot{f}$ denotes the material time-rate of a field f. If we introduce the specific free energy

$$\psi = \varepsilon - \theta\eta, \tag{5}$$

the entropy inequality (4) can be rewritten in the form

$$\varrho(\dot{\psi} + \eta\dot{\theta}) - S\cdot D + \frac{1}{\theta}q\cdot\operatorname{grad}\theta \leq 0. \tag{6}$$

We assume that ψ and η are determined constitutively via the relations

$$\psi = \hat{\psi}(\theta) = c\theta(1 - \log\frac{\theta}{\theta_0}) \qquad \text{and} \qquad \eta = \hat{\eta}(\theta) = c\log\frac{\theta}{\theta_0}, \tag{7}$$

where $c = \text{constant} > 0$ denotes the specific heat and $\theta_0 > 0$ is a given base temperature. Granted these assumptions, a simple calculation shows that

$$\dot{\psi} + \eta\dot{\theta} = 0, \tag{8}$$

whereby the inequality (6) reduces to

$$-S{\cdot}D + \frac{1}{\theta}q{\cdot}\text{grad}\,\theta \le 0. \tag{9}$$

Next, we suppose that the strain-rate D and the dissipative contribution S to the stress obey a Bingham thermo-visco-plastic relation

$$D = \begin{cases} 0 & \text{if } |S| < s_y(\theta), \\ \dfrac{1}{\mu(\theta)}(|S| - s_y(\theta))S & \text{if } |S| > s_y(\theta), \end{cases} \tag{10}$$

with $\mu(\theta) > 0$ the reciprocal mobility and $s_y(\theta) > 0$ the yield stress, and, further, that the heat conduction is of Fourier type, so that

$$q = -\kappa\,\text{grad}\,\theta, \tag{11}$$

with $\kappa = \text{constant} > 0$ the thermal conductivity. With these assumptions, it transpires that

$$S{\cdot}D - \frac{1}{\theta}q{\cdot}\text{grad}\,\theta = \left.\begin{cases} \dfrac{1}{\theta}\kappa|\text{grad}\,\theta|^2 & \text{if } |S| < s_y(\theta), \\ \dfrac{1}{\mu(\theta)}(|S| - s_y(\theta))|S|^2 + \dfrac{1}{\theta}\kappa|\text{grad}\,\theta|^2 & \text{if } |S| > s_y(\theta) \end{cases}\right\} \ge 0, \tag{12}$$

from which we conclude that the reduced entropy inequality (9) is guaranteed to hold in all processes.

For $|S| > s_y(\theta)$, the choice (10) implies that

$$S = \left(\mu(\theta) + \frac{s_y(\theta)}{|D|}\right)D. \tag{13}$$

Hence, provided $|S| > s_y(\theta)$, the linear momentum balance $(3)_1$ takes the form

$$\varrho\dot{v} = -\text{grad}\,p + \varrho g + \text{div}\left(\left(\mu(\theta) + \frac{s_y(\theta)}{|D|}\right)D\right) \tag{14}$$

and the angular momentum balance $(3)_2$ is satisfied trivially. Further, from the definition (5) of ψ and the relations (7) determining ψ and η in terms of θ, we have that

$$\varepsilon = c\theta, \tag{15}$$

whence, bearing in mind (11) and (13), the energy balance (3)$_3$ simplifies to

$$\varrho c \dot{\theta} = \kappa \operatorname{div}(\operatorname{grad}\theta) + (\mu(\theta)|\boldsymbol{D}|^2 + s_y(\theta)|\boldsymbol{D}|). \tag{16}$$

For $|\boldsymbol{S}| < s_y(\theta)$, consistent with the requirement $\boldsymbol{D} = \boldsymbol{0}$ imposed by (10), the velocity field $\boldsymbol{v}$ must be uniform (and, thus, in particular, obey $\operatorname{div}\boldsymbol{v} = 0$), viz.,

$$\boldsymbol{v} = \text{constant}, \tag{17}$$

while the temperature θ field is determined from the heat equation

$$\varrho c \dot{\theta} = \kappa \operatorname{div}(\operatorname{grad}\theta). \tag{18}$$

The condition $|\boldsymbol{S}| = s_y(\theta)$ merely determines the boundaries between regions of viscous flow, where the governing partial differential equations are the condition of incompressibility (1), the linear momentum balance (14), and the energy balance (16), and regions of plastic flow, where the velocity field is constant and the sole partial differential equation is the heat equation (18).

3 Isothermal Case

A conventionally held belief is that lava domes exhibit a finite yield stress that controls their shape and explosivity. To explore this effect, we study an isothermal process in which an incompressible viscoplastic material spreads over a horizontal plate.

3.1 Governing Equations

Consider an incompressible Bingham thermo-visco-plastic material extruded from a point source onto a horizontal plate. Assume that, throughout this process, the temperature field remains uniform in space and time-independent, viz. $\theta = \theta_* = \text{constant}$. Define $s_* = s_p(\theta_*)$ and $\mu_* = \mu(\theta_*)$. Then, assuming that the stress power terms of the energy balance are negligible, the governing equations in the viscous zone are

$$\left. \begin{array}{l} \operatorname{div}\boldsymbol{v} = 0, \\[2mm] \varrho\dot{\boldsymbol{v}} = -\operatorname{grad}p + \operatorname{div}\left(\left(\mu_* + \dfrac{s_*}{|\boldsymbol{D}|}\right)\boldsymbol{D}\right) + \varrho\boldsymbol{g}, \end{array} \right\} \tag{19}$$

while the surface separating the viscous and plastic zones is determined simply by the equation

$$|\boldsymbol{S}| = s_*, \tag{20}$$

and, the governing equations in the plastic region are

$$\left. \begin{array}{l} \operatorname{div}\boldsymbol{v} = 0, \\[2mm] \varrho\dot{\boldsymbol{v}} = -\operatorname{grad}p + \varrho\boldsymbol{g}, \end{array} \right\} \tag{21}$$

with the velocity field v uniform in the vertical direction. We choose cylindrical coordinates (r, ϑ, z), with origin $\mathbf{0}$ centered at the source of extrusion and the positive z-axis oriented vertically (opposing gravity), and we let u, v, and w denote the r, θ, and z components of $\boldsymbol{v}$.

We assume that no slip may occur at the base $z = 0$, so that

$$u(r, \vartheta, 0, t) = v(r, \vartheta, 0, t) = w(r, \vartheta, 0, t); \tag{22}$$

further, the surface $z = h(r, \vartheta, t)$ is material, whereby

$$h_t(r, \vartheta, t) + u(r, \vartheta, h(r, \vartheta, t), t)h_r(r, \vartheta, t) + \frac{1}{r}v(r, \vartheta, h(r, \vartheta, t), t)h_\vartheta(r, \vartheta, t)$$
$$= w(r, \vartheta, h(r, \vartheta, t), t), \quad (23)$$

and free of traction, so that

$$\boldsymbol{T}(r, \vartheta, h(r, \vartheta, t), t)\boldsymbol{n}(r, \vartheta, t) = \boldsymbol{0}, \tag{24}$$

with

$$\boldsymbol{n}(r, \vartheta, t) = \frac{-h_r(r, \vartheta, t)\boldsymbol{e}_r + \dfrac{1}{r}h_\vartheta(r, \vartheta, t)\boldsymbol{e}_\vartheta + \boldsymbol{e}_z}{\sqrt{1 + h_r^2(r, \vartheta, t) + \dfrac{1}{r^2}h_\vartheta^2(r, \vartheta, t)}} \tag{25}$$

the outward unit normal on the dome surface.

Let H and L denote, respectively, the characteristic height and characteristic radius of the extruded layer and restrict attention to that portion of the extrusion process in which H remains small compared to L. We may then define the nondimensional parameter

$$\epsilon = \frac{H}{L} \ll 1. \tag{26}$$

Let U denote the characteristic fluid velocity in the viscous zone. We then consider a scaling with

$$r = L\tilde{r}, \qquad \vartheta = \tilde{\vartheta}, \qquad z = H\tilde{z}, \qquad t = \frac{U}{L}\tilde{t}, \tag{27}$$

and

$$\left. \begin{aligned} u(r, \vartheta, z, t) &= U\tilde{u}(\tilde{r}, \tilde{\vartheta}, \tilde{z}, \tilde{t}), \\ v(r, \vartheta, z, t) &= U\tilde{v}(\tilde{r}, \tilde{\vartheta}, \tilde{z}, \tilde{t}), \\ w(r, \vartheta, z, t) &= \epsilon U\tilde{w}(\tilde{r}, \tilde{\vartheta}, \tilde{z}, \tilde{t}), \\ p(r, \vartheta, z, t) &= \varrho g H\tilde{p}(\tilde{r}, \tilde{\vartheta}, \tilde{z}, \tilde{t}), \end{aligned} \right\} \tag{28}$$

with $g = |\boldsymbol{g}|$ the magnitude of the gravitational acceleration.

Further, we suppose that

$$U = \frac{\varrho g H^3}{\mu_*}.$$

(29)

Inserting the foregoing expressions in the equations (19) that hold in the viscous zone and dropping the superposed tildes on the dimensionless variables yields the dimensionless expression of the constraint of incompressibility

$$\frac{1}{r}\frac{\partial(ru)}{\partial r} + \frac{1}{r}\frac{\partial v}{\partial \vartheta} + \frac{\partial w}{\partial z} = 0$$

(30)

and the dimensionless equations enforcing momentum balance

$$\left.\begin{aligned}
\epsilon^2 F^2 \left(\frac{\partial u}{\partial t} + u\frac{\partial u}{\partial r} + \frac{v}{r}\frac{\partial u}{\partial \vartheta} + w\frac{\partial u}{\partial z}\right) &= -\frac{\partial p}{\partial r} + \frac{\partial S_{rz}}{\partial z} + \epsilon^2\left(\frac{\partial S_{rr}}{\partial r} + \frac{1}{r}\frac{\partial S_{r\vartheta}}{\partial \vartheta}\right), \\
\epsilon^2 F^2 \left(\frac{\partial v}{\partial t} + u\frac{\partial v}{\partial r} + \frac{v}{r}\frac{\partial v}{\partial \vartheta} + w\frac{\partial v}{\partial z}\right) &= -\frac{1}{r}\frac{\partial p}{\partial \vartheta} + \frac{\partial S_{\vartheta z}}{\partial z} + \epsilon^2\left(\frac{\partial S_{r\vartheta}}{\partial r} + \frac{1}{r}\frac{\partial S_{\vartheta\vartheta}}{\partial \vartheta}\right), \\
\epsilon^2 F^2 \left(\frac{\partial w}{\partial t} + u\frac{\partial w}{\partial r} + \frac{v}{r}\frac{\partial w}{\partial \vartheta} + w\frac{\partial w}{\partial z}\right) &= -\frac{\partial p}{\partial \vartheta} - 1 + \epsilon^2\left(\frac{\partial S_{rz}}{\partial r} + \frac{1}{r}\frac{\partial S_{\vartheta z}}{\partial \vartheta} + \frac{\partial S_{zz}}{\partial z}\right),
\end{aligned}\right\}$$

(31)

with

$$F = \frac{\varrho g H^{\frac{3}{2}}}{\mu_*}$$

(32)

the dimensionless Froude number, the components $S_{rr}, S_{r\vartheta}, S_{rz}, S_{\vartheta\vartheta}, S_{\vartheta z}$, and S_{zz} of the extra stress S, are given by

$$\left.\begin{aligned}
S_{rr} &= 2\left(1 + \frac{B}{E}\right)\frac{\partial u}{\partial r}, \\
S_{r\vartheta} &= \left(1 + \frac{B}{E}\right)\left(\frac{\partial v}{\partial r} - \frac{v}{r} + \frac{1}{r}\frac{\partial u}{\partial \vartheta}\right), \\
S_{rz} &= \left(1 + \frac{B}{E}\right)\left(\frac{\partial u}{\partial z} + \epsilon^2\frac{\partial w}{\partial r}\right), \\
S_{\vartheta\vartheta} &= 2\left(1 + \frac{B}{E}\right)\left(\frac{1}{r}\frac{\partial v}{\partial \vartheta} + \frac{u}{r}\right), \\
S_{\vartheta z} &= \left(1 + \frac{B}{E}\right)\left(\frac{1}{r}\frac{\partial w}{\partial \vartheta} + \epsilon^2\frac{\partial w}{\partial r}\right), \\
S_{zz} &= 2\left(1 + \frac{B}{E}\right)\frac{\partial w}{\partial z},
\end{aligned}\right\}$$

(33)

where E is defined as

$$E = \left((u_z + \epsilon^2 w_z)^2 + 2\epsilon^2 u_r^2 + 2\epsilon^2\left(u_r + \frac{u}{r}\right)^2 + 2\epsilon^2\left(\frac{u}{r} + \frac{v_\vartheta}{r}\right)^2\right.$$

$$\left. + (v_z + \epsilon^2\frac{w_\vartheta}{r})^2 + \epsilon^2\left(\frac{u_\vartheta}{r} + v_r - \frac{v}{r}\right)^2\right)^{1/2}$$

(34)

and

$$B = \frac{\sqrt{2}s_* L}{\varrho g H^2} \tag{35}$$

is the dimensionless Bingham number.

We now assume that u, v, w, p and h possess regular expansions of the form

$$\left. \begin{aligned} u &= u_0 + \epsilon u_1 + O(\epsilon^2), \\ v &= v_0 + \epsilon v_1 + O(\epsilon^2), \\ w &= w_0 + \epsilon w_1 + O(\epsilon^2), \\ p &= p_0 + \epsilon p_1 + O(\epsilon^2), \\ h &= h_0 + \epsilon h_1 + O(\epsilon^2), \end{aligned} \right\} \tag{36}$$

in which case the relations (33) imply that the stress components admit regular expansions of the form

$$\left. \begin{aligned} S_{rr} &= (S_{rr})_0 + \epsilon (S_{rr})_1 + O(\epsilon^2), \\ S_{r\vartheta} &= (S_{r\vartheta})_0 + \epsilon (S_{r\vartheta})_1 + O(\epsilon^2), \\ S_{rz} &= (S_{rz})_0 + \epsilon (S_{rz})_1 + o(\epsilon^2), \\ S_{\vartheta\vartheta} &= (S_{\vartheta\vartheta})_0 + \epsilon (S_{\vartheta\vartheta})_1 + O(\epsilon^2), \\ S_{\vartheta z} &= (S_{\vartheta z})_0 + \epsilon (S_{\vartheta z})_1 + O(\epsilon^2), \\ S_{zz} &= (S_{zz})_0 + \epsilon (S_{zz})_1 + O(\epsilon^2). \end{aligned} \right\} \tag{37}$$

At leading order, equations (31) give

$$\frac{\partial p_0}{\partial r} = \frac{\partial (S_{rz})_0}{\partial z}, \qquad \frac{1}{r} \frac{\partial p_0}{\partial \vartheta} = \frac{\partial (S_{r\vartheta})_0}{\partial z}, \qquad \frac{\partial p}{\partial z} = -1. \tag{38}$$

Then, applying the boundary conditions, we obtain

$$p_0(r, \vartheta, z, t) = -(h_0(r, \vartheta, t) - z), \tag{39}$$

while $(38)_{1,2}$ yield

$$\left. \begin{aligned} (S_{rz})_0(r, \vartheta, z, t) &= -(h_0(r, \vartheta, t) - z)\frac{\partial h_0(r, \vartheta, z)}{\partial r}, \\ (S_{\vartheta z})_0(r, \vartheta, z, t) &= -(h_0(r, \vartheta, t) - z)\frac{1}{r}\frac{\partial h_0(r, \vartheta, z)}{\partial \vartheta}. \end{aligned} \right\} \tag{40}$$

Alternatively, writing

$$E_0 = \sqrt{\left(\frac{\partial u_0}{\partial z}\right)^2 + \left(\frac{\partial v_0}{\partial z}\right)^2}, \tag{41}$$

the relations (40) can be expressed as

$$(S_{rz})_0 = \left(1 + \frac{B}{E_0}\right)\frac{\partial u_0}{\partial z}, \qquad (S_{\theta z})_0 = \left(1 + \frac{B}{E_0}\right)\frac{\partial v_0}{\partial z}. \tag{42}$$

Assume now, that the interface between viscous region and the plastic region can be represented as a surface $z = Y(r, \vartheta, t)$. The limiting value of the stress in the viscous zone must equal the yield stress, so that

$$\sqrt{(S_{rz}(r, \vartheta, t))^2 + (S_{\vartheta z}(r, \vartheta, t))^2} = B; \tag{43}$$

further, the velocity field must obey

$$\frac{\partial u_0(r, z, \vartheta, t)}{\partial z}\bigg|_{z=Y(r,\vartheta,t)} = \frac{\partial u_0(r, z, \vartheta, t)}{\partial z}\bigg|_{z=Y(r,\vartheta,t)} = 0, \tag{44}$$

which yields

$$Y(r, \vartheta, t) = h_0(r, \vartheta, t) - \frac{B}{\sqrt{\left(\dfrac{\partial h_0(r, \vartheta, t)}{\partial r}\right)^2 + \dfrac{1}{r^2}\left(\dfrac{\partial h_0(r, \vartheta, t)}{\partial \vartheta}\right)^2}}. \tag{45}$$

As immediate consequences of the foregoing, we find that, for $0 \le z \le Y(r, \vartheta, t)$,
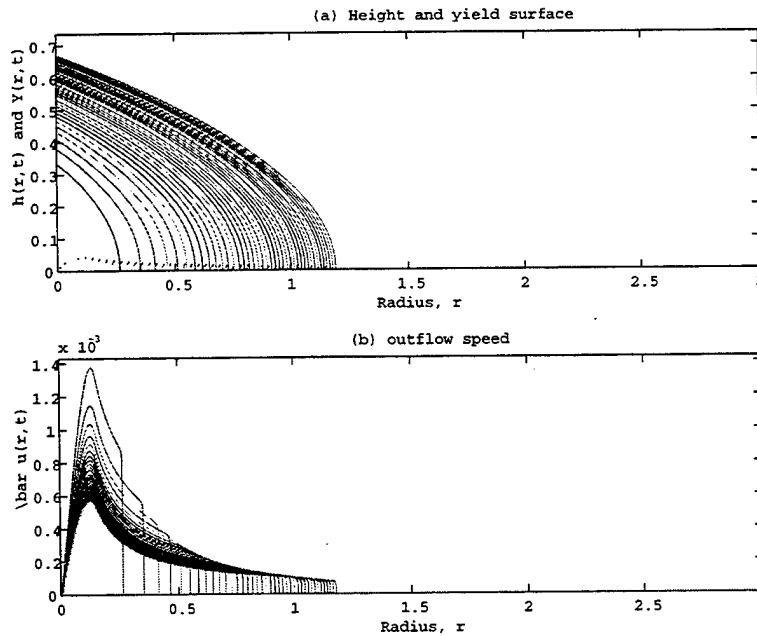
Figure 1: $B = 0.1$, $w_s = 0.1$, initial-value problem: $h(r, t = 0) = 0.001e^{-r/5}$

241

$$
\left.
\begin{aligned}
\frac{\partial u_0(r,\vartheta,z,t)}{\partial z} &= \big(z - Y(r,\vartheta,t)\big)\frac{\partial h_0(r,\vartheta,t)}{\partial r}, \\
\frac{\partial v_0(r,\vartheta,z,t)}{\partial z} &= \big(z - Y(r,\vartheta,t)\big)\frac{1}{r}\frac{\partial h_0(r\,\vartheta,t)}{\partial \vartheta}.
\end{aligned}
\right\}
\tag{46}
$$

On the other hand, for $Y(r,\vartheta,t) \le z \le h_0(r,\vartheta,t)$, we have that

$$
u_0(r,\vartheta,t) = -\frac{1}{2}h_{0r}(r,\vartheta,t)Y^2(r,\vartheta,t)
\tag{47}
$$

We integrate the constraint (30) of incompressibility over the vertical coordinate z from $z = 0$ to $z = h(r,\vartheta,t)$ and using (46), insert the expansions in the resulting equation, giving, to the leading order

$$
\frac{\partial h_0(r,\vartheta,t)}{\partial t} + \frac{1}{r}\frac{\partial}{\partial r}\Big(r\int_0^{h_0(r,\vartheta,t)} u_0(r,\vartheta,z,t)\,dz\Big) + \frac{1}{r}\frac{\partial}{\partial \vartheta}\Big(\int_0^{h_0(r,\vartheta,t)} v_0(r,\vartheta,z,t)\,dz\Big)
$$
$$
= w_s(r,\vartheta,t), \quad (48)
$$

where $w_s(r,\vartheta,t) = w(r,\vartheta,0,t)$ is the velocity on vertical direction at $z = 0$. If the slurry is ejected from a source hole with radius r_0, then at $r = r_0$, the velocity must vanish while at $r = 0$ the velocity must attain its maximum value; here we choose w_s to both ϑ and t independent with the form:

$$
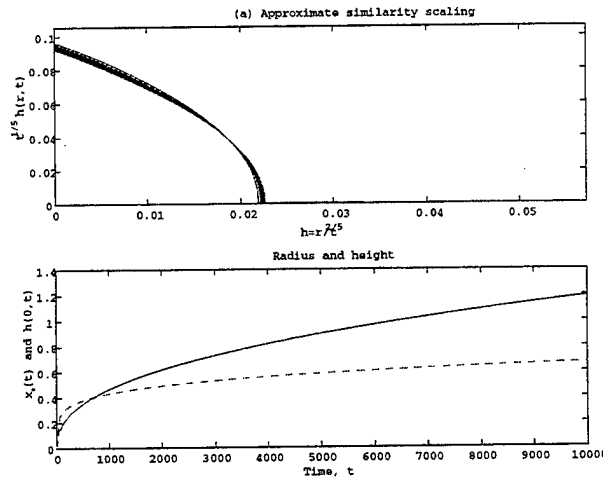w_s(r,\vartheta,t) = w_0(r - r_0)^2
\tag{49}
$$

Figure 2: Same conditions as that of figure 1.

We assume also that the govering equations are independent of temperature field θ at leading order, such that $h_0 = h_0(r,t)$, $Y = Y(r,t)$, etc.

Therefore, we obtain evolution equation for the leading order height h_0 of the dome,

$$\frac{\partial h_0(r,t)}{\partial t} + \frac{1}{r}\frac{\partial}{\partial r}(r h_0(r,t)\bar{u}(r,t)) = w_s(r,t), \tag{50}$$

with

$$h_0(r,t)\bar{u}(r,t) = \left(\int_0^{h_0(r,t)} u_0(r,z,t)\,dz\right) = -\frac{1}{6}Y^2(r,t)\frac{\partial h_0(r,t)}{\partial r}(3h_0(r,t) - Y(r,t)), \tag{51}$$

and the height $Y(r,t)$ of yield surface being

$$Y(r,t) = h_0(r,t) + \frac{B}{\frac{\partial h_0(r,t)}{\partial r}}, \tag{52}$$

Figure 1(a) shows how h_0 evolves with time along the radial direction. The dotted line is the yield surface. Figure 1(b) shows the depth averaged velocity field along the radial direction. From Figure 2(a), an approximate similarity solution is found with $h(r,t) = r^{1/5}f(r/t^{2/5})$, which has been proposed previously[2] from the real lava field measurements and some scaling analyses.

3.2 Laboratory simulation

3.2.1 Material

Real lava is known to have a finite yield stress. The simplest substance possessing this characteristic is a slurry. Two slightly different slurries were used in these experiments. The first of these, which we call material #1, is a 1 : 1 by weight mixture of kaoline and de-ionized water. The second slurry, which we call material #2 is a 1.2 : 1 by weight mixture of kaoline and de-ionized water. A dial-reading viscometer (Brookfield Laboratory Viscometer company) was used to measure the yield stresses and apparent viscosities. For these slurries, which display Non-newtonian response, the measured viscosity is called the apparent viscosity. The measured material properties of these materials appear in Table 1.

Table 1

Property	Material #1 kaoline + water 1 : 1 by weight	Material #2 kaoline + water 1.2 : 1 by weight	Material #3 kaoline + peg 600 wax 1 : 1.25 by weight
Density ϱ (g/cm^3)	1.36	1.48	1.44
Apparent viscosity η (P)	200	300	30
Yield stress s_y (dyne/cm^2)	437	2000	55
Specific heat c (J/kg×K)	–	–	1.78×10^3
Apparent viscosity η (P)	–	–	1.44×10^{-7}
Solidification temperature θ_s (K)	–	–	290

3.2.2 Experimental apparatus

Our experimental apparatus is depicted in Figure 3. The kaoline/water slurry was mixed 2 days ahead of the experiment and, once again, immediately prior to the experiment, was thoroughly mixed again using a power mixer so that no slump would occur. Operations are conducted at a room temperature of 20°C and a relative humidity of 30%. The slurry is placed in an acrylic circular cylinder 90 cm long and 11 cm in diameter. One end of the cylinder was connected via a pipe and micropump through a flow meter to a water bucket; the other end of cylinder was connected with a plastic hose (3 cm in diameter) to a horizontal aluminuum

Figure 3: Overview of the experimental apparatus

plate which has a 3 cm hole in diameter in the center. Ejection of the slurry was controlled
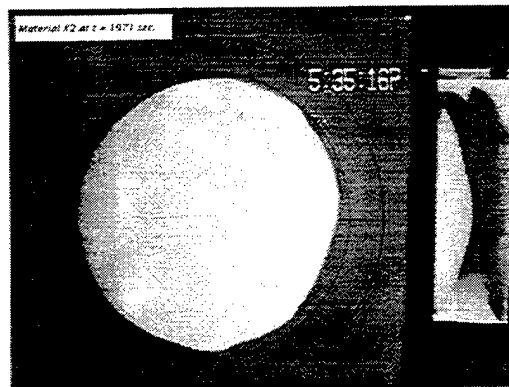
Figure 4: Snap shot of top and side view of the growing dome. note the sprial texture on the surface.

by pumping water into the cylinder behind the piston. When filter papers were placed on the smooth aluminuum plate, there was barely any change in the flow structure, which shows that

the no-slip boundary condition on the base is a valid approximation. Each run lasted between 10 and 40 minutes, depending on the flow rate and the slurry used; each run was stopped when the slurry stored in the cylinder was fully ejected.

A dome around 40 cm in diameter was obtained with each run. A CCD camera was placed 1.5 m above the top of the plate; further, a mirror placed at a 45°C angle to the edge of the plate enabled the CCD camera to include both a side-view and a top-view in the same frame. Measurements of dome radius and height were later taken from the videotapes by transfering the video frames to a computer. During this experiment, the slurry was in direct contact with air upon eruption from the source hole. Some interesting surface texture was observed during the dome growth,(cf. Figure 4). In particular, two intersecting sets of slip lines were observed. This surface texture became distinct away from the center of the dome.

3.3 Data analyis and comparison

From the measurement of the experimental data, we can find the corresponding dimensionless Bingham number and flow rate appearing in equation (52) and then, solving the resulting equation (50) numerically, we can compare the experimental data with the predications from our mathematical model. Clearly, the results from mathematical model for the isothermal problem fit very well with the experimental measurements, (cf. Figure 5). The error in Figure 5(b) is a systematic underestimate of the dome height, an underestimate, is likely due to errors in the measurement of apparent viscosity and yield stress.
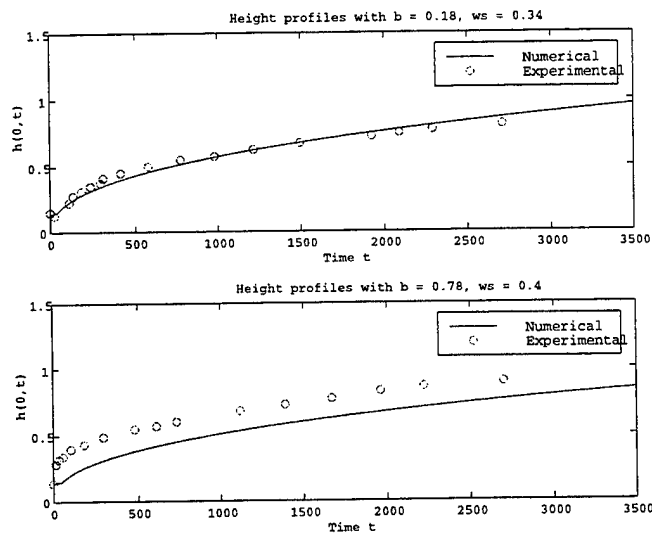

Figure 5: Comparsion of experimental data and predication from the mathematical model.

4 Thermal Effects

To account for the effect of surface cooling, we now consider the full thermo-visco-plastic model. To provide insight regarding the basic physics of dome formation with surface cooling, we first discuss the results of laboratory simulations.

4.1 Laboratory simulation

4.1.1 Material

A mixture of PEG600 wax (polyethylene glycol wax) with kaoline powder (1.25 : 1 by weight) was chosen, we call it material #3, (see table 1 for the detailed properties). PEG600 has a solidification temperature slightly lower than the room temperature and its density is greater than that of water. Further, the viscosity of material #3 is temperature dependent.

4.1.2 Apparatus

The basic setup from the isothermal experiment is retained. In addition, a $60 \times 60 \times 20$ cm acrylic box was built above the aluminium plate. During the experiment, this box was filled with circulating cold water the temperature of which was controlled by the refrigating bath system. Before and after each run, the injection hole was plugged from above to separate the slurry from the cold water. The shape and surface texure of the dome under cooling displayed
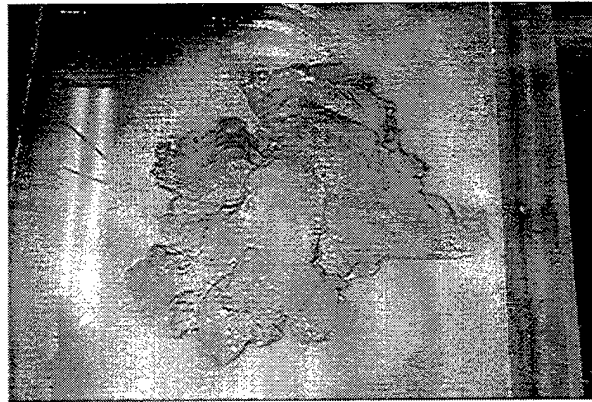

Figure 6: Snap shot after slurry is ejected into an ambient water bathing at temperature $7.5^\circ C$

dependence on the ambient water temperature and the flow rate of the slurry. When the ambient water temperature was higher than 10°C, the extruded slurry grew symmetrically throughout the experiment, except that some rims of small fingers developed at the flow front. In particular, when the ambient water temperature was lower than 10°C, Further, the surface cooled immediately once the slurry was ejected from the source and the dome structure became asymmetric with three to six lobes developing (cf. Figure 6). Clearly the shape and

morphology of the dome is much more complicated in the presence of surface cooling, which reflects more closely the circumstances prevailing during the growth of real lava domes.

4.2 Governing Equations

With thermal effects included, (30) and (31) remain valid, however, the relation (33) determining the stress components become temperature dependent. Recall that for $|\boldsymbol{S}| > s_y(\theta)$, the choice (10) implies that

$$\boldsymbol{S} = \left(\mu(\theta) + \frac{s_y(\theta)}{|\boldsymbol{D}|}\right)\boldsymbol{D}. \tag{53}$$

Here, we assume that the reciprocal mobility has the spedific form

$$\mu(\theta) = \mu_* e^{-\gamma(\theta - \theta_0)} \tag{54}$$

and that the yield stress is constant, viz.,

$$s(\theta) = s_* \tag{55}$$

Consider, now, the energy balance (16) with the boundary conditions:

$$\theta_z(r, \vartheta, 0, t) = 0, \qquad \kappa\theta_z(r, \vartheta, h(r, \vartheta, t), t) = -\alpha(\theta(r, \vartheta, h(r, \vartheta, t), t) - \theta_0) \tag{56}$$

Where α is the cooling rate. Substitute (54) and (55) into the energy balance equation (16), and non-dimensionalizing using the same scaling in equation (3.9)-(3.11) of the isothermal problem, we arrive at the non-dimensional form:

$$\dot{\theta} = \frac{\kappa}{\varrho c}\operatorname{div}(\operatorname{grad}\theta) + \frac{\mu_* UL}{\varrho c H^2 \theta_*}e^{-\gamma(\theta - \theta_0)}(\mu u_z^2 + B u_z) \tag{57}$$

where θ_* is the characteristic temperature. The second term on the right hand side of (57) is of order $O(\epsilon)$. This indicates that the heat generated by the viscous force is very small. Further, assuming that governing equations are independent of ϑ, we have

$$\dot{\theta} = \bar{\kappa}\theta_{zz} + \frac{\bar{\kappa}}{r}\frac{\partial}{\partial r}(r\theta_r), \tag{58}$$

with $\bar{\kappa}$ the dimensionless diffusivity. We introduce the depth averaged temperature field $\bar{\theta}$ through

$$h(r,t)\bar{\theta}(r,t) = \left(\int_0^{h(r,t)}\theta(r,t)\,dz\right). \tag{59}$$

We integrate (58) over the vertical coordinate z from $z = 0$ to $z = h(r,t)$ and apply the boundary conditions to find, that after dropping bars,

$$h\theta_t = -w_s(\theta - \theta_v) - \theta\alpha - h\bar{u}\theta_r + \frac{\kappa}{r}\frac{\partial}{\partial r}(rh\theta_r) \tag{60}$$

where θ_v is the temperature of the slurry at the vent. Furthermore, the height evolution equation can be derived as in the isothermal case, the only differnece being due to the temperature dependence of the viscosity.

$$\left.\begin{aligned} h_t &= w_s - \frac{1}{r}\frac{\partial(rh\bar{u})}{\partial r}, \\ h\bar{u} &= -\frac{1}{6}y^2(3h-y)h_r e^{\gamma(\theta-\theta_0)}, \end{aligned}\right\} \tag{61}$$

As before,

$$y(r,t) = h_0(r,t) + \frac{B}{\frac{\partial h_0(r,t)}{\partial r}}, \tag{62}$$

The coupled system of two partial differential equations consisiting of (60) and (61) was solved numerically. There are two noteworthy limiting cases of the governing equations (60) and (61).
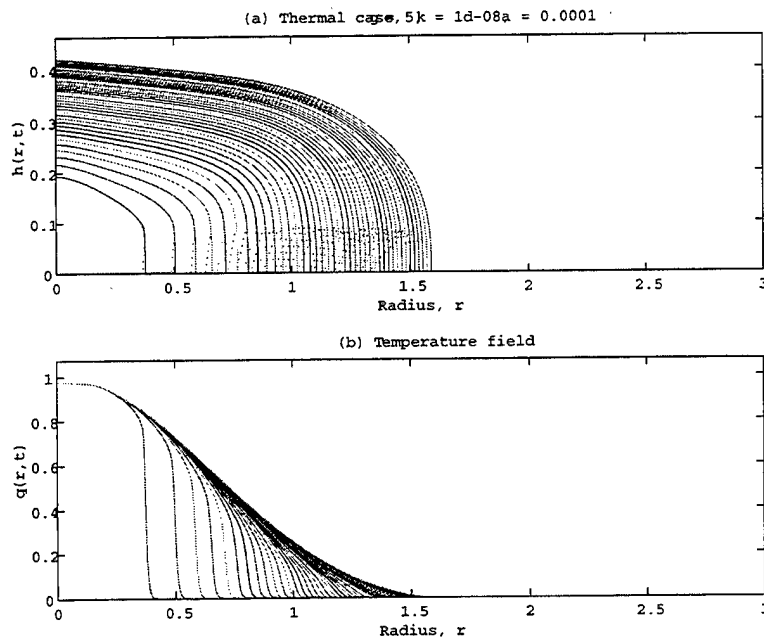
Figure 7: Height and termperature field with smaller cooling rate.

If the cooling rate is small, i.e. $\alpha = 10^{-4}$, the temperature field θ is approximately the vent temperature θ_v. Once the slurry moves past the source, the convection term $h\bar{u}\theta_r$ is balanced by the cooling term $\alpha\theta$, therefore, we have:

$$\left.\begin{aligned} \theta &\to \theta_v & \text{as} & \quad r \le r_0 \\ \bar{u}\theta_r &\to -\frac{\alpha\theta}{h} & \text{as} & \quad r \ge r_0 \end{aligned}\right\} \tag{63}$$

248

Since the diffusitivity is very small in this case, the temperature field will eventually reach a steady state after enough time steps. It is found that the temperature field does affect the shape of the dome height, (cf.Figure 7).

The other interesting limiting case is when the cooling rate is considerably larger, i.e $\alpha = 10^{-1}$. From (60), the cooling term is approximately balanced with the source term because h and $\bar{u}$ are both small. Therefore, from (60), we have

$$\theta = \frac{w_s \theta_0}{\alpha + w_s},\qquad (64)$$

where $w_s = w_0(r - r_0)^2$,
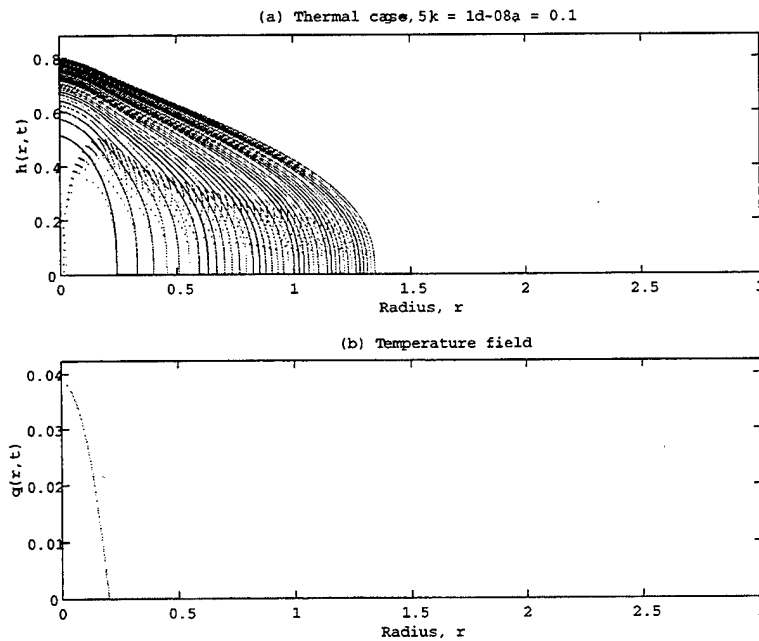
Figure 8: Height and termperature field with larger cooling rate.

$$\left.\begin{array}{lll}\theta \to \theta_v & \text{as} & r \leq r_0 \\ \theta \to 0 & \text{as} & r \geq r_0\end{array}\right\}\qquad (65)$$

Comparing Figures 7 and 8, the only parameter changes is the cooling rate. For higher cooling rates, the height of the dome grows more slowly; meanwhile, the dome grows more rapidly along the radial direction. This explains some aspects of what is observed in the thermal experiments.

5   Conclusion and future work

We formulated a continuum model. From our isothermal study, it was found that results from this model agree fairly well with those obtained from experimental simulations. The

modeling is sucessful in several aspects. First of all, granted an accurate measurement of the viscosity and yield stress of the material, the height evolution equation (3.32) gives a very good predication for the dome growth during the isothermal experiment. Secondly, an approximate similarity solution for equation (3.32) was found, a solution that compares well with the previous field measurements and experimental data.

For the thermal problem, a simplified model was proposed that enables us to explain qualatively of the relation between cooling rate and the dome growth. Two limiting cases were considered and studied numerically, showing that with larger cooling rate, the dome grows more slowly in the vertical direction, which is consistent with what we have observed in our experiments. On the other hand, for the real lava dome, the diffusivity is rather small. Therefore the diffusion term in the energy equation should be neglected; Within the molten lava, initially, the temperature will be constant everywhere, but once the lava surface cools, a thin thermal boundary layer will initially form and travel from the surface to the molten part of lava. Originally, this layer is very thin and lies in the plug region. Consider the energy balance equation (16). No depth averaged fields were used here. Since κ is small, both the diffusion term and the heat generated by the viscous force term are negligible at leading order and equation (16) becomes $\dot{\theta} = 0$. At this stage, the thermal boundary layer is so thin that the velocity in this layer equals the plug velocity which is negligible; therefore, the temperature field remains constant and the growth of lava domes will not be effected by this thin thermal boundary layer. When the thermal boundary layer becomes thicker, especially when its thickness gets close to or exceeds the thickness of the plug region, the temperature field in the entire domain will be substantially changed and the viscosity and yield stress will also change. The velocity field will then be effected, since the flow is controlled by coupled partial differential equations (1), (14), (16) deduced from the mass, momentum and energy balances. The dome growth will become very complicated. Since, under this circumstance, it is very difficult to model the problem, further studies are needed.

For the thermal experiment, nonaxisymmetry is observed when surface begins to cool. Physically, we can explain this as followings. Since the dome is initially symmetric when the slurry is ejected from the source onto a horizontal surface, given a small perturbation to the height, the dome height of some portions will be increased while that of others will be decresed; for those portions with increased height, the cooling rate becomes smaller compared with that of the initial state; material then becomes more viscous and this portion of the material can flow out easily; meanwhile, in the portions with decreased height, the cooling rate becomes larger which makes the material less viscous and more plastic like, hence this poriton is in stead dammed-up. That's how nonaxisymmetric structure eventually develop.

Also, realistically, surface cooling and solidification are both important factors in the flow morphology. If "lobes" observed in the thermal experiment are caused by the solidification of the material, we assume that they are very superficial and fragmented; hence the associated forces are small, thereafter, solidification factor is not considered here.

Instability analyis and flow morphology studies will be the direction for the future work.

250

6 Acknowledgements

References

[1] G. Hulme, "The interpretation of lava flow morphology," Geophys. J. R. astr. Soc. **39**, 361 (1974).

[2] S. Blake, "Viscoplastic models of lava domes," in IAVCEI Proceedings in Volcanology, Vol.2, edited by J. Fink (Springer-Verlag, 1989).

[3] C. R. J. Kilburn, "General patterns of flow field growth: Aa and blocky lavas ," Journal of Geophysical Research, **96**, 19,721 (1991)

[4] M. Dragoni, S. Pondrelli & A. Tallarico, "Longitudinal deformatioon of a lava flow: the influence of Bingham rheology," Journal of Volcanology Geothermal Research, **52**, 247 (1992)

[5] J. Fink & R. Griffiths, " A laboratory analog study of the surface morphology of lava flows extruded from point and line sources," Journal of Volcanology Geothermal Research, **54**, 19 (1992)

[6] M. V. Stasiuk, C. Jaupart & R. S. Sparks, "Influence of cooling on lava-flow dynamics," Geology, **21**, 335 (1993)

[7] R. Griffiths & J. Fink, "Effects of surface cooling on the spreading of lava flows and domes," J. Fluid. Mech., **255**, 667 (1993)

[8] R. Griffiths & J. Fink, "Solidifying Bingham extusions: a model for the growth of silicic lava domes," J. Fluid. Mech., **347**, 13 (1997)

[9] J. Fink & R. Griffiths, "Morphology, eruption rates, and rheology of lava domes: Insights from laboratory models," Journal of Geophysical Research, **96**, 19,721 (1991)

Chaos in the 'Sliced Cone' Model of Wind-driven Ocean Circulation

Andrew Kiss

1   Introduction

Recent analytical and numerical results by Salmon [Salmon, 1992] and Becker and Salmon [Becker and Salmon, 1997] have shown that the barotropic flow in simple β-plane models of wind-driven ocean circulation is dramatically altered when the vertical boundaries usually employed in such models are replaced by continental slopes on which the depth goes gradually to zero at the boundaries. The sloping topography acts to guide the barotropic flow and moves the western boundary currents away from the lateral boundaries and onto the lower part of the slope. This produces a vorticity distribution which is more prone to instabilities than in the case of vertical sidewalls and diminishes the role of lateral viscosity at the boundary in dissipating potential vorticity, leaving Ekman friction as the dominant dissipation mechanism.

The 'sliced cone' model was introduced by Griffiths and Veronis [Griffiths and Veronis, 1997] to investigate the effect of sloping sidewalls on homogeneous wind-driven flow on a simulated β-plane in the laboratory. This model is a variant of Pedlosky and Greenspan's 'sliced cylinder' model [Pedlosky and Greenspan, 1967] in which the vertical sidewalls have been replaced by an azimuthally uniform slope around the perimeter of the basin. The presence of closed geostrophic contours provides a "short cut" for the western boundary current of the interior Sverdrup flow, allowing the current to delay dissipation of the potential vorticity imparted by the wind until just before it rejoins the interior flow.

The laboratory results showed that the flow can become unsteady when the wind stress forcing is anticyclonic and exceeds a critical strength. The fluctuations are periodic for moderately supercritical forcing, but become aperiodic under relatively strong forcing. This paper presents an analysis of the time dependence displayed by numerical simulations of the flow in this apparatus as a function of forcing strength.

2   The 'sliced cone' model

The laboratory model employed by Griffiths and Veronis [Griffiths and Veronis, 1997] utilized a basin of the form shown in Figure 1, filled with water and bounded above by a rigid horizontal lid. The base of the apparatus rotates with a constant angular velocity $\Omega\hat{\mathbf{k}}$ about a vertical axis, whilst the rigid lid has a slightly different angular velocity $(1 + \epsilon)\,\Omega\hat{\mathbf{k}}$ in order to simulate a spatially uniform wind stress curl. The sidewall has a 45° slope relative to the horizontal

and this cone is intersected by a plane with slope 1:10 which forms the central part of the bottom boundary. Figure 1 shows that in this geometry the geostrophic contours (contours of constant depth) are circles near the rim and D-shaped curves when they cross the interior. All geostrophic contours are closed curves, in contrast to the 'sliced cylinder' in which all geostrophic contours are blocked by the vertical sidewalls. The potential vorticity gradient imposed by the shallow slope in the interior is analogous to the potential vorticity gradient of a β-plane and allows us to identify directions in the apparatus with various points of the compass, as shown in the figure (note that the apparatus rotates in the northern hemisphere sense). The width $2a$ of the apparatus is 97.3 cm and the depth H at the center is 12.5 cm.
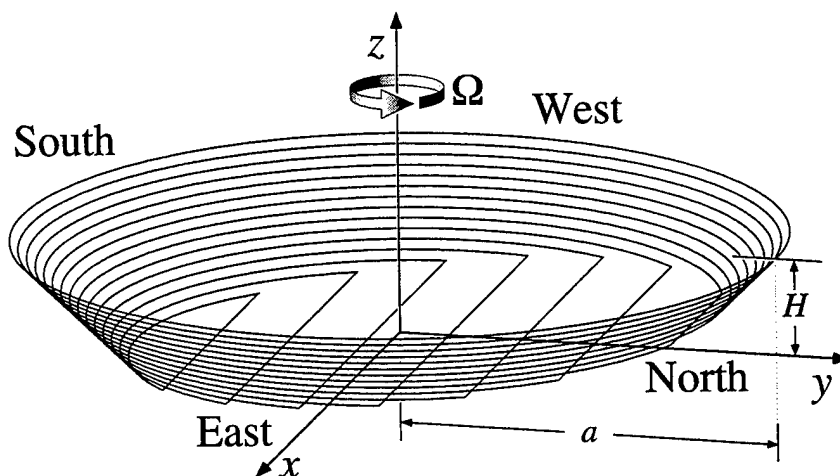

Figure 1: Perspective diagram of the 'sliced cone' model used in the laboratory and numerical experiments. The curves are contours of constant depth (geostrophic contours), and the compass directions are defined in terms of the potential vorticity gradient imposed by the sloping bottom in the interior.

The type of flow seen in this apparatus depends on ϵ and the Ekman number $E = \frac{\nu}{\Omega H^2}$, where ν is the kinematic viscosity of the fluid (water in our case). We can also define a Rossby number by $Ro = |\epsilon|$. A linear analysis ($Ro=0$) based on an expansion in powers of $E^{\frac{1}{2}}$ was presented in [Griffiths and Veronis, 1998]. This analysis showed that the zeroth order flow is along geostrophic contours, and is therefore about ten times faster on the slope than in the interior due to the order of magnitude difference of the bottom slopes in these regions. The $E^{\frac{1}{2}}$-order correction introduces the effect of wind forcing in the interior, resulting in a cross-contour Sverdrup flow which gives a northwest-southeast tilt to the streamlines in the interior but relatively little change to the slope current. At the next order a Stewartson $E^{\frac{1}{4}}$ layer at the junction between the rapid slope current and the slow interior flow makes the azimuthal velocity continuous in this region.

The laboratory study by Griffiths and Veronis [Griffiths and Veronis, 1997] showed that the sign of ϵ has a dramatic effect on the stability of the flow at finite Ro, through a mechanism clarified by the numerical investigation of [Kiss and Griffiths, 1998]. When $\epsilon > 0$ (cyclonic

forcing) the circulation was steady for all values of Ro and E investigated. Under anticyclonic forcing ($\epsilon < 0$) the slope current enters the interior as a jet when Ro is large, and the flow becomes unstable for large enough Ro and small enough E. The laboratory results showed that there are four main regimes as a function of Ro and E for anticyclonic forcing. For small Ro the asymptotic state after spin-up is a steady circulation (apart from some extremely small-amplitude fluctuations seen in the laboratory which the numerical model used here did not reproduce). The flow becomes unstable at a critical value of Ro, which depends on the value of E. For large Ro the only instability which appears is a pinching-off of cyclonic eddies from the cyclonic meander in the western boundary current jet. At small E the situation is more complicated: the first instability to appear is a growing wave in the anticyclonic shear layer at the the west of the interior, in which anticyclonic eddies appear at the west and grow as they are advected northwards until they dissipate when they collide with the southern edge of the jet. At larger values of Ro the cyclonic loop in the jet also becomes unstable and sheds cyclonic eddies. Initially both the cyclonic and anticyclonic instabilities are periodic, but at large Ro the flow for any E appears to become chaotic.

These laboratory observations raise interesting questions as to the nature of the transitions between these regimes, and the route to chaos in this system. This research project was a numerical investigation of these transitions, using the techniques of dynamical systems theory in an approach similar to that of [Jiang et al., 1995, Meacham and Berloff, 1997, Berloff and Meacham, 1997]. The behavior of the system under anticyclonic forcing was studied as a function of Ro at a fixed value of E (1.5075×10^{-5}). This value was chosen in order to study the more interesting situation in which both cyclonic and anticyclonic eddy shedding can appear. In the next two sections the formulation and implementation used in the numerical model are discussed; the rest of this paper is devoted to a presentation and discussion of the methods used and the results obtained.

2.1 Formulation

The equations of motion for this system (relative to coordinates rotating with angular velocity $\Omega \hat{\mathbf{k}}$) are:

$$\partial_t \mathbf{u} + Ro\,(\mathbf{u} \cdot \nabla)\,\mathbf{u} + 2\hat{\mathbf{k}} \times \mathbf{u} = -\nabla p + E\nabla^2 \mathbf{u} \tag{1}$$

and

$$\nabla \cdot \mathbf{u} = 0, \tag{2}$$

where $\hat{\mathbf{k}}$ is the unit vector in the z direction (vertical), p is the pressure divided by the density and we have scaled the velocity $\mathbf{u}$, time t and length by $U = |\epsilon\Omega H|$, $|\Omega^{-1}|$ and H, respectively. The importance of advection and viscosity are parameterized by the Rossby number $Ro = \frac{U}{\Omega H} = |\epsilon|$ and Ekman number $E = \frac{\nu}{\Omega H^2}$, respectively, where ν is the kinematic viscosity of the fluid. Gravitational and centrifugal accelerations are not relevant to this system, since there is no free surface and no stratification.

We shall separate the vertical and horizontal components of the velocity by writing $\mathbf{u} = \mathbf{u}_H + \hat{\mathbf{k}}w$, where $\hat{\mathbf{k}} \cdot \mathbf{u}_H = 0$. For the parameters used in this study it is a very good approximation to assume (outside the Ekman layers) that $\mathbf{u}_H$ is independent of z and horizontally nondivergent, so we have

$$\mathbf{u}_H = \hat{\mathbf{k}} \times \nabla_H \psi, \tag{3}$$

where ψ is the streamfunction and ∇_H denotes the horizontal gradient operator.

Taking the vertical component of the curl of the momentum equation 1 yields an equation for the vertical vorticity ζ:

$$\partial \zeta t + Ro\, J(\psi, \zeta) = (2 + Ro\, \zeta)\, \partial wz + E\nabla_H^2 \zeta, \tag{4}$$

where

$$\zeta = \nabla_H^2 \psi \tag{5}$$

and $J(a, b) \equiv \partial ax \partial by - \partial ay \partial bx$ is the two-dimensional Jacobian operator. The assumption that $\partial \mathbf{u}_H z = 0$ implies (via 2) that $\frac{\partial^2 w}{\partial z^2} = 0$, allowing us to find ∂wz by using steady, linear Ekman matching conditions[1] for w at the top and bottom boundaries. Since the bottom slope is not small, a coordinate-free form of equation (4.9.32) in [Pedlosky, 1987] (valid where the radius of curvature of the bottom topography is much larger than the Ekman layer thickness) was used to find w on the bottom boundary. Combining this with the upper Ekman matching condition yields

$$\partial wz = \frac{E^{\frac{1}{2}}}{2(1-h)} \left(\zeta_T - (1+\sigma)\,\zeta - s\sigma J\left(s^{-1} J(\psi, h), h\right) \right) - \frac{J(\psi, h)}{(1-h)}, \tag{6}$$

where $\zeta_T = 2\frac{\epsilon}{|\epsilon|}$ is the vorticity of the lid, $1 - h$ is the scaled fluid depth, $s = |\nabla_H h|$ is the bottom slope and $\sigma = \left(1 + s^2\right)^{\frac{1}{4}}$. On the sloping sidewall we have $\partial h\theta = 0$ (where θ is the azimuthal coordinate) and 6 has the form

$$\partial wz = \frac{E^{\frac{1}{2}}}{2(1-h)} \left(\zeta_T - (1+\sigma)\,\zeta - \frac{s^2\sigma}{r^2} \frac{\partial^2 \psi}{\partial \theta^2} \right) - \frac{J(\psi, h)}{(1-h)}, \tag{7}$$

where r is the radial coordinate. In the interior the bottom slope is so small that its effect on the bottom Ekman layer can be neglected, giving

$$\partial wz = \frac{E^{\frac{1}{2}}}{2(1-h)} \left(\zeta_T - 2\zeta \right) - \frac{J(\psi, h)}{(1-h)}. \tag{8}$$

The no-slip boundary condition gives

$$\psi = \partial \psi r = 0 \qquad \text{at} \quad r = \frac{a}{H}. \tag{9}$$

---

[1] Steady, linear Ekman matching is valid for flows which are nearly steady over one rotation period [Beardsley, 1975b] and have $Ro \ll E^{\frac{1}{4}}$ [Bennetts and Hocking, 1973]. The latter criterion is violated for the more strongly forced results presented here, but the close similarity of the calculated flows to those seen in the laboratory suggests that the error involved in using linear Ekman conditions is insignificant. Thus it was felt that using the much more complicated nonlinear Ekman conditions was not justified for our purposes.

2.2 The numerical model

The numerical experiments were conducted with a highly efficient sliced-cylinder code developed by Page [Page, 1982] and described in detail in his PhD thesis [Page, 1981]. The algorithm is the same as that presented by Beardsley [Beardsley, 1975a], which was in turn based on the refinement by Israeli [Israeli, 1970] of a scheme proposed by Pearson [Pearson, 1965]. For this study the code was modified to include the effect of the sloping sidewalls on the bottom Ekman layer. The code solves 4 and 5, where ∂wz is found by using 7 on the slope[2] and 8 in the interior. This system generalizes that analyzed in [Griffiths and Veronis, 1998] by including advection, lateral viscosity and time dependence. Spatial derivatives are calculated using second-order centered differences on a polar grid, except at the origin where an integral treatment is used. The vorticity equation 4 is solved using the alternating-direction implicit method, and a fast Fourier transform in θ is used to solve the Poisson equation 5 for ψ. Since the nonlinearity in 4 couples it to 5, these equations are solved iteratively within each timestep until both ψ and ζ converge. This in-timestep iteration also serves to converge ζ at the boundary to a value which is consistent with the no-slip boundary condition 9, using optimal relaxation. The algorithm is unconditionally stable for zero Ro and retains its stability for all reasonable values of Ro. The numerical results reported here were obtained using 160 grid points in the radial direction and 512 in the azimuthal direction (with no stretching in either direction) and a timestep of $10^{-3}E^{-\frac{1}{2}} \approx \frac{1}{8}$ rotation periods, giving good spatial and temporal resolution. A comparison of numerical and laboratory results for the northward velocity under cyclonic forcing is shown in Figure 2.

3 Methods

Although some use was made of sequences of snapshots of the ψ and ζ fields, the primary diagnostic we used to study the time dependence of the computed flows was the basin integral of the kinetic energy, $K(t) = -\iint \psi(t)\zeta(t)dA$. Another quantity plotted in the following section is the normalized fluctuation in K, $K'(t) = \frac{K(t)-\bar{K}}{\bar{K}}$, where $\bar{K}$ is the time-average of K in the statistically steady state. Time series of K' calculated at each time step were analyzed by several techniques:

3.1 Power spectra

Power spectra of the time series allowed identification of the primary frequencies present, and provided a means of discriminating between quasiperiodic and chaotic time series.

3.2 Delay coordinates

The spatial resolution used in the model implies that this numerical system has a phase space with over 80000 dimensions. However as we shall see the trajectory of the state vector is confined to a manifold with a much smaller dimension than that of the full phase

---

[2] 7 is not evaluated on the lateral boundary itself (where $1 - h$ vanishes) because this is where 9 is imposed
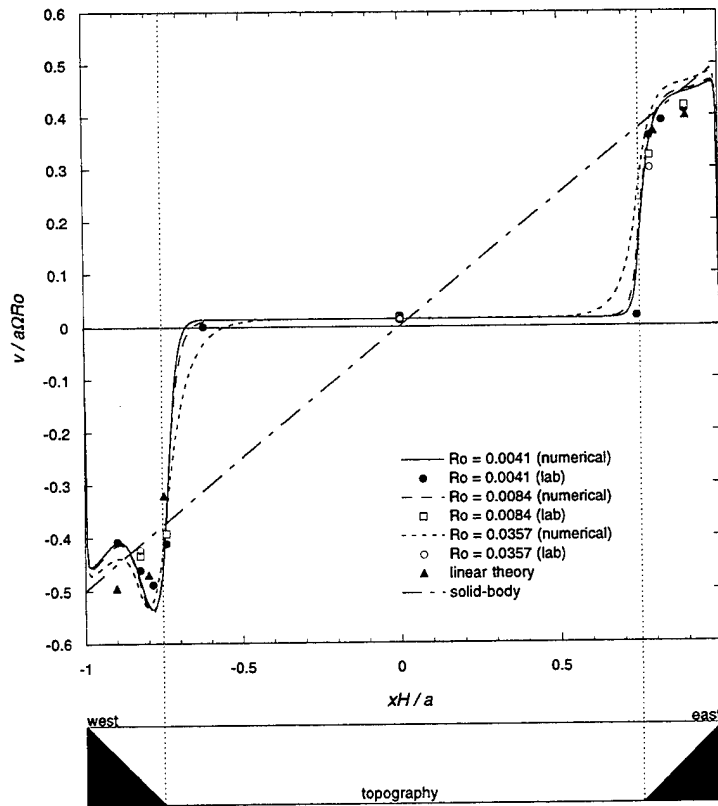
Figure 2: Laboratory and theoretical results from [Griffiths and Veronis, 1997] and [Griffiths and Veronis, 1998] compared with numerical results for the northward component of the normalized velocity as a function of position along the line $y = 0$, for cyclonic forcing.

space. The technique of delay-space reconstruction allows a trajectory to be extracted from the time series which has the same topological properties as the trajectory in the full phase space [Takens, 1981]. The delay-space trajectory is constructed by forming the time-dependent n - dimensional vector $\mathbf{X}(t; \tau)$, whose components are $X_i = K'(t - (i-1)\tau)$, where τ is a fixed delay time. The topological properties of the trajectory are independent of the choice of τ, but in order to obtain a trajectory which is not too contorted it is best to choose τ so that X_i and X_{i+1} are neither strongly correlated nor strongly uncorrelated. The delay used in the results presented here was 7.52 days, about a quarter of the shortest period (25 to 31 days). Trajectories were produced using embedding dimensions n of 2 or 3.

3.3 Poincaré sections

We found Poincaré sections to be a useful diagnostic tool for studying the structure of phase space trajectories and the manner in which the system converged to its final state. They were constructed by choosing a plane of interest in delay space (say, $X_k = c$ for some component k) and recording the position at which the trajectory passed through the plane in the direction of increasing X_k. The set of these intersection points comprises a Poincaré section of the trajectory. The results presented here used $c = 0$, the asymptotic mean value of K'.

4 Results

Numerical results were obtained for many different Rossby numbers, concentrated about values of Ro corresponding to transitions between regimes. The numerical model was integrated until the system reached a statistically steady state (at least several hundred days, and longer when close to a bifurcation) and the integration was continued to obtain a long time series in order to study the time dependence of the asymptotic state. The results are summarized in Figure 3, which shows the time average $\bar{K}$ of the asymptotic basin-integrated kinetic energy as a function of Ro. It is clear that there are several transitions between regimes, which take place abruptly at critical values of the Rossby number. The most interesting region, in which the behavior changes from periodic to quasiperiodic and ultimately to chaotic, takes place over a relatively small range of Ro. Over some of this range there is a second branch of solutions. The details of these regimes and the transitions between them are discussed below.

4.1 Fixed point (steady flow)

For $Ro < Ro_1 \approx 8.5 \times 10^{-3}$ the flow converges to a steady state of the form shown in Figure 4, in which flow is closely aligned with depth contours on most of the slope and is driven across depth contours by the wind stress in the interior. These regions are joined by a region of strong anticyclonic vorticity at the bottom of the slope where dissipation of vorticity by the bottom Ekman layer allows flow across depth contours. The inertial overshoot where the slope current rejoins the interior at the west becomes more pronounced as Ro is increased. A time series of the normalized energy perturbation K' at $Ro = 1.0 \times 10^{-3}$ is shown in Figure 5. At this Rossby number the flow converges directly to the steady state without oscillations. Closer to the transition to unsteady flow the convergence is oscillatory (see Figure 6). The power spectrum of the extremely small-amplitude decaying oscillation at $Ro = 7.5 \times 10^{-3}$ shows that the oscillation frequency is around 0.027 cycles per day. This spectral peak has been labeled A for future reference.

4.2 Limit cycle (periodic flow)

When $Ro_1 < Ro < Ro_2 \approx 2.64 \times 10^{-2}$, the flow is unsteady and displays a periodic train of growing anticyclonic waves in the anticyclonic shear layer at the west. Close to the bifurcation point the oscillations in K' have an extremely small amplitude, as shown in Figure 7 for $Ro = 10^{-2}$. The frequency at $Ro = 10^{-2}$ is 0.032 cycles per day, close to that of the decaying
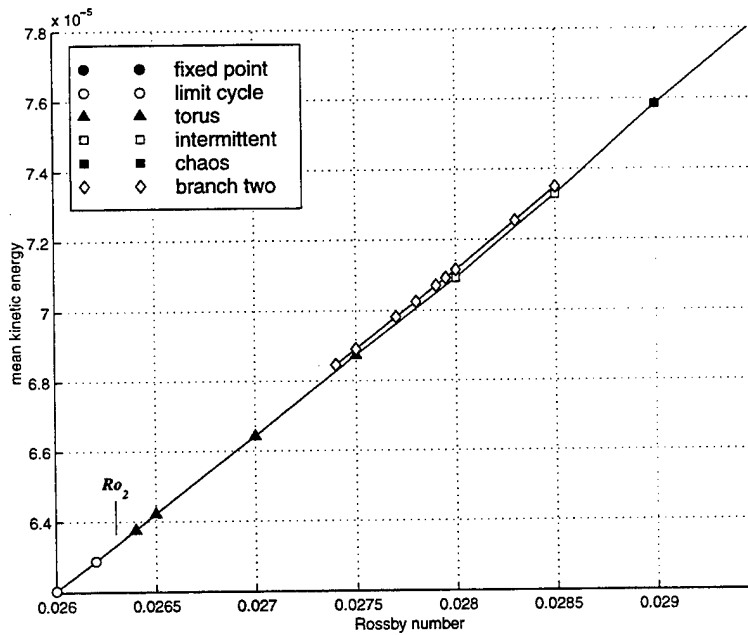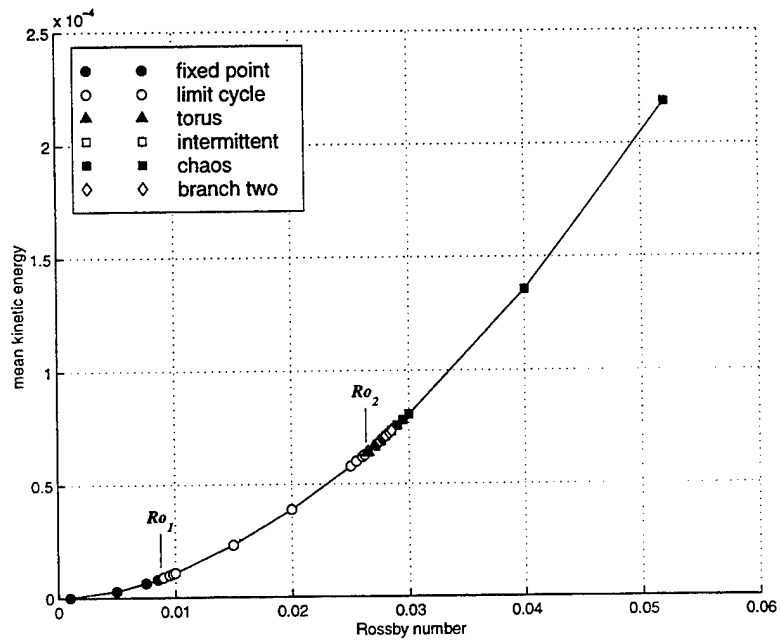
Figure 3: Time average $\bar{K}$ of the basin-integrated kinetic energy as a function of Ro. a) the complete range of Ro investigated; b) a closeup of the transition from a limit cycle to chaos, showing the presence of two branches for a range of Ro.
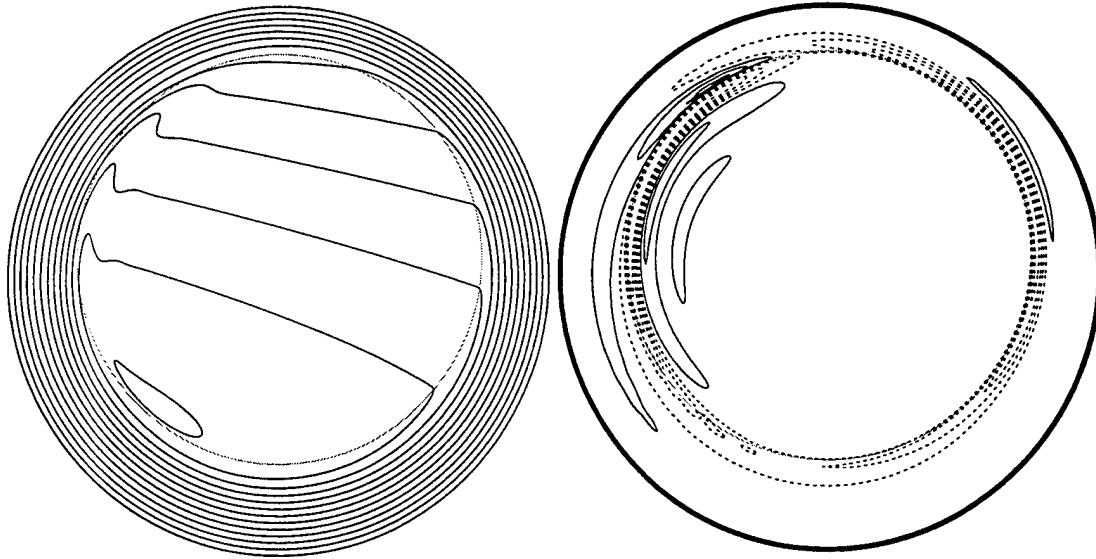
Figure 4: Contours of ψ (left) and ζ (right) for $Ro = 5 \times 10^{-3}$. Contours of anticyclonic ζ are dashed and the grey ellipse marks the bottom of the slope. North is at the top and the mean flow is clockwise.
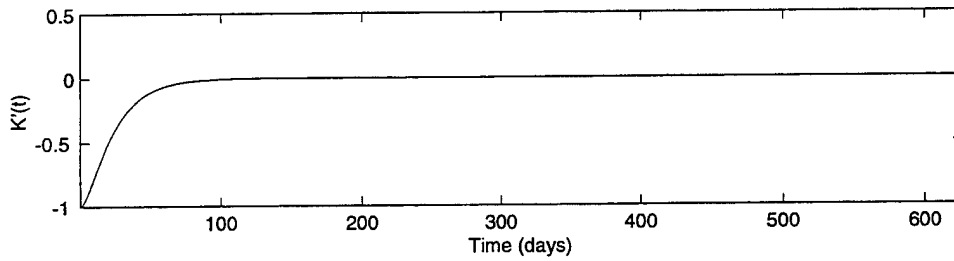

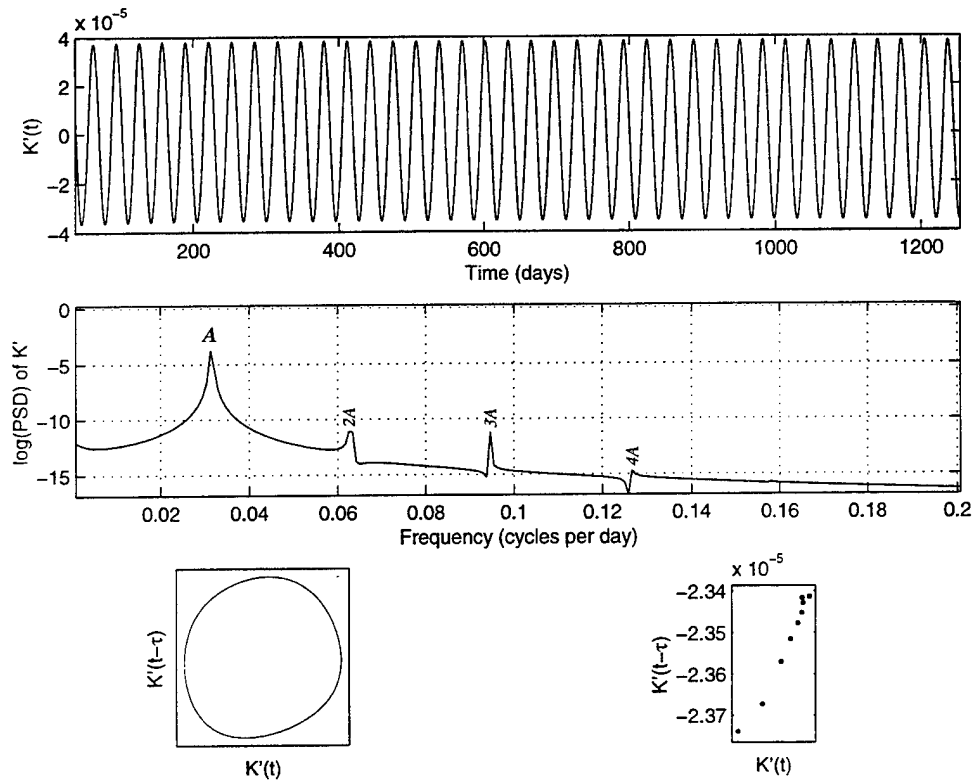Figure 5: Time dependence of K' with $Ro = 1.0 \times 10^{-3}$.
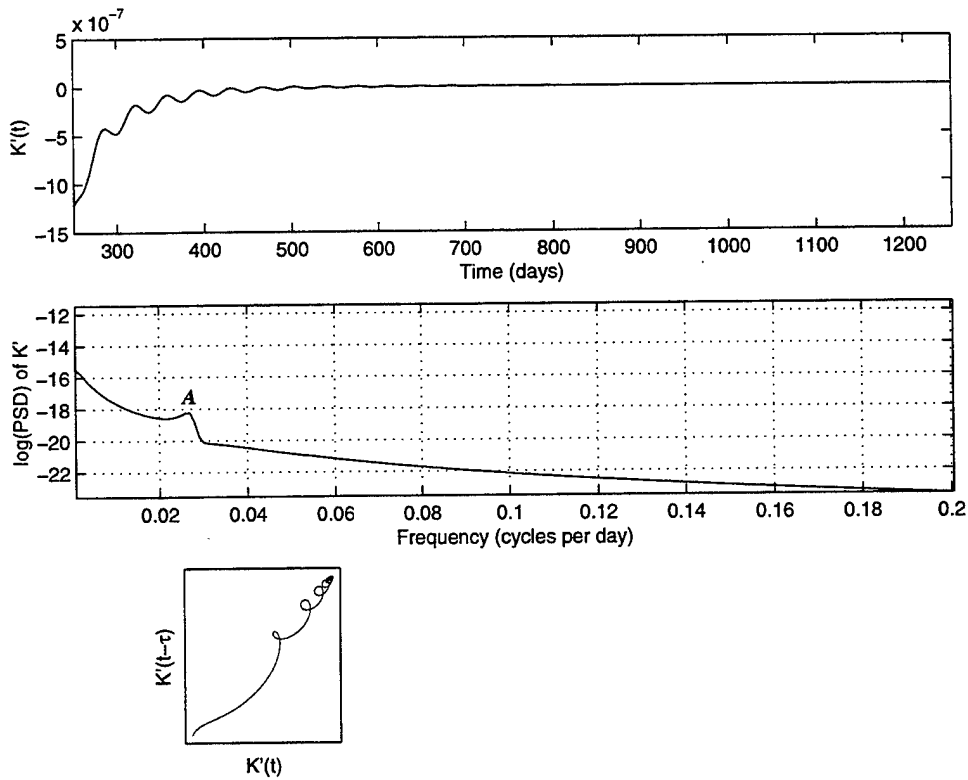
Figure 6: Time dependence of K' with $Ro = 7.5 \times 10^{-3}$. Top: time series; middle: power spectrum of time series (the zero frequency peak has been suppressed); bottom left: delay-space trajectory for the time series.

Figure 7: Time dependence of K' with $Ro = 1.0 \times 10^{-2}$. Top: time series; middle: power spectrum of time series (the zero frequency peak has been suppressed); bottom left: delay-space trajectory for the time series; bottom right: Poincaré section of the delay-space trajectory.

oscillation at $Ro = 7.5 \times 10^{-3}$. The other peaks in the power spectrum are harmonics of this fundamental frequency, as they must be for a periodic oscillation. The phase - space trajectory in Figure 7 has the form of a limit cycle; the Poincaré section (which has axes scaled to fit the range of the intersection points) shows that convergence to this invariant set does not involve any oscillations. These observations of time series for Ro in the vicinity of Ro_1 provide strong evidence that the onset of time-dependence takes place by a supercritical Hopf bifurcation at $Ro = Ro_1$.

The physical nature of the instability which occurs at Ro_1 can be seen by computing the average streamfunction field over one period and subtracting this from the instantaneous field at a given time. Mean and perturbation streamfunctions at $Ro = 9.5 \times 10^{-3}$ are shown in Figure 8. The perturbation streamlines are inclined into the mean velocity gradient in a manner consistent with extraction of energy from the mean flow, as discussed by Pedlosky [Pedlosky, 1987]. This barotropic instability is associated with the cross-flow extremum of the potential vorticity $q = (2 + Ro\zeta)/(1 - h)$ at the bottom of the slope, as discussed in [Kiss and Griffiths, 1998]. The positive perturbations in ψ coincide with regions of increased anticyclonic vorticity, and
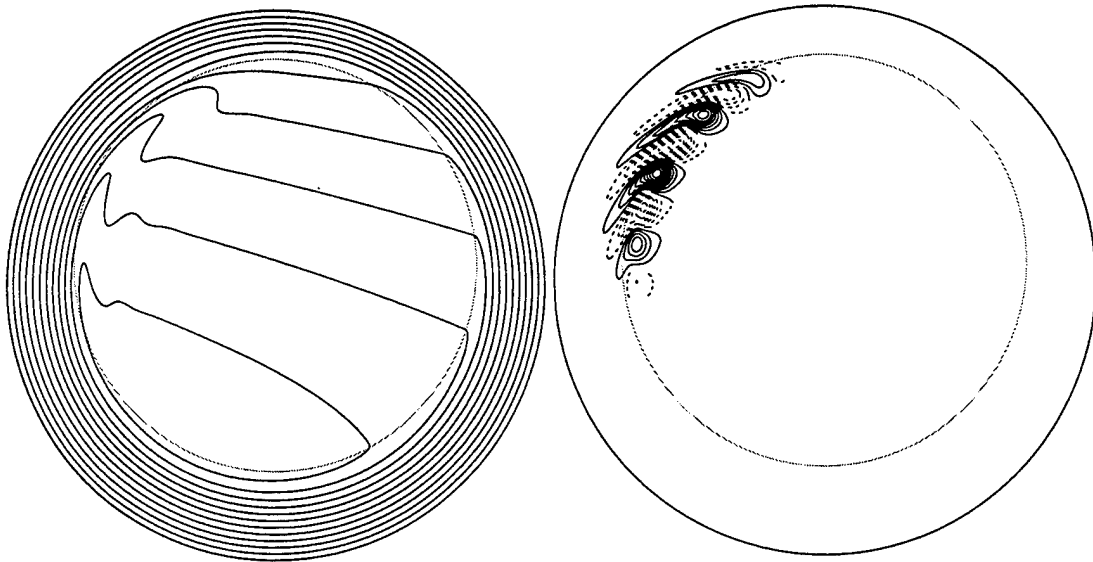
Figure 8: Contours of ψ averaged over one oscillation (left) and the difference in ψ from this field at one time (right; the contour interval has been reduced by a factor of 30). $Ro = 9.5 \times 10^{-3}$; contours of negative ψ are dashed and the grey ellipse marks the bottom of the slope. North is at the top and the mean flow is clockwise.

hence to maxima in the vorticity waves seen in the anticyclonic shear layer. The waves grow as they are advected northwards with the flow until they reach the end of the outflow region from the slope current, where they die out. Each kinetic energy peak corresponds to an anticyclone reaching its maximum amplitude before being advected into the region where it decays.

As Ro is increased towards Ro_2 the amplitude of the anticyclonic perturbations becomes larger, until they are sufficiently strong to produce closed contours of ψ, resulting in a northward-traveling train of anticyclonic eddies. The vorticity of the anticyclones acts to stretch out the jet when they arrive at its southern edge, making it extend southeastwards into the interior and intensifying its cyclonic meander. The jet then retracts back to its former length as each anticyclone dissipates, before being stretched again by the arrival of the subsequent anticyclone. When Ro is large enough, these periodic perturbations to the jet result in a cyclonic eddy pinching off from the cyclonic loop in the jet as each anticyclone dissipates. This process is shown in Figure 9, which shows snapshots of ζ at a local maximum and the following local minimum of K.

Figure 10 shows the time behavior at $Ro = 2.62 \times 10^{-2}$, just before the second bifurcation. The frequency has increased to 0.039 cycles per day, and the oscillation has a much larger amplitude but is still periodic. However in contrast to the case of $Ro = 10^{-2}$, the convergence to the limit cycle is now oscillatory, the decaying oscillation having a frequency of about 0.017 cycles per day. This new spectral peak will be denoted B.
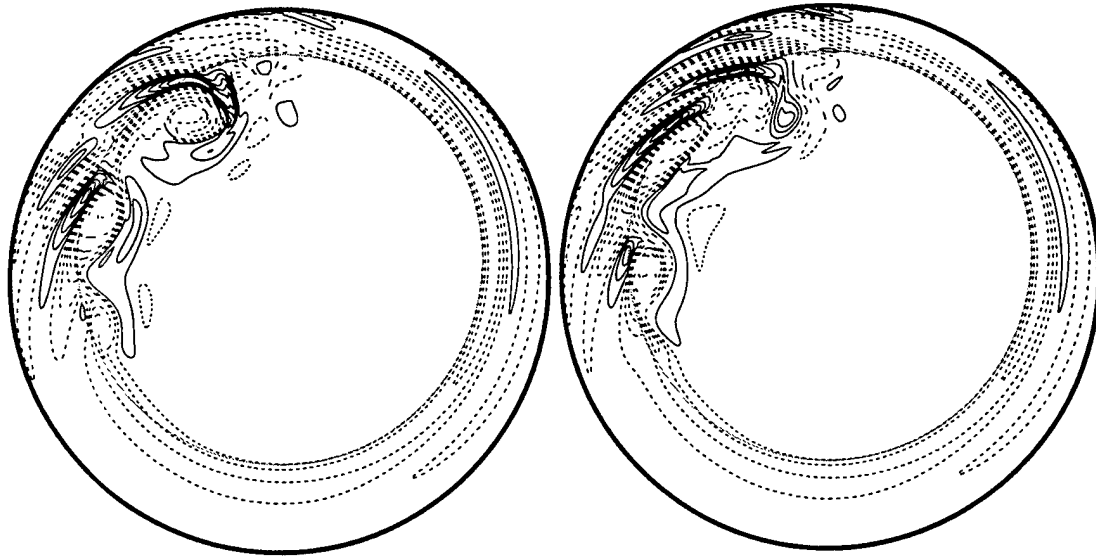
263

Figure 9: Contours of ζ at two different times for $Ro = 2.5 \times 10^{-2}$. Left: at a local maximum of K; right: at the subsequent minimum of K. Contours of negative ζ are dashed. Note how the strong anticyclone wraps a tongue of cyclonic vorticity around itself, which sheds a cyclonic eddy when the anticyclone dissipates. An animation of this sequence can be viewed at http://rses.anu.edu.au/gfd/link/AK/WHOIGFD.html

4.3 Torus (quasiperiodic or phase-locked flow)

A very slight increase in Ro from $Ro = 2.62 \times 10^{-2}$ to $Ro = 2.64 \times 10^{-2}$ produces a transition from periodic to quasiperiodic flow, giving a trajectory which is a torus, as shown in Figure 11. The oscillation denoted B is now no longer decaying, and appears as a peak in the power spectrum at a frequency which is indistinguishable from that of the decaying oscillation at $Ro = 2.62 \times 10^{-2}$. The winding number of the trajectory on the torus is $B/A = 0.433$. The numerous other peaks in the spectrum are cross-harmonics of A and B, as indicated in the figure. Once again, this transition seems to have taken place by a Hopf bifurcation. As for strongly forced periodic flow, relative maxima and minima of K' correspond respectively to the arrival of a large anticyclone at the southern side of the jet, and the subsequent shedding of a cyclone. This basic cycle has a period $1/A$, but is amplitude-modulated by the second period $1/B$, giving rise to the cross-harmonics of A and B in the power spectrum.

As Ro increases, the Poincaré section becomes an increasingly distorted loop, and the amplitude of the peak with frequency $A - 2B$ becomes larger. At $Ro = 2.70 \times 10^{-2}$ these long-period fluctuations are periodic, but at $Ro = 2.75 \times 10^{-2}$ the fluctuations appear to become aperiodic (although a longer time series would be needed to confirm this). Figure 12 shows the time dependence of the kinetic energy at $Ro = 2.75 \times 10^{-2}$, in which the peak at $A - 2B$ has become large, corresponding to the conspicuous variations with a period of about 500 days visible in the time series.
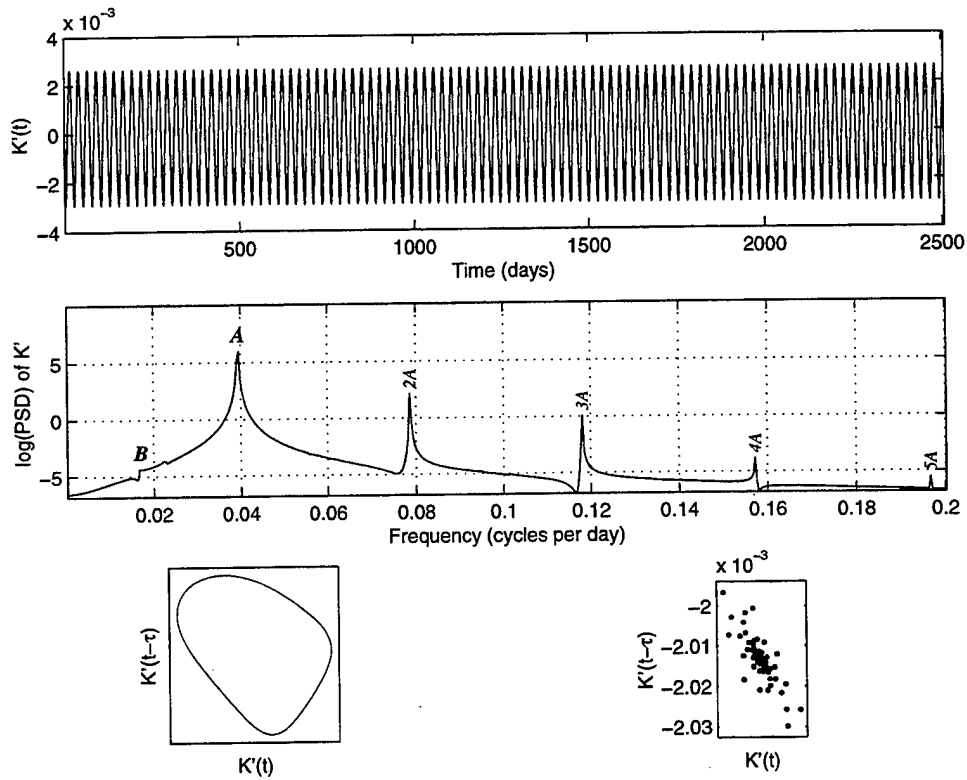
Figure 10: Time dependence of K' with $Ro = 2.62 \times 10^{-2}$. Top: time series; middle: power spectrum of time series (the zero frequency peak has been suppressed); bottom left: delay-space trajectory for the time series; bottom right: Poincaré section of the delay-space trajectory.
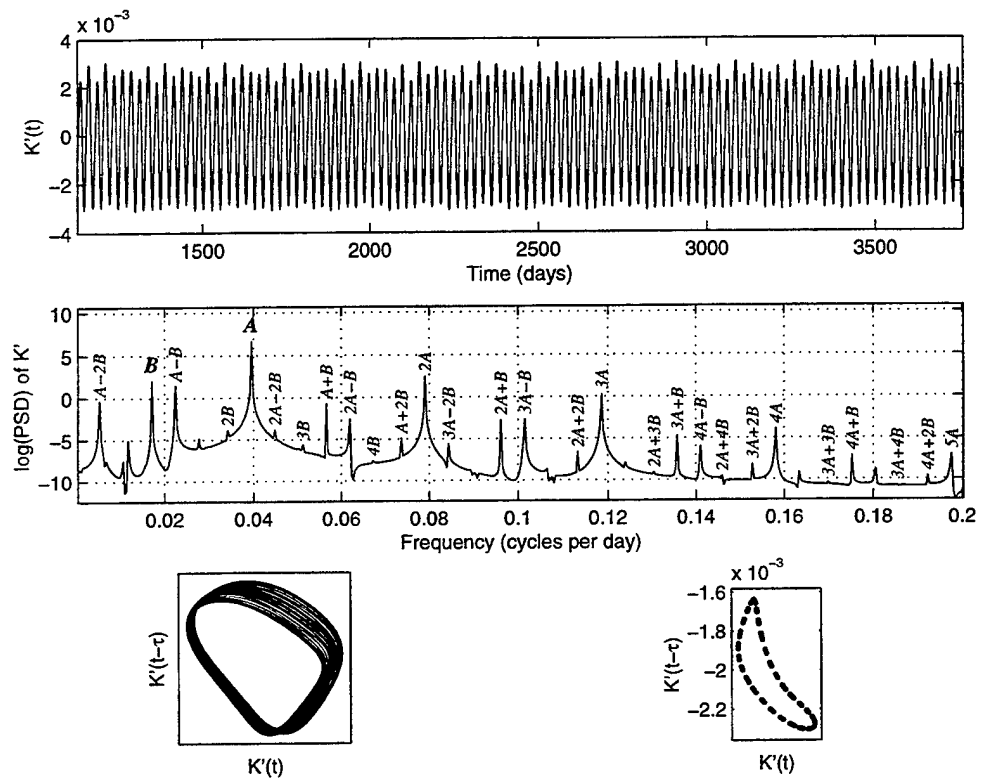
Figure 11: Time dependence of K' with $Ro = 2.64 \times 10^{-2}$. Top: time series; middle: power spectrum of time series (the zero frequency peak has been suppressed); bottom left: delay-space trajectory for the time series; bottom right: Poincaré section of the delay-space trajectory.
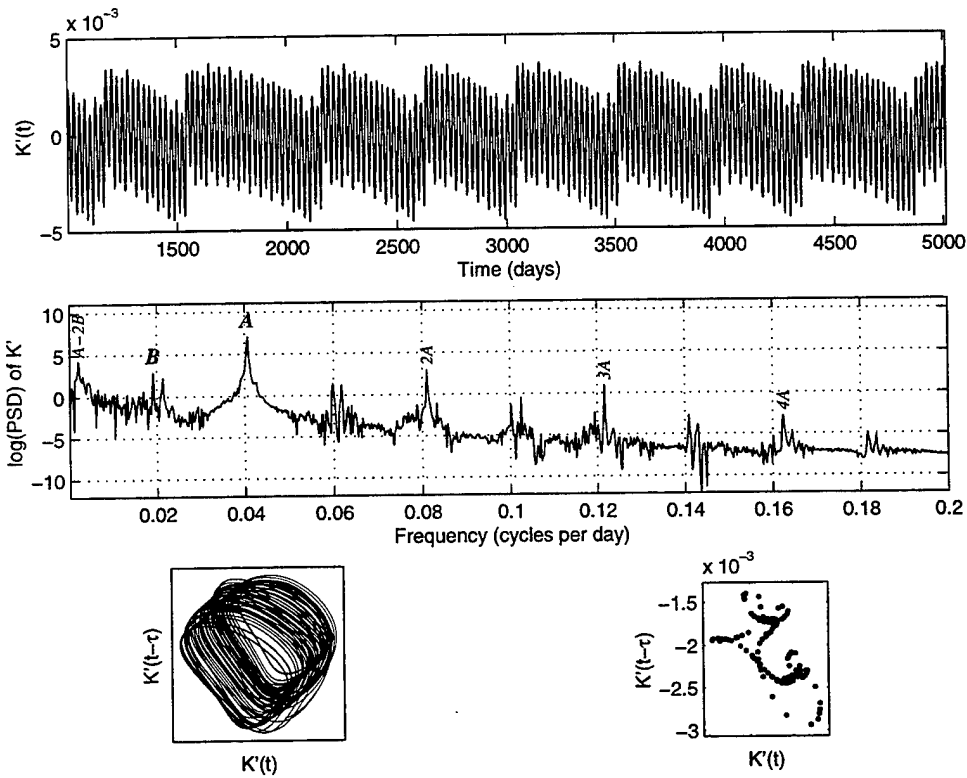
Figure 12: Time dependence of K' with $Ro = 2.75 \times 10^{-2}$. Top: time series; middle: power spectrum of time series (the zero frequency peak has been suppressed); bottom left: delay-space trajectory for the time series; bottom right: Poincaré section of the delay-space trajectory.
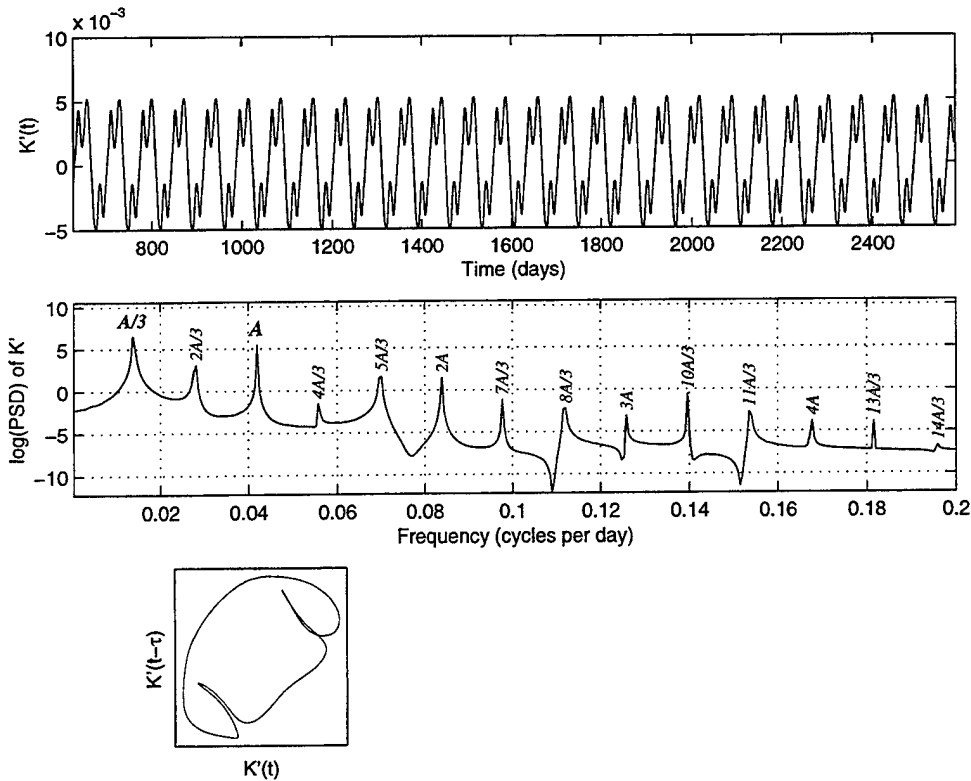
Figure 13: Time dependence of K' with $Ro = 2.75 \times 10^{-2}$, on branch 2. Top: time series; middle: power spectrum of time series (the zero frequency peak has been suppressed); bottom left: delay-space trajectory for the time series.

4.4 The second branch

The numerical results show that there is an additional branch of solutions (which will be referred to as branch two) over at least the range $2.74 \times 10^{-2} \leq Ro \leq 2.85 \times 10^{-2}$, as can be seen in Figure 3. Figure 13 shows a kinetic energy time series for a flow on branch two with $Ro = 2.75 \times 10^{-2}$ (the same value as in Figure 12). The time series is periodic, and now the fundamental frequency is $A/3$. This is not simply a case of B being locked on to $A/3$, since the trajectory does not lie on the torus of branch one.

A numerical run which has converged to a final state on branch two can be used as an initial condition for a run at a different value of Ro, allowing this branch to be traced out over a range of Ro. Following this procedure it was found that the branch could not be extended for $Ro < 2.74 \times 10^{-2}$ (where it actually seems to be a torus). Further numerical experiments are required in order to understand the disappearance of this branch at lower values of Ro. As Ro is increased the attractor for this branch seems to remain qualitatively similar to that seen at $Ro = 2.75 \times 10^{-2}$, until at $Ro = 2.83 \times 10^{-2}$ it appears that a period-doubling bifurcation has occurred and the basic period becomes $A/6$ (see Figure 14). The behavior of this attractor at
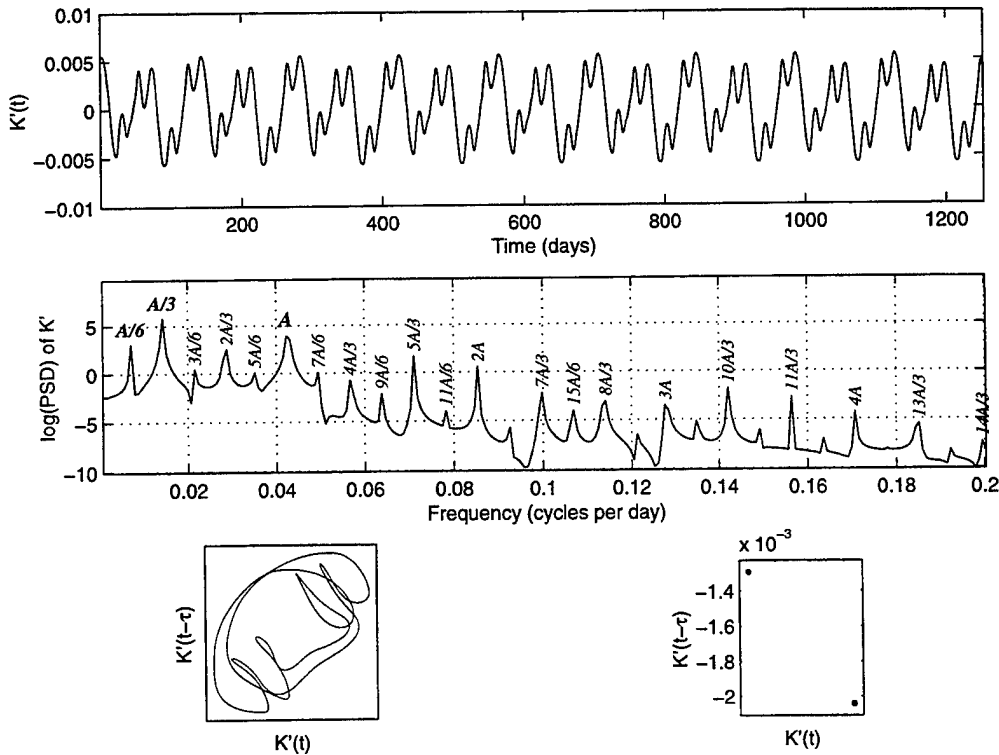
Figure 14: Time dependence of K' with $Ro = 2.83 \times 10^{-2}$, on branch 2. Top: time series; middle: power spectrum of time series (the zero frequency peak has been suppressed); bottom left: delay-space trajectory for the time series; bottom right: Poincaré section of the delay-space trajectory.

larger Ro has not been sufficiently investigated for conclusions to be drawn about the ultimate fate of this branch.

4.5 The path to chaos

The attractor corresponding to the first branch appears to go through several changes for Ro between about 2.75×10^{-2} and 2.90×10^{-2}. At $Ro = 2.79 \times 10^{-2}$ it was found that integrations started from initial conditions on branch one at lower Ro result in a trajectory which quickly leaves the branch one set and converges to the same branch two attractor which is obtained if initial conditions on branch two are used (see Figure 15).

It is tempting to conclude from Figure 15 that the attractor for branch one has become unstable for this Rossby number, leaving the branch two attractor as the only possible final state. However this explanation is less convincing in the light of the results shown in Figure 16 of a run at $Ro = 2.80 \times 10^{-2}$ started from an initial condition on branch one. Integrations started from branch two show convincingly that the second branch is an attracting limit cycle
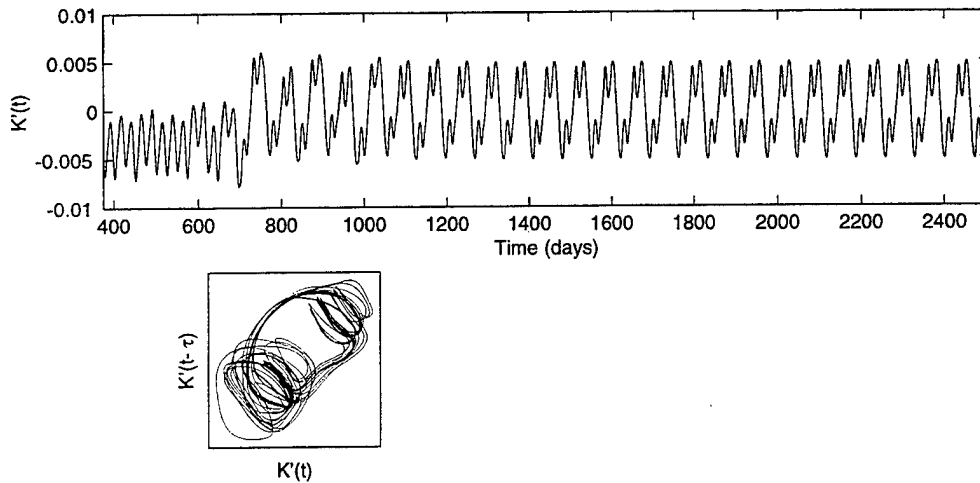
Figure 15: Time dependence of K' with $Ro = 2.79 \times 10^{-2}$ for an integration started from branch 1 initial conditions, but which results in a final state on branch 2. Top: time series; bottom : delay-space trajectory for the time series.

at this Rossby number, yet the trajectory shown in Figure 16 seems unable to converge to the second branch attractor. The trajectory remains mostly in the vicinity of the torus seen at lower Ro, but displays intermittent excursions on trajectories close to the branch two attractor. It is possible that the system would eventually settle on the branch two attractor, but there is no indication that this will happen from the time series of 5000 days shown Figure 16.

At $Ro = 2.85 \times 10^{-2}$, a run initialized on branch one appears to switch erratically between the two types of behavior (see Figure 17). The second branch was actually discovered by taking the ψ and ζ fields at a time when the trajectory was following type two behavior and using this as an initial condition for a run at lower Rossby number. The alternation between these two types of behavior is very intriguing and further numerical experiments at intermediate values of Ro are needed to understand it fully. It is possible that the original attractors have become joined by a heteroclinic orbit involving an unstable periodic orbit. In order to follow up this possibility it would be necessary to solve for the unstable periodic orbit which remains after the second Hopf bifurcation, and trace its location in phase space as Ro increases.

At larger Ro the trajectory appears to be less closely bound to either of the original attractors, perhaps indicating that they have both become more strongly unstable. At $Ro = 3.0 \times 10^{-2}$ the trajectory bears no obvious resemblance to either original attractor (see Figure 18). The power spectrum has become broad-band (a hallmark of chaos) but the peak at A can still be discerned. Runs at $Ro = 4.0 \times 10^{-2}$ and $Ro = 5.2 \times 10^{-2}$ were also chaotic, with broad-band power spectra.
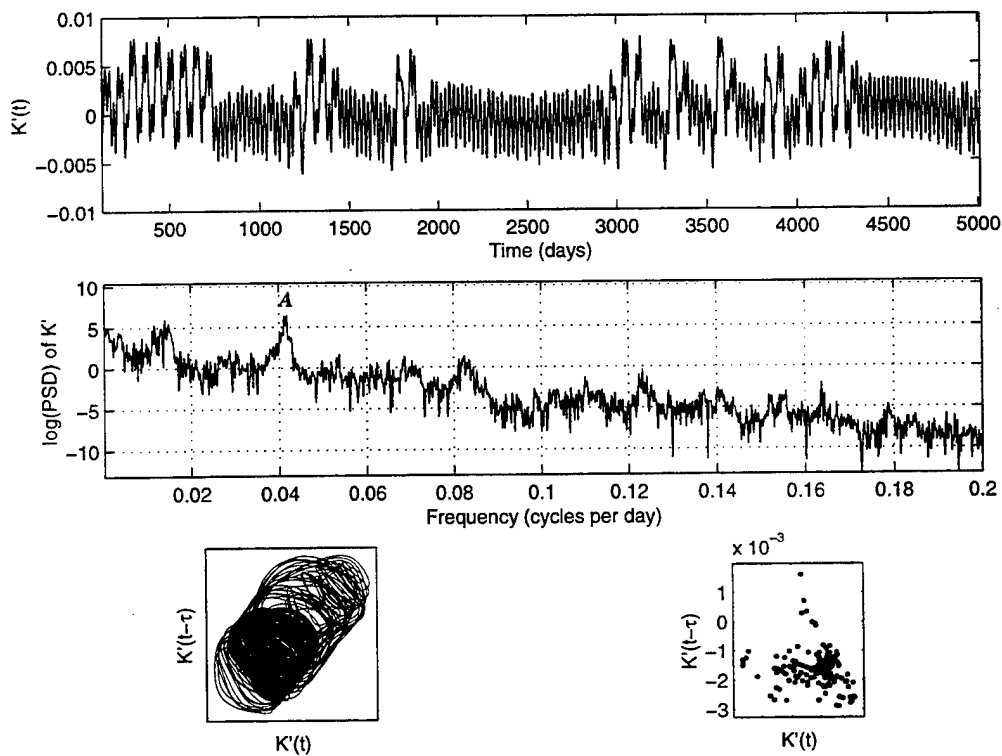
270

Figure 16: Time dependence of K' with $Ro = 2.80 \times 10^{-2}$ for an integration started from branch 1 initial conditions. Top: time series; middle: power spectrum of time series (the zero frequency peak has been suppressed); bottom left: delay-space trajectory for the time series; bottom right: Poincaré section of the delay-space trajectory.

Figure 17: Time dependence of K' with $Ro = 2.85 \times 10^{-2}$ for an integration started from branch 1 initial conditions. Top: time series; middle: power spectrum of time series (the zero frequency peak has been suppressed); bottom left: delay-space trajectory for the time series; bottom right: Poincaré section of the delay-space trajectory.
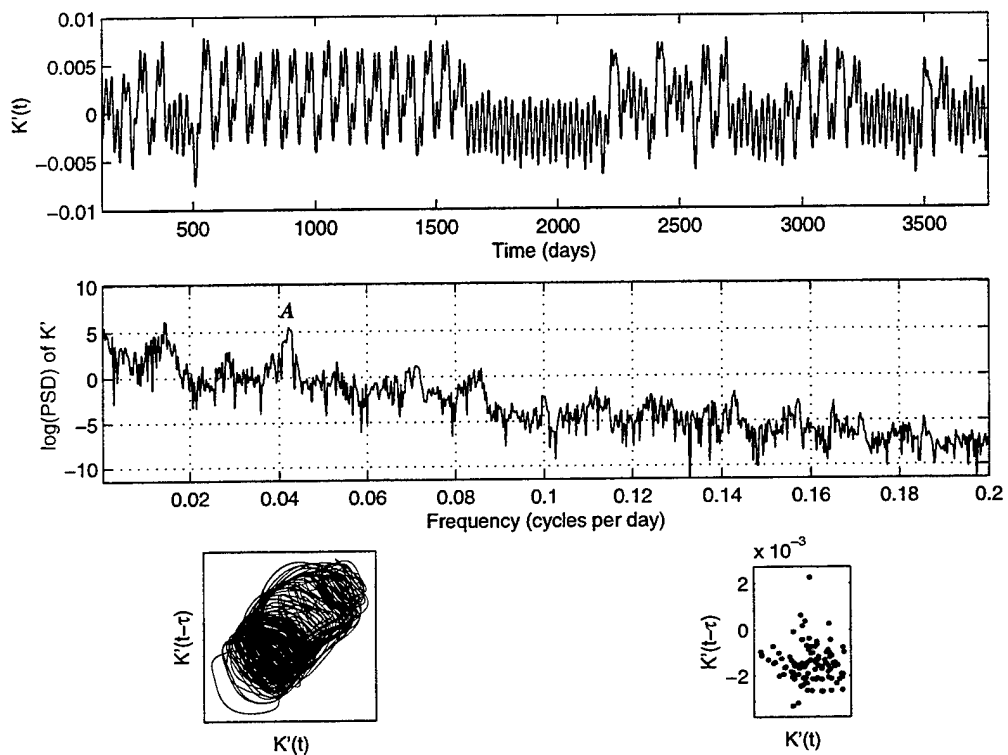
Figure 18: Time dependence of K' with $Ro = 3.0 \times 10^{-2}$ for an integration started from branch 1 initial conditions. Top: time series; middle: power spectrum of time series (the zero frequency peak has been suppressed); bottom left: delay-space trajectory for the time series; bottom right: Poincaré section of the delay-space trajectory.
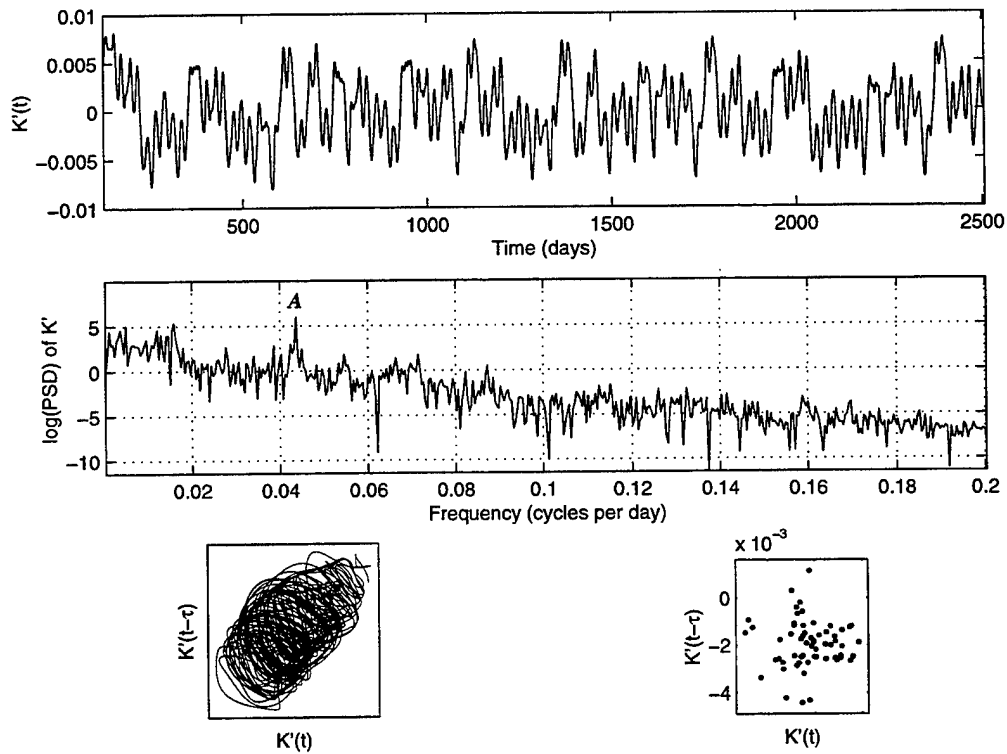
5 Conclusions

The numerical results reported here show that the sliced cone model can display a great richness of complicated behavior including multiple attracting states and a transition to chaos. These results are of particular interest because the model can be realized in the laboratory, allowing the study of low-dimensional chaos in a real physical system. In particular these results show that the transitions from a fixed point to a limit cycle and then to a torus take place via Hopf bifurcations. At larger Rossby number the behavior of the system becomes more complex. A second solution branch appears which coexists with the original branch at moderate Ro. As Ro increases the time series appear to become intermittent when started from the original branch, switching erratically between oscillations characteristic of each branch. These transitions become more frequent at larger Ro, until at $Ro \approx 2.9 \times 10^{-2}$ the delay space trajectory bears little resemblance to either branch and the behavior seems to be chaotic for all larger values of Ro.

6 Future work

There remain several interesting avenues for future study of this system. These include an elucidation of the mechanism by which the flow becomes chaotic (which could involve interaction with unstable periodic orbits or unstable fixed points), and the extent of the second branch as a function of Rossby number. Much longer time series are needed to better understand the chaotic dynamics above $Ro \approx 2.85 \times 10^{-2}$. A sufficiently long time series may show that the Poincaré map is a fractal set, and allow the fractal dimension of the chaotic attractor to be calculated. Longer time series could also clarify whether the erratic behavior seen for $2.80 \times 10^{-2} \leq Ro \leq 2.85 \times 10^{-2}$ is truly chaotic or a chaotic transient.

The behavior of the system as a function of E is yet to be studied using these techniques, and it would be interesting to discover more about the suppression of the anticyclonic instability as E is increased.

The insights provided by this numerical approach to the sliced cone also open up new lines of enquiry using the laboratory apparatus. It would be interesting to look in the laboratory for some of the features of the numerical results, such as the second branch and the intricate dependence of the flow behavior on Ro in the transition from a toroidal attractor to chaos. If time series could be obtained from the flow in the laboratory, the same delay-space techniques could be applied to laboratory data, allowing a detailed comparison with the numerical results. However this would be technically demanding, since the variations in velocity and pressure are very difficult to detect.

7 Acknowledgments

References

[Beardsley, 1975a] Beardsley, R. C. (1975a). A numerical investigation of a laboratory analogy of the wind-driven ocean circulation. In *NAS Symposium on Numerical Models of Ocean Circulation, Durham, New Hampshire, 1972*, page 311, Washington DC. National Academy of Sciences.

[Beardsley, 1975b] Beardsley, R. C. (1975b). The 'sliced-cylinder' laboratory model of the wind-driven ocean circulation, part 2: Oscillatory forcing and Rossby wave resonance. *J. Fluid. Mech.*, 69(1):41–64.

[Becker and Salmon, 1997] Becker, J. M. and Salmon, R. (1997). Eddy formation on a continental slope. *J. Mar. Res.*, 55:181–200.

[Bennetts and Hocking, 1973] Bennetts, D. A. and Hocking, L. M. (1973). On nonlinear Ekman and Stewartson layers in a rotating fluid. *Proc. R. Soc. Lond. A.*, 333:469–489.

[Berloff and Meacham, 1997] Berloff, P. S. and Meacham, S. P. (1997). The dynamics of an equivalent-barotropic model of the wind-driven circulation. *J. Mar. Res.*, 55(3):407–451.

[Griffiths and Veronis, 1997] Griffiths, R. W. and Veronis, G. (1997). A laboratory study of the effects of a sloping side boundary on wind-driven circulation in a homogeneous ocean model. *J. Mar. Res.*, 55:1103–1126.

[Griffiths and Veronis, 1998] Griffiths, R. W. and Veronis, G. (1998). Linear theory of the effect of a sloping boundary on circulation in a homogeneous laboratory model. *J. Mar. Res.*, 56:75–86.

[Israeli, 1970] Israeli, M. (1970). A fast implicit numerical method for time dependent viscous flows. *Studies Appl. Math.*, 49(4):327–349.

[Jiang et al., 1995] Jiang, S., Jin, F.-F., and Ghil, M. (1995). Multiple equilibria, periodic, and aperiodic solutions in a wind-driven, double-gyre, shallow-water model. *J. Phys. Oceanogr.*, 25:764–786.

[Kiss and Griffiths, 1998] Kiss, A. E. and Griffiths, R. W. (1998). Flow dynamics in the 'sliced cone' model of wind-driven ocean circulation. In Melbourne, W. H., editor, *13th Australasian fluid mechanics conference, Melbourne, Australia, 1998*, Victoria 3168, Australia. Monash University.

[Meacham and Berloff, 1997] Meacham, S. P. and Berloff, P. S. (1997). Barotropic, wind-driven circulation in a small basin. *J. Mar. Res.*, 55:523–563.

[Page, 1981] Page, M. A. (1981). *Rotating fluids at low Rossby number*. Phd thesis, University College, London.

[Page, 1982] Page, M. A. (1982). A numerical study of detached shear layers in a rotating sliced cylinder. *Geophys. Astrophys. Fluid Dyn.*, 22:51–69.

[Pearson, 1965] Pearson, C. E. (1965). A computational method for viscous flow problems. *J. Fluid Mech.*, 21(4):611–622.

[Pedlosky, 1987] Pedlosky, J. (1987). *Geophysical fluid dynamics.* Springer, New York, 2 edition.

[Pedlosky and Greenspan, 1967] Pedlosky, J. and Greenspan, H. P. (1967). A simple laboratory model for the oceanic circulation. *J. Fluid Mech.*, 27(2):291–304.

[Salmon, 1992] Salmon, R. (1992). A two-layer Gulf Stream over a continental slope. *J. Mar. Res.*, 50:341–365.

[Takens, 1981] Takens, F. (1981). *Dynamical systems and turbulence, Warwick 1980*, volume 898 of *Lecture notes in mathematics.* Springer-Verlag, Berlin.

Decadal Oscillations in the
Mid-Latitude Ocean-Atmosphere System

Blanca Gallego

1 Introduction

Climate variability at decadal time scales has been an emerging area of interest in recent years. Evidence reported in [1, 2, 3] suggests that the North Pacific ocean-atmosphere system exhibits variability of an oscillatory nature at the time scale of a few decades; it is hypothesized that the ocean-atmosphere coupling plays an important role in the generation of this decadal variability. Similar oscillatory modes have also been observed in the Atlantic [4]; however in this case the existence of a strong thermohaline circulation makes unclear the role of the wind-driven flow in the generation of the oscillations.

The North Pacific decadal oscillations have also been found in various coupled GCMs (Global Climate Models) (e.g. [5, 3]). The sea surface temperature anomalies 1) are large-scale, extending almost across the entire Pacific basin, and 2) have dipolar structure, with the positive and the negative anomalies flipping signs every half-period.

In this work, an idealized model for the large-scale, coupled dynamics of the mid-latitude wind-driven oceanic circulation and the atmosphere has been derived. In this model, the ocean and the atmosphere are coupled through wind stress and heat fluxes at the air-sea interface. The equations are based on global heat and global momentum balances, along the same lines as in [6]. However, the model is significantly simpler than in [6], and allows a good understanding of the physics involved. In particular, it is able to capture the sustained oscillations at decadal time scales, consistent with the above mentioned observations and numerical models.

2 The Model

The geometry of the model consists of an oceanic box with $0 < x < L_x$ as the zonal coordinate, $0 < y < L_y$ as the meridional coordinate and $-H < z < 0$ as the vertical coordinate. The atmospheric box representing the troposphere has the same meridional extent.

In what follows the heat and mechanical balances of the atmospheric and oceanic parts are considered, which lead to the set of equations that describe the model.

2.1 Oceanic Mechanical Balance: Potential Vorticity Equation

The quasi-geostrophic equivalent barotropic potential vorticity equation on a mid-latitude beta plane is considered. After integrating in z and neglecting the relative vorticity term (whose

contribution is small for large-scale motions), the ocean flow is governed by,

$$\frac{\partial\psi}{\partial t} - c\frac{\partial\psi}{\partial x} = \frac{R^2}{\rho_w H}\frac{\partial\tau_s}{\partial y} + c\delta\frac{\partial^2\psi}{\partial x^2}.\tag{1}$$

Here, ψ represents the depth averaged streamfunction, R is the deformation radius, $c = \beta R^2$ is the speed of the long Rossby waves, ρ_w is the sea-water density, τ_s represents the zonal component of the atmospheric surface wind stress and $\delta \ll L_x$ is the width of the western boundary layer.

Taking τ_s to be constant in x, $\tau_s = \bar{\tau}_s(y,t)$, where the overbar stands for zonal average, and imposing the boundary conditions $\psi = 0$ at $x = 0, L_x$, the solution of (1) can be expressed in the form:

$$\psi = \psi_I(x,y,t) - \psi_I(0,y,t)\exp(-x/\delta) + O(\delta).\tag{2}$$

Here, ψ_I is the depth-averaged streamfunction in the interior and is determined by the wind-stress curl through the relation,

$$\psi_I = \frac{R^2}{\rho_w H}\int_{t-\frac{L_x-x}{c}}^{t}\frac{\partial\bar{\tau}_s}{\partial y}dt'.\tag{3}$$

Therefore, the zonally averaged meridional velocity in the interior has the form:

$$\bar{v}_I = \frac{1}{L_x}\int_{\delta}^{L_x}\frac{\partial\psi_I}{\partial x}dx = -\frac{R^2}{L_x\rho_w H}\int_{t-\frac{L_x}{c}}^{t}\frac{\partial\bar{\tau}_s}{\partial y}dt'.\tag{4}$$

Note that $\bar{v}_I$ at a given time t, is fully determined by the wind stress curl at the times from $t-\frac{L_x}{c}$ to the actual time t, where $\frac{L_x}{c}$ represents the time that it takes a Rossby wave to cross the basin. This equation represents the baroclinic response of the ocean to an imposed wind-stress through propagation of Rossby waves from the eastern boundary. In this idealized formulation, the time that it takes the ocean to adjust to a given wind stress is given by the Rossby wave crossing time $\frac{L_x}{c}$ and is of the order of ten years. If the wind stress undergoes changes at shorter time scales, the ocean-atmosphere system finds itself in a dynamical situation in which the ocean is continuously trying to be in Sverdrup balance with the overlying wind. In doing so, Rossby waves are continuously being generated in the eastern boundary and moving westward carrying with them information about the wind that was blowing at the times they were formed. Therefore, this is the equation that contains the memory of the system.

The following section details how to determine this wind-stress curl, $\frac{\partial\bar{\tau}_s}{\partial y}$.

2.2 Atmospheric Momentum Balance: Zonal Momentum Equation

The natural way of representing large-scale, mid-latitude, atmospheric dynamics in a simple fashion, is to consider the modification by the baroclinic eddies of the mean zonal flow. Specifically, we consider the zonally averaged x-momentum equation, which for quasi-geostrophic motions on a mid-latitude beta plane is given by,

$$\frac{\partial\bar{u}}{\partial t} = f_o\bar{v} - \frac{\partial(\overline{u'v'})}{\partial y} + \frac{1}{\rho_a}\frac{\partial\bar{\tau}}{\partial z}.\tag{5}$$

The overbar stands for the zonal average and the prime stands for the departure from the average, f_o and ρ_a are the Coriolis parameter and atmospheric density respectively and the last term represents vertical transfer of zonal momentum by the stress, $\bar{\tau}$. Integrating over the vertical direction and assuming steady equilibrium, one finds:

$$-\int_0^\infty \rho_a \frac{\partial(\overline{u'v'})}{\partial y} dz = \bar{\tau}_s. \tag{6}$$

This equation represents the zonally and vertically averaged momentum budget for the atmosphere. The zonally averaged wind stress is balanced by the horizontal convergence of momentum flux by the eddies in the entire troposphere.

Using the definition of quasi-geostrophic potential vorticity,

$$q = f_o + \beta y + v_x - u_y + \frac{f_o}{\rho_a}\frac{\partial}{\partial z}\left(\frac{\rho_a}{S}\theta\right) \tag{7}$$

where q and θ represent potential vorticity and potential temperature respectively and S is the static stability of the atmosphere which is taken to be constant for simplicity, it is possible to relate the zonally averaged eddy fluxes of momentum, heat and potential vorticity. The relation between these three fluxes is given by,

$$\rho_a(\overline{q'v'}) = \nabla \cdot \vec{F}_{E-P} = -\frac{\partial\left(\rho_a(\overline{u'v'})\right)}{\partial y} + f_o\frac{\partial}{\partial z}\left(\frac{\rho_a}{S}(\overline{\theta'v'})\right), \tag{8}$$

where $\vec{F}_{E-P}$ is the Eliassen-Palm flux. This relation allows the wind stress curl to be expressed in terms of θ and q, which, unlike the momentum u, are conserved following the particle trajectories. This is a desired property when considering the parameterization of eddy fluxes.

2.2.1 Parameterization of Eddy Fluxes

The classical way of parameterizing eddy fluxes uses an analogy with molecular diffusion, considering them proportional to the mean gradients. Thus, the eddy flux divergence is parameterized as:

$$\frac{\partial(\overline{q'v'})}{\partial y} = -k\frac{\partial^2\bar{q}}{\partial y^2} \tag{9}$$

$$\frac{\partial(\overline{\theta'v'})}{\partial y} = -k\frac{\partial^2\bar{\theta}}{\partial y^2} \tag{10}$$

where the parameter k represents the eddy diffusivity, i.e. the rate of change of mean square displacement of $\bar{\theta}$ and $\bar{q}$ by baroclinic eddies. In the present model this parameterization is simplified by considering relaxation to the planetary average, that is,

$$\frac{\partial(\overline{q'v'})}{\partial y} = \nu(\bar{q} - \bar{q}_A) \tag{11}$$

$$\frac{\partial(\overline{\theta'v'})}{\partial y} = \nu(\bar{\theta} - \bar{\theta}_A). \tag{12}$$

The subscript "A" stands for the meridional average and ν is the eddy relaxation rate. Following [7] and having in mind the fact that eddy activity is higher near the surface, ν is taken of the form: $\nu = \nu_o \exp(-z/d)$. For the purpose of the present work, this parameterization is qualitatively similar to the classical diffusion analogy, while being simpler.

Because large scales are the focus of this work, relative vorticity is neglected compared to planetary vorticity and vortex stretching, similarly as in the ocean momentum budget.

Finally, considering the change with height of the atmospheric density $\rho_a = \rho_o \exp(-z/D)$, and defining the effective eddy scale-height: $\frac{1}{d_e} = \frac{1}{D} + \frac{1}{d}$, the equation for the wind-stress curl is given by:

$$\frac{\partial \bar{\tau}_s}{\partial y} = d_e \rho_o \nu_o \left(\beta(y - \frac{L_y}{2}) + \frac{f_o}{Sd}(\bar{\theta}_s - \bar{\theta}_{sA}) \right). \tag{13}$$

The boundary conditions are no net wind stress: $\int_0^{L_y} \bar{\tau}_s = 0$, in addition to $\bar{\tau}_s = 0$ at $y = 0, L_y$. The requirement of no net wind stress determines the constant d. The wind stress curl as expressed in the previous equation depends on the zonally average surface potential temperature $\bar{\theta}_s$. Finding an expression for this variable is, therefore, the next step in the derivation of the model.

2.3 Atmospheric Heat Balance: Potential Temperature Equation

The zonally averaged thermodynamic energy equation for the atmosphere is:

$$\frac{\partial \bar{\theta}}{\partial t} = -\frac{1}{\rho_a} \frac{\partial (\rho_a \overline{\theta w})}{\partial z} - \frac{\partial (\overline{\theta' v'})}{\partial y} + \frac{1}{C_{pa} \rho_a} \frac{\partial \bar{Q}}{\partial z} \tag{14}$$

where C_{pa} represents specific heat and $\bar{Q}$ is the diabatic heat flux. Since the typical time scales of atmospheric potential temperature changes, in response to variations in the sea surface temperature, are of the order of weeks, and therefore, much shorter than the typical time scales of evolution of the latter (of the order of years), it is reasonable to neglect the time derivative of $\bar{\theta}$ and assume that the atmosphere adjusts instantaneously to the ocean. Integrating vertically, the remaining equation gives a balance between the horizontal heat flux divergence by eddies in the troposphere and the net diabatic heat fluxes at the vertical boundaries, that is,

$$C_{pa} \int_0^{\infty} \rho_a \frac{\partial (\overline{\theta' v'})}{\partial y} dz = F - r\lambda(\bar{\theta}_s - \bar{T}_s). \tag{15}$$

Here F represents the net radiative incoming flux at the top of the atmosphere and it is given by the difference between the net incoming solar radiation, F_{SOLAR} and the outgoing long-wave radiation, $F_{LONG-WAVE}$. The first one is a prescribed function of latitude chosen to be,

$$F_{SOLAR} = F_o + \tilde{F}_1(y) = F_o + F_1 cos(\frac{\pi y}{L_y}), \tag{16}$$

the latter is estimated by linearizing the gray Stefan-Boltzmann law and is given by,

$$F_{LONG-WAVE} = A + B\bar{\theta}_s. \tag{17}$$

The second term of the right hand side of (15) denotes the exchange of heat flux at the air-sea interface. It is a typical bulk formulae equation which represents relaxation to the zonally averaged sea surface temperature $\bar{T}_s$ with λ being the bulk transfer coefficient and r being the fraction of the earth's surface that is covered by oceans.

Using the eddy flux parameterization in (12), the final expression for the zonally averaged atmospheric potential temperature is,

$$(\bar{\theta}_s - \bar{\theta}_{sA}) = (1 - a)\left((\bar{T}_s - \bar{\theta}_{sA}) + \frac{\tilde{F}_1}{r\lambda}\right) \tag{18}$$

where $0 < a < 1$, is given by $a = 1 - \frac{r\lambda}{C_{pa}\nu_o\rho_o d_e + B + r\lambda}$ and contains the contribution from the baroclinic eddies.

The next and final step needed to close the system is to find an expression for the sea surface temperature as a function of the known variables.

2.4 Oceanic Heat Balance: Upper Ocean Heat Content Equation

It is assumed, for simplicity, that the temperature T of the model oceanic layer is independent of depth ($T = T_s$). The vertically integrated heat balance equation is:

$$\frac{\partial T}{\partial t} + \frac{\partial(uT)}{\partial x} + \frac{\partial(vT)}{\partial y} = \frac{\lambda}{C_{pw}\rho_w H}(\bar{\theta}_s - T) + \epsilon\nabla^2_h T. \tag{19}$$

Where ϵ is the heat diffusivity coefficient and (u, v) is now the oceanic wind-driven velocity. Note that, except from the western boundary layer balance, this is the only equation where a viscous or diffusive term has been introduced explicitly. In the absence of this term, the warm waters that are transported poleward by the subtropical gyre and the cold waters that are transported equatorward by the subpolar gyre would meet somewhere in the middle forming a discontinuous front. Therefore, this term, represents the only way of direct communication between the gyres which in the present formulation mostly "feel" each other through the atmosphere.

Since the atmospheric model only "sees" the zonally averaged oceanic temperature, the natural way to proceed is to separate T into its zonally averaged part, $\bar{T}$ and its departure from the average, T'. The upper ocean heat content (19) can then be split into the two equations:

$$\frac{\partial \tilde{T}}{\partial t} + \frac{\partial(\overline{vT'})}{\partial y} = \frac{\lambda}{C_{pw}\rho_w H}(-a\tilde{T} + \frac{\tilde{F}(1-a)}{r\lambda}) + \epsilon\frac{\partial^2 \tilde{T}}{\partial y^2} \tag{20}$$

$$\frac{\partial T'}{\partial t} + u\frac{\partial T'}{\partial x} + v\frac{\partial T'}{\partial y} + v\frac{\partial \tilde{T}}{\partial y} - \frac{\partial(\overline{vT'})}{\partial y} = -\frac{\lambda}{C_{pw}\rho_w H}T' + \epsilon\frac{\partial^2 T'}{\partial y^2}. \tag{21}$$

Here (18) has been used to write $\bar{\theta}_s$ as a function of $\bar{T}$, and a new variable $\tilde{T}$ has been introduced for convenience. It represents the zonally averaged oceanic temperature after removing the

281

meridionally averaged value of the atmospheric surface potential temperature, so that $\tilde{T} = \bar{T} - \bar{\theta}_{sA}$.

The first thing to notice is that the relaxation rate for $\tilde{T}$ is smaller than that for T' by the factor $a(<1)$. This is because the atmospheric potential temperature depends on $\tilde{T}$ not on T'. Therefore, on the time scales over which $\tilde{T}$ changes, T' rapidly reaches equilibrium. The next step is to look for an expression that diagnostically relates T' to $\tilde{T}$. In the limit $\frac{v}{L_y} << \frac{\lambda}{C_{pa}\rho_w H}$, the term $v\frac{\partial \tilde{T}}{\partial y}$ balances the relaxation term $\frac{-\lambda}{C_{pw}\rho_w H}T'$. This approximation is not strictly valid in the range of parameters used later, however it is qualitatively correct.

This diagnostic relation allows to express the advective term in the $\tilde{T}$ equation in the following way,

$$\frac{\partial(\overline{vT'})}{\partial y} = -\frac{C_{pw}\rho_w H}{\lambda}\frac{\partial}{\partial y}(\overline{v^2}\frac{\partial \tilde{T}}{\partial y}) \tag{22}$$

so that the effect of meridional advection by the gyres on the zonally averaged temperature is down mean gradient temperature diffusivity proportional to $\overline{v^2}$.

Moreover, it can be shown that the largest contribution to $\overline{v^2}$ comes from the western boundary layer velocity, v_{BL}, so that at first order in δ, $\overline{v^2}$ can be expressed as,

$$\overline{v^2} = \frac{1}{L_x}\int_0^{L_x} dx(v_I{}^2 + v_{BL}{}^2 + 2v_I v_{BL}) \simeq \overline{v_{BL}^2} \simeq \frac{\bar{v}_I^2 L_x}{2\delta}. \tag{23}$$

The final expression for the evolution of the oceanic temperature is,

$$\frac{\partial \tilde{T}}{\partial t} - \frac{C_{pw}\rho_w H}{\lambda \Delta}\frac{\partial}{\partial y}(\bar{v}_I^2 \frac{\partial \tilde{T}}{\partial y}) = \frac{\lambda}{C_{pw}\rho_w H}\left(-a\tilde{T} + \frac{\tilde{F}_1(1-a)}{r\lambda}\right) + \epsilon\frac{\partial^2 \tilde{T}}{\partial y^2} \tag{24}$$

with boundary conditions of no normal heat flux, $\frac{\partial \tilde{T}}{\partial y} = 0$ at $y = 0, L_y$. Here $\Delta = \frac{2\delta}{L_x}$.

This last equation, together with (4), (13) and (18) compose the closed set of equations of the model.

2.5 Final set of equations

In order to simplify the notation, the following redefinition of variables will be used from here on: $T = \tilde{T}$, $\theta = \bar{\theta}_s - \bar{\theta}_{sA}$, $\tau = \bar{\tau}_s$, and $v = \bar{v}_I$. The system of equations is non-dimensionalized using,

$$y = L_y y^* \tag{25}$$

$$t = \alpha^{-1}t^* \quad (\alpha = \frac{\lambda}{C_{pa}\rho_w H}) \tag{26}$$

$$(\theta, T) = \frac{F_1}{r\lambda}(\theta^*, T^*) \tag{27}$$

$$v = \frac{d_e\rho_o\nu_o L_y}{\rho_w H}v^* \tag{28}$$

$$\tau = d_e\rho_o\nu_o\beta L_y{}^2\tau^*. \tag{29}$$

The set of equations in their non-dimensional form are given by,

$$\theta = (1-a)[T + f(y)] \tag{30}$$

$$\frac{\partial \tau}{\partial y} = y - \frac{1}{2} + \gamma\theta \tag{31}$$

$$v = -\frac{1}{t_o}\int_{t-t_o}^{t} \frac{\partial \tau}{\partial y}dt' \tag{32}$$

$$\frac{\partial T}{\partial t} - \mu\frac{\partial}{\partial y}(v^2\frac{\partial T}{\partial y}) = -aT + (1-a)f(y) + \sigma\frac{\partial^2 T}{\partial y^2} \tag{33}$$

where

$$f(y) = cos(\pi y) \tag{34}$$

$$\gamma = \frac{f_o}{Sd}\frac{F_1}{r\lambda\beta L_y} \tag{35}$$

$$\mu = (\frac{d_e\rho_o\nu_o}{\rho_w H\alpha})^2\frac{1}{\Delta} \tag{36}$$

$$\sigma = \frac{\epsilon}{\alpha(L_y)^2}, \tag{37}$$

$$t_o = \frac{L_x}{c}\alpha \tag{38}$$

where t_o is the non-dimensional delay time given by the ratio of the Rossby wave crossing time and the oceanic temperature decay time, and the asterisks have been dropped.

Combining (30), (31) and (32) into a single equation for the velocity v as a function of the temperature T, one finds,

$$v = -(y - \frac{1}{2}) - \gamma(1-a)f(y) - \gamma(1-a)\frac{1}{t_o}\int_{t-t_o}^{t} T(y,t')dt'. \tag{39}$$

This relation, given v at $t = 0$, can also be expressed as:

$$\frac{\partial v}{\partial t} = -\gamma(1-a)\left(T(y,t) - T(y,t-t_o)\right) \tag{40}$$

The final model set of equations is reduced to the equations (33) and (39). The advantages of this formulation are:

- Simplicity (only one dimension in space, and only two dependent variables, v and T)
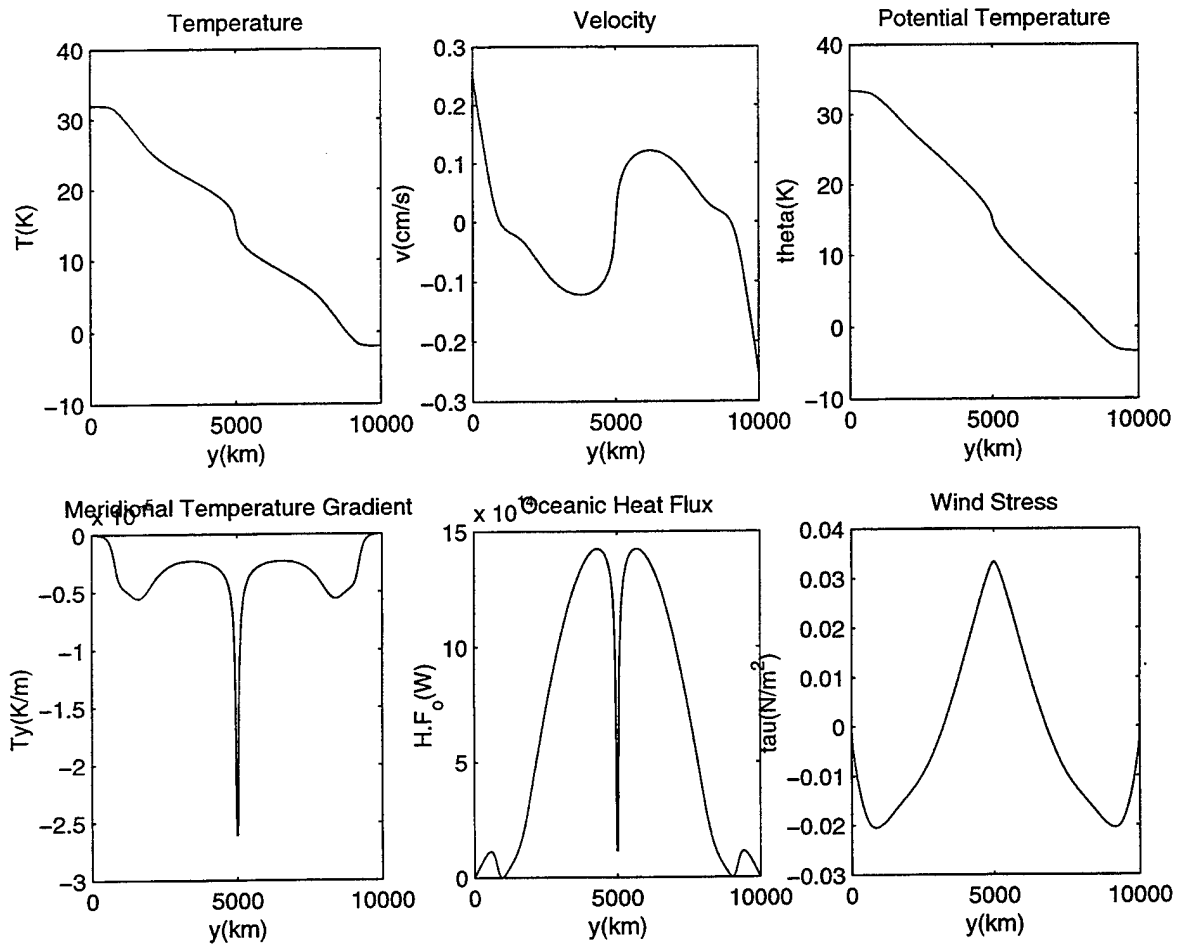
- No need to resolve the boundary layer explicitly

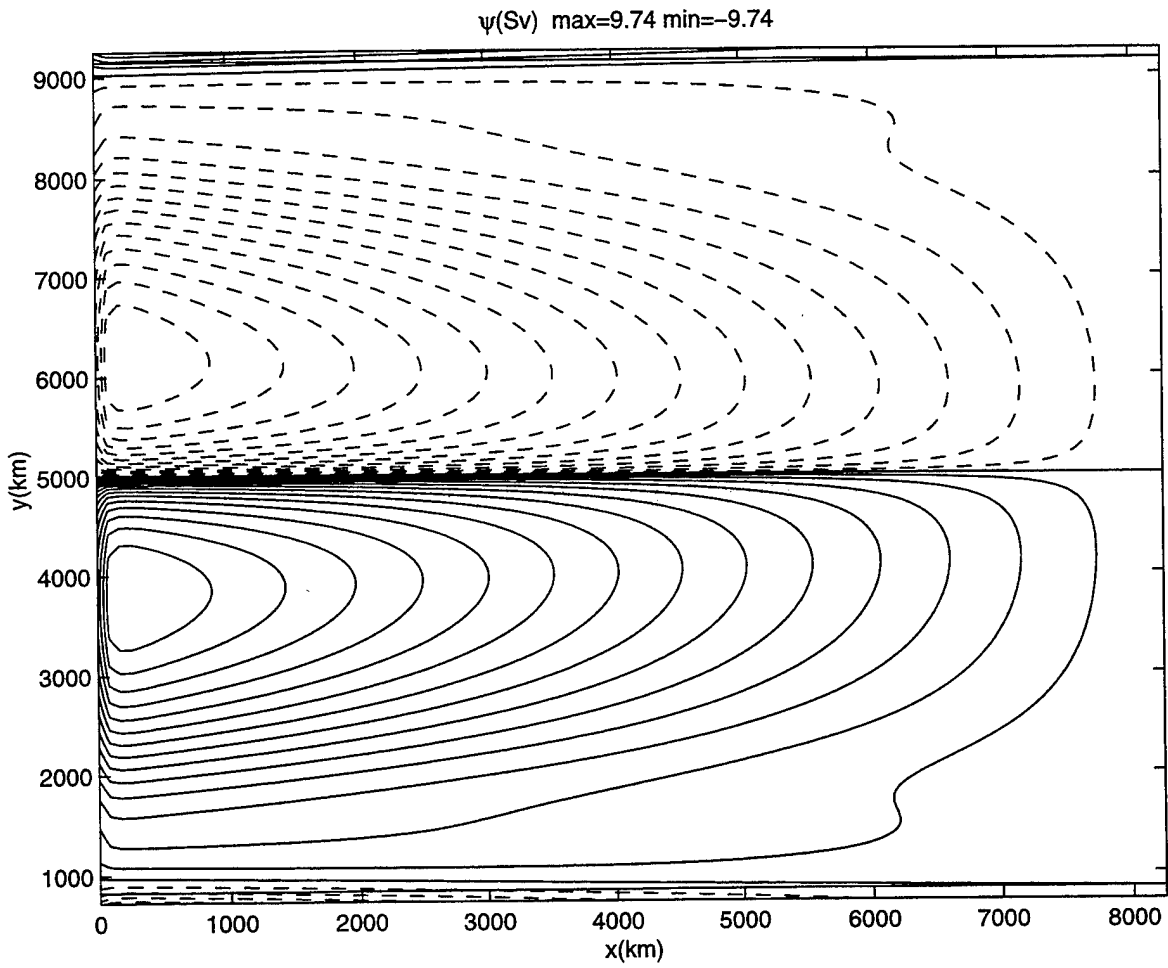Figure 1: Latitudinal dependence of various physical magnitudes at a given time

ψ(Sv) max=9.74 min=−9.74

Figure 2: Streamfunction at a given time

285

$L_x = 0.825 \times 10^7 m$	$\rho_o = 1.25\text{kg } m^{-3}$	$A = 200W m^{-2}$	$S = 5 \times 10^{-3} \ K \ m^{-1}$
$L_y = 10^7 m$	$\rho_w = 1000\text{kg } m^{-3}$	$B = 2.475W m^{-2} K^{-1}$	$\beta = 2 \times 10^{-11} m^{-1} s^{-1}$
$H = 10^3 m$	$C_{pa} = 1000 J K^{-1} \text{kg}^{-1}$	$F_1 = 125W m^{-2}$	$f_o = 10^{-4} s^{-1}$
$\Delta = 0.015$	$C_{pw} = 4000 J K^{-1} \text{kg}^{-1}$	$\lambda = 23W m^{-2} K^{-1}$	$R = 2.8 \times 10^4 m$
$D = 10^4 \ m$	$\nu_o = 10^{-6} s^{-1}$	$r = 0.3$	$\sigma = 3 \times 10^{-3}$

Table 1: Parameter values

3 Results and Discussion

The system of equations presented in the previous section is solved numerically using Crank-Nicholson scheme for the integration of the temperature equation, centered differential scheme for the spatial derivatives and the trapezoidal rule to solve the integral in time for the velocity equation. At each time step, $t + dt$, the knowledge of the temperature field at times from $t - t_o$ to t is required. The radiative equilibrium temperature is used as the initial guess and it is assumed that the previous history of the temperature field, when unknown, is constant in time and equal to the initial condition.

A Hopf bifurcation is found when moving in the parameter space increasing the importance of the non linearity with respect to the diffusivity. This corresponds to an increase in the ratio $\frac{\mu}{\sigma}$ in (33). The results presented below have been obtained at a point in the parameter space near the bifurcation point and inside the region of sustained oscillations.

A list of the parameter values used in this calculation is presented in table 1.

Figure 1 shows a snapshot of the oceanic temperature and its meridional gradient,of the wind-driven oceanic velocity and of the oceanic heat flux, as well as the atmospheric potential temperature and wind stress fields as a function of latitude for a given time. They all have realistic values, although the equator to pole oceanic temperature difference, the oceanic velocity and the wind stress are weaker than observed. A contour plot of the corresponding oceanic streamfunction is presented in figure 2. Note that in this figure (and from here on), the displayed meridional extent is the central region between the two minima of wind stress, where the subpolar and subtropical gyres are enclosed.

3.1 The oscillations

The evolution of the oceanic temperature and velocity fields during about 3/2 of an oscillation period is presented in figure 3. Their corresponding anomalies are shown in figure 4. The basic features of the oscillations are:

- They are decadal oscillations with a period of about 40 years (slightly more than twice the delay time (17 years)).

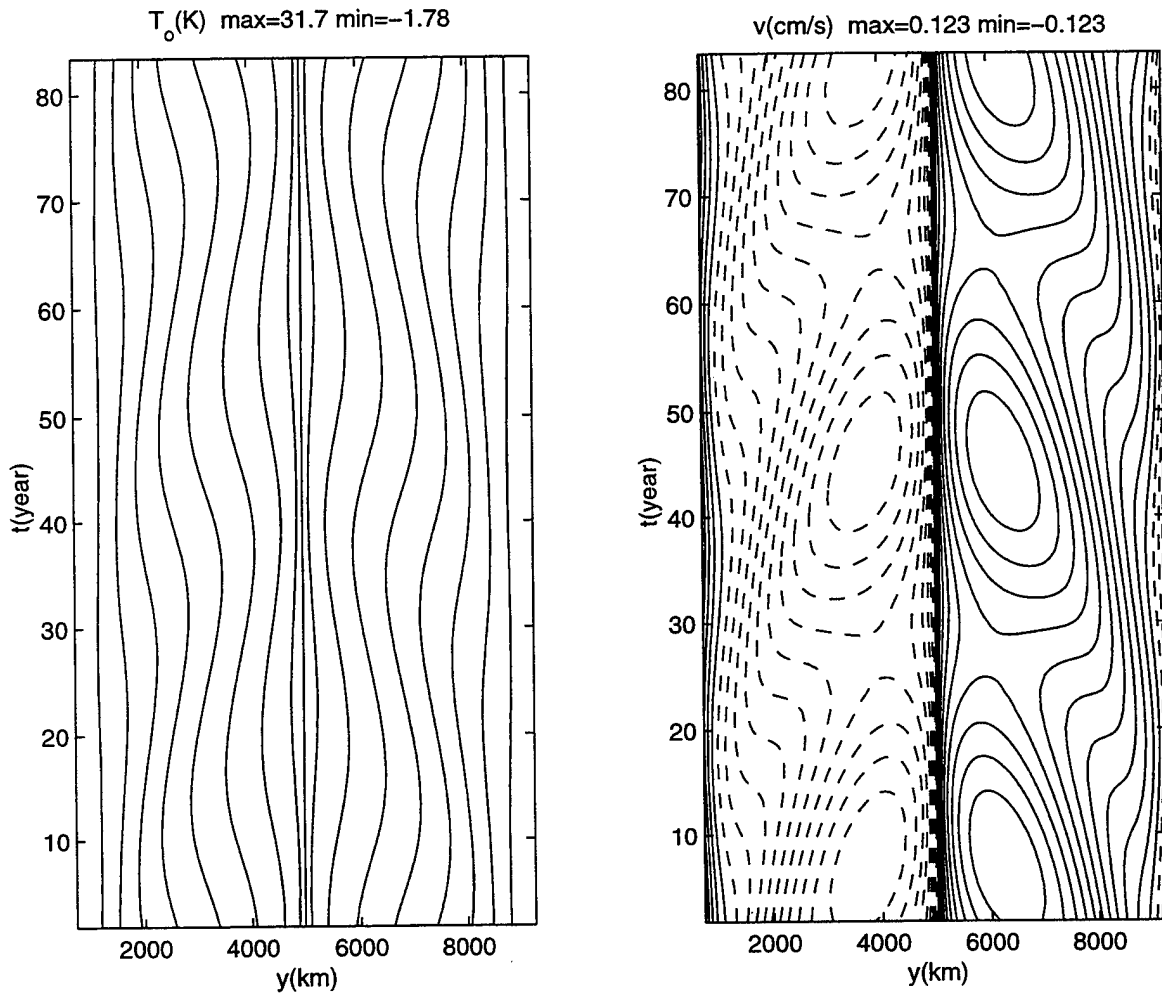- They are large-scale, extending over most of the basin.

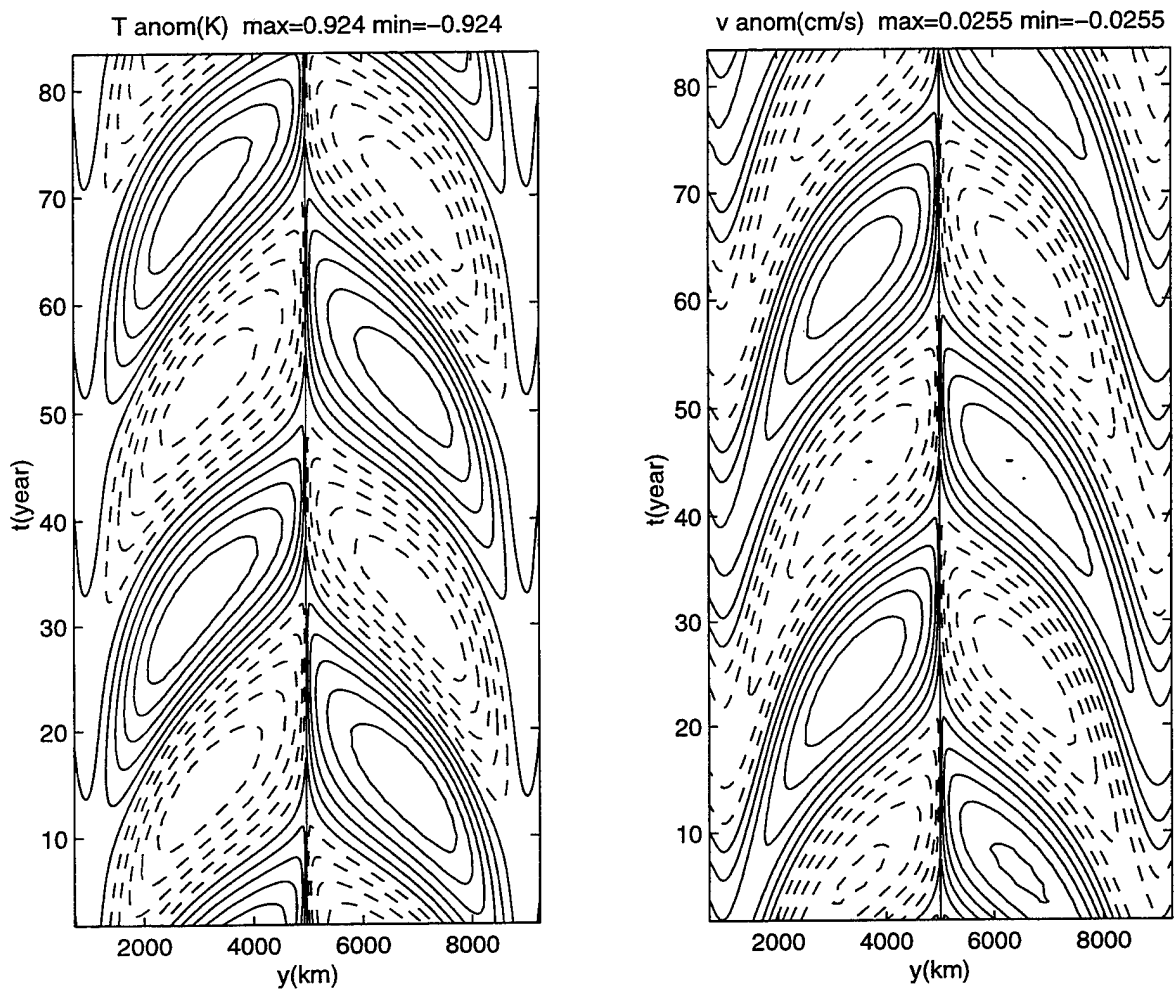Figure 3: Time evolution of oceanic temperature and velocity

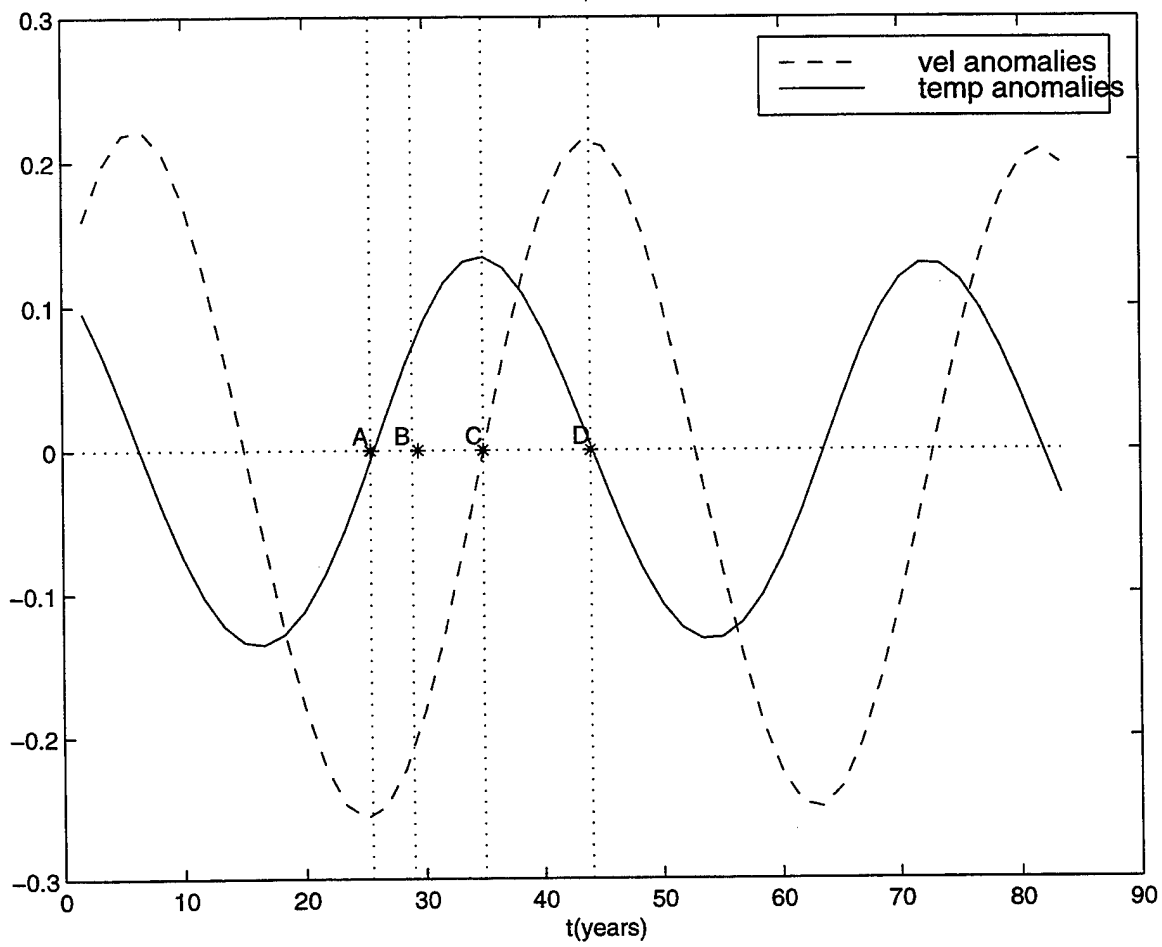Figure 4: Time evolution of oceanic temperature and velocity anomalies

Figure 5: Time evolution of normalized oceanic temperature and velocity anomalies at latitude $y = 3500km$
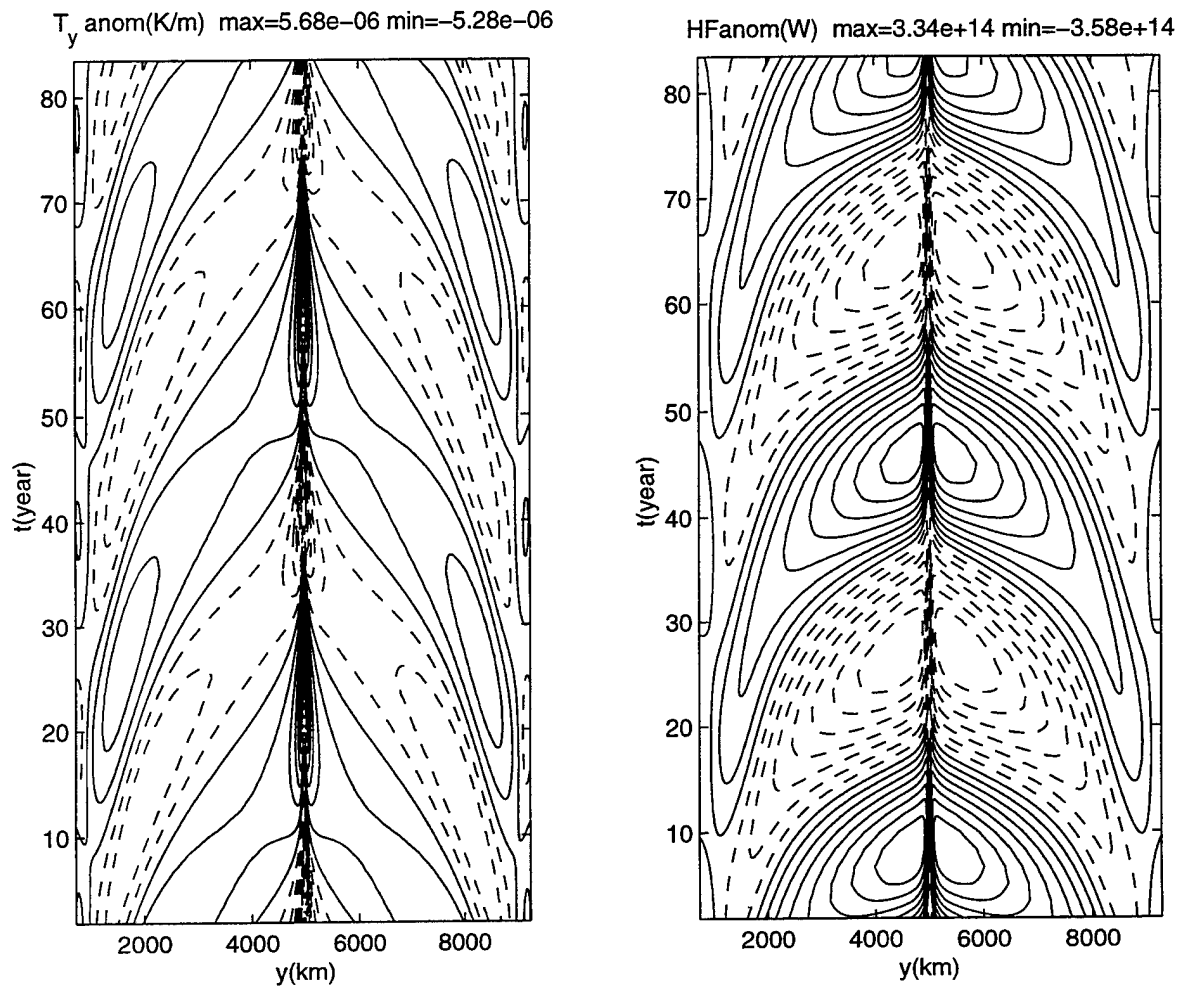
Figure 6: Time evolution of oceanic meridional temperature gradient and heat flux anomalies

- They are small in amplitude, with a root meansquare variance of about 1% in the oceanic temperature and about 10% in the oceanic velocity.

- They are characterized by temperature anomalies, which are antisymmetric about the zero wind stress curl line, and which flip signs in each phase of the oscillation.

- The oceanic temperature and velocity fields are 90 degrees out of phase.

Figure 5 shows the time evolution of the temperature and the velocity anomalies (normalized by their mean values), at a fixed latitude ($y = 3500km$) in the subtropical gyre. Consider the point in time in which there are no temperature anomalies and the circulation in the gyres is weakest. This corresponds to point A in figure 5. As time goes on, the subtropical gyre becomes warmer while the subpolar gyre becomes colder,(point B in figure 5). As a consequence, the meridional temperature gradient is reinforced, which causes an increase in the wind-stress curl. If the ocean responded instantaneously, the resulting stronger circulation in the gyres would advect temperature opposing to the temperature gradient anomaly until equilibrium is reached. However, in the presence of a lag time, the velocity in the gyres depends not only on the actual, increased wind-stress but also on the wind-stress which was forcing the ocean in the past 17 years. At that time, there was a negative temperature anomaly in the subtropical gyre and a positive one in the subpolar gyre and therefore a reduced wind-stress curl. The reduced velocity allows the temperature anomaly to grow until about 10 years later, when the effect of the increased temperature spins up the gyre. Thus, it is not until some years, that the oceanic circulation anomaly starts changing sign in response to the variations in temperature (point C in figure 5). As the circulation becomes stronger, it begins to reduce the temperature anomaly and eventually changes its sign. Then, the second phase of the oscillation starts, (point D in figure 5).

Note that the storage term in the oceanic temperature equation plays an important role. In its absence an initial perturbation in meridional distribution of oceanic temperature would be "instantaneously" damped through heat transport and fluxes at the air-sea interface, arresting the oscillations. Also note that this would not be the case if, in the delay equation (40), the temperature modes at time ($t - t_o$) had a larger amplitude than those at time t.

The evolution of the oceanic meridional temperature gradient and of the oceanic heat flux anomalies are shown in figure 6.

4 Conclusions and Future Work

- An idealized model for the coupled large-scale dynamics of the midlatitude atmosphere and the wind-driven ocean circulation has been derived.

- In this model, the ocean and the atmosphere are coupled through wind stress and heat fluxes at the air-sea interface.

- The formulation can be reduced to two equations. One describes the time evolution of the oceanic temperature and the other represents the transient oceanic velocity response to the wind-stress curl.

- Sustained oscillations at decadal time scales have been found which resemble those found in the observations and in the results of more comprehensive numerical models. They have small amplitude and large-scale meridional extent.

- These oscillations owe their existence to the time lagged response of the ocean to changes in the wind stress curl associated with Rossby wave propagation. An adjustment time of the oceanic temperatures to changes in the circulation is also required.

Areas of future work could include:

- Further exploration of the parameter space.

- Analysis of the solutions in comparison with observations as well as with results from coupled GCMs.

- Addition of an asymmetric component in the radiative forcing. Can we obtain chaotic behavior?.

- Multiple equilibria?. Equations (33) and (39) can be simplified further by considering the spatial extension in Fourier series of T and v and retaining only the mode that is directly forced by radiation. As a result, the system is reduced to two ordinary differential equations in time. A calculation of the steady states of this system for different parameter values led to multiple equilibria for sufficiently small values of Δ, i.e. for the case of a narrow western boundary layer. An exploration of the possible existence and causes of multiple equilibria in the non-truncated system could be a next step.

- Teleconnections. The mechanisms by which the ocean basins communicate with each other through the atmosphere are still not well understood. The model presented here can be expanded to represent two ocean basins (which would have different delay times) so that it can be used to explored these mechanisms.

5   Acknowledgments

References

[1] Kevin Trenberth and James Hurrell, "Decadal Atmosphere-Ocean Variations in the Pacific,", *Climate Dynamics*, (1994) 9:303–319.

[2] N. E. Graham, "Decadal-Scale Climate Variability in the 1970s and 1980s", *Climate Dynamics*, (1994) 10:135–162.

[3] M. Latif and T. P. Barnett, "Decadal Climate Variability over the North Pacific and North America: Dynamics and Predictability", *Journal of Climate*, Vol. 9, No. 10, October 1996.

[4] T. Delworth, S. Manabe and R. J. Stouffer, "Interdecadal Variations of the Thermohaline Circulation in a Coupled Ocean-Atmosphere Model", *Journal of Climate*, (1993) 6:1993–2011.

[5] M. Latif and T. P. Barnett, "Causes of Decadal Climate Variability over the North Pacific and North America", *Science*, Vol. 266, October 1994.

[6] Paola Cessi, "Thermal Feedback on Wind-Stress as a Contributing Cause of CLimate Variability", submitted to *Journal of Climate*.

[7] J. S. A. Green, "Transfer properties of the Large Scale Eddies and the General Circulation of the Atmosphere", *Quart. J. R. Met. Soc.,*, 96:157–185

University of California, San Diego
SIO Library 0175C
9500 Gilman Drive
La Jolla, CA 92093-0175

Hancock Library of Biology & Oceanography
Alan Hancock Laboratory
University of Southern California
University Park
Los Angeles, CA 90089-0371

Gifts & Exchanges
Library
Bedford Institute of Oceanography
P.O. Box 1006
Dartmouth, NS, B2Y 4A2, CANADA

NOAA/EDIS Miami Library Center
4301 Rickenbacker Causeway
Miami, FL 33149

Research Library
U.S. Army Corps of Engineers
Waterways Experiment Station
3909 Halls Ferry Road
Vicksburg, MS 39180-6199

Marine Resources Information Center
Building E38-320
MIT
Cambridge, MA 02139

Library
Lamont-Doherty Geological Observatory
Columbia University
Palisades, NY 10964

Library
Serials Department
Oregon State University
Corvallis, OR 97331

Pell Marine Science Library
University of Rhode Island
Narragansett Bay Campus
Narragansett, RI 02882

Working Collection
Texas A&M University
Dept. of Oceanography
College Station, TX 77843

Fisheries-Oceanography Library
151 Oceanography Teaching Bldg.
University of Washington
Seattle, WA 98195

Library
R.S.M.A.S.
University of Miami
4600 Rickenbacker Causeway
Miami, FL 33149

Maury Oceanographic Library
Naval Oceanographic Office
Building 1003 South
1002 Balch Blvd.
Stennis Space Center, MS, 39522-5001

Library
Institute of Ocean Sciences
P.O. Box 6000
Sidney, B.C. V8L 4B2
CANADA

National Oceanographic Library
Southampton Oceanography Centre
European Way
Southampton SO14 3ZH
UK

The Librarian
CSIRO Marine Laboratories
G.P.O. Box 1538
Hobart, Tasmania
AUSTRALIA 7001

Library
Proudman Oceanographic Laboratory
Bidston Observatory
Birkenhead
Merseyside L43 7 RA
UNITED KINGDOM

IFREMER
Centre de Brest
Service Documentation - Publications
BP 70 29280 PLOUZANE
FRANCE

50272-101

REPORT DOCUMENTATION PAGE	1. REPORT NO. WHOI-99-01	2.	3. Recipient's Accession No.

4. Title and Subtitle

Astrophysical and Geophysical Flows as Dynamical Systems; 1998 Summer Study Program in Geophysical Fluid Dynamics

5. Report Date
January 1999

6.

7. Author(s) Neil J. Balmforth, Director

8. Performing Organization Rept. No.
WHOI-99-01

9. Performing Organization Name and Address

Woods Hole Oceanographic Institution
Woods Hole, Massachusetts 02543

10. Project/Task/Work Unit No.

11. Contract(C) or Grant(G) No.

(C) N00014-97-1-0934

(G) OCE-9314484

12. Sponsoring Organization Name and Address

National Science Foundation
Office of Naval Research

13. Type of Report & Period Covered
Technical Report

14.

15. Supplementary Notes

This report should be cited as: Woods Hole Oceanog. Inst. Tech. Rept., WHOI-99-01.

16. Abstract (Limit: 200 words)

The theme of the 1998 Goephysical Fluid Dynamics (GFD) Summer Program at the Woods Hole Oceanographic Institution was Astrophysical and Geophysical Flows as Dynamical Systems. Antonello Provenzale of the Institute of Cosmogeophysics in Italy was the principal lecturer for the summer, and Charles Tresser of IBM gave a series of seminars on introductory dynamical systems theory. In addition to the usual intense schedule of seminars on a variety of unfocussed topics falling into the general theme of the summer, the program included three "theme weeks." The first was focussed on climate dynamics, the second on bifurcation and pattern theory, and the third was the special "Mixing Week." Ten GFD Fellows, at various stages of their graduate work, undertook supervised research projects. This volume contains notes from the principal lectures and the Fellow's Reports. The program is made possible through the support of the National Science Foundation and the Office of Naval Research.

17. Document Analysis   a. Descriptors
nonlinear dynamics
fluids
geophysical fluid dynamics

b. Identifiers/Open-Ended Terms

c. COSATI Field/Group

18. Availability Statement	19. Security Class (This Report) UNCLASSIFIED	21. No. of Pages 308
Approved for public release; distribution unlimited.	20. Security Class (This Page)	22. Price

(See ANSI-Z39.18)   *See Instructions on Reverse*   OPTIONAL FORM 272 (4-77)
(Formerly NTIS-35)
Department of Commerce